# International Ocean Discovery Program
# Expedition 350 Preliminary Report

## Izu-Bonin-Mariana Rear Arc

## The missing half of the subduction factory

30 March–30 May 2014

Expedition 350 Scientists

Published by
International Ocean Discovery Program

## Publisher's notes



This publication was prepared by the International Ocean Discovery Program U.S. Implementing Organization (IODP-USIO): Consortium for Ocean Leadership, Lamont-Doherty Earth Observatory of Columbia University, and Texas A&M University, as an account of work performed under the International Ocean Discovery Program. Funding for the program is provided by the following agencies:

National Science Foundation (NSF), United States

Ministry of Education, Culture, Sports, Science and Technology (MEXT), Japan

European Consortium for Ocean Research Drilling (ECORD)

Ministry of Science and Technology (MOST), People's Republic of China

Korea Institute of Geoscience and Mineral Resources (KIGAM)

Australian Research Council (ARC) and GNS Science (New Zealand), Australian/New Zealand Consortium

Ministry of Earth Sciences (MoES), India

Coordination for Improvement of Higher Education Personnel, Brazil

## Disclaimer



## Copyright



Citation:
Expedition 350 Scientists, 2014. Izu-Bonin-Mariana rear arc: the missing half of the subduction factory. *International Ocean Discovery Program Preliminary Report,* 350. http://dx.doi.org/10.14379/iodp.pr.350.2014

## ISSN

World Wide Web: 2372-9562

September 2014

# Expedition 350 participants

## Expedition 350 scientists

**Yoshihiko Tamura**
**Co-chief Scientist**
Research and Development Center for Ocean Drilling Science
Japan Agency for Marine-Earth Science and Technology (JAMSTEC)
2-15 Natsushima-cho
Yokosuka 237-0061
Japan
**tamuray@jamstec.go.jp**

**Cathy J. Busby**
**Co-chief Scientist**
Department of Earth Science
University of California, Santa Barbara
Santa Barbara CA 93106
USA
**cathy@eri.ucsb.edu**

**Peter Blum**
**Expedition Project Manager/Staff Scientist**
International Ocean Discovery Program
Texas A&M University
1000 Discovery Drive
College Station TX 77845
USA
**blum@iodp.tamu.edu**

**Gilles Guèrin**
**Logging Staff Scientist**
Borehole Research Group
Lamont-Doherty Earth Observatory of Columbia University
PO Box 1000, 61 Route 9W
Palisades NY 10964
USA
**guerin@ldeo.columbia.edu**

**Graham D.M. Andrews**
**Volcanologist**
Department of Geology
California State University Bakersfield
9001 Stockdale Highway
Bakersfield CA 93311
USA
**gandrews1@csub.edu**

**Abigail K. Barker**
**Petrologist**
Institute of Earth Sciences
Uppsala University
Villavägen 16
752 36 Uppsala
Sweden
**abigail.barker@geo.uu.se**

**Julien L.R. Berger**
**Petrologist**
Laboratoire GET
Observatoire Midi-Pyrenees
Universite Paul Sabatier, Toulouse III
14, Avenue Edouard Belin
31400 Toulouse
France
**julien.berger@get.obs-mip.fr**

**Everton M. Bongiolo**
**Volcanologist**
Departamento de Geologia
Universidade Federal do Rio de Janeiro
Avendia Athos da Silveira Ramos, 274, Bloco G
Campus Ilha do Fundao, Cidade Universitaria
Rio de Janeiro 21941-916
Brazil
**ebongiolo@geologia.ufrj.br**

**Manuela Bordiga**
**Paleontologist (nannofossils)**
Department of Earth Science, Paleobiology
Uppsala University
Villavägen 16
752 36 Uppsala
Sweden
**manuela.bordiga@geo.uu.se**

**Susan M. DeBari**
**Petrologist**
Department of Geology
Western Washington University
516 High Street
Mail Stop 9080
Bellingham WA 98225
USA
**debari@geol.wwu.edu**

**James B. Gill**
**Petrologist**
Earth and Planetary Sciences
University of California, Santa Cruz
Santa Cruz CA 95064
USA
**gillord@ucsc.edu**

**Cedric Hamelin**
**Petrologist**
Centre for Geobiology
University of Bergen
Allegaten 41
N-5007 Bergen
Norway
**ced.hamelin@gmail.com**

**Jihui Jia**
**Physical Properties Specialist**
Kyoto University
Department of Urban Management
C1-1-118 Kyotodaigaku-Katsura Nishikyo-ku
Kyoto 615-8540
Japan
**justinbrilliance@gmail.com**

**Eleanor H. John**
**Paleontologist (foraminifers)**
Department of Earth Sciences
Cardiff University
Main Building
Cardiff CF10 3AT
United Kingdom
**eleanor.h.john@googlemail.com**

**Ann-Sophie Jonas**
**Organic Geochemist**
Department of Organic Geochemistry
Institute of Geosciences
Christian-Albrechts-Universität zu Kiel
Ludewig-Meyn-Strasse 10
24118 Kiel
Germany
**ann-sophie.jonas@web.de**

**Martin Jutzeler**
**Sedimentologist**
Marine Geoscience Group
National Oceanography Centre
European Way, Waterfront Campus
Southampton SO14 3ZH
United Kingdom
**jutzeler@gmail.com**

**Myriam A.C. Kars**
**Paleomagnetist**
Kochi University
Center for Advanced Marine Core Research
B200 Monobe
Nankoku 783-8502
Japan
**jm-mkars@kochi-u.ac.jp**

**Zachary A. Kita**
**Paleontologist (nannofossils)**
Department of Earth and Atmospheric Sciences
University of Nebraska, Lincoln
214 Bessey Hall
Lincoln NE 68588
USA
**zkita@huskers.unl.edu**

**Kevin Konrad**
**Inorganic Geochemist**
College of Earth, Ocean and Atmospheric Sciences
Oregon State University
104 CEOAS Administration Building
Corvallis OR 97331
USA
**Konradke@geo.oregonstate.edu**

**Susan H. Mahony**
**Physical Properties Specialist**
Department of Earth Sciences
University of Bristol
Wills Memorial Building, Queen's Road
Bristol BS8 1RJ
United Kingdom
**sue.mahony@bris.ac.uk**

**Michelangelo Martini**
**Physical Properties Specialist**
Instituto de Geología
Universidad Nacional Autónoma de México
Ciudad Universitaria
04510, Mexico, D.F.
**mmartini@geologia.unam.mx**

**Takashi Miyazaki**
**Inorganic Geochemist**
Research and Development Center for Ocean Drilling Science
Japan Agency for Marine-Earth Science and Technology (JAMSTEC)
2-15 Natsushima-cho
Yokosuka 237-0061
Japan
**tmiyazaki@jamstec.go.jp**

**Robert J. Musgrave**
**Paleomagnetist**
School of Geosciences
The University of Sydney
Sydney NSW 2006
Australia
**robert.musgrave@trade.nsw.gov.au**

**Debora B. Nascimento**
**Volcanologist**
Departamento de Geologia
Universidade Federal do Rio de Janeiro
Avendia Athos da Silveira Ramos, 274, Bloco G
Campus Ilha do Fundao, Cidade Universitaria
Rio de Janeiro 21941-916
Brazil
**debora@geologia.ufrj.br**

**Alexander R.L. Nichols**
**Petrologist**
Research and Development Center for Ocean Drilling Science
Japan Agency for Marine-Earth Science and Technology (JAMSTEC)
2-15 Natsushima-cho
Yokosuka 237-0061
Japan
**nichols@jamstec.go.jp**

**Julia M. Ribeiro**
**Igneous Petrologist**
Department of Geosciences
University of Texas at Dallas
800 West Campbell Road ROC
Richardson TX 75080
USA
**juliaribeiro@utdallas.edu**

**Tomoki Sato**
**Physical Properties Specialist**
Research and Development Center for Ocean Drilling Science
Japan Agency for Marine-Earth Science and Technology (JAMSTEC)
2-15 Natsushima-cho
Yokosuka 237-0061
Japan
**t-sato@jamstec.go.jp**

**Julie C. Schindlbeck**
**Volcanologist**
GEOMAR Helmholtz Center for Ocean Research Kiel
Wischhofstraße 1-3, Building 8A Room 211
24148 Kiel
Germany
**jschindlbeck@geomar.de**

**Axel K. Schmitt**
**Inorganic Geochemist**
Department of Earth, Planetary, and Space Sciences
University of California, Los Angeles
595 Charles Young Drive E Geology Building
Room 3640
Los Angeles CA 90095
USA
**axel@argon.epss.ucla.edu**

**Susanne M. Straub**
**Petrologist**
Geochemistry Division
Lamont-Doherty Earth Observatory of Columbia University
61 Route 9W
Palisades NY 10964
USA
**smstraub@ldeo.columbia.edu**

**Maryline J. Vautravers**
**Paleontologist (foraminifers)**
Department of Earth Sciences
University of Cambridge
Downing Street
Cambridge CB2 3EQ
United Kingdom
**mv217@cam.ac.uk**

**Yang Yang**
**Inorganic Geochemist**
Guangzhou Institute of Geochemistry
Chinese Academy of Sciences
511 Kehua Street, Tianhe District
Guangzhou, Guangdong
P.R. China
**yangyang@gig.ac.cn**

## Education and outreach

**Lesley E. Allen**
**Education Officer**
Truro College
Truro
Cornwall TR1 3XX
United Kingdom
**lesleya@truro-penwith.ac.uk**

**Julia M. DeMarines**
**Education Officer**
Denver Museum of Nature and Science
2001 Colorado Boulevard
Denver CO 80205
USA
**Julia.DeMarines@gmail.com**

## SIEM Offshore AS officials

**Steve Bradley**
Master of the Drilling Vessel

**Wayne Malone**
Offshore Installation Manager

## Technical support

**Lisa Brandt**
**Chemistry Laboratory**

**Kristin Bronk**
**X-ray/Microbiology Laboratory**

**Timothy Bronk**
**Assistant Laboratory Officer**

**Chad Broyles**
**Curatorial Specialist**

**Lisa Crowder**
**Assistant Laboratory Officer**

**Emily Fisher**
**Thin Section Laboratory**

**Clayton Furman**
**Logging Engineer**

**Tim Fulton**
**Imaging Specialist**

**Randy Gjesvold**
**Marine Instrumentation Specialist**

**Thomas Gorgas**
**Physical Properties Laboratory**

**Rachael Gray**
**Chemistry Laboratory**

**Kevin Grigar**
**Operations Superintendent**

**Margaret Hastedt**
**Core Laboratory**

**Michael Hodge**
**Marine Computer Specialist**

**Zenon Mateo**
**Underway Geophysics Laboratory**

**William Mills**
**Laboratory Officer**

**Algie Morgan**
**Applications Developer**

**Beth A. Novak**
**Paleomagnetism Laboratory**

**Garrick Van Rensburg**
**Marine Instrumentation Specialist**

**Thomas Wick**
**Marine Computer Specialist**

**Hai (James) Zhao**
**Applications Developer**

**Jean Wulfson**
**Publications Specialist**

# Abstract

International Ocean Discovery Program (IODP) Hole U1436A (proposed Site IBM-4GT) lies in the western part of the Izu fore-arc basin, ~60 km east of the arc-front volcano Aogashima, ~170 km west of the axis of the Izu-Bonin Trench, 1.5 km west of Ocean Drilling Program (ODP) Site 792, and at 1776 meters below sea level (mbsl). It was drilled as a 150 m deep geotechnical test hole for potential future deep drilling (5500 meters below seafloor [mbsf]) at proposed Site IBM-4 using the D/V *Chikyu*. Core from Site U1436 yielded a rich record of Late Pleistocene explosive volcanism, including distinctive black glassy mafic ash layers that may record large-volume eruptions on the Izu arc front. Because of the importance of this discovery, Site U1436 was drilled in three additional holes (U1436B, U1436C, and U1436D), as part of a contingency operation, in an attempt to get better recovery on the black glassy mafic ash layers and enclosing sediments and to better constrain the thickness of the mafic ash layers.

IODP Site U1437 is located in the Izu rear arc, ~330 km west of the axis of the Izu-Bonin Trench and ~90 km west of the arc-front volcanoes Myojinsho and Myojin Knoll, at 2117 mbsl. The primary scientific objective for Site U1437 was to characterize "the missing half of the subduction factory"; this was because numerous ODP/Integrated Ocean Drilling Program sites had been drilled in the arc to fore-arc region (i.e., ODP Site 782A Leg 126), but this was the first site to be drilled in the rear part of the Izu arc. A complete view of the arc system is needed to understand the formation of oceanic arc crust and its evolution into continental crust. Site U1437 on the rear arc had excellent core recovery in Holes U1437B and U1437D, and we succeeded in hanging the longest casing ever in the history of R/V *JOIDES Resolution* scientific drilling (1085.6 m) in Hole U1437E and cored to 1806.5 mbsf.

The stratigraphy at Site U1437 was divided into seven lithostratigraphic units (I–VII) that were distinguished from each other based on the proportions and characteristics of tuffaceous mud/mudstone and interbedded tuff, lapilli tuff, and tuff breccia. The section is much more mud rich than expected, with ~60% tuffaceous mud for the section as a whole (89% in the uppermost 433 m) and high sedimentation rates of 100–260 m/My for the upper 1320 m (Units I–V). The proportion (40%) and grain size of tephra are much smaller than expected for an intra-arc basin, composed half of ash/tuff and half of lapilli tuff of fine grain size (clasts < 3 cm). These were deposited by suspension settling through water and from density currents, in relatively distal settings. Volcanic blocks are only sparsely scattered through the lowermost 25% of the

section (Units VI and VII, 1320–1806.5 mbsf), which includes hyaloclastite, in situ quench-fragmented blocks, and a rhyolite peperite intrusion (i.e., proximal deposits). The transition from unconsolidated to lithified rocks occurred progressively; however, sediments were considered lithified from 427 mbsf (top of Hole U1437D) downward. Alteration resulted in destruction of fresh glass from ~750 mbsf downward, but minerals are less altered. Because of the alteration, the deepest biostratigraphic datum was at ~850 mbsf and the deepest paleomagnetic datum was at ~1300 mbsf. Additional age control deeper than this depth is provided by an age range of 10.97–11.85 Ma inferred from a nannofossil assemblage at ~1403 mbsf and a preliminary U-Pb zircon concordia intercept age of 13.6 +1.6/–1.7 Ma, measured postcruise on a rhyolite peperite in Unit VI at ~1390 mbsf.

Based on the seismic profiles, the Miocene–Oligocene hiatus (~17–23 Ma) was predicted to lie at ~1250 mbsf, but strata at that depth (Unit V, 1120–1312 mbsf) are much younger (~9 Ma), indicating that we recovered a thicker Neogene section of volcaniclastics and associated igneous rocks than anticipated. Our preliminary interpretation of shipboard geochemistry is that arc-front versus rear-arc sources can be distinguished in the upper, relatively distal 1320 m of section (Units I–V), whereas the lower, proximal 25% of the section (Units VI–VII) may be geochemically heterogeneous, suggesting that the rear-arc magmas only fully compositionally diverged after ~13 Ma.

## Background and objectives

International Ocean Discovery Program (IODP) Expedition 350 was one of three closely related IODP expeditions carried out in sequence in the Izu-Bonin-Mariana (IBM) arc system in 2014 (Figs. **F1, F2, F3**). Expedition 350 was the first expedition to be drilled in the Izu rear arc; all previous Integrated Ocean Drilling Program sites were drilled in or near the Izu-Bonin arc front or fore arc (Fig. **F1B**), leading to an incomplete view of Izu arc magmatism. Thus, the main objective of Expedition 350 was to reveal the history of "the missing half" of the subduction factory (Tamura et al., 2013). The second expedition (351) will focus on IBM arc origins by drilling west of the Kyushu-Palau Ridge (Fig. **F3**), where it is inferred that the foundation, origin, and early evolution of the IBM arc are recorded (Arculus et al., 2013). The third expedition (352) will examine the processes of subduction initiation, by drilling the outer IBM fore arc (Pearce et al., 2013).

The goal of Expedition 350 was to core and log one site on the Izu rear arc, Site U1437 (proposed Site IBM-3C). This site was chosen to provide a temporal record of rear-arc magma compositions, ideally from Eocene to Neogene time, allowing comparison with the previously drilled fore-arc magmatic record and determination of across-arc geochemical variations throughout the history of the arc system. Rear-arc magmatic evolution is important to understand because the chemistry of the samples dredged from the tops of rear-arc volcanoes are more similar to the average composition of continental crust than those of frontal volcanoes and seismic crustal structure suggests that the rear arc overlies the majority of "continental type" crust in the Izu arc system (Tamura et al., 2013). The Izu rear arc is therefore important for understanding how arc magmas and intracrustal differentiation produces crust that is similar in composition to the "averaged continental crust."

A secondary goal of Expedition 350 was to obtain a geotechnical core for a potential future deep (5500 mbsf) drilling program at Site U1436 (proposed Site IBM-4) with the D/V *Chikyu*. Although this operation took only 1 day of the 60 day expedition, it yielded a rich, relatively complete record of Late Pleistocene fore-arc sedimentation that is strongly influenced by frontal arc explosive volcanism. This is highly complementary to the main objective of Expedition 350, the rear-arc subduction factory (Site U1437), and will enable us to further understand the formation and the evolution of the Izu arc system.

Before presenting our scientific results, we first review general information on the evolution of the IBM arc system and then provide background on three topics related to our scientific results in the Izu arc: the evidence that Paleogene crust lies beneath both drilled sites, the Quaternary arc-front volcanic record, and the Neogene rear-arc volcanic record.

## Evolution of the IBM arc system

The IBM arc formed in response to subduction of the Pacific plate over the past 52 My (Stern et al., 2003). Subduction began as part of a hemisphere-scale foundering of old, dense lithosphere in the western Pacific (Bloomer et al., 1995; Cosca et al., 1998). During the subduction initiation stage (~52–47 Ma), igneous activity successively produced low-K mid-ocean-ridge basalt (MORB)-like tholeiite, boninite, and subordinate low-K rhyolite across the region that now lies in the fore arc. This suggests that sinking of the downgoing plate was rapidly followed by a dramatic episode of asthenospheric upwelling and melting, sometimes enhanced by solute-bearing water fluxes

released from the downgoing plate, over a zone that was thousands of kilometers long and as wide as 200 km (Reagan et al., 2010). As subduction proceeded, hydrous mantle melting overprinted decompression mantle melting, establishing the first mature arc in Eocene to Oligocene time (Taylor, 1992; Ishizuka et al., 2006a, 2006b, 2011). This mature arc is labeled the "Kyushu-Palau arc" on Figure **F2A** and **F2B.** Eocene arc-front lava, dated at ~40–42 Ma by $^{40}Ar/^{39}Ar$ by Ishizuka et al. (2011), has been drilled in what is now the Izu fore-arc basement. However, no Oligocene arc rocks (lava or intrusions) have been recovered in the Izu arc, although Oligocene turbidites with andesitic clasts rest upon Eocene lava in what is now the fore arc (Taylor, Fujioka, et al., 1990; Gill et al., 1994), indicating that Oligocene arc volcanism occurred somewhere west in the region. By ~25 Ma, rifting began along the length of the Kyushu-Palau arc (Fig. **F2C**), and opening of the Shikoku Basin isolated the rear-arc volcanoes from the arc-front volcanoes (Fig. **F2D**), producing the Kyushu-Palau Ridge remnant arc, which has Eocene and Oligocene rear-arc rocks. However, Oligocene Kyushu-Palau arc-front rocks have not been found, although they are inferred to underlie the Neogene IBM arc on Figure **F2B** and **F2C.** Moreover, they may lie beneath the rear arc, as inferred by Kodaira et al. (2008) and discussed further below (see Figs. **F4, F5**). Seafloor spreading of the Shikoku and Parece Vela Basins at ~25–17 Ma was likely accompanied by a hiatus in arc magmatism (Fig. **F2D**), but the fore-arc sedimentary record shows that arc-front volcanism resumed by ~17 Ma (Stern et al., 2003), referred to as the Neogene arc, and shown as the IBM arc on Figure **F2D** and **F2E,** where the Neogene IBM arc front is shown in nearly the same position as the Paleogene arc front. However, pre-Quaternary rocks have not been recovered from the IBM arc front, perhaps because they are buried or could be partly remelted and/or remobilized during the Quaternary. In contrast, the Izu rear arc (Fig. **F2E**) has not been extensively buried or modified by Quaternary magmatic processes, so Neogene rocks are well preserved; these are dominated by ~17 to 3 Ma northeast-trending rear-arc seamount chains (Fig. **F6**), described in **"Neogene rear arc volcanism, Izu arc."** The Marianas segment of the IBM arc (Fig. **F1A**) differs from the Izu segment by lacking the rear-arc seamount chains; instead, a new episode of arc rifting began at ~7 Ma, resulting in opening of the Mariana Trough back-arc basin by seafloor spreading at ~3–4 Ma (Fig. **F3**) (Yamazaki and Stern, 1997). Rifting of the Izu arc began at ~3 Ma, behind the arc front, described in **"Neogene rear arc volcanism, Izu arc."**

We know more about the Neogene history of the IBM arc than we do about its Paleogene history; yet it is thought that most of the IBM crust was generated in the Paleogene (Eocene–Oligocene; Kodaira et al., 2008). Furthermore, silicic volcanoes of the Quaternary arc front and Miocene granitic rocks in the Izu collision zone on Honshu

are inferred to have formed by melting of Eocene–Oligocene arc crust (Tamura et al., 2009, 2010). As discussed in **"Scientific results,"** Neogene rhyolite volcanism may be more important in the Izu rear-arc seamount chain than previously thought and could have resulted from melting of Paleogene "arc basement." For this reason, we will now review the evidence for Paleogene arc basement highs in the Izu arc and discuss constraints on their age and origin.

## Paleogene arc basement highs in the Izu arc

Magnetic and seismic surveys, summarized in this section, indicate that both IODP Sites U1436 and U1437 lie along buried north–south ridges that consist of magmatic crystalline rocks, which are inferred to be Oligocene–Eocene (Paleogene) in age. However, no Oligocene lava or crystalline rocks have been found in the Izu arc, as summarized here.

Three conspicuous, approximately north–south rows of long-wavelength magnetic anomalies were identified by Yamazaki and Yuasa (1998) in the Izu-Bonin arc system and attributed to loci of middle- to lower-crustal magmatic bodies (Fig. **F3**):

- The western north–south anomaly corresponds to the Kyushu-Palau Ridge, where Eocene and Oligocene lava was dredged; these have been geochemically characterized as rear-arc magmas (Ishizuka et al., 2011), rifted off the Paleogene arc during the opening of the Shikoku Basin (Kodaira et al., 2008).
- The eastern north–south anomaly lies in the modern fore arc near the arc front and corresponds to the Shin-Kurose Ridge (Fig. **F3**) (Yamazaki and Yuasa, 1998), also referred to as the Izu fore-arc high (Taylor, Fujioka, et al., 1990). The Shin-Kurose Ridge/fore-arc high forms a bathymetric high in the northern Izu arc and is buried beneath Oligocene to Quaternary volcaniclastic and sedimentary rocks in the southern Izu arc, at Ocean Drilling Program (ODP) Site 792 and Site U1436. Andesite lava in the lowest 82 m at Site 792 was referred to as "Oligocene basement," on the basis of K/Ar ages (Taylor, Fujioka, et al., 1990; Taylor, 1992). However, $^{40}Ar/^{39}Ar$ dating on the lava from two different depths gave consistent and well-defined plateaus of 40.4 ± 0.8 Ma and 40.6 ± 0.3 Ma, or Eocene ages (Ishizuka et al., 2011) (Fig. **F7**). Similarly, andesite lava "basement rocks" drilled in the modern fore-arc basin outboard of this, at ODP Site 793, are Eocene (41 Ma; Ishizuka et al., 2011). Farther outboard, in the outer arc high drilled at ODP Site 786, the basement consists of boninite lava (45.3–46.7 Ma) overlain by andesite lava (44.7 Ma; all by $^{40}Ar/$

$^{39}$Ar; Ishizuka et al., 2006a), all Eocene in age. Thus, Oligocene basement has not been found in the fore arc.

- The central north–south magnetic anomaly lies buried in the Izu rear arc (Fig. **F3**) and is referred to as the Nishi-shichito Ridge (Figs. **F4, F5**) (Yamazaki and Yuasa, 1998). This basement high has not been drilled and was one of the objectives of Expedition 350. Kodaira et al. (2008) ran a wide-angle seismic profile along the length of the rear-arc Nishi-shichito Ridge and compared it to a wide-angle seismic profile made along the length of the arc front by Kodaira et al. (2007a, 2007b) (Fig. **F5**). They divided the arc front into segments based on variations in the thickness of middle crust and did the same for the rear-arc Nishi-shichito Ridge. They concluded that although the thickness of the middle crust for each rear-arc segment is smaller than the frontal arc, the bulk compositions of the crust are almost identical. Furthermore, they used the match on middle crustal thicknesses to infer that the Nishi-shichito Ridge is a "paleo-arc" that obliquely rifted off the volcanic front in an extension direction parallel to the northeast–southwest Sofugan Tectonic Line (Fig. **F4**). The Sofugan Tectonic Line is the boundary between the Izu and Bonin arc segments (Fig. **F3**); south of it lies the prominent Bonin Ridge and the deep fault-bounded Ogasawara Trough to the west, produced by Eocene to early Oligocene arc magmatism and back-arc extension, respectively. This prominent arc ridge and fault-controlled back-arc basin are not present north of the Sofugan Tectonic Line, so we speculate that the Sofugan Tectonic Line originated as an accommodation fault between a region of high extension to the south and little or no extension to the north. Kodaira et al. (2008) propose that oblique rifting of the Nishi-shichito Ridge paleo-arc off the arc front occurred during the opening of the Shikoku Basin, sometime after ~30 Ma. If the oblique rifting model is correct, the crystalline basement beneath Site U1437, not reached during Expedition 350, may represent rear-arc crust but formed in a position much closer to the arc front than it is now; alternatively, it may represent arc-front crust that has become stranded in the rear arc by rifting. New seismic surveys undertaken in preparation for drilling at Site U1437, described briefly in **"Scientific results,"** also support the interpretation that the rear arc is underlain by Paleogene arc basement rocks.

## Quaternary arc-front volcanic record, Izu arc

A brief overview of Quaternary arc-front volcanism is provided as background for discussion of Pleistocene tephra encountered at Sites U1436 and U1437.

The IBM volcanic arc system is an excellent example of an intraoceanic convergent margin where the effects of crustal anatexis and assimilation are considered to be minimal (Stern et al., 2003; Tatsumi and Stern, 2006). Nonetheless, volume estimates of rock types from the Quaternary Izu arc suggest that dacite and/or rhyolite form a major mode, although basalt and basaltic andesite (<57 wt% $SiO_2$) are clearly the predominant eruptive products (Tamura and Tatsumi, 2002). About half of the edifices at the Quaternary volcanic front are calderas dominated by rhyolite (Figs. **F8, F9**) (Yuasa and Kano, 2003). Turbidites sampled during ODP Leg 126 in the Izu arc, which range in age from 0.1 to 31 Ma, are similarly bimodal (Gill et al., 1994).

The Quaternary volcanic front of the Izu arc shows along-strike correlations between crustal structure and the average composition of volcanic front magmas, shown by an active source wide-angle seismic study along the northernmost 550 km of the Izu arc front (Fig. **F5**). As illustrated in Figure **F8,** there is an along-arc periodic variation in average crustal thickness with a wavelength of ~80–100 km, reflecting variations in the thickness of the middle crust (whereas the lower crust has uniform thickness). These periodic variations correlate well with the average chemical composition of the overlying arc volcanoes; that is, the thicker middle crust underlies the basaltic island volcanoes, whereas the thinner middle crust underlies the rhyolitic submarine volcanoes (mainly calderas). Thus, the velocity structure of this part of the Izu arc crust, which has a complex 50 My history, appears to correlate well with the chemical composition of the Quaternary volcanoes. Contrary to the situation common for continental arcs, the basaltic volcanoes overlie lower average velocity (more continental-like) crust compared with the silicic volcanoes, which overlie thinner middle crust. This may indicate that the silicic volcanoes formed by melting of Eocene–Oligocene arc crust (Tamura et al., 2009) and that this process thinned the middle crust beneath them in some way. If this model is correct, the rear arc may show similar variation (i.e., silicic volcanoes on thinner middle crust and more mafic volcanoes on thicker middle crust). However, rear-arc Miocene volcanoes (white stars in Fig. **F5**) and underlying crustal structure (possibly Oligocene–Eocene) do not correlate each other like the volcanic front.

## Neogene rear-arc volcanism, Izu arc

We refer to all Neogene volcanic rocks behind the Izu arc front as rear-arc volcanic rocks. Rear-arc volcanic rocks (Fig. **F10**) include (1) the ~17–3 Ma east northeast–trending basaltic to rhyolitic rear-arc seamount chains, (2) the <3 Ma bimodal back-arc knolls of the broad extensional zone, and (3) the <1.5 Ma bimodal volcanic rocks

of the active rift immediately behind the arc front. Thus, Izu rear-arc volcanism falls into two magmatic suites: the <3 Ma bimodal rift-type magmas and the ~17–3 Ma basalt to rhyolite rear-arc seamount-type magmas. Both types lie within the rear part of the arc (i.e., behind the arc front) and lie on arc crust, although the westernmost end of the rear-arc seamount chains lies on Shikoku Basin oceanic crust. The bimodal rift-type magmas differ from both the volcanic front and the rear-arc seamount chains in trace element and radiogenic isotopic ratios; this has been variably attributed to (1) a transition from flux to decompression mantle melting as arc rifting commences, (2) a change in the character of slab-derived flux, or (3) a change in the magma source mantle through mantle wedge convection (Hochstaedter et al., 1990a, 1990b, 2001; Ishizuka et al., 2003a, 2006b; Tollstrup et al., 2010).

The Izu rear-arc seamount chains are as long as ~80 km and strike N60°E (Fig. **F6**). The tops of the Izu rear-arc volcanic chains were sampled by dredging, and their compositions range from basalt to rhyolite (Ishizuka et al., 1998, 2003b; Hochstaedter et al., 2000). Three main hypotheses have been proposed for the origin of the seamount chains:

1. They are related to compression caused by collision between the southwest Japan and Izu arcs, associated with opening of the Japan Sea (Karig and Moore, 1975a; Bandy and Hilde, 1983).
2. They formed along Shikoku Basin transform faults (Yamazaki and Yuasa, 1998).
3. They overlie diapirs in the mantle wedge (Fig. **F11**), such as the “hot fingers” proposed for northeast Japan (Tamura et al., 2002).

In some cases (e.g., Manji and Genroku seamount chains), the seamount chains seem aligned with large volcanoes on the volcanic front (e.g., Aogashima and Sumisu, respectively) (Fig. **F6**); however, the alignment is imperfect, and it is not clear which hypothesis a perfect alignment would support.

A striking characteristic of volcanic arcs is the asymmetry in geochemical characteristics with distance from the trench, which was known prior to the advent of plate tectonics (Kuno, 1959; Dickinson and Hatherton, 1967). Izu arc-front rocks are low-K, but the rear-arc type lava is medium- to high-K (Gill, 1981) (Fig. **F12**). Similarly, arc-front volcanic rocks are strongly depleted in incompatible light rare earth elements (REEs) relative to the middle and heavy REEs, whereas lava from rear-arc seamount chains is enriched in light REEs. Gamma radiation logs obtained during Expedition 350 rear-arc drilling should record higher K, U, and Th and lower Th/U than those from drilling at the Izu-Bonin fore-arc sites, where tephra come from the arc front. On

both $K_2O$ versus $SiO_2$ and REE plots, the composition of the rear-arc seamount chain magmas is more similar to the continental crust composition than the arc-front magmas (Fig. **F12**). Thus, the Izu rear-arc magmatism and crust formation appears to be a better analog to generate continental crust than the arc front.

Although Site U1437 is in a location chosen to be topographically shielded from arc front–derived sediment gravity flows, arc front–derived ash fall and turbidity current deposits may be present. However, it should be possible to distinguish between arc-front and rear-arc seamount chain sources because the lava of the rear-arc seamount chains is enriched in alkalis, high–field strength elements (HFSE) (e.g., Nb and Zr), and other incompatible elements but has less enriched Sr, Nd, Hf, and Pb isotopes compared to the lava of the volcanic front (Hochstaedter et al., 2001; Ishizuka et al., 2003a; Tamura et al., 2007) (Fig. **F12**). However, the <3 Ma bimodal volcanic rocks of the broad extensional zone and narrow active rift are not easily distinguished from rear-arc seamount chain or arc-front rocks (Hochstaedter et al., 2001), and Site U1437 may not be shielded from sediment gravity flows from those sources. Therefore, we expect to be able to distinguish rear-arc and arc-front magmas for all rocks ranging from 17 to 3 Ma but not necessarily for rocks <3 Ma.

We do not know if arc geochemical asymmetry was present early in the history of the arc (in the Paleogene) or if it is strictly a Neogene feature. These two options are presented as "from the beginning" and "from the middle" hypotheses in Figure **F13.** Paleogene rocks were drilled in the fore arc, so their chemistry is known; however, no drilling has been done in the rear arc, so its Paleogene chemistry is unknown.

Site U1437 lies in a ~20 km wide basin in the low area between two major constructional volcanic ridges: the Manji and Enpo rear-arc seamount chains. It is therefore classified as a volcano-bounded intra-arc basin using the criteria elucidated by Smith and Landis (1995) as illustrated in Figure **F14.** In contrast, the active rift to the east of Site U1437 is a fault-bounded intra-arc basin. For simplicity, the volcano-bounded basin bounded by the Enpo and Manji rear-arc seamount chains is referred to as the Enpo-Manji volcano-bounded basin (Fig. **F15**). Similarly, we propose that future workers refer to other basins between rear-arc seamount chains by the names of the chains that bound them (e.g., Genroku-Enpo Basin and Manji-Kan'ei Basin, Fig. **F6**).

# Scientific results

## New descriptive scheme for volcaniclastic rocks

The lithologic classification of sedimentary, volcaniclastic, and igneous rocks recovered by Expedition 350 uses a new scheme for describing volcaniclastic and nonvolcaniclastic sediments but uses generally established (International Union of Geological Sciences) schemes for igneous rocks (Fig. **F16;** Tables **T1, T2, T3, T4**). The new scheme was devised to improve description of volcaniclastic sediments and their mixtures with nonvolcanic (siliciclastic, chemical, and biogenic) sediments but maintaining the usefulness of prior schemes for describing nonvolcanic sediments (Fig. **F16**). The new scheme follows the recommendations of a dedicated core description workshop held in January 2014 in College Station, Texas (USA), prior to the cruise, that was attended by participants of all 2014 IODP expeditions (349, 350, 351, and 352) and was modified and tested during Expedition 350. The new scheme was devised for use in a spreadsheet-based descriptive information capture program designed by IODP (DESClogik), and the spreadsheet configurations were modified to use this scheme. This scheme was devised to facilitate the understanding of volcano-sedimentary processes by making reproducible and quantifiable observations of volcanic input to the sedimentary record. Also during Expedition 350, the new scheme shown in Figure **F16** was applied to microscopic description of core samples, and the DESClogik microscope spreadsheet configurations were modified to use this scheme.

### Rationale

During Expedition 350, sediments and sedimentary rocks were classified using a rigorously nongenetic approach, which integrates volcanic particles into the sedimentary descriptive scheme typically used by IODP (Fig. **F16**). This is necessary because volcanic particles are the most abundant particle type in arc settings like those drilled during the IBM expeditions. The methodology developed allows, for the first time, a comprehensive description of volcanogenic and nonvolcanogenic sediments and sedimentary rocks and integrates with descriptions of coherent volcanic and igneous rocks (i.e., lava and intrusions) and the coarse clastic material derived from them. This classification allows expansion to bioclastic and nonvolcanogenic detrital realms.

The purpose of the new classification scheme (Fig. **F16**) is to include volcanic particles in the assessment of sediments and rocks recovered in cores, be accessible to scientists with diverse research backgrounds and experiences, allow relatively quick and smooth data entry, and display data seamlessly in graphical presentations. The new

classification scheme is based entirely on observations that can be made by any scientist at the macroscopic and microscopic level, with no genetic inferences, making the data more reproducible from user to user.

Classification and nomenclature of deposits with volcanogenic clasts has varied considerably throughout the last 50 y (Fisher, 1961; Fisher and Schmincke, 1984; Cas and Wright, 1987; McPhie et al., 1993; White and Houghton, 2006), and no consensus has yet been reached. Moreover, even the most basic descriptions and characterizations of mixed volcanogenic and nonvolcanogenic sediments are fraught with competing philosophies and imperfectly applied terminology. Volcaniclastic classification schemes are all too often overly based on inferred modes of genesis, including inferred fragmentation processes or inferred transport and depositional processes and environments. However, submarine-erupted and deposited volcanic sediments are typically much more difficult to interpret than their subaerial counterparts, partly because of more complex density-settling patterns through water relative to air (e.g., the ability of pumice to float is proportional to the volume of a clast) and the ease with which very fine grained sediment is reworked by water. Soft-sediment deformation, bioturbation, and low-temperature alteration are also more significant in the marine realm relative to the terrestrial realm.

The goal of the new classification scheme is to make the description of volcanic-sedimentary mixtures more accessible to nonspecialists and also more "database ready" so that volcanic inputs can be evaluated quantitatively.

### Units

Sediments and sedimentary rocks, including volcaniclastic, siliciclastic, and bioclastic, were described at the level of (1) the descriptive interval (a single descriptive line in the DESClogik spreadsheet) and (2) the lithostratigraphic unit (Table **T1**). A descriptive interval typically consists of a single lithofacies distinct from those immediately above and below it (e.g., an ash interval intercalated between mudstone intervals); it is typically analogous to beds, with thicknesses classified in the same way (e.g., Ingram, 1954). In the case of closely intercalated, monotonous, repetitive successions (e.g., alternating thin sand and mud beds), lithofacies were grouped within the descriptive interval; this was done by using the lithology prefix "closely intercalated," followed by the principal name, which represents the most abundant facies, followed by suffixes for the subordinate facies, in order of abundance (Fig. **F16**). Lithostratigraphic units (Table **T1**) are assemblages of multiple descriptive intervals containing similar facies that are typically tens to hundreds of meters thick. Litho-

stratigraphic units should be clearly distinguishable from each other by several characteristics, such as composition, bed thickness, grain size class, and internal homogeneity. Following IODP tradition, they are numbered sequentially Unit I, Unit II, and so on, from the top to the bottom of the core.

### Sedimentary lithologic classes

The new descriptive scheme used during Expedition 350 defines four sedimentary lithologic classes, based on types of particles (Fig. **F16;** Table **T2**):

1. Volcanic lithologic class, defined as >75% volcanic particles.
2. Tuffaceous lithologic class, containing 25%–75% volcanic-derived particles mixed with nonvolcanic particles. The definition of the term "tuffaceous" (25%–75% volcanic particles) is modified from Fisher and Schmincke (1984).
3. Nonvolcanic siliciclastic lithologic class, containing <25% volcanic siliciclastic particles, where nonvolcanic siliciclastic particles dominate chemical and biogenic particles.
4. Biogenic lithologic class, containing <25% volcanic siliciclastic particles, where nonvolcanic siliciclastic particles are subordinate to chemical and biogenic particles.

### Principal names

In our new scheme, the principal name for sediments and sedimentary rocks is based on grain size (Fig. **F16**) and is purely descriptive; it does not depend on interpretations of fragmentation, transport, or depositional or alteration processes. The sedimentary grain size classes of Wentworth (1922) are used for the nonvolcanic siliciclastic and tuffaceous lithologic classes, whereas the grain size classes of Fisher and Schmincke (1984) are used for the volcanic lithologic class.

We use the general term "particles" to refer to the fragments that make up volcanic, tuffaceous, and nonvolcanic siliciclastic sediments and sedimentary rocks, regardless of the size of the fragments. However, we adopt a strict definition of the terms "grains" and "clasts," using clasts to describe particles >2 mm in size and grains to describe particles <2 mm in size. This size cut-off (2 mm) corresponds to the sand–granule grain size division of Wentworth (1922) and the ash–lapilli grain size divisions of Fisher (1961), Fisher and Schmincke (1984), Cas and Wright (1987), and McPhie et al. (1993) (Table **T3**). In addition, we include important information on the angularity of clasts by using the term "conglomerate" for a deposit where the clasts are exclusively (>95 vol%) rounded and subrounded, "breccia-conglomerate" where clasts are

predominantly (>50 vol%) rounded and/or subrounded, and "breccia" where clasts are predominantly (>50 vol%) angular.

### Prefixes

During Expedition 350, the prefix "monomict" was applied where clast compositions were restricted to a single type and "polymict" was applied where clast compositions of multiple types were present (Fig. **F16**). Where not obscured by alteration, an estimate of the compositional range of volcanic clasts was represented on macroscopic descriptions by three entries: "mafic," "bimodal," and "evolved," with intervals described as mafic inferred to be basalt and basaltic andesite and intervals described as evolved inferred to be intermediate and silicic in composition. In macroscopic analysis, mafic versus evolved intervals are defined by the grayscale index of the main particle component, with mafic grains and clasts usually ranging from black to dark gray and evolved grains and clasts ranging from dark gray to white. Microscopic examination further aided in assigning the prefix mafic or evolved using glass shard color and mineralogy; however, precise determination of bulk composition requires chemical analysis. During Expedition 350, the prefix "matrix-supported" was used where smaller particles visibly envelop each of the clasts and "clast-supported" was used where clasts (defined as >2 mm in diameter, above) form the sediment framework.

### Suffixes and other parameters

The suffix is used for a subordinate component that deserves to be highlighted. It is restricted to a single term (e.g., "with foraminifer," "with crystals," etc.). Bed thicknesses followed the terminology of Ingram (1954), and for simplicity, sorting values were restricted to three terms (well, moderately, and poor) and clast roundness values were also restricted to three terms (rounded, subrounded, and angular). Volcanic components included three major types (vitric, crystal, and lithic) sorted by their abundance into "dominant," "2nd order," and "3rd order." Vitric clasts and grains include pumice and scoria (light colored and dark colored, respectively) as well as dense glass, and "fiamme" was used to describe flat wispy volcanic particles with no implication for origin (e.g., welding versus burial/diagenetic compaction). Crystals are described as grains because they are <2 mm in size, and their shape (euhedral, subhedral, or anhedral) and type (e.g., quartz or feldspar) is noted where possible. Lithic grains and clasts were described as angular, subrounded, or rounded with types (e.g., volcanic evolved or volcanic mafic) noted. In macroscopic descriptions, matrix can be well, moderately, or poorly sorted with types (e.g., vitric, crystal, or lithic) noted.

### Summary of volcaniclastic rock descriptive scheme

The new volcaniclastic descriptive scheme applied during Expedition 350 uses a more nongenetic approach than proposed by previous authors because the sediments and rocks are named based on materials that are visible macroscopically and microscopically and not on the basis of inferred fragmentation, transport, and depositional processes (i.e., pyroclasts, autoclasts, hydroclasts, epiclasts, and reworked volcanic clasts [Fisher and Schmincke, 1984; Cas and Wright, 1987; McPhie et al., 1993]). Nonetheless, process interpretations can be entered as comments in the database; these may include inferences regarding fragmentation processes, eruptive environments, mixing processes, transport processes, alteration, and so on. The new descriptive scheme allows more quantitative evaluation of volcanic input and its nature, as demonstrated in the various lithostratigraphy, geochemistry, and interpretation sections in this report.

## Site U1436: Izu fore-arc record of arc-front explosive volcanism

Site U1436 is located at 32°23.88′N, 140°21.93′E (1776 m water depth), in the western part of the Izu-Bonin fore-arc basin ~60 km east of the arc-front volcano Aogashima and ~170 km west of the axis of the Izu-Bonin Trench, 1.5 km west of Site 792 (Figs. **F1, F3, F17**).

The plan for Site U1436 was to carry out a 1 day operation to core 150 meters below seafloor (mbsf) and collect geotechnical samples in preparation for potential future drilling at proposed Site IBM-4. Here, the *Chikyu* is proposed to drill 5.5 km below seafloor to reach arc middle crust, which is inferred to represent juvenile continental crust. The origin of continental crust remains one of the biggest unsolved problems in Earth science because continental crust, though volumetrically insignificant on a planetary scale, is an important reservoir for many trace and minor elements. The "andesite model" proposes that subduction zone magmatism produces the nuclei of new continental crust. However, the processes involved (e.g., partial melting of mantle sources, crystallization differentiation, or other processes) remain poorly understood. Ultra-deep drilling into arc crust is the best way to sample unprocessed juvenile continental-type crust as it is first generated at intraoceanic arcs, before its primary features are overprinted by accretion or incorporation into a larger or more mature continent. Geotechnical Site U1436 is important for assessing the suitability of near surface conditions for this ambitious undertaking.

Although Site U1436 was scheduled as a geotechnical hole for proposed Site IBM-4, it yielded a rich, relatively complete record of Late Pleistocene fore-arc sedimentation, strongly influenced by frontal arc explosive volcanism. This is highly complementary to the main objective of Expedition 350, the rear-arc subduction factory (Site U1437), in terms of understanding the Izu arc system as a whole. In addition, Site U1436 gave scientists the opportunity to "test drive" the newly devised descriptive scheme for volcaniclastic rocks, described above.

The Izu fore arc is a repository of ash/tuff erupted in the Izu-Bonin frontal arc because the wind prevailingly blows from west to east. Mafic effusive eruptive products are better preserved on the frontal arc islands, whereas more silicic materials from explosive volcanism are preserved in adjacent deep ocean basins. The major objective of Site U1436 (besides collecting geotechnical samples) is to characterize the chemistry, age, provenance, and textural characteristics of mafic and silicic explosive volcanic products from the arc front in order to better understand outputs that are not preserved on land. At Site U1436, this stratigraphic record consists of tuffaceous mud interstratified with mafic and evolved ash and lapilli ash.

### Age model, biostratigraphy, paleomagnetism, and physical properties

A 131.72 m succession of Pleistocene to Pliocene sediments was recovered over a cored interval of 150 m at Site U1436 (Fig. **F18**). Thirteen out of sixteen biostratigraphic datums and one magnetostratigraphic datum were selected to construct an age-depth relationship for this site and to estimate the linear sedimentation rates (LSRs) and mass accumulation rates (MARs). Biostratigraphic and magnetic reversal data are in agreement for the Late–Middle Pleistocene section, and the age model was constructed using all datum types. Both the biostratigraphic and magnetostratigraphic datums indicate a possible hiatus between Cores 350-U1436C-17F and 350-U1436A-14X (66–74 mbsf), with linear segments above (0–66 mbsf) and below (74–127 mbsf) the inferred hiatus; LSRs are 71 m/My above the inferred hiatus and 45 m/My below it. At nearby Site 792, a hiatus was identified at 87 mbsf. A comparison of LSRs between Sites U1436 and 792 over the same interval shows broadly similar values (81–120 m/My at Site 792) in the Late–Middle Pleistocene sequence. In the late Pliocene to early Pleistocene interval, however, Site U1436 shows a low LSR (46 m/My) compared to that of Site 792 (122 m/My). This difference could be due to underestimation of the LSR below the hiatus at Site U1436 because the tie points are not well constrained as a result of the rarity of marker species. The higher MAR in the younger part of the succession could explain the higher LSR, which could be related to greater volcanic input.

The biochronology at Site U1436 was primarily based on planktonic foraminifers and calcareous nannofossils. All the core catcher samples from Holes U1436A–U1436C were examined, and studies of both fossil groups showed that the upper 132 m of the cored interval in Hole U1436A (the deepest hole) spans the last 2.7 My (late Pliocene–Holocene). The timing of bioevents in the undisturbed part of the succession agrees with paleomagnetic data down to the Brunhes/Matuyama reversal (0.781 Ma) in Section 350-U1436A-9H-3. Deeper than 66 mbsf, several nannofossil and foraminifer bioevents were missing, indicating the presence of a hiatus. Below this potential hiatus, the rarity of markers and the occurrence of reworked specimens made identifying bioevents difficult. Planktonic foraminifers and calcareous nannofossils were generally well preserved and abundant, except in some layers where the concentration of biogenic constituents was reduced via dilution by volcaniclastics. The Pleistocene/Pliocene boundary was placed between Cores 350-U1436A-18X and 20X based on the presence of the top of *Globorotalia pseudomioceanica* (2.39 Ma) in Sample 350-U1436A-18X-CC and the top of *Globoturborotalita decoraperta* (2.75 Ma) in Sample 350-U1436A-20X-CC. Benthic foraminifer assemblages (i.e., extinction of Stilostomelidae) corroborate this biochronology.

Paleomagnetic analysis in Hole U1436A comprised archive-half demagnetization and remanence measurement at 10 mT steps to 40 mT. Severe core disturbance resulted in complete destruction of the depositional remanence in many intervals, and discontinuous recovery (Fig. **F18**) compromised the recognition of magnetostratigraphy in the lower half of the hole. Nevertheless, intervals of continuous mud recovery yielded a good paleomagnetic record, with the drill string overprint largely removed. The base of normal Chron C1n (the Brunhes/Matuyama boundary; 0.781 Ma) was recorded in one of the last continuous mud intervals, at Sample 350-U1436A-9H-3, 25 cm (56.8 mbsf). The reversal appears sharp because it occurred in the time interval between two successive depositional events.

One discrete paleomagnetic cube was sampled per section in undisturbed mud and silt. Discrete samples in the discontinuous record below the hiatus allowed us to recognize two additional datums: top of normal Chron C1r.1n (0.988 Ma) between Samples 350-U1436A-9H-4, 66–68 cm (reversed), and 10F-2, 64–66 cm (normal), and base of normal Chron C1r.1n (1.072 Ma) between Samples 10F-2, 64–66 cm, and 16X-2, 53–55 cm (reversed). Discrete samples and a patchy record in the archive half superconducting rock magnetometer (SRM) measurements indicate that Core 17X is all reversed polarity and probably still lies in the Matuyama interval (<1.778 Ma), which is

however, not consistent with biochronology and thus has not been included in the age model.

Physical properties show an abrupt change at the ~50 mbsf inferred hiatus, below which recovery rates decrease. Shear strength, natural gamma radiation, and color reflectance L* parameter all decrease in the interval deeper than 50 mbsf, which is likely related to an increase in the relative abundance of mafic ash layers in that interval. Mafic ash layers have an average magnetic susceptibility value that is more than twice as high as the average value for evolved layers.

## Lithostratigraphy

Out of the 71.6 m of core recovered in Hole U1436A, a total of 5.5 m of whole-round samples were removed for shore-based geotechnical testing and shipboard paleontological and interstitial water analysis. Of the remaining recovery, 65.7 m was measured and described as a single lithostratigraphic unit (Unit I) (Fig. **F19**). Unit I consists of mud with dispersed ash (referred to as tuffaceous mud) with intercalated intervals of ash and lapilli ash (~150 intervals total). Of these, ~80 intervals are mafic ash and scoria lapilli ash and ~70 intervals are evolved ash and pumice lapilli ash. In total, Unit I comprises ~40 m of tuffaceous mud and ~26 m of ash and lapilli ash. The mafic intervals are 50% thicker than the evolved beds, for a total mafic to evolved thickness ratio of 1.5:1. Representative images of the tuffaceous mud and mafic and evolved tephra are shown in Figure **F20A–F20C.**

Mud intervals average 25 cm in thickness, are up to 420 cm thick, and are massive and bioturbated. They consistently contain abundant ash, mainly vitric with rare crystals, and foraminifers. The mud is light gray to dark gray brown, commonly with a greenish hue. Rare glauconite (1–2 cm thick) occurs in the mud near the top contacts with evolved ash intervals.

The mafic ash and scoria lapilli ash intervals average 14 cm in thickness and are up to 230 cm thick, but this maximum thickness was probably greatly expanded by core disturbance (Core 350-U1436A-8H, the distinctive black glassy mafic ash discussed further below). The evolved ash and pumice lapilli ash intervals average 9 cm in thickness and are up to 60 cm thick. Pumice and scoria lapilli clasts are commonly <1 cm in size and angular; larger clasts are up to ~3 cm in size and subrounded. Most of the mafic lapilli ash intervals have subordinate pumice, and most of the evolved lapilli ash intervals have subordinate scoria. Most mafic and evolved intervals are normally

graded with sharp bottom contacts and diffuse/gradational tops showing upcore increase in mud content.

The tuffaceous mud is interpreted to record hemipelagic background sedimentation with substantial ash contribution from explosive eruptions and/or resedimentation products, presumably originating chiefly from the Izu-Bonin arc front. Mafic and evolved ash and lapilli ash intervals may record distinct explosive events, also from the Izu-Bonin arc front, although evolved ash may be from more distal sources. The mode of transport and deposition of the mafic and evolved ash and lapilli ash intervals is not clear but involves some combination of subaqueous fallout and vertical settling through the water column and/or sediment gravity flows.

A very distinctive ash facies occurs in two intervals in Core 350-U1436A-8H (intervals 8H-1, 0 cm, to 8H-2, 110 cm, and 8H-3, 49–64 cm), referred to as the black glassy mafic ash (Fig. **F20C, F20D**). The lower ash is 15 cm thick and is underlain and overlain by tuffaceous mud (Fig. **F20C**). The upper ash is 220 cm thick, lies at the top of a core, and shows evidence for thickening by core disturbance; therefore, its original thickness is not known. Both layers contain macroscopically visible foraminifers. The two distinctive black glassy mafic ash intervals are the most mafic deposits analyzed shipboard at Site U1436 (basaltic andesite). Under the microscope the glass is brown to greenish brown (polarized light) with few microlites. Glass particles are flat, blocky, curviplanar and/or plastically deformed, and contain vesicles (Fig. **F20D**). The distinctive black glassy ash facies appears unusually homogeneous in componentry and texture, suggesting an eruption-fed origin. The overwhelmingly glassy nature of the ash further suggests subaqueous explosive eruption, and its sorting may suggest deposition by vertical settling through the water column from an ash plume. These two black glassy mafic ash layers attracted a great deal of interest in the science party because they could possibly be the product of large-volume mafic explosive eruptions. For this reason, we returned to Site U1436 to drill three more holes (U1436B, U1436C, and U1436D) in hopes of recovering undisturbed cores containing these layers and were finally successful in Hole U1436D.

## Geochemistry

Inorganic and organic geochemistry measurements at Site U1436 aimed to characterize the interstitial water chemistry and elemental composition of igneous rocks and sediment samples as well as to determine the hydrocarbon gas concentrations within the sediments.

Headspace samples were analyzed routinely from every core in Hole U1436A as part of the shipboard hydrocarbon safety program. No hydrocarbon gases other than methane were detected in the cored sequences. Methane was either present in very low concentrations near or below the detection limit with an average concentration of 2.5 parts per million by volume (ppmv). Downhole interstitial water compositions obtained from selected whole-round samples (~1 per core) from Hole U1436A are generally in good concordance with previous observations at nearby Site 792 (Leg 126). Pore water Na/Cl scatters around an average of 0.86 throughout the sampled interval, which is equivalent to modern seawater. Variations in pore water compositions may be controlled by stronger seawater infiltration into porous ash-rich sections compared to muddy deposits. The most prominent deviations occur in pore waters from mud collected at ~13–27 mbsf, where sulfate concentrations subtly decrease (minimum = 25.8 mM) compared to seawater (28.9 mM) with concomitant subtle increases in pH and alkalinity and decreases in calcium. Magnesium concentrations are slightly elevated compared to Site 792 values at the same depths and show no evidence for magnesium sequestration because of volcanic glass alteration and clay mineral precipitation observed in the deeper sections of Site 792.

Concentrations of major elements and several trace elements in solid samples from Hole U1436A were measured by inductively coupled plasma–atomic emission spectroscopy (ICP-AES) and additional portable X-ray fluorescence (pXRF) analysis (Fig. **F21**). Reconnaissance pXRF and ICP-AES results show excellent agreement for $K_2O$ and CaO; ICP-AES data include light elements ($SiO_2$, $Al_2O_3$, and $Na_2O$) not reliably obtained by pXRF, and pXRF data appear more reliable for zirconium. Composite lapilli ($n$ = 11) and bulk ash samples ($n$ = 3) were analyzed for a complete set of major elements by ICP-AES. Loss on ignition (LOI) values range between 0.54 and 3.8 wt% (9.8 wt% for impure mud with ash) and are generally higher in evolved ash and lapilli samples compared to mafic samples. These LOI values are elevated compared to those from regional fresh subaerial volcanic rocks and are indicative of secondary hydration of volcanic glass.

All but one of the Hole U1436A tephra samples define broadly linear trends in Harker diagrams ($SiO_2$ = 54.4–70.1 wt%). They classify as low-K rocks and are indistinguishable from intermediate to acidic rocks from basalt-dominant island volcanoes of the arc front (e.g., Aogashima Volcano ~56 km to the west), although basalt (with <53 wt% $SiO_2$; present in arc-front volcanoes) has not been found in the tephra at Site U1436. The most mafic samples are from the black glassy ash lithofacies and are basaltic andesite (55 wt% $SiO_2$). One interval of evolved lapilli ash (at ~45 mbsf) con-

tains pumice with elevated $K_2O$, indicating that it did not come from Aogashima or the East Aogashima Caldera ~45 km to the west, which have lower $K_2O$. This pumice is similar in composition to those from submarine calderas including three within 65 km of the drill site (Myojin Knoll, Myojinsho, and South Hachijo), which exist south and north of Aogashima. Rhyolite-dominant submarine caldera volcanoes with elevated $K_2O$ are common in the arc front (Tamura et al., 2009).

Turbidites (younger than 1 Ma) from Site 792, which is 1.5 km east of Site U1436, have compositions similar to tephra collected at Site U1436. However, they are a little lower in $TiO_2$ and higher in $K_2O$ at the same $SiO_2$ content compared with the main trend of Site U1436 tephra, except for the high $K_2O$ pumice. Turbidites, by their nature, show a mixing trend between mafic and felsic end-members. Thus, the differences between turbidites and tephra at Sites 792 and U1436, respectively, are consistent with the existence of two types of pumice at Site U1436, which results in the mixing line being different from fractionation trends shown in Site U1436 tephra.

## Site U1437: Izu rear arc

Site U1437 is located in the Izu rear arc and is ~330 km west of the axis of the Izu-Bonin Trench (Figs. **F1, F3**) and ~90 km west of the arc-front volcanoes Myojinsho and Myojin Knoll (Fig. **F22A**) at 2117 meters below sea level (mbsl).

The preliminary results of seismic surveys for Site U1437 are summarized briefly here from Tamura et al. (2013); full results of the seismic surveys will be presented in a full paper at a later time after drilling results are integrated (M. Yamashita, pers. comm., 2014). Numerous lines were shot in two different campaigns; parts of three seismic sections that cross at Site U1437 are plotted on Figure **F22B** and described here (Figs. **F15A, F15B, F23**). Line IBr5 is the longest seismic line, running east–west from the Manji rear-arc seamount chain across the Enpo seamount chain to the arc front; it was shot both by wide-angle ocean-bottom seismometer (OBS) and by multichannel seismic (MCS) (Fig. **F23**). The wide-angle OBS survey shows the velocity structure of the upper ~10 km, and the MCS line shows the upper ~5 km. Generally, the velocity transition to >5 km/s is thought to represent the transition to igneous rocks, perhaps representing arc upper crust lava or crystalline rocks, and the velocity transition to 6 km/s is generally thought to represent the transition to middle crust (e.g., see boundaries picked in Fig. **F23**). Tamura et al. (2013) estimated the 5 km/s iso-velocity contour to lie at ~2100 mbsf at Site U1437 and suggested that these rocks could be Oligocene–Eocene "igneous basement," consisting of lava and/or intrusions. Line IBM3-NW5

(Fig. F15A) clearly shows that Site U1437 lies in a volcano-bounded basin between the Enpo and Manji rear-arc seamount chains.

## Shipboard age model

At Site U1437 it was possible to identify a Pleistocene to upper Miocene succession (Fig. F24). Fourteen biostratigraphic and 29 magnetostratigraphic datums obtained in the upper 1303 mbsf of the succession were selected to construct the age-depth model. The age model has not been extended deeper than 1303 mbsf because no biostratigraphic or magnetostratigraphic datums are detectable from 1303 to 1806 mbsf. Also, no biostratigraphic datums are recognized deeper than 867 mbsf; thus, the age model for 867–1303 mbsf was constructed using only magnetic reversal datums.

Seven intervals were selected to calculate the LSR, assuming constant sedimentation rates within those intervals. The LSRs range from a minimum of 98 m/My to a maximum of 259 m/My. The highest LSR (259 m/My) is found from the top of lithostratigraphic Unit II through the upper part of Unit III, to ~825 mbsf. A minimum LSR of 98 m/My is recorded from 825 to 844 mbsf. Lithostratigraphic Units IV and V record an increase in LSR with values of 157 and 105 m/My.

An offset in the LSR between intervals 868–1056 and 1122–1302 mbsf corresponds to the change from Hole U1437D to U1437E and also to a missing interval in the magnetostratigraphy. The probable explanation is a normal fault between the two holes, resulting in a partial loss of section within lithostratigraphic Unit IV. If the LSRs within lithostratigraphic Unit V are extrapolated to Unit VI, ages are about 0.6 Ma less than the minimum age constraint given by the nannofossil assemblage in Sample 350-U1437E-36R-CC (10.97–11.85 Ma at 1403 mbsf); a hiatus or erosion is the most likely explanation for this discrepancy, given that sedimentation rates would be expected to be high in the coarse-grained Unit VI.

One additional age control point was added postcruise before publication of this report. Sample 350-U1437E-35R-1, 76 cm, to 35R-2, 55 cm (1388.86–1390.07 mbsf) from igneous Unit 1 (see below) has a preliminary U-Pb zircon concordia intercept age of 13.6 +1.6/–1.7 Ma (2σ error; mean square of weighted deviation [MSWD] = 2.12; number of analyses $n$ = 9) (Schmitt, pers. comm., 2014).

## Lithostratigraphy and physical properties

Site U1437 was drilled in three holes (U1437B, U1437D, and U1437E), which we divide into seven lithostratigraphic units (Fig. F25; Table T4), described in this section.

Physical properties for Site U1437 (Fig. **F25B, F25C**) are discussed with reference to the lithostratigraphic units below. Summary lithostratigraphic logs for Holes U1437B, U1437D, and U1437E are shown in Figure **F26A, F26B,** and **F26C,** respectively. The downhole evolution in proportion of mud and volcaniclastics is shown in Figure **F27,** dividing the volcaniclastics further into relative proportion of mafic and evolved materials (Holes U1437B and U1437D) or composition of volcanic clasts (Hole U1437E).

Lithostratigraphic Units I–VII are distinguished from each other based on the proportion and characteristics of tuffaceous mud/mudstone and interbedded tuff, lapilli tuff, and tuff breccia. The tuffaceous mud/mudstone is strongly to intensely bioturbated. Alteration becomes more pervasive and increases in intensity downhole in both holes; it is initially predominantly glauconitic–smectitic and eventually becomes more chloritic. Iron sulfides are pervasive throughout both holes, especially as replacements of worm burrows, and according to rock magnetic properties, greigite is progressively replaced by pyrite downhole in Hole U1437D. Compaction of sediment at Site U1437 increases linearly from ~0% shallower than ~410 mbsf to ~36% at the base of Hole U1437D (~1100 m). The transition from unconsolidated to lithified rocks occurred progressively; however, sediments were considered lithified from 427 mbsf (top of Hole U1437D) downward.

### *Lithostratigraphic Unit I*

Unit I (interval U1437B to 350-U1437D-28R-2, 112 cm; 0–682.12 mbsf) is 0–4.3 Ma in age, 682.12 m thick, and consists largely (88%) of mud or mudstone with >25% dispersed ash, referred to as tuffaceous mud/tuffaceous mudstone (Fig. **F3**). For fine-grained deep marine sediment, it has a high average sedimentation rate (~165 m/My, described above). Unit I has minor (12%) tephra, consisting almost entirely of ash (unlithified) or tuff (lithified) intervals ($n$ = 649); only 11 of these intervals contain lapilli, for a total thickness of 59 cm, or just 1.2% of the tephra. Furthermore, the lapilli are small, averaging ~1 cm in size. Ash or tuff beds have a median thickness of just 8 cm, whereas tuffaceous mud/mudstone intervals have a median thickness of 26 cm. The sparseness, thinness, and fine grain size of discrete tephra layers in lithostratigraphic Unit I is enigmatic, given the fact that it accumulated in close proximity to volcanoes of the active rift and back-arc knolls extensional zone (<3 Ma) and rear-arc seamount chains (>3 Ma), in addition to lying within 90 km of the arc front (Fig. **F6**).

The tuffaceous mudstone of Unit I contain abundant fine colorless glass shards and rare crystals, plus carbonate materials such as foraminifers. They are typically biotur-

bated and commonly have green horizons (possibly glauconite) where they overlie evolved ash/tuff. Pyrite clots and greigite are associated with bioturbation in the mudstone.

The ash/tuff intervals of Unit I include both evolved (white to dark gray) and mafic (black) intervals (Fig. **F28**); however, the evolved ash/tuff intervals ($n$ = 480) are four times as common as the black mafic ash/tuff intervals. The evolved ash/tuff intervals are on average only 7 cm thick but individual intervals can reach a maximum of 70 cm, with the thickest intervals occurring mainly between 100–140 and 530–600 mbsf. The evolved ash/tuff intervals are mainly vitric with sharp bases and tops that grade upward into mudstone, some with a crystal-rich base dominated by plagioclase with lesser pyroxene. Some ash/tuff intervals are laminated with darker layers richer in crystals and pumice grains and lighter layers richer in glass shards. Hornblende is found in only 7% of the evolved ash/tuff intervals; these are mainly in the lowermost part of lithostratigraphic Unit I, where hornblende-bearing ash has elevated $K_2O$ contents relative to most of the other evolved ash intervals, suggesting that these record rear-arc seamount volcanism rather than arc-front or rift volcanism (see **"Geochemistry"**). A subset of ash/tuff intervals ($n$ = 47) is described as bimodal because microscopic inspection reveals that these intervals contain >25% of both colorless and colored mafic glass, but colorless glass predominates in most cases. There are only 11 lapilli ash/lapilli tuff and lapillistone intervals in lithostratigraphic Unit I, bearing subrounded mafic scoria and/or evolved pumice and subordinate lithic clasts.

Unit I is divided into three units on the basis of physical properties (PP Units 1, 2, and 3, Fig. **F25B**). PP Unit 1 (0–430 mbsf) is characterized by a downhole increase in bulk density (from 1.5 to 1.6 g/cm$^3$) and $P$-wave velocity (from 1501 to 1848 m/s) and a corresponding downhole decrease in porosity (from 70 to 65 vol%). The top of PP Unit 2 (430–550 mbsf) is marked by an initial increase in porosity (from 61 to 67 vol%) then a downhole continuation of the decrease observed through PP Unit 1. The top of PP Unit 3 (550–682 mbsf) is characterized by a sharp increase in porosity (from 52 to 65 vol%) and a corresponding decrease in bulk density (from 1.8 to 1.6 g/cm$^3$), followed by more normal downhole trends similar to those seen in PP Unit 2. The color reflectance ratio of a*/b* displays a significant decrease in the scatter of the data, indicating that color is less variable through PP Unit 3 than in PP Unit 2. The base of PP Unit 3 corresponds to the base of lithostratigraphic Unit I (Fig. **F25B**).

### *Lithostratigraphic Unit II*

Unit II (interval 350-U1437D-28R-3, 0 cm, to 32R-CC, 28 cm; 682.12–728.1 mbsf) is 44.38 m thick, with much more abundant tephra (~75%) and much less tuffaceous mudstone (~25%) than is present in Units I or III (Figs. **F26, F27**). Additionally, tephra in Unit II is coarser in grain size than that of Units I and III (Fig. **F26**), with pumice lapilli tuff and pumice lapillistone forming slightly more than half of the thickness of the tephra and tuff forming slightly less than half. Tephra in Unit II also differs from that of Units I and III by being entirely evolved (no mafic tephra present; Figs. **F27, F28**). Tephra has pumice clasts and planar bedding, cross bedding, and normally or reversely graded intervals (Fig. **F29**) and is on average 16 cm thick with a maximum of 95 cm.

Unit II has three lithofacies types. The first lithofacies, evolved tuff, pumice lapilli tuff, and pumice lapillistone, are monomictic and contain plagioclase, clinopyroxene, orthopyroxene, and amphibole crystals in variable proportions. The second lithofacies, dark gray evolved tuff, is similar to the darker colored evolved tuff in Unit I. They are commonly graded with a sharp base overlain by a crystal-rich layer that grades upward into a vitric tuff, commonly bioturbated where overlain by tuffaceous mudstone. The third lithofacies, tuffaceous mudstone, is similar to the tuffaceous mudstone of Unit I but is more strongly lithified and altered to green clay minerals (likely glauconite and smectite) plus pyrite. Pumice is commonly devitrified or replaced by palagonite, zeolites, or clay minerals.

PP Unit 4 (682–728 mbsf) corresponds to lithostratigraphic Unit II (Fig. **F25B**) and is characterized by an increase in the scatter of density and porosity, a significant increase in *P*-wave velocity values and range, an abrupt increase in magnetic susceptibility (MS) (average of 476 IU versus 138 IU for PP Unit 3), and an abrupt decrease in natural gamma radiation (NGR) from ~20 to ~5 cps.

### *Lithostratigraphic Unit III*

Unit III (interval 350-U1437D-33R-1, 0 cm, to 63R-2, 26 cm; 728.1–1017.88 mbsf) is 289.7 m thick and is composed of tuffaceous mudstone (~64%) and lesser tuff (~35%) (Figs. **F26, F27**). It contains only ~1% lapilli tuff (3.1 m in total). All the tuff intervals and the rare lapilli tuff intervals are evolved (Fig. **F27**). Unit III also contains one distinctive interval (1.91 cm thick) that consists of deformed mudstone intraclasts (up to ~20 cm in size) and clasts of scoria and pumice (up to 5 cm), supported in a tuffaceous mudstone matrix; this is interpreted to represent a submarine debris flow de-

posit. Unit III shows an increase in fine-grained tuff (relative to tuffaceous mudstone) in its basal ~80 m (Fig. F27); above that, Unit III is similar to Unit I, except that it lacks the mafic tuff that makes up ~20% of the tuff in Unit I.

The tuffaceous mudstone intervals in Unit III have abundant bioturbation (Fig. F30) and, in the lower part of the core, dark laminae that may reflect higher clay content. The evolved tuff intervals generally have sharp basal contacts, some with a crystal-rich basal layer, and bioturbated tops that grade into tuffaceous mudstone. The evolved tuff is composed of glass and pumice or fiamme grains and crystals, including feldspar, clinopyroxene, orthopyroxene, and occasional hornblende.

Two main facies are recognized in the evolved tuff of Unit III (Fig. F30):

- Dark gray evolved tuff, which is medium-grained to coarse-grained, and owes its dark color to the presence of crystals and pumice (Fig. F30A–F30D). It is identical to the dark gray tuff of Units I and II and not described further here.
- White and green fine-grained tuff, which is much finer grained and better sorted than other evolved tuff at Site U1437, in places appearing chert-like (Fig. F30E). The fine-grained tuff has laminations produced by alternation of glass shard–rich layers (white) and layers of mixed shards, pumice, and crystal fragments (gray-green), repeated over intervals up to several meters thick, with no bioturbation or mudstone interbeds. Thus, the intervals seem to record fairly continuous but pulsating sedimentation. The laminations commonly show soft-sediment deformation, supporting the interpretation that the white and green fine-grained tuff intervals were deposited rapidly (see below). White to gray-green fine-grained tuff intervals form much of the tephra in the lower part of Unit III, where the tephra content is highest for this unit (except for its uppermost part; Fig. F27A). The white and green fine-grained tuff lithofacies also occurs in Unit IV (described below).

The top of lithostratigraphic Unit III corresponds to the upper boundary of PP Unit 5 (728–794 mbsf) (Fig. F25B), defined by an increase in NGR values to ~16 counts/s and a decrease in the scatter of *P*-wave velocity, followed downhole by the continuation of the *P*-wave trend observed in PP Unit 3. PP Unit 6 is contained within lithostratigraphic Unit III. The top of PP Unit 6 (794–846 mbsf) is defined by an increase in the scatter of the *P*-wave velocity and color reflectance (a*/b*) values. The top of PP Unit 7 (846–1018 mbsf) is marked by an initial ~0.3 g/cm$^3$ decrease in bulk density and a corresponding increase in porosity (846 to ~860 mbsf), followed by regular trends downhole and marked by significant scatter. The top of PP Unit 7 is also characterized by an abrupt decrease in the average MS value from 491 IU (PP Unit 6) to 167 IU. The

base of PP Unit 7 coincides with boundaries between lithostratigraphic Units III and IV, described below.

### *Lithostratigraphic Unit IV*

Lithostratigraphic Unit IV (interval 350-U1437D-64R-1, 8 cm, to 350-U1437E-6R-3, 122 cm; 1017.88–1120.11 mbsf) is 102.23 m thick and is dominated by polymictic tuff and lapilli tuff, in contrast to Unit III (dominated by tuffaceous mudstone) and Unit V (dominated by monomictic lapilli tuff). Unit IV consists of coarse-grained tuff and polymictic lapilli tuff and lapillistone (78%), with minor tuffaceous mudstone (22%) becoming more frequent toward the base.

Unit IV consists of four lithofacies, in order of abundance:

- Normal-graded polymictic lapilli tuff and lapillistone. Lapilli are small (average 3–5 mm, up to 1.5 cm). Lithic clasts dominate over vitric (mainly pumice) clasts, and lithic clasts are light to dark in color, but nearly all are plagioclase-pyroxene andesites; hornblende is rare.
- White and green fine-grained tuff. This is identical to the white and green fine-grained tuff described under Unit III (above), characterized by laminae of very fine grained vitric tuff (white) alternating with fine- to medium-grained pumice and crystal tuff (green). Similarly, it forms thick, unbioturbated intervals up to 5.54 m thick with planar lamination or soft-sediment deformation. The glass shards are too altered in thin section to allow determination of their original morphology.
- Dark gray evolved tuff. Also like those described under Units I, II, and III (above), this is a dominantly medium- to coarse-grained evolved tuff that owes its dark color to the presence of crystals (plagioclase with minor clinopyroxene) and pumice.
- Tuffaceous mudstone. This is also like that described in Units I, II, and III, except perhaps more bioturbated and with pumice lapilli in two intervals.

The upper boundary of PP Unit 8 (1018–1140 mbsf) corresponds to the upper boundary of lithostratigraphic Unit IV. PP Unit 8 is characterized by an increase in the average MS value to 916 IU and a shift to very low (~1 W[m·K]) thermal conductivity.

### *Lithostratigraphic Unit V*

Lithostratigraphic Unit V (interval 350-U1437E-6R-3, 122 cm, to 27R-CC, 15 cm; 1120.11–1312.21 mbsf) is 192.1 m thick and is distinguished largely on the basis of its intervals of monomictic, reversely graded pumice lapilli tuff (Fig. **F31A**); these distinctive beds contrast with the polymictic, dominantly lithic lapilli tuff of the over-

lying and underlying units (IV and VI). Like Units I, III, and IV, Unit V also has tuffaceous mudstone (69%) and evolved tuff intervals (15%). Lapilli tuff accounts for only 16% of Unit V, but the monomictic reversely graded pumice lapilli tuff recurs throughout Unit V.

Each monomictic reversely graded pumice lapilli tuff interval in Unit V has (Fig. **F31A**) (1) a sharp base, typically eroded into the underlying tuffaceous mudstone, overlain by (2) evolved tuff with abundant glass shards and grains of pumice, in turn grading upward into (3) pumice lapilli tuff with flattened or unflattened pumice that become progressively larger upward (i.e., reverse graded). This passes upward into (4) tuffaceous calcareous mudstone. This lithofacies is thus composed almost entirely of vitric material (glass shards and pumice).

The tuff in Unit V varies in color from light green to dark gray to brown and has variable vitric-crystal contents (Fig. **F31B**). The lapilli tuff in Unit V has volcanic lithic lapilli and pumice with crystals of plagioclase, pyroxene, and opaque minerals (Fig. **F31C**). Soft-sediment faults are present in tuffaceous mudstone and tuff, with small offsets of 1–10 cm (Fig. **F30D**).

The upper boundary of PP Unit 9 (1140–1315 mbsf) is 20 m below the upper boundary of lithostratigraphic Unit V and is defined by a decreased scatter in density, porosity, *P*-wave velocity, and NGR counts, as well as a downhole decrease in the thermal conductivity.

#### *Lithostratigraphic Unit VI*

Lithostratigraphic Unit VI (interval 350-U1437E-28R-1, 0 cm, to 42R-3, 60 cm; 1320.00–1459.80 mbsf) is 139.80 m thick and is characterized by an abundance of polymictic lithic and pumice lapilli tuff, although it also contains monomictic pumice lapilli tuff (Fig. **F32**). The top of lithostratigraphic Unit VI is marked by the first appearance of multiple intervals of polymictic lapilli tuff, and its base is marked by the top of the very distinctive black monomictic glassy lapillistone and lapilli tuff in the upper part of Unit VII. Unit VI is dominated by lapilli tuff and lapillistone (~57%) with lesser tuff (32%) and minor tuffaceous mudstone (11%). The polymictic lapilli tuff and lapillistone form very thick beds (>1.5 m, the length of a core section, or up to 2.8 m thick assuming complete recovery between core sections). Tuff averages 0.24 m in thickness, to a maximum of 1.43 m. Tuff and tuffaceous mudstone is interbedded.

Polymictic lithic and pumice lapilli tuff are four times more abundant than monomictic pumice lapilli tuff in Unit VI; monomictic varieties contain only pumice (Fig. **F32A**), whereas polymict varieties have evolved and lesser mafic volcanic lithic clast types as well as pumice (Fig. **F32B**). The polymictic lithic and pumice lapilli tuff show a complete gradation from clast-supported to matrix-supported (Fig. **F32C**), whereas the monomictic pumice lapilli tuff is all matrix-supported (Fig. **F32A**).

Lithic lapilli clasts in Unit VI are dominantly

- Porphyritic andesite with plagioclase and clinopyroxene. These range from nonvesicular to highly vesicular (up to ~50% vesicles), locally filled with zeolites, clay minerals, and/or chalcedony. Clasts of this type also occur as scattered small blocks (>6.4 cm in size) in the polymictic lapilli tuff.
- Rhyolite-dacite, which becomes more common near the rhyolite intrusive sheet with peperitic boundaries, described as Igneous Unit 1 below. These include crystal poor and porphyritic varieties, with amphibole, plagioclase, and quartz.

Pumice lapilli clasts in Unit VI are light to dark green and commonly flattened by compaction and lithification into fiamme; less flattened pumice clasts have vesicles filled with chlorite (Fig. **F32B, F32D**). Red to brown mudstone clasts are also present in Unit VI.

Physical properties do not show distinct changes at the top of Unit VI but are gradational into the unit from the base of Unit V. NGR declines from ~10–12 counts/s at the base of Unit V to a sustained ~5–6 counts/s in Unit VI. MS increases into Unit VI and becomes less variable as compared with Unit V. Porosity and *P*-wave velocity show no appreciable change from Units V to VI. The base of Unit VI (Section 350-U1437E-42R-3, 60 cm) coincides with a sustained one order of magnitude reduction in MS and a sustained but minor reduction in *P*-wave velocity. Porosity increases slightly into Unit VII but becomes much less variable. Conversely, NGR ceases to be stable and becomes highly variable in the upper part of Unit VII.

#### *Igneous Unit 1*

The only igneous unit observed at Site U1437 consists of a single rhyolite intrusion at 1389 mbsf, which lies within lithostratigraphic Unit VI (Fig. **F33**). Core recovery was much lower in igneous Unit 1 (45%) than it was in the host volcaniclastic rock (~94%), and the recovered igneous Unit 1 core material was affected by fragmented core disturbance, probably due to greater competency of rhyolite intrusion than the

surrounding volcaniclastic host. Therefore, although only 1.2 m thickness was described for igneous Unit 1, its maximum thickness is estimated at 6.5 m assuming all the material not recovered from this interval was part of igneous Unit 1. Its true thickness probably lies somewhere between 1.2 and 6.5 m.

Igneous Unit 1 was described by the general term rhyolite-dacite, but shipboard geochemical analysis (discussed below) shows that it is a rhyolite with 74.5% $SiO_2$. It has sieve-textured subhedral plagioclase (up to 4 mm, ~7%), euhedral hornblende (up to 0.5 mm, ~3%), large anhedral to subhedral quartz (up to 8 mm, ~1%) with fresh glassy melt inclusions, some opaque minerals, and rare zircon (20 µm in size). Flow banding is observed across the entire unit in various orientations (Fig. **F33B**). The groundmass varies from cryptocrystalline near the upper and lower contacts to fine grained in the center of the unit. The upper margin is chilled, and the overlying lapilli tuff is baked, indicating that igneous Unit 1 is an intrusion rather than a clast or lava. The presence of xenoliths of the host unit supports the interpretation that it is an intrusion. The lower contact of igneous Unit 1 is a peperite, defined as a magma-wet sediment mixture (Busby-Spera and White, 1987); the contact shows complex mingling between the intrusion and the host, including crenulated lobate margins on the intrusion and dispersal of the magma into the host on the microscopic scale (Fig. **F33C**).

### *Lithostratigraphic Unit VII*

The top of Unit VII is at 1459.8 mbsf (Sample 350-U1437E-42R-3, 60 cm), and Hole U1437E ended in Unit VII, which was described to a depth of 1800.3 mbsf (79R-3, 83 cm). Unit VII is 340.5 m thick, and ~90% is extremely thick bedded, nongraded, nonstratified, poorly sorted, coarse-grained angular andesitic lapilli tuff, in places with blocks tens of centimeters in size. Some clasts have quenched margins, jigsaw-fit textures, intricate fluidal margins, or peperitic margins; as discussed below, these indicate hot emplacement of clasts, or of margins of lava or intrusions, or both. Thus Unit VII is interpreted to be a vent-proximal deposit. Unit VII is divided into upper and lower parts (above and below 1643.73 mbsf).

The upper part (183.93 m thick) of Unit VII is dominated by a black, glassy, homogeneous, nonstratified deposit of unaltered angular lapillistone and lapilli tuff with abundant large clinopyroxene glomerocrysts and plagioclase glomerocrysts. The glass is isotropic and nonvesicular, and bubble-wall shards or broken crystals are absent (Fig. **F34A, F34B**). Only a few sparsely phyric volcanic lithic clasts are present, some with quenched margins, and a few red oxidized clasts are present. The black glassy lapilli tuff and lapillistone lack stratification completely, except for one thin (~25 cm

thick) interval of crudely stratified ash. The black glassy lapillistone and lapilli tuff are interpreted to be hyaloclastite formed by autobrecciation and quenching of lava in a submarine environment (discussed further below).

The lower part (156.57 m thick) of Unit VII is dominated by green (more altered) angular andesite lithic lapilli tuff with blocks up to 53 cm in size. Like the black glassy lapillistone and lapilli tuff unit that forms the upper part of lithostratigraphic Unit VII, these lithic lapilli tuff and tuff breccia are massive, but they are intercalated with stratified lithic lapilli tuff and tuff (also altered green). The clasts are also more heterogeneous, with variable plagioclase and pyroxene contents, and they range from nonvesicular to moderately vesicular, with vesicles mostly filled with secondary minerals. Some of the clasts show evidence for hot emplacement (Fig. **F34C**), including intricate fluidal margins, quenched margins and breadcrust texture, jigsaw-fit brecciated margins, and in at least one case, a clast appears to be surrounded by sediment with a baked margin. Additionally, clasts with broken chilled margins are absent; these would be expected if the clasts were transported and deposited after they cooled. In core, it is not possible to determine whether all of these features formed on clasts that were emplaced at high temperatures or if some of these features formed on the complexly embayed margins of small intrusive bodies or lava bodies. Further support of hot emplacement is provided by paleomagnetic inclinations from two of the "clasts" (discussed further below).

The green lower part of Unit VII also has minor intervals of tuff, averaging ~20 cm thick, with variable color (brown, dark gray, red-brown, and green). These thin tuff intervals are stratified or massive, nongraded or normally graded (with rare reverse grading), and commonly contain minor lapilli.

PP Units 11–13 occur within lithostratigraphic Unit VII, with the top of PP Unit 11 (1460–1580 mbsf) corresponding with the top of lithostratigraphic Unit VII. PP Unit 11 is characterized by an abrupt decrease in the MS values and a decreased scatter in density, porosity, and *P*-wave velocity values. NGR counts from the upper part of PP Unit 11 are higher than in PP Unit 10 and then decrease again in the lower part of PP Unit 11. The upper boundary of PP Unit 12 (1580–1742 mbsf) is defined by an abrupt increase in the MS relative to PP Unit 11. Density and *P*-wave velocity increase downhole, whereas porosity decreases. The top of PP Unit 13 (1742–1800.3 mbsf) is marked by a decrease in *P*-wave velocity and thermal conductivity, which then increase downhole toward the bottom of the hole.

## Geochemistry

### *Hydrocarbon gases*

Samples for hydrocarbon gas analysis from headspace ($n$ = 184) were collected and analyzed for every core at Site U1437 in compliance with the shipboard hydrocarbon safety program. Methane was the only hydrocarbon gas above detection limits in sediment headspace samples in Holes U1437B and U1437D. Methane abundances gradually increase with depth, with the highest abundances at ~750–1459 mbsf (Fig. **F35**), and reach maximum values of 638 ppmv at 920 mbsf, which is still well below critical safety thresholds. The zone of methanogenesis is unusually deep because of a release of sulfate below the sulfate reduction zone (27–83 mbsf; see **"Pore fluid analysis"** and **"Rock magnetism"**), which may be buffering the methanogenesis by anaerobic methanogens. Deeper than 1459 mbsf, methane concentrations decrease again and are <10 ppmv in the lowermost sections of the cored sequence. Coincidently upon starting drilling in Hole U1437E, ethane was also detected with maximum abundances of 13 ppmv at 1275 mbsf (Fig. **F35**). In the horizons where both methane ($C_1$) and ethane ($C_2$) were detected (Sections 350-U1437E-4R-2 through 42R-3; 1105–1450 mbsf), $C_1/C_2$ values are <100, possibly indicating the organic matter is mature and the hydrocarbon gases are thermogenic. However, $C_1/C_2$ never reached the critical threshold to cause drilling operations to be halted according to the shipboard safety program.

### *Pore fluid analysis*

Interstitial water (IW) samples ($n$ = 59) were squeezed from whole-round core sections between 5 and 10 cm long that targeted muddy intervals in cores between 8.3 and 693 mbsf. The interstitial water salinity and chlorinity profiles are characterized by moderate increases above seawater values with depth. The chloride profile is nearly constant in Hole U1437B between 18 and 401 mbsf. Bromide shows a gradual decrease with depth but in contrast to Hole U1436A is poorly correlated with Cl. Higher chlorinity with depth indicates hydration of volcanic ash and the formation of hydrous alteration products such as clays and zeolites. These reactions consume $H_2O$ and increase pore water salinity and chlorinity. Variations in Ca, Mg, and B abundances with depth are consistent with this interpretation.

Depth profiles for alkalinity, pH, ammonium, sulfate, and phosphate (Fig. **F36**) are highly complementary and characterized by prominent deviations from seawater compositions over the uppermost 50 m of the profile, followed by a more gradual re-

versal to near seawater compositions at depth. The sharp decrease in sulfate between the surface (~24 mM) and ~50 m depth (~5 mM) is mirrored by an approximately equimolar increase in alkalinity, which is consistent with microbial sulfate reduction and the release of $HCO_3^-$ into solution according to the simplified net reaction

$$2CH_2O \text{ (organic matter)} + SO_4^{2-} = 2HCO_3^- + H_2S.$$

Microbial activity could also be responsible for production of phosphate, which peaks at nearly 100 mM, or ~100× seawater abundance, at 55.5 mbsf, and ammonium, which peaks at 2094 µM at 82.5 mbsf.

The overall shape of the sulfate profile, strong depletion in a shallow region of microbially mediated sulfate reduction, and a gradual return to seawater compositions is peculiar but has been previously documented in several holes (ODP Leg 170 Site 1039 and Integrated Ocean Drilling Program Expeditions 334 and 344 Site U1381). In these cases it was attributed to the infiltration and upward diffusion of sulfate-rich fluids from below the zone of sulfate reduction (Expedition 334 Scientists, 2012; Harris et al., 2013). We hypothesize that this region of fluid influx coincides with a zone of poor core recovery, grain-size increase, and strong seismic attenuation at ~300 mbsf in Hole U1437B. This zone is also characterized by a broad peak in pore water Li that would be consistent with vertical diffusion from a zone of horizontal fluid infiltration (see below).

Variations in IW major elements (Na, Ca, and Mg) (Fig. **F37**) are best evaluated by separating the trends observed over a shallow depth range (0–100 mbsf) attributed to biologic processes from those at greater depth (>100 mbsf), which are more strongly controlled by processes such as distal fluid migration and diagenesis. At ~450–500 mbsf, the trends for Na, Ca, and Mg show prominent breaks: Na and Ca increase more strongly with depth, with a Ca concentration versus depth gradient of 0.14 mM/m, and Mg strongly decreases at –0.11 mM/m to a minimum of 9.6 mM at 693 mbsf. Lithification increases at about the same depth producing dominantly tuffaceous mudstone from tuffaceous mud. Moreover, the abundance of mafic and evolved tuff increases deeper than ~450 mbsf, and therefore the increase in Ca with concomitant depletion in Mg is reasonably attributed to alteration of volcanic glass and the formation of smectite (e.g., Riedel et al., 2006).

Depth discontinuities of IW minor components (B, Ba, Fe, Li, Mn, Si, and Sr; Li and Si shown in Fig. **F37**) often correlate with the changes described above. B depth vari-

ations mirror the hockey stick profile for pH by very gradually decreasing from near seawater compositions to ~600 mbsf followed by a sharp drop to the terminal depth of IW sampling at 693 mbsf. The correlation of this decrease with strong depletions of deep pore waters in Mg and concomitant increases in pH and Ca suggests absorption of B in clays formed from alteration of volcanic glass. Ba and Fe concentrations show little variability with depth and often scatter widely over small depth intervals.

Li displays a hump-shaped profile with a maximum (70 µM) between 283 and 343 mbsf (Fig. **F37**). Li declines deeper than 343 mbsf to a local minimum at 459 mbsf, coincident with the sulfate minimum (Fig. **F36**). The main hump of the Li profile is consistent with the ingression of a high-Li fluid at this depth, which corresponds to a zone of poor core recovery that also matches a major seismic reflector at ~300 mbsf. This situation is similar to observations for Integrated Ocean Drilling Program Expedition 344 Site U1380, where a horizon of elevated Li concentrations correlated with a shear zone interpreted to act as a conduit for fluids with elevated source temperatures (Harris et al., 2013). The upward decrease in Li in the Site U1437 profile suggests progressive dilution, whereas the downward decrease indicates uptake of Li by clay minerals formed during alteration of volcanic glass.

The Mn depth profile mimics the hockey stick profile for chlorinity, except for an excursion to high Mn concentrations in the near-surface IW sample from Core 350-U1437D-2H (8.4 mbsf). Dissolved Si parallels the hump-shaped Li depth profile.

At shallow depth, the progressive dissolution of diatoms could be responsible for Si increases, whereas transformation of biogenic opal-A to opal-CT could act as a sink for Si (Fig. **F37**) (Littke et al., 1991). The peak in IW Si (~1250 µM) qualitatively agrees with the decline in diatom preservation with depth (they are last observed in Core 350-U1437D-6R at 471 mbsf), and the decrease of Si below the putative opal-A to opal-CT transition zone correlates with accelerated B uptake (Brumsack and Zuleger, 1992). Furthermore, downhole logging data indicate a temperature of ~50°C at the transition; coupled with an age of ~3.5 Ma, these conditions appear optimal for forming opal-CT (Hein et al., 1979). Alternatively, the Si maximum at intermediate depth could also be attributed to fluid influx, analogous to Li. Sr defines a complex downhole profile, displaying a minimum of 52 µM at 37 mbsf, consistent with the zone of sulfate reduction and $CaCO_3$ precipitation, which shows a broad maximum at this depth. Although Sr concentrations are depleted at shallow depth, the Sr/Ca ratio peaks at ~45 µM/mM at ~100 mbsf. This is consistent with diagenetic carbonate recrystallization, which releases Sr into the pore waters (Baker et al., 1982). Coinciden-

tally, the depth interval with near-seawater Sr/Ca at ~370 mbsf corresponds to the Li maximum and might indicate the influx of modified seawater along fast pathways.

### *Mud and mudstone bulk geochemistry*

A total of 229 sediment samples were collected at Site U1437 and analyzed for concentrations of $CaCO_3$, total carbon (TC), total organic carbon (TOC), and total nitrogen (TN) (Fig. **F38**) using coulometry and elemental analyses, respectively. The atomic ratios of TOC and TN ($TOC/TN_{at}$) were calculated to determine the source of the sedimentary organic matter. Total carbon contents are highly variable over the whole cored sequence and range between 0.26 wt% at 17 mbsf (Section 350-U1437B-3H-2W) and 6.89 wt% at 913 mbsf (Section 350-U1437D-53R-1W) with an average value of 3.2 wt%. $CaCO_3$ shows a highly variable profile with average concentrations of 21.9 wt%. Minimum (0.46 wt%) and maximum (57.1 wt%) $CaCO_3$ concentrations occur at the same depths as minimum and maximum TC values, respectively. Plotting the five-point average values of $CaCO_3$ contents reveals two intervals with comparatively high $CaCO_3$ contents in the uppermost ~170 m of the cored sequence (Fig. **F38**). Another interval with elevated $CaCO_3$ contents is observed at ~900 mbsf. Thereafter, $CaCO_3$ contents gradually decrease with depth.

The observed strong and short-termed variations in sedimentary $CaCO_3$ weight percentages may not be a result of highly variable inputs of $CaCO_3$ reaching the seafloor but a result of varying inputs of detrital material such as clay and ash, which may act as diluents.

TOC contents range from below detection to a maximum of 3.64 wt% at 508 mbsf (average = 0.45 wt%) throughout the cored sequence and are comparatively higher in the upper ~230 mbsf, where the TOC average is 0.61 wt%, although there are several peaks with elevated TOC contents thereafter. Despite these peaks, TOC contents remain at a low level of 0.26 wt% deeper than ~230 mbsf.

TN contents are generally low throughout Site U1437. Values range up to a maximum of 0.1 wt% with an average of 0.024 wt% and highest TN contents in the uppermost ~230 m of the cored sequence. Deeper than that depth, TN contents decrease continuously, probably as a result of nitrogen loss during diagenesis.

$TOC/TN_{at}$ ratios vary from 2.33 to 213 with an average of 18.6, suggesting a mixed input of both marine- and terrestrial-derived organic matter. Typical values for marine sources of organic matter range between 4 and 10, whereas terrestrial-derived organic

matter has $TOC/TN_{at}$ ratios >20. However, the TOC and TN values at Site U1437 show only a very weak correlation ($R^2$ = 0.18), possibly suggesting an important contribution of inorganic nitrogen sources. Ammonium adsorbed to clay particles can make up a significant TN fraction in organic-poor marine sediments (Müller, 1977). The admixtures of this inorganic nitrogen species and organic nitrogen may lead to overestimation of marine-derived organic matter, which is typically enriched in nitrogen (Meyers, 1994).

### *Major and trace elements*

Major and trace element compositions of mud indicate mixing between at least three major components. Based on variations in CaO and $K_2O$ (Fig. **F39**), these are characterized as (1) high CaO/low $K_2O$, (2) low CaO/low $K_2O$, and (3) low CaO/high $K_2O$. Sr and Rb display similar compositional patterns (Fig. **F39**) and can be interpreted as the trace element equivalents of CaO and $K_2O$, respectively, with CaO and Sr being dominantly contributed by marine carbonate (with stoichiometric CaO = 56 wt% for pure $CaCO_3$, and average Sr = 1100 ppm; Morse and Mackenzie, 1990), whereas $K_2O$ or Rb are essentially nil in marine carbonates but comparatively enriched in volcanic ash or terrigenous clays (e.g., Plank, 2014). A significant amount of carbonate in mud is supported by large LOI values (average = 16 wt%), although this value may overestimate $CaCO_3$ because of the presence of $H_2O$ and minor volatile components such as N or S. Direct determination of $CaCO_3$ in a different set of samples (see above) yielded an average of 21.9 wt% and a maximum of 57.1 wt%. The identification of Components 2 and 3 is tentative because of the limitations of shipboard data in frequency and number of elements analyzed, but binary variation diagrams for $K_2O$ versus CaO and Rb versus Sr are consistent with the low $K_2O$-low Rb component (2) being Izu arc front and rear arc. Izu arc-front volcanism includes basalt-dominant island volcanoes with compositionally related rhyolites and compositionally distinct rhyolites from submarine calderas (e.g., Tamura et al., 2009). Rhyolites from submarine calderas (R2 type in Tamura et al., 2009) are higher in $K_2O$ and Rb compared to rhyolites from basalt-dominant island volcanoes (R1 type), but R2 rhyolites still fall short of the high $K_2O$ and Rb abundances at low CaO and $K_2O$ in some of the mud samples. The same holds for the average composition of rear-arc tephra determined from Site U1437 data (Fig. **F39**). We therefore invoke another component with $K_2O$ and Rb higher than the arc-front or rear-arc compositions. A suitable match for this component (3) is distal Ryukyu arc ash (Scudder et al., 2009), whereas terrigenous sediment such as Chinese loess (Chen et al., 2001) is insufficiently enriched in $K_2O$ and Rb to match end-member (3) in mixing triangles (Fig. **F39**). This explanation does not rule out the presence

of terrigenous clays, but their presence would be geochemically cryptic because it would plot close to a binary join between arc-front and rear-arc ash (2) and distal Ryukyu ash (3) in Figure **F39.** Dilution of ash and clay components by siliceous oozes is also possible but hard to quantify with the existing geochemical data.

Downhole variations in mud geochemistry are monitored by minor and trace elements (Rb, Zr, and $TiO_2$; Fig. **F40**). These elements are only contributed in significant amounts by ash or terrigenous sediment, and Zr/Y is invariant with dilution from carbonates and siliceous oozes and alteration. Zr/Y from ICP-AES ($n$ = 10) and pXRF ($n$ = 38) closely agree and show systematic decreases with depth that correlate with decreasing Rb and Zr. $TiO_2$, by contrast, increases especially below the transition from lithostratigraphic Unit III to IV at 1018 mbsf. This indicates a larger contribution from ash and clay relative to carbonate, which mirrors the increase in $TiO_2$ (Fig. **F40**). The overall average for Site U1437 mud is Zr/Y = 3.1, which is slightly higher than in mud from fore-arc Site U1436 (Zr/Y = 2.7) but not as elevated as the average subducting sediment composition for the Izu-Bonin trench at 31°20′N (ODP Leg 185 Site 1149; Zr/Y = 3.3; Plank and Langmuir, 1998). Significant variations in Zr/Y with depth are detected by both pXRF and ICP-AES analyses of mud: maximum Zr/Y in mud from Unit I is 4.4, whereas values as low as 1.6 are detected in Units III–VI (no mudstone was recovered from Unit VII). Importantly, the decrease in Zr/Y is correlated with downhole decreases in Rb (Fig. **F40**). It thus appears unlikely that the downhole trends in Zr/Y reflect variations in ash provenance from local sources (i.e., arc front versus rear arc), which are both extremely depleted in Rb, but rather a declining influence of terrigenous clay or distal ash, especially from sources with high Zr/Y and Rb such as the Ryukyu arc. This agrees with findings from Site 1149 (Scudder et al., 2009) and suggests a remarkable far-field influence of <3.5 Ma volcanic activity in the Ryukyu arc on the chemistry in fine-grained sediment in the northwest Pacific Ocean.

### Rock magnetism

Rock magnetic measurements at Site U1437 comprised saturation isothermal remanent magnetization (SIRM) acquisition, backfield demagnetization of SIRM by a 300 mT field to yield the $S_{-0.3T}$ ratio, stepwise acquisition of partial anhysteretic remanent magnetization (pARM), thermal demagnetization analysis, and anisotropy of magnetic susceptibility (AMS).

Through Holes U1437B and U1437D, a number of significant features in the downhole distribution of rock magnetic properties correlated with features of the physical properties, pore fluid geochemistry, and hydrocarbon geochemistry records. Overall,

the rock magnetic properties show a downhole trend suggesting that after initial biologically mediated reduction in the sulfate reduction zone to produce greigite, the proportion of greigite gradually decreased, presumably though slow completion of the iron sulfide reduction chain to convert this ferrimagnetic sulfide to paramagnetic pyrite. Superimposed on this trend is a break at ~400 mbsf, where SIRM/k, $S_{-0.3T}$, and magnetic foliation all show step changes. This represents a sudden downhole increase in the proportion of magnetic sulfides, followed by gradual returns to trend over the 300 m below. The return to trend in SIRM and $S_{-0.3T}$ occurs in the lower part of lithostratigraphic Unit I and appears to be complete by the Unit I/II boundary at ~680 mbsf, corresponding also to the top of PP Unit 2 (Fig. **F41**). After initial sulfate reduction, sulfate recovers over a diffusion zone extending to ~275 mbsf, where there appears to be a fluid source (see **"Pore fluid analysis"**) and plateaus from there to ~400 mbsf; over this interval $S_{-0.3T}$ values drop to below 0.97, suggesting renewed and enhanced production of greigite. Deeper than ~400 mbsf, sulfate increases again downhole to near-seawater concentrations at ~460 mbsf, corresponding to the highest value of SIRM/k in all samples measured at Site U1437, and remains high to the deepest IW sample taken at 700 mbsf. Greigite concentration inferred from the rock magnetic parameters decreases downhole below 460 mbsf, returning to the background trend at ~680 mbsf, corresponding to the Unit I/II boundary and the top of PP Unit 2. A second source of fluid at ~460 mbsf appears to be driving both sulfate concentration and greigite genesis.

Surprisingly, given the apparent continuity of broadly similar lithologies through lithostratigraphic Units I–V across Holes U1437B, U1437D, and U1437E, rock magnetic properties in Hole U1437E do not follow the trends seen through Holes U1437B and U1437D. The background log-linear downhole decrease in SIRM/k that persists throughout Units I–IV is absent from Units V and VI. Instead, SIRM/k values appear to be randomly scattered over a wide range. Coercivity spectra from pARM analysis also show a wide range, from very magnetically soft (peak coercivity < 20 mT) to harder (broad coercivity peak from 20 to 30 mT) without any systematic downhole trends. Magnetite in samples from Hole U1437E appears to be dominated by large multidomain (MD) grains (presumably because of complete dissolution of finer magnetite grains), prompting our use of liquid nitrogen pretreatment to remove MD-carried overprints.

The break between Holes U1437D and U1437E manifests as an apparently instantaneous change in polarity and a break in magnetostratigraphy. Normal polarity of Subchron C3An.2n persisted to the bottom of Hole U1437D, but cores in Hole U1437E,

which started at the same subbottom depth as the base of Hole U1437D, commenced immediately in reversed polarity. Pattern matching of the polarity record in Hole U1437E indicated that the reversed polarity interval began immediately above normal Subchron C4n.1n. This apparent loss of section can be most easily explained by the presence of a normal fault intercepting at a depth range near the break between the two holes; this fault may have been responsible for the poor hole conditions that terminated Hole U1437D. Differences in fluid circulation systems between the fault footwall and hanging wall could be the cause of both the sudden appearance of ethane at the top of Hole U1437E (see **"Hydrocarbon gases"**) and the contrasting rock-magnetic properties of the two holes.

## Igneous geochemistry

### *Sampling, data acquisition, and data treatment*

Analyses were carried out by pXRF and ICP-AES, and samples included ash and tuff (pXRF $n$ = 88; ICP-AES $n$ = 26), lapilli tuff and lapillistone (pXRF $n$ = 7; ICP-AES $n$ = 14), igneous clasts (pXRF $n$ = 39; ICP-AES $n$ = 9), and a rhyolite sheet (pXRF $n$ = 1; ICP-AES $n$ = 1). Reconnaissance pXRF and ICP-AES analyses generally agree within <20% (relative) for elements that can be analyzed by both techniques. ICP-AES data reported here include only samples with analytical totals of 100% ± 5% (after ignition).

Identifying tephra sources at Site U1437 requires accounting for the detrimental effects of pervasive alteration, which causes element mobility. These effects are most severe for alkali elements and Ba (Gill et al., 1994) and less so for elements that are insoluble in seawater (Ti, Al, and Fe; e.g., Stroncik and Schmincke, 2002). High–field strength element ratios such as Zr/Y remain largely unaffected by alteration (Gill et al., 1994). Another concern is contamination with pelagic sediment, especially in fine-grained ash or tuff samples, which can impact major and trace elements such as CaO and Sr that are enriched in calcareous materials. HFSE ratios are reliable indicators here because they are invariant with regard to carbonate abundances (estimated from CaO). All major elements are plotted normalized to 100 wt% volatile-free.

### *Tephra compositions and provenance*

Rear-arc seamount and arc-front volcanoes are geochemically distinct in several major and trace elemental as well as isotopic parameters. Here, we compare shipboard analyses with a compilation of literature data, which we grouped into two major categories, and these fields are shown in Figures **F42A, F42B,** and **F43:**

1. Izu arc front includes basalt-dominant island volcanoes and rhyolite-dominant submarine calderas (Tamura et al., 2009), as well as tephra samples collected in the fore-arc region (Jordan et al., 2012; Gill et al., 1994; Bryant et al., 2003; Straub et al., 2003, 2010). The basalt-dominant island volcanoes also produced minor amounts of rhyolite (termed R1 type by Tamura et al., 2009), which have lower Zr/Y (1.1–3.2) than rhyolite erupted from submarine calderas (R2 type; Zr/Y = 2.7–5.5; Tamura et al., 2009).
2. Rear-arc volcanic rocks include all the rear-arc seamount volcanoes from 3 to 17 Ma (Hochstaedter et al., 2001; Ishizuka et al., 2002, 2003a, 2003b, 2006a, 2006b; Machida et al., 2003, 2008; Tollstrup et al., 2010), which are generally higher in Zr/Y (1.4–6.7) compared to arc-front rocks at comparable $SiO_2$, but there is some overlap between R2 arc-front rhyolites and rear-arc seamount rocks.

Volcanism younger than ~3 Ma immediately to the west of the arc front also comprises bimodal eruptions in active rift basins, ridges, and seamounts, collectively termed back-arc knolls (Tollstrup et al., 2010). For simplicity, we excluded these compositions from plotting but we note that they are often transitional between Category 1 and 2 rocks. This limits unambiguous source assignments for samples younger than 3 Ma from Site U1437.

Lava from rear-arc volcanoes has higher $K_2O$, Sr, and Zr/Y ratios at the same $SiO_2$ content than that of arc-front volcanoes (Figs. **F42B, F43, F44**). Thus, $K_2O$, Sr, and Zr/Y ratios at the same $SiO_2$ of tephra suggest they came from either arc-front or rear-arc volcanoes. This discrimination is only applicable to the Neogene tephra.

### *Unit I*

Unit I samples from 0 to 440 mbsf (<3 Ma) include 6 ICP-AES and 13 pXRF analyses of mostly fine-grained ash and rare lapilli. They range from basaltic andesite to rhyolite and have relatively low $K_2O$ abundances (0.35–1.48 wt%), generally overlapping with compositions of arc-front and active rift volcanic rocks (Fig. **F42**). Unit I samples from 440 to 682 mbsf (3–4.2 Ma) include 2 ICP-AES and 19 pXRF analyses of tuff that range in composition from andesite to rhyolite. These have slightly higher $K_2O$ contents (0.50–2.43 wt%) compared to the <3 Ma ash and have low Zr/Y (2.2–2.3) similar to arc-front lava and tephra (Fig. **F43**). With the possible exception of high-$SiO_2$ Samples 350-U1437B-1H-3W, 13–14 cm (3.1 mbsf; $SiO_2$ = 71.6 wt%), 7H-3W, 12–13 cm (55.7 mbsf; $SiO_2$ = 70.2 wt%), and 12R-6W, 98–100 cm (531.7 mbsf; $SiO_2$ = 75.1 wt%), most ash is a mixture between mafic and evolved end-members, which may not be

representative of the magma compositions. Reconnaissance pXRF analyses for shallow Unit I (<3 Ma) yielded Zr/Y from 2.1 to 8.4 with a median value of 3.2 ($n$ = 13). The high Zr/Y Sample 35X-2W, 6–7 cm (244 mbsf), is a lapilli tuff and is thus likely proximal, although its Zr/Y exceeds that of known rear-arc eruptions. Low Zr/Y samples (e.g., Sample 5H-5W, 32–33 cm, at 40 mbsf) are fine-grained mafic ash, consistent with a distal origin from the arc front. Unit I (>3 Ma) samples show a similar range in pXRF Zr/Y (1.7–6.0) and a median Zr/Y (2.9) that is indistinguishable from those of shallower tephra from Unit I, consistent with ICP-AES analyses (Fig. **F43**). Low Zr/Y (2.3) of the high-silica tuff Sample 12R-6W, 98–100 cm (531.7 mbsf), suggests a possible origin as a R1 rhyolite associated with a basalt-dominant island volcano in the arc front (Tamura et al. 2009).

### *Unit II*

Unit II (682.12–726.50 mbsf; age model ~4.2–4.4 Ma) is marked by a shift in grain size and style of deposition containing the first lapilli tuff and lapillistone deposits. Unit II samples include 3 ICP-AES and 4 pXRF analyses of tuff and lapilli tuff ranging from andesite to dacite with $K_2O$ contents from 0.39 to 2.22 wt% (Fig. **F42**). Sample 350-U1437D-29R-2W, 4–5 cm (691 mbsf), represents an individual lithified pumice clast that is dacitic in composition ($SiO_2$ = 63.6 wt%) with high LOI (6.9 wt%) suggesting some alteration. This is supported by elevated MgO concentrations (6.48 wt%) relative to $SiO_2$. However, Zr/Y (6.2) is elevated to a level that is only found in rear-arc lava (Fig. **F43**). Bulk lapilli tuff Sample 30R-2W, 122–125 cm (701.2 mbsf), comprises intricate layers with variable proportions of glass and crystals (feldspar, amphibole, clinopyroxene, biotite, and minor quartz), whereas Sample 30R-6W, 58–61 cm (706.2 mbsf), consists primarily of fresh and devitrified glass with plagioclase and amphibole of uniform grain size. Both are dacites (68.3 and 67.6 wt% $SiO_2$) with moderate $K_2O$ concentrations of 2.12 and 1.89 wt%, respectively, consistent with a rear-arc origin (Fig. **F42**).

### *Unit III*

Unit III (726.50–1017.88 mbsf; age model ~4.3–6 Ma) consists primarily of altered green tuffaceous mudstone with occasional interbedded tuff. Fourteen tephra samples analyzed by ICP-AES have intermediate compositions ranging from basaltic andesite to dacite and are mostly similar to the arc-front field in $K_2O$ versus $SiO_2$ (Fig. **F42**). There are four exceptions: Samples 350-U1437D-40R-7W, 44–46 cm (805.2 mbsf), 41R-1W, 0–2 cm (805.8 mbsf), 42R-5W, 40–43 cm (820.5 mbsf), and 43R-2W, 31–33 cm (826.9 mbsf), which have elevated $K_2O$. Sr concentrations vary greatly (up

to 804 ppm) and are elevated compared to Unit I and II tephra as well as lava from the volcanic front and typically higher than rear-arc lava. Two basaltic andesite Samples 40R-7W, 44–46 cm (805.2 mbsf), and 41R-1W, 0–2 cm (805.8 mbsf), contain exceptionally low Sr concentrations (45 and 139 ppm), for which the closest equivalent are Manji Seamount volcanic rocks with potassic alteration (Sr = 107 ppm; Ishizuka et al., 2002).

All but three tephra samples display elevated Zr/Y compared to rocks from basalt-dominant volcanic islands in the Izu arc front, which generally have Zr/Y peaks at 2.5. This includes several tephra samples that are coarse-grained tuff to minor lapilli tuff. Low Zr/Y (<2.5) tephra in Unit III comprises andesitic tuff Samples 350-U1437D-40R-7W, 44–46 cm (805.2 mbsf), 55R-6W, 95–97 cm (940 mbsf), and 56R-5W, 0–4 cm (947.55 mbsf; Zr/Y = 1.8), in which glass shards are often altered (Fig. **F43**). Despite the presence of some low Zr/Y tephra likely derived from basalt dominant volcanoes in the arc front, high Zr/Y tephra is predominant in Unit III, as indicated by the overall median of Zr/Y (3.1) (pXRF $n$ = 43; ICP-AES $n$ = 14), which is elevated above the average for arc-front basalts, intermediates, and R1 rhyolites.

### *Unit IV*

Samples analyzed by ICP-AES comprise a single andesite clast (Sample 350-U1437D-68R-2W, 43–46 cm; 1049.2 mbsf) and three bulk lapilli tuff samples (69R-1W, 37–39 cm, 1056.5 mbsf; 72R-1W, 44–46 cm, 1085.7 mbsf; and 350-U1437E-6R-3W, 106–109 cm, 1120.0 mbsf). All samples show evidence for alteration. Samples 350-U1437D-69R-1W, 37–39 cm (1056.5 mbsf), and 72R-1W, 44–46 cm (1085.7 mbsf), also have low CaO relative to $SiO_2$ and anomalously high $K_2O$ (4.78 and 4.88 wt%, respectively) and are characterized by high abundances of submicroscopic alteration phases (~40 and ~50%, respectively). Sample 350-U1437E-6R-3W, 106–109 cm (1120.0 mbsf), has high FeO* (Fig. **F42**), consistent with pervasive chlorite alteration visible in thin section. With this caveat, we interpret the elevated Zr/Y (median Zr/Y from pXRF = 4.1; $n$ = 41) and ICP-AES (average Zr/Y = 3.6; $n$ = 4) as supporting evidence for the comparatively large grain size indicating proximal sources in the rear arc, most likely Manji Seamount (Fig. **F43**).

### *Unit V*

Nine tephra samples (4 lapilli tuff, 3 tuff, 1 lapilli stone, and 1 tuff breccia) analyzed by ICP-AES from Unit V (1120.11–1312.21 mbsf) show large composition variations from basaltic andesite to rhyolite and are chemically more depleted than Unit IV te-

phra. Samples 350-U1437E-7R-7W, 71–74 cm (1130.9 mbsf), 16R-6W, 114–117 cm (1211.6 mbsf), 19R-1W, 104–105 cm (1233.7 mbsf), and 27R-1W, 99–102 cm (1311.3 mbsf), have slightly higher $K_2O$ (0.91–1.70 wt%) than arc-front rocks (Fig. **F44**). The other five ICP-AES samples in Unit V have low $K_2O$ (0.34–0.69 wt%). This includes a rhyolite tuff with fiamme (Sample 20R-2W, 25–26 cm; 1244.0 mbsf) that displays low $K_2O$ (0.69 wt%) and high Ba (620 ppm) and Sr (566 ppm) concentrations, suggesting the influence of alteration on the chemical composition (Fig. **F42**). Four tephra samples (tuff breccia, lapillistone, lapilli tuff, and tuff) display elevated Zr/Y (>3) that are higher than compositions for basalt-dominant island volcanoes in the arc front, including Samples 16R-6W, 114–117 cm (1211.6 mbsf), 17R-2W, 114–117 cm (1211.6 mbsf), 19R-1W, 104–105 cm (1233.7 mbsf), and 20R-2W, 25–26 cm (1244.0 mbsf). The lack of systematic variations between $K_2O$ and Zr/Y (both potential discriminants between rear-arc and arc-front sources) is interpreted to result from intense alteration. Sample 7R-7W, 71–74 cm (1130.9 mbsf), for example, is an andesitic tuff that has rear arc-like $K_2O$ (0.98 wt%) but low Zr/Y (1.6) indicative of an arc-front magma composition. On the contrary, Sample 17R-2W, 114–117 cm (1216.0 mbsf), a lapillistone with andesite clasts, has low $K_2O$ (0.53 wt%) but high Zr/Y (3.9).

### *Unit VI*

Six samples from Unit VI (1320.00–1459.80 mbsf) analyzed by ICP-AES are four lapilli tuff samples, one andesite clast, and one rhyolite intrusion (igneous Unit 1). Three lapilli tuff samples and a clast are basaltic andesite in compositions. Single andesite clast Sample 350-U1437E-41R-2W, 1–3 cm (1448.0 mbsf), has slightly higher $K_2O$ (0.90 wt%) relative to $SiO_2$ than expected if it evolved along the arc-front trend (Fig. **F42**), yet its Zr/Y (2.4) is well within the range of basalt-dominant arc-front lava and tephra (Fig. **F43**). Three lapilli tuff Samples 28R-4W, 42–44 cm (1324.5 mbsf), 31R-4W, 63–65 cm (1353.8 mbsf), and 34R-4W, 31–32 cm (1382.1 mbsf), also have low Zr/Y (1.8–2.1), consistent with low $K_2O$ (0.21–0.58 wt%) except for 34R-4W, 31–32 cm (1382.1 mbsf), which is moderately enriched in $K_2O$ (1.15 wt%). Nineteen pXRF analyses on Unit VI samples yielded a median Zr/Y of 2.5, consistent with low Zr/Y in ICP-AES analyses (2.2; $n = 8$) and confirm the generally depleted nature of Unit VI tephra. One unusual composition is that of Sample 34R-5W, 50–53 cm (1383.5 mbsf), which has high $SiO_2$ = 85.6 wt% indicating silicification, which is consistent with the presence of chalcedony observed petrographically.

The rhyolite intrusion (igneous Unit 1; Sample 350-U1437E-35R-2W, 42–44 cm; 1390.0 mbsf) is a highly evolved rhyolite with extremely low Sr (8 ppm) and Ba (16

ppm), unusually low $K_2O$ (0.48 wt%), but high Zr/Y (5.8) (Figs. **F42, F43**). Its origin remains elusive with limited shipboard analyses, but high-silica rhyolites with extremely low abundances of feldspar-compatible trace elements such as Sr and Ba are interpreted to be products of protracted fractional crystallization rather than direct products of crustal melting (Mahood and Halliday, 1988).

#### *Unit VII*

Six volcanic lithic clasts from volcanic breccia in Unit VII (1459.8–1806.5 mbsf) were analyzed by ICP-AES comprising five andesites and one dacite. All but one sample are highly depleted in $K_2O$ (0.11–0.77 wt%) similar to arc-front rocks (Fig. **F42**). Sample 350-U1437E-70R-2W, 95–97 cm (1721.4 mbsf), displays slightly higher $K_2O$ (1.05 wt%) compared to other Unit VII samples. This sample also has significantly higher Ba and lower Cr and Cu compared to the other three andesite samples at equivalent $SiO_2$ (Samples 43R-2W, 99–101 cm, at 1468.2 mbsf; 44R-2W, 36–38 cm, at 1477.1 mbsf; and 51R-1W, 31–34 cm, at 1544.1 mbsf), suggesting different volcanic sources. All Unit VII ICP-AES samples have comparatively low Zr/Y (average = 2.6; $n$ = 3), overlapping with the range of pXRF analyses of clasts from this unit (average = 3.0; $n$ = 45). These values generally fall between the peak in Zr/Y for basalt-dominant island volcanoes in the arc front and Zr/Y in rear-arc lava (Fig. **F43**).

### Possible effects of alteration and grain size on chemical compositions of tephra

The presence of low-temperature alteration (indicated by the presence of biotite) and high-temperature alteration (indicated by the presence of epidote) has been observed from dredged and submersible samples on the Manji Seamount (Ishizuka et al., 2002). These alterations can greatly affect major and trace element compositions evident in steep depletions in CaO relative to increasing $SiO_2$ (Fig. **F42**). We focus on Zr and Y because they are relatively fluid immobile and remain robust during alteration (Gill et al., 1994). This is supported by published Manji Seamount data that have near-constant Zr/Y even when highly altered (Ishizuka et al., 2002). Consequently, we use primarily shipboard Zr/Y analyses as an indicator for magmatic provenance and to distinguish between rear-arc and arc-front sources.

### Tephra provenance and in situ magma evolution

Downhole geochemical variations in Units I–V generally reflect the relative proportions of distal arc-front and proximal rear-arc volcanic sources (Fig. **F44**). As a general trend, coarse-grained tephra from Units II and IV show stronger rear-arc affinity compared to fine-grained tuff from Units I, III, and V. Complications for provenance arise

from mixing evident by mafic and evolved glass shards in fine-grained tephra samples and pervasive green alteration in Units III and V.

The predominance of ash layers from Unit I containing low $K_2O$ relative to $SiO_2$ indicates a likely volcanic front or active rift (ash <2 Ma) provenance. Some <3 Ma tephra in Unit I with high Zr/Y could thus be mixtures of mafic and evolved (high Zr/Y rhyolites of the R2 type of Tamura et al., 2009) ash derived from arc-front volcanoes, but this cannot be confirmed without onshore in situ analyses of glass. The coarse-grained deposits from Units II and IV indicate proximal sources. Active Manji Seamount chain volcanoes around the time of deposition of Unit II (4.2–4.3 Ma) were the Meireki Seamount (3.76 Ma; Ishizuka et al., 1998) ~20 km to the north and the Daigo-Higashi Aogashima Knoll (5.05 Ma; Ishizuka et al., 2003b) ~40 km to the northeast of Site U1437. Both are rhyolite volcanoes with similar $SiO_2$ contents (72–76 wt%), whereas Meireki Seamount volcanic rocks have higher $K_2O$ (~3 wt%) but lower Zr/Y (~2.8) compared to the Daigo-Higashi Aogashima Knoll ($K_2O$ = ~1.5 wt%; Zr/Y = ~4.4) (Hochstaedter et al., 2001). Although the limited data (five analyses in total) available for both seamounts preclude reliable geochemical matching with Unit II tephra, they are potential sources for coarse-grained lapilli from Unit II considering their geographic locations, ages, and chemical composition. Similarly, single clast compositions of Unit IV can be tentatively matched to available data for Manji Seamount volcanic rocks (~6.5–6.9 Ma; Ishizuka et al., 2002). Two high-$K_2O$ tephra resemble the high-K Manji Seamount rocks with potassic alteration, whereas most tephra from Unit IV follow the trend for altered Manji Seamount rocks leading to depletions in CaO with increasing $SiO_2$ (Fig. **F42**) (Ishizuka et al., 2002).

Unit V is primarily mud, and given the pervasive alteration throughout this interval it is difficult to provide an accurate provenance for tephra. Based on ICP-AES Zr/Y data and the only moderately elevated median Zr/Y from pXRF (2.7; $n$ = 39) (Fig. **F43**), we tentatively interpret Unit V to be geochemically transitional, with tephra and clast compositions that include both rear-arc and arc-front sources. The presence of volcanic breccia (with clast sizes up to 40 cm) in Units VI and VII supports proximal volcanic deposition. However, the Zr/Y values of blocks within breccia vary widely between 0.4 and 4.0. Similar compositional heterogeneity exists in the late Miocene Shirahama group in the Izu Peninsula of southern Japan, which represents accreted rocks of rear-arc origin (Tamura, 1994, 1995; Tamura and Nakamura, 1996; Tani et al., 2011). The Shirahama lava is divided into tholeiitic and calc-alkaline series, which have low Zr/Y and high Zr/Y, respectively. However, the late Miocene Shirahama lava

does not display the same degree of depletion seen in the $K_2O$ contents of Unit VI and VII blocks.

## Summary and interpretation of volcaniclastic deposits

The 1800 m thick section drilled at Site U1437 is dominantly fine grained, with tuffaceous mudstone making up 58% of the section. The discrete thin ash/tuff layers that make up 21% of the described core are the products of some combination of subaqueous suspension fallout and dilute density currents, as discussed further below. Only 20% of the described core contains particles coarser than 2 mm (lapilli), and those are almost entirely restricted to fine-grained lapilli (<2 cm); only the basal two lithostratigraphic units (VI and VII) have coarser lapilli and scattered blocks, and those two units make up only ~25% of the 1800 m thick section.

The mud/mudstone that dominates Site U1436 is featureless except where ash tuff layers grade up into mudstone and bioturbation is marked by mixing of the ash into the mud. Therefore, it seems likely that virtually all primary sedimentary structures in the mud/mudstone were obliterated by bioturbation. That makes it impossible to determine whether the mud was deposited from hemipelagic rain, dilute turbid flows, bottom currents (e.g., related to the Kuroshio Current), or some combination thereof. Future geochemical work is expected to contribute to an understanding of the provenance of the mud/mudstone. Any hypothesis for the origin of the mud/mudstone must take into the consideration the fact that the dominantly mud/mudstone section drilled at Site U1437 accumulated at unusually high rates for such fine-grained material (Fig. **F44**).

### Interpretation of eruption and depositional processes

Despite the dominance of featureless mudstone in the section drilled at Site U1437, macroscopic and microscopic shipboard analysis of the discrete ash/tuff and lapilli ash/lapilli tuff beds at Site U1436 allows us to make preliminary interpretations about the eruption, transport, and depositional processes that produced them. This analysis deals with deposits from all of the lithostratigraphic units described above (Units I–VII).

#### *Evolved ash/tuff and mafic ash/tuff*

The sharp basal contacts, good sorting, and normal grading in this lithofacies could indicate deposition by suspension settling through water, seafloor hugging density

currents, or some combination (e.g., vertical density currents that transition into lateral density currents when they reach the seafloor in a manner envisioned by Carey [1997] and Manville and Wilson [2004]). These are the only volcaniclastic deposits in Units I and III besides the tuffaceous mudstone.

#### *Intercalated white to green tuff*

This lithofacies is fine grained, with laminations produced by alternation of glass shard–rich layers (white) and layers of mixed shards, pumice, and crystal fragments (gray-green), repeated over intervals up to several meters thick, with no bioturbation or mudstone interbeds. Thus, the intervals seem to record fairly continuous but pulsating sedimentation, probably from unsteady density currents, over a relatively short period of time for each interval (possibly days or weeks). The very large quantity of very fine glass shards in this facies suggests either phreatomagmatic eruption with extremely efficient glass fragmentation or extreme sorting of products from dry pyroclastic eruptions. This lithofacies occurs in Units III and IV.

#### *Monomictic pumice lapilli tuff and lapillistone*

This lithofacies is relatively well sorted with abundant interstratified well-sorted crystal and vitric tuff, and is stratified, with planar and cross lamination, sharp bases, and grading bioturbated tops. This lithofacies is interpreted to represent sediment gravity flow deposits, and the monomictic composition may indicate that at least some were eruption fed. This lithofacies dominates Unit II.

#### *Monomictic tuff with pumice and fiamme*

This lithofacies consists of poorly sorted beds with basal scour, composed largely of ash-sized material, with lesser pumice lapilli or fiamme that become more abundant upward in each bed, indicating density grading. The monomict composition and the presence of abundant evolved glass shards, pumice, and broken crystals suggest that these were fed from pyroclastic eruptions. This lithofacies occurs in Unit V.

#### *Polymictic, evolved lapilli tuff and lapillistone*

This lithofacies occurs as very thick (multimeter) relatively well sorted intervals with no internal stratification, composed of volcanic clasts of a variety of evolved types. These characteristics suggest deposition from high-concentration density currents, probably by mass wasting or resedimentation from one or more silicic volcanoes; al-

ternatively, this facies could be products from pyroclastic eruptions that remobilized large volumes of lithic clasts. This lithofacies is most abundant in Units IV and VI.

#### *Black glassy lapillistone and lapilli tuff*

This lithofacies occurs as one massive ~184 mm thick deposit of nonvesiculated glass lapilli clasts, which together with the lack of bubble-wall shard or broken crystals, indicates fragmentation by autobrecciation and quenching of lava in a submarine environment (i.e., hyaloclastite). The few nonglassy clasts in the deposit suggest minor accidental incorporation of clasts during transport, but most of the unit is monomict and nonstratified, indicating minimal resedimentation. A lack of mudstone interbeds indicates rapid accumulation. This lithofacies forms the upper half of Unit VII.

#### *Coarse-grained massive lapilli tuff with in situ quench-fragmented blocks*

This lithofacies consists of extremely thick intervals of nonstratified, very poorly sorted monomict andesite lapilli tuff with blocks, with intercalated stratified lithic lapilli tuff and tuff. Clasts in the extremely thick nonstratified intervals are angular or have very irregular shapes, indicating very minimal transport. Many intervals contain blocks and coarse lapilli that are glassy and some have glassy rims and poorly inflated breadcrust textures/cauliflower texture, indicating that clasts came to rest at high temperatures. Other intervals have a small percentage of other clast types, suggesting at least some resedimentation. In some intervals, very angular, jigsaw-fit hyaloclasts (formed of quenched glass) indicate in situ mixing of hot clasts and/or intrusions with the host hyaloclastic tuff breccia, all of the same andesitic composition. The lack of clasts with broken glassy rims indicates minimal resedimentation. Like the black glassy lapilli tuff, a lack of mudstone interbeds indicates rapid accumulation, although these show more evidence of more episodic deposition because they are intercalated with stratified lithic lapilli tuff and tuff. This lithofacies forms the lower half of Unit VII.

### Interpretation of depositional environment at Site U1437: deepwater basinal succession

As noted above, the section drilled at Site U1437 accumulated in a deepwater volcano-bounded basin between the Manji and Enpo seamount chains. In this section we argue that the section is best described as a deepwater basinal succession and that the term “volcaniclastic apron” is inappropriate, expect perhaps for the basal 25% of the section.

Although some workers use the term volcaniclastic apron to loosely refer to any accumulation of sediment around a volcano or chain of volcanoes, the term has been used in a much more rigorous sense by sedimentologists over the past 40 y (Karig and Moore, 1975b; Sample and Karig, 1982; Carey and Sigurdsson, 1984; Farquharson et al., 1984; Fisher, 1984; Busby-Spera, 1985, 1988; Cas and Wright, 1987; Smith, 1987; White and Busby-Spera, 1987; Houghton and Landis, 1989; Palmer and Walton, 1990; Fisher and Smith, 1991; Fisher and Schmincke, 1994; Smith and Landis, 1995; Orton, 1996; Wright, 1996; Mitchell, 2000; Carey, 2000; Gamberi, 2001; Karátson and Németh, 2001; Allen et al., 2006; Casalbore et al., 2010; Carey and Schneider, 2011). In these papers, a volcaniclastic apron is defined as a thick accumulation of coarse volcanic debris that fringes a volcano or a chain of volcanoes and builds outward from them; volcaniclastic aprons are fan shaped or are composed of coalescing fans that form a wedge. They are steep in their proximal reaches, with abundant large lithic blocks and slumps, passing smoothly into medial to distal reaches that have gentler slopes, formed of debris flow and coarse-grained pyroclastic density current deposits. For example, the "volcanic apron" of Gran Canaria (Shipboard Scientific Party, 1995) is a volcaniclastic apron (Funck et al., 1996), consisting of volcano-flank seismically chaotic pillow breccia and hylaoclastite and poorly stratified debris flow deposits, which pass basinward into crudely stratified slump, debris flow, and turbidity current deposits. Volcaniclastic aprons form in both nonmarine and marine environments, and they commonly prograde into basins with time, producing an overall upward-coarsening sequence.

The section drilled at Site U1437 differs from volcaniclastic aprons in the following ways:

- It is mostly mudstone (~60% of the section as a whole) deposited from hemipelagic rain, dilute turbid flows, bottom currents, or some combination thereof; the section is not mainly composed of volcanic debris.
- The grain size of volcanic clasts in discrete tephra layers is much smaller than that reported from volcaniclastic aprons (20% ash and ~20% fine-grained lapilli, for the section as a whole).
- There is no geomorphic or seismic stratigraphic evidence for fan- or wedge-shaped sediment bodies or of chaotic facies; instead, the upper 75% of the section (above Units VI and VII) is extremely well stratified, consistent with its fine grained character.

- Little firm evidence for sediment gravity flow deposits exists in the upper 75% of the section, except for Unit II, which is thin; most of the tephra could represent suspension fallout.
- Volcanic blocks are very rare and sparsely scattered through the lowermost 25% of the section (Units VI and VII).

The submarine fans and aprons of siliciclastic deepwater systems are relatively coarse grained constructional features, whereas the basin plain beyond is flat and fine grained with laterally continuous deposits (Reading and Richards, 1994; Stow et al., 1996; Richards, 2009). The upper 75% of the section drilled at Site U1437 is more analogous to the basin plain; it is a fine-grained, well-stratified sequence that is best referred to as a deepwater basinal succession, not a volcaniclastic apron. The lower 25% of the section, in contrast, contains vent-proximal deposits with geochemistry that differs from the upper 75% of the section; therefore, the lower 25% of the section could represent the proximal part of a volcaniclastic apron, although it may instead represent a localized deposit within the deepwater basinal succession.

### Interpretation of event periodicity using tephra

Tephra beds within marine sediments have long attracted attention for their potential to provide a time-precise, high-resolution record of volcanic activity (e.g., Kennett and Thunell, 1975; Cambray and Cadet, 1994). In this section we present a preliminary assessment of volcanic event periodicity for the part of the section at Site U1436 that has good age control (Units I–III), which extends to 1097 mbsf and to 6.9 Ma (Fig. **F45**). This is possible because combined Holes U1437B and U1437D cored a 1097 m thick section of mudstone with abundant centimeter- to decimeter-thick tephra beds with high recovery (average = 80% ± 23%). The excellent biostratigraphic and magnetostratigraphic data in these holes demonstrate that the tephra represents a time series of instantaneous volcanic events that were preserved within rapidly accumulating tuffaceous mud that show no evidence for hiatuses (see Fig. **F24**).

Each tephra bed >1 cm thick entered in DESClogik was considered to be a single volcanic event, and for each bed the thickness and depositional age were obtained using sedimentation rates calculated in the age model. Tephra bed abundances were calculated in time slices of 100 ky, and a linear correction for core recovery was applied to the number of tephra beds per time interval; for example, if 3 tephra beds were recorded at 50% recovery, the corrected number of tephra beds would be 6.

The corrected curve (Fig. **F45**) shows a tephra maximum at 4.3–4.7 Ma (lithostratigraphic Unit II) and two additional maxima at ~2.0–2.2 Ma and ~3.1–3.2 Ma; a minor peak lies at ~0.35 Ma.

The 2.0–2.2 Ma tephra abundance maximum coincides with the maximum in sedimentation rate at ~1.9–2.5 Ma (230–360 mbsf), which is consistent with the interpretation that high sedimentation rates are linked to high influx of tephra. The age of the most pronounced tephra maximum (4.3–4.7 Ma) is permissive of a source in the ~16–3 Ma rear-arc seamount chain, which is consistent with the relatively coarse grain size of Unit II (lapilli tuff) relative to tephra in Units I and II (mainly ash/tuff). The abundance maximum at ~2.0–2.2 Ma is clearly too young to represent rear-arc seamount chain volcanism.

# Site summaries

## Site U1436

### Background and objectives

Site U1436 is located at 32°23.88′N, 140°21.93′E (1776 m water depth), in the western half of the Izu-Bonin fore-arc basin, ~60 km east of the arc-front volcano Aogashima and ~170 km west of the axis of the Izu-Bonin Trench.

The plan for Site U1436 was to carry out a 1 day operation to core 150 mbsf and collect geotechnical samples in preparation for potential future drilling at proposed Site IBM-4. Here, the *Chikyu* is proposed to drill 5.5 km below seafloor to reach arc middle crust, which is inferred to represent juvenile continental crust. The origin of continental crust remains one of the biggest unsolved problems in Earth science because continental crust, though volumetrically insignificant on a planetary scale, is an important reservoir for many trace and minor elements. The andesite model proposes that oceanic arcs produce the nuclei of new continental crust. However, the processes involved (e.g., partial melting of mantle sources, crystallization differentiation, or other processes) remain poorly understood. Ultra-deep drilling into arc crust is the best way to sample unprocessed juvenile continental-type crust as it is first generated at intraoceanic arcs, before its primary features are overprinted by accretion or incorporation into a larger or more mature continent. This geotechnical Site U1436 is important for assessing the suitability of near-surface conditions for this ambitious undertaking.

Although Site U1436 was scheduled as a geotechnical hole for proposed Site IBM-4, it yielded a rich, relatively complete record of Late Pleistocene fore-arc sedimentation, strongly influenced by frontal arc explosive volcanism. This is highly complementary to the main objective of Expedition 350, the rear-arc subduction factory (Site U1437), in terms of understanding the Izu arc system as a whole. In addition, Site U1436 gave scientists the opportunity to "test drive" a newly devised descriptive scheme for volcaniclastic rocks drafted at an IODP workshop in January and elaborated during the early part of Expedition 350. This scheme was devised to facilitate the understanding of volcano-sedimentary processes by making reproducible and quantifiable observations of volcanic input to the sedimentary record.

The Izu fore arc is a repository of ash/tuff intervals erupted in the Izu-Bonin frontal arc because the wind blows from west to east. Mafic effusive eruptive products are better preserved on the frontal arc islands, whereas more silicic materials from explosive volcanism are preserved in adjacent deep ocean basins. Rhyolites are also abundant in other oceanic arcs; thus, models for the crustal evolution of oceanic arcs must explain their bimodal volcanism. Basalts and rhyolites of the Izu arc front share radiogenic isotope characteristics that make them clearly distinguishable from active rift lava immediately behind the arc front, as well as from rear-arc lava behind (west of) the active rifts. However, a puzzling feature of the arc front is that basalt volcanoes lie on thick middle crust and rhyolite volcanoes lie on thin middle crust, in apparent contrast with continental margin arcs. A major objective of Site U1436, therefore, is to characterize the chemistry, age, provenance, and textural characteristics of mafic and silicic explosive volcanic products that are sampled in the fore arc to better understand outputs that are not preserved on land.

## Science results

### *Operational overview*

The transit from Keelung, Taiwan, started on 4 April 2014 and ended at 1142 h on 8 April, marking the beginning of operations at Site U1436. A seafloor survey was conducted first and verified that no subsea communications cables exist in the drilling area. Hole U1436A (9–10 April) cored from 0 to 150 mbsf using the advanced piston corer (APC), half-length APC (HLAPC), and extended core barrel (XCB), recovering 71.64 m (48% recovery) of tephra and mud.

After operations were prematurely terminated at Site U1437 on 25 May, the science party decided to use the remaining time to core two or three additional holes and at-

tempt to recover additional intervals of conspicuous black ash layers found 7 weeks earlier in Hole U1436A at ~50 mbsf that were severely disturbed by coring, in order to better constrain their thickness and thus the explosivity of the eruption that generated them. The short transit from Site U1437 to Site U1436 took from 0930 to 1700 h on 25 May, and contingency operations were conducted from 25 to 27 May.

Hole U1436B was positioned 20 m north of Hole U1436A and cored from 0 to 61.8 mbsf, obtaining 61.79 m (100% recovery). Hole U1436C is located 20 m south of Hole U1436A and was cored from 0 to 70.4 mbsf, obtaining 70.38 m (100% recovery). The final Hole U1436D was positioned 20 m east of Hole U1436A, and after washing down to 40 mbsf, coring from 40 to 62.0 mbsf obtained 22.07 m (100% recovery).

The ship remained on station at Site U1436 until 0900 h on 29 May before the short voyage to Yokohama, Japan, arriving on 30 May and ending Expedition 350.

### *Lithostratigraphy*

Coring at Site U1436 recovered 71.64, 61.79, 70.38, and 22.07 m of sediment from Holes U1436A, U1436B, U1436C, and, U1436D, respectively. These sediments are described as a single lithostratigraphic unit (Unit I) consisting of intercalated (1) tuffaceous mud, (2) mafic ash and scoria lapilli ash (~80 intervals in Hole U1436A), and (3) evolved ash and pumice lapilli ash (~70 intervals in Hole U1436A), culminating in a total of ~40 m of tuffaceous mud and ~26 m of volcaniclastic sediment. The mafic intervals in Hole U1436A are 50% thicker than the evolved intervals, giving a mafic to evolved thickness ratio of 1.5:1. Ash and lapilli ash layers make excellent stratigraphic markers for hole-to-hole correlations. Tuffaceous mud intervals are massive, average 0.25 m in thickness, and are up to 4.20 m thick. They comprise >25% of vitric and crystal particles; foraminifers and bioturbation are present. The tuffaceous mud is light gray to dark gray-brown, commonly with a greenish hue. Rare glauconite (0.01–0.02 m thick layers) occurs at the top contacts of evolved ash intervals with tuffaceous mud.

The mafic ash and scoria lapilli ash intervals average 0.14 m in thickness and are up to 2.30 m thick (Core 350-U1436A-8H). Mafic ash and scoria lapilli layers are commonly severely disturbed because of their granular fabric. The evolved ash and pumice lapilli ash intervals are 0.09 m thick on average and up to 0.60 m thick. Pumice and scoria lapilli are ~30 mm (commonly <10 mm), and small lapilli are angular, whereas coarser lapilli are subrounded. Most mafic and evolved intervals are normally

graded, with sharp bottom contacts and diffuse/gradational tops showing upcore increase in mud content. Most lapilli ash intervals are polymictic.

One very distinctive facies, the black glassy mafic ash, occurs in all holes between 49.1 and 53.6 mbsf (intervals 350-U1436A-8H-1, 0 cm, to 8H-2, 108 cm; 350-U1436B-10H-1, 0 cm, to 10H-2, 26 cm; 350-U1436C-11F-1, 106 cm, to 11F-2, 40 cm; and 350-U1436D-7F-2, 15–73 cm). It consists of massive, nongraded, nonstratified, very well sorted glass shards with minor feldspar and pyroxene crystals and foraminifers. Based on its undisturbed appearance in Holes U1436C and U1436D, the true thickness was determined to be 55 cm, with sharp upper and lower boundaries. The glass is brown to greenish brown with few microlites; glass particles are flat, blocky, curviplanar and/or plastically deformed, and contain vesicles. An apparent second black glassy mafic ash layer was observed at interval 350-U1436A-8H-3, 49–64 cm, but an equivalent was not found in the other three holes. Upon further examination of that interval, we concluded that it must have been formed by flow-in.

The tuffaceous mud is interpreted to record hemipelagic background sedimentation with substantial ash contribution from explosive eruptions or resedimentation from density currents, presumably predominantly from the Izu-Bonin arc front. Mafic and evolved ash and lapilli ash intervals may record distinct explosive events, also from the Izu-Bonin arc front, although evolved ash may include far-field volcanism. The mode of transport and deposition of the mafic and evolved volcaniclastic layers include both vertical settling through the water column and/or water-supported density currents. The distinctive 0.55 m thick black glassy mafic ash facies is unusually homogeneous in componentry, grain size, and texture, suggesting an eruption-fed origin, and the angular and fluidal shapes of the ash particles suggest they are products of a subaqueous explosive eruption.

### *Geochemistry*

Inorganic and organic geochemistry measurements at Site U1436 aimed to characterize the interstitial water chemistry and elemental composition of igneous rocks and sediment samples as well as to determine the hydrocarbon gas concentrations within the sediments. Headspace samples were analyzed routinely from every core in Hole U1436A as part of the shipboard hydrocarbon safety program. No hydrocarbon gases other than methane were detected in the cored sequences. Methane was either present in very low concentrations near or below the detection limit with an average concentration of 2.5 ppmv.

Downhole interstitial water compositions obtained from selected whole-round samples (~1 per core) from Hole U1436A are generally in good concordance with previous observations at nearby Site 792. Pore water Na/Cl scatters around an average of 0.86 throughout the sampled interval, equivalent to modern seawater. Variations in pore water compositions may be controlled by stronger seawater infiltration into porous ash-rich sections compared to muddy deposits. The most prominent deviations occur in pore waters from mud collected at ~13–27 mbsf, where sulfate concentrations subtly decrease (minimum = 25.8 mM) compared to seawater (28.9 mM), with concomitant subtle increases in pH and alkalinity and decreases in calcium. Magnesium concentrations are slightly elevated compared to Site 792 values at the same depths and show no evidence for magnesium sequestration caused by volcanic glass alteration and clay mineral precipitation observed in the deeper sections of Site 792.

Concentrations of major elements and several trace elements in solid samples from Hole U1436A were measured by ICP-AES and additional pXRF analysis. Reconnaissance pXRF and ICP-AES results show excellent agreement for $K_2O$ and CaO; ICP-AES data include light elements ($SiO_2$, $Al_2O_3$, and $Na_2O$) not reliably obtained by pXRF, and pXRF data appear more reliable for zirconium. Composite lapilli ($n$ = 11) and bulk ash samples ($n$ = 3) were analyzed for a complete set of major elements by ICP-AES. LOI values range between 0.54 and 3.8 wt% (9.8 wt% for impure mud with ash) and are generally higher in evolved ash and lapilli samples compared to mafic samples. These LOI values are elevated compared to those from regional fresh subaerial volcanic rocks and are indicative of secondary hydration of volcanic glass. All but one of the Hole U1436A tephra samples define broadly linear trends in Harker diagrams ($SiO_2$ = 54.4–70.1 wt%). They are low-K rocks and indistinguishable from intermediate to acidic rocks from basalt-dominant island volcanoes of the arc front (e.g., Aogashima Volcano ~56 km to the west), although basalt (having <53 wt% $SiO_2$; present in arc-front volcanoes) has not been found in the tephra at Site U1436. The most mafic samples are from the black glassy ash lithofacies, but these are basaltic andesite. One interval of evolved lapilli ash (at ~45 mbsf) has elevated $K_2O$, indicating that it did not come from Aogashima or the East Aogashima Caldera ~45 km to the west, which have lower $K_2O$. However, rhyolite-dominant submarine volcanoes with elevated $K_2O$ are common in the arc front, including three within 65 km of the drill site (Myojin Knoll, South Hachijo, and Myojinsho).

### *Physical properties*

A significant shift in all physical properties is observed at ~50 mbsf: shear strength, NGR, and color reflectance L* parameter all decrease in the interval deeper than 50 mbsf, likely related to an increase in relative abundance of mafic ash layers in that interval. Physical properties data were examined for the specific intervals identified as mafic and evolved ash layers. Mafic ash layers have an average magnetic susceptibility value that is more than twice as high as the average value for evolved layers. The average NGR value for mafic layers is approximately half that for evolved layers. Reflectance L* values for mafic and evolved ash layers can be grouped into three luminance (lightness) ranges: 17–35 includes only mafic layers, 35–50 includes a mixture of mafic and evolved layers, and 50–78 includes only evolved layers. The 2.2 m thick mafic ash layer at ~50 mbsf yields a wide range of *P*-wave values, supporting the suspicion that the layer is affected by core disturbance (stretching). The general downhole shift in physical properties and ash types at ~50 mbsf also coincides with an inferred hiatus and significant decrease in recovery rate (see below).

### *Paleomagnetism*

Paleomagnetic analysis in Hole U1436A comprised archive-half demagnetization and remanence measurement at 10 mT steps up to 40 mT. Severe core disturbance resulted in complete destruction of the depositional remanence in many intervals, and discontinuous recovery compromised the recognition of magnetostratigraphy in the lower half of the hole. Nevertheless, intervals of continuous mud recovery yielded a good paleomagnetic record, with the drill string overprint largely removed. The base of normal Chron C1n (the Brunhes/Matuyama boundary; 0.781 Ma) was recorded in one of the last continuous mud intervals (350-U1436A-9H-3, 25 cm; 56.8 mbsf). The reversal appears sharp because it occurred in the time interval between two successive depositional events.

One discrete paleomagnetic cube was sampled per section in undisturbed mud and silt. We demagnetized these at 5 mT steps up to 20 mT. Less intense and magnetically softer overprinting of these discrete samples meant that the demagnetized inclination at 20 mT tightly clustered around the expected geocentric axial dipole (GAD) inclination of ±51°. For this reason, we halted demagnetization and measurement of most discrete samples at this level, continuing to 25 mT only in samples near and below the base of Chron C1n to improve the isolation of the reversed polarity remanence. Discrete samples in the discontinuous record below the hiatus allowed us to recognize two additional datums: the top of normal Chron C1r.1n (0.988 Ma) between Samples

350-U1436A-9H-4, 66–68 cm (reversed), and 10F-2, 64–66 cm (normal), and the base of normal Chron C1r.1n (1.072 Ma) between Samples 10F-2, 64–66 cm, and 16X-2, 53–55 cm (reversed). Discrete samples and a patchy record in the archive-half SRM measurements indicate that Core 17X is all reversed polarity and probably still lies in the Matuyama interval (<1.778 Ma).

### *Biostratigraphy*

The biochronology at Site U1436 was primarily based on planktonic foraminifers and calcareous nannofossils. All the core catcher samples from Holes U1436A–U1436C were examined, and studies of both fossil groups showed that the upper 132 m of the cored interval in Hole U1436A (the deepest hole) spans the last 2.7 My (late Pliocene–Holocene). The timing of bioevents in the undisturbed part of the succession agrees with paleomagnetic data down to the Brunhes/Matuyama reversal (0.781 Ma) in Section 9H-3. Deeper than 66 mbsf, several nannofossil and foraminifer bioevents were missing, indicating the presence of a hiatus. Below this potential hiatus, the rarity of markers and the occurrence of reworked specimens made identifying bioevents difficult.

Planktonic foraminifers are generally well preserved and abundant, except in some layers where the concentration of biogenic constituents was reduced via dilution by volcaniclastics. The Pleistocene/Pliocene boundary (2.588 Ma) was placed within Cores 350-U1436A-18X and 20X based on the presence of the top of *G. pseudomiocenica* (2.39 Ma) in Sample 18X-CC and the top of *G. decoraperta* (2.75 Ma) in Sample 20X-CC. Benthic foraminifer assemblages (i.e., extinction of Stilostomelidae) corroborate this biochronology.

Calcareous nannofossils were also generally abundant and well preserved. The Late–Middle Pleistocene sequence is defined by the presence of *Emiliania huxleyi* in Sample 350-U1436A-3H-CC (16.9 mbsf) and *Pseudoemiliania lacunosa* in Sample 5H-6, 134–139 cm (34.6 mbsf). Between Samples 10F-CC (62.1 mbsf) and 13X-CC (65.05 mbsf), no additional Pleistocene bioevents were recorded. Sample 15X-CC (83.29 mbsf) contained *Calcidiscus macintyrei*, a marker for the early Pleistocene. The sequence below Sample 17X-CC (104.3 mbsf) contained few markers that characterize the Pleistocene/Pliocene boundary. Only rare specimens of diagnostic discoasterids were present, and some could be reworked. In this interval, Biozones CN12d, CN12c, and CN12b were tentatively identified on the basis of the top of *Discoaster brouweri*, top of *Discoaster pentaradiatus*, and top of *Discoaster surculus*, respectively.

#### *Age model*

Thirteen out of 16 biostratigraphic datums and one magnetostratigraphic datum were selected to construct an age-depth relationship for Site U1436. The model consists of two linear segments above (0–66 mbsf) and below (74–127 mbsf) the inferred hiatus, with LSRs of 71 and 45 m/My and MARs of 8.0 and 5.3 g/cm$^2$/ky, respectively.

## Site U1437

### Background and objectives

Site U1437 is located in the Izu rear arc, ~330 km west of the axis of the Izu-Bonin Trench and ~90 km west of the arc-front volcanoes Myojinsho and Myojin Knoll at 2117 mbsl. Expedition 350 was the first expedition to be drilled in the Izu rear arc; all other ODP/Integrated Ocean Drilling Program sites have been in or near the Izu-Bonin arc front or fore arc, leading to an incomplete view of Izu arc magmatism as a whole. The main objective of Expedition 350 was to reveal the history of this "missing half" of the subduction factory.

Site U1437 (proposed Site IBM-3C) was chosen to provide a temporal record of rear-arc magma compositions, ideally from Eocene to Neogene time, allowing comparison with the previously drilled fore-arc magmatic record and determination of across-arc geochemical variation throughout the history of the arc system. A striking characteristic of volcanic arcs is the asymmetry in geochemical characteristics with distance from the trench, which was known prior to the advent of plate tectonics. The Izu arc shows this asymmetry, and its rear-arc magmas are much more similar to continental crust than the Izu arc-front magmas. The Izu rear arc is therefore important for understanding how intracrustal differentiation produces crust that is similar to the "average continent."

The Izu arc front is a ~900 km long volcanic chain whose Quaternary geology can be characterized by (1) basalt-dominated volcanoes spaced at ~100 km intervals, some of which form islands, and (2) submarine rhyolite-dominated calderas. All Neogene volcanic rocks behind the Izu arc front are referred to as rear-arc volcanic rocks and include three types: (1) the east northeast–trending basaltic to dacitic rear-arc seamount chains (~17–3 Ma); (2) a broad extensional zone with small bimodal volcanoes referred to the back-arc knolls, which overlaps with the eastern part of the rear-arc seamount chains (<3 Ma); and (3) a narrow active rift with bimodal volcanic rocks that lies immediately behind the arc front (<1.5 Ma). The chemistry of the arc-front mag-

mas should be distinguishable from that of the rear-arc seamount chains because the rear-arc seamount chains are enriched in alkalis and high–field strength elements and other incompatible elements and have less enriched Sr, Nd, Hf, and Pb isotopes, compared to the volcanic front. However, the <3 Ma bimodal volcanism is transitional between the two in chemistry as well as space; therefore, we can distinguish rear-arc and arc-front magmas for all rocks older than 3 Ma but not for rocks younger than 3 Ma. Because the objective was to study the temporal evolution of rear-arc magmatism, Site U1437 was chosen in a location that should be topographically shielded from arc front–derived sediment gravity flows (although arc front–derived ash fall may be present). Another objective at Site U1437 was to determine if arc geochemical asymmetry was present early in the history of the arc (in the Paleogene) or if it is strictly a Neogene feature.

Site U1437 lies in a volcano-bounded basin that formed between the Manji and Enpo rear-arc seamount chains, which are two of several Izu rear-arc seamount chains that are up to ~50 km long and strike N60°E. Three main hypotheses have been proposed for the origin of the seamount chains:

1. They are related to compression caused by collision between the southwest Japan and Izu arcs, associated with opening of the Japan Sea.
2. They formed along Shikoku Basin transform faults.
3. They overlie diapirs in the mantle wedge, such as the hot fingers proposed for northeast Japan, which predicts that the rear-arc seamount chains young from west to east.

Site U1437 was chosen to learn about the temporal evolution of the Manji and Enpo seamount chains.

## Science results

### *Operational overview*

After the 7.5 h, 77 nmi transit from Site U1436 to U1437, operations at this site were conducted from 10 April 2014 to 24 May (44 days).

Five holes were completed at Site U1437. Hole U1437A (10 April) was a jet-in test with an APC/XCB bottom-hole assembly (BHA). A seafloor camera survey was first conducted to confirm that no subsea cables were present at the site.

Hole U1437B (11–14 April), located 10 m north of Hole U1437A, was cored with the APC (0–89.2 mbsf), the HLAPC (89.2–145.7 mbsf), and the XCB (145.7–439.1 mbsf), with a total recovery of 243 m (55%).

The plan for Hole U1437C (14–15 April), located 20 m south of Hole U1437B, was to drill without coring to 425 mbsf, which is several meters above the total depth cored in Hole U1437B, and then start RCB coring. At 309.7 mbsf, the bit got stuck and had to be dropped at the bottom of the hole to free the pipe, ending operations in this hole.

Hole U1437D (15–26 April) was positioned 10 m west of Hole U1437A in a second attempt to drill and core a deep RCB hole. Drilling without coring extended from the seafloor to 427.2 mbsf. RCB coring from 427.2 to 980.4 m recovered 434.56 m (79% recovery). At this time, the bit had been rotating for 51.5 h and required changing, so we decided to stop coring, deploy a free-fall funnel, and collect wireline log data.

Three logging strings were successfully deployed in Hole U1437D: the triple combo with the magnetic susceptibility sonde (MSS) (92 to ~960 mbsf), the Formation MicroScanner (FMS)-sonic (92–950 mbsf), and the Vertical Seismic Imager to acquire a vertical seismic profile (VSP) (14 stations; 175–875 mbsf). The hole was in excellent condition, with a diameter barely exceeding the bit size for most of the hole. The data recorded were therefore of high quality.

RCB coring in Hole U1437D resumed with a new bit, and the hole was deepened from 980.4 to 1104.6 mbsf, recovering 69.29 m (56%). Drilling problems forced us to pull out of the hole at this point. The total cored interval in Hole U1437D was 677.4 m, with 503.8 m recovered (74%).

We decided to drill and case a new hole to the total depth of Hole U1437D and then core and log it as deep as time permitted. This decision was prompted by (1) the increasing risk with penetration depth of not being able to clean the hole and (2) the fact that the ship was carrying ~1100 m of 11¾ inch casing, just enough to cover the interval cored to date, which made this the optimal time to install the casing.

The ship moved ~20 m northeast to begin operations in Hole U1437E (26 April–24 May). The casing deployed in this hole consists of a 20.7 m long 20 inch casing connected to the reentry cone, a 264 m long 16 inch casing string hung from the casing hanger in the reentry cone, and a R/V *JOIDES Resolution* record-breaking 1085.6 m

long 10¾ inch casing string, also hung from the reentry cone. It took ~12 days to complete the total casing installation.

RCB coring for the duration of three 50 h bit life cycles extended Hole U1437E from 1104.0 to 1806.5 mbsf and recovered 387.45 m of core (55% recovery). When preparing for the fourth bit deployment, the fiber-optic cable for the camera needed to reenter Hole U1437E had broken. This prematurely ended the expedition's operations in Hole U1437E. Hole U1437E is currently in excellent condition for logging and/or further coring operations, preferably attempted soon, before the hole deteriorates.

At 0930 h on 24 May, the ship was under way for contingency operations at Site U1436.

### *Lithostratigraphy*

Cores from three consecutively cored holes at Site U1437 recovered a coherent stratigraphy from 0 to 1806.50 mbsf: Cores 350-U1437B-1H through 55X (0–439.10 mbsf), 350-U1437D-2R through 73R (427.20–1104.60 mbsf), and 350-U1437E-4R through 79R (1104.00–1806.5 mbsf). Overlap between the bottom of one hole and the top of the next is minimal. The majority of the recovered core is sedimentary, dominated by tuffaceous mud and mudstone with intercalated volcaniclastic layers in the uppermost 1300 m (Units I–V), with a gradual change to dominantly volcaniclastic layers in the lowermost 500 m (Units VI and VII). Overall, 62% of the cored depth interval was recovered and described. Tuffaceous mud and mudstone comprise 58.5% of the described rocks, ash and tuff comprise 21.0%, and lapilli-sized volcaniclastics comprise 20.3% (with <0.5% volcaniclastics coarser than lapilli).

The seven lithostratigraphic units (I–VII) are distinguished from each other based on the proportion and characteristics of volcaniclastic intervals relative to tuffaceous mud and mudstone. Their upper and lower boundaries are defined by the appearance or reappearance of distinct marker layers as described in the following paragraphs.

The tuffaceous mud and mudstone in all units contain clay minerals, foraminifers, igneous crystals, and glass shards in varying proportions. Bioturbation is intense. Ash and tuff intervals often are normally graded, consist of glass shards and crystals, and commonly have a crystal-rich layer at the base of the interval. Layer bases usually are sharp, whereas upper contacts often grade into increasingly bioturbated tuffaceous mud and mudstone such that there is a continuum between the lithofacies. Matrix- and clast-supported polymictic lapilli tuff intervals become very thick and highly

abundant at certain depths and are typically the basis of unit boundaries. The clasts in these coarse-grained intervals become more lithic rich toward the base of the recovered sequence. Only one igneous unit was defined (igneous Unit 1) based on the presence of a 1.2 m thick rhyolite with chilled margins and peperitic contacts with surrounding volcaniclastic material.

Compaction of sediment at Site U1437 increases linearly from ~0% shallower than ~410 mbsf to ~36% at the base of Hole U1437D. Although the transition from unconsolidated to lithified rocks occurred progressively, sediments were considered lithified from 427 mbsf (top of Hole U1437D) downhole. Alteration becomes more pervasive downhole in Holes U1437B and U1437D; initially it is predominantly glauconitic-smectitic and eventually becomes more chloritic. Fresh glass is observed from Unit I to the top of Unit III. Within Unit III, glass is progressively altered to cryptocrystalline aggregates of clay minerals, probably dominated by smectite. From Units IV to VII, glass is totally altered with the exception of the uppermost vitric-rich part of Unit VII, where colorless glass is preserved. Crystals are not affected by alteration until Unit VII, where orthopyroxene is replaced by cryptocrystalline brown aggregates of clay minerals and plagioclase is partly altered to clay minerals and epidote. The downhole increase in alteration intensity and the transition from smectite to chlorite and prehnite indicates alteration is partly related to burial. Iron sulfides occur as aggregates throughout all holes, especially as replacements of worm burrows, and according to rock magnetic properties, greigite is progressively replaced by pyrite downhole in Hole U1437D. Glauconite layers and reduced iron sulfides associated with burrows are a result of biogenic alteration under reducing conditions. Some volcanic clasts in Units IV–VII display higher temperature alteration assemblages comprising prehnite, biotite, and epidote, related to high-temperature (>300°C) alteration before final deposition.

Unit I extends from 0 to 682.12 mbsf and encompasses all of Hole U1437B to interval 350-U1437D-28R-2, 112 cm, in Hole U1437D. Unit I is dominated by tuffaceous mud and mudstone (88% of total described material) alternating with thin evolved, mafic, or bimodal ash/tuff intervals and minor lapilli ash/lapilli tuff intervals. Average bed thicknesses are 0.36 m for mud and mudstone, 0.08 m for ash and tuff, and 0.06 m for lapilli ash and lapilli tuff. The tuffaceous mud and mudstone from this unit are interpreted to result from background sedimentation of hemipelagic clay and carbonate mixed with substantial volumes (>25%) of dispersed volcanic material. This background sedimentation is punctuated by episodic deposition of ash layers, derived by eruption-fed or resedimented seafloor-hugging density currents, or suspension set-

tling of subaerially distributed ash through the water column. The Unit I/II boundary is marked by the first appearance of monomictic lapilli tuff, which is the characteristic lithofacies within Unit II; this change is reflected in the physical properties (e.g., increase in magnetic susceptibility, see below).

Unit II extends from 682.12 to 726.50 mbsf in Hole U1437D (interval 350-U1437D-28R-3, 0 cm, to 32R-CC, 7 cm). It is characterized by abundant intervals of evolved thick- to very thick-bedded evolved tuff (40% of total described rocks) and monomictic pumice lapilli tuff and lapillistone (37%) intercalated with lesser tuffaceous mudstone (23%). The top of Unit II is defined by the first lapilli tuff in a 44.38 m thick sequence dominated by intervals of lapilli-sized tephra. Average bed thicknesses are 0.16 m for evolved tuff, 0.20 m for lapilli tuff and lapillistone, and 0.19 m for tuffaceous mudstone. Unit II volcaniclastics are interpreted to have been deposited by seafloor-hugging density currents that transported lapilli, pumice grains, and crystal fragments. The thickest and graded intervals are inferred to be eruption fed. Minor (22%) intercalated tuffaceous mudstone indicates periods of volcanic quiescence during deposition of Unit II. The Unit II/III boundary is marked by the first interval of tuffaceous mudstone below the last occurrence of intercalated lapilli tuff and lapillistone.

Unit III extends from 726.50 to 1017.88 mbsf in Hole U1437D (interval 350-U1437D-32R-CC, 7 cm, to 64R-1A, 8 cm). It is dominated by tuffaceous mudstone (63% of the described rocks) with intercalated intervals of evolved tuff and minor evolved lapilli tuff and lapillistone. Average bed thicknesses are 0.23 m for the tuffaceous mudstone, 0.11 m for the tuff, and 0.15 m for the lapilli tuff. Near the top of Unit III (interval 34R-3, 78 cm, to 34R-4, 118 cm) lies a single distinctive 1.91 m thick tuffaceous breccia with mudstone intraclasts (up to ~20 cm in size) interpreted as a submarine debris flow deposit. The overall abundance of mudstone and lack of coarse-grained volcaniclastic material in Unit III suggests an origin similar to that described for Unit I. Unit III shows an increase in fine-grained tuff (relative to tuffaceous mudstone) in its basal ~80 m, possibly produced by phreatomagmatism. The Unit III/IV boundary is defined by an increase in grain size and abundance of pumiceous lapilli tuff; tuffaceous mudstone decreases below this boundary.

Unit IV extends from 1017.88 to 1120.11 mbsf, from the bottom of Hole U1437D and into Hole U1437E (interval 350-U1437D-64R-1A, 8 cm, to 350-U1437E-6R-3, 122 cm). The unit is characterized by coarse sand-sized tuff (53% of described rocks), polymictic lapilli tuff, and minor polymictic lapillistone (25%). Tuffaceous mudstone is only

a minor part of the unit (22% of the described rocks), becoming more frequent toward the base. The top of Unit IV is defined by the uppermost interval of a succession of massive intervals of clast-supported polymictic lapilli tuff intervals. Two tuff lithofacies are found in Unit IV: a light green tuff showing planar and convolute stratifications and a massive and coarser dark gray to black tuff. Average bed thicknesses are 0.24 m for tuff, 0.43 m for lapilli tuff, and 0.16 m for tuffaceous mudstone. Volcaniclastic intervals in Unit IV are interpreted to have been deposited by voluminous high-concentration density currents derived from mass wasting of islands or seamounts or by pyroclastic eruptions that remobilized large volumes of lithic clasts. The base of Unit IV is defined by the last interval of polymictic lapilli tuff >0.50 m thick for the next 146.66 m (well into Unit V).

Unit V (1120.11–1320.00 mbsf; interval 350-U1437E-6R-3, 122 cm, to 27R-CC, 15 cm) is similar to Units I and III in that it is dominated by tuffaceous mudstone intercalated with tuff. However, a distinctive characteristic of Unit V is the presence of multiple intervals of monomictic, reversely graded fiamme-rich lapilli tuff with mudstone. The top of Unit V is defined by the interval immediately beneath the final >70 cm thick polymictic lapilli tuff of Unit IV. Heavily bioturbated silt-sized tuffaceous mudstone comprises 69% of the described rocks in the unit, evolved tuff comprises 15%, and lapilli tuff and lapillistone constitute 16%. Average bed thicknesses are 0.27 m for tuffaceous mudstone, 0.06 m for evolved tuff, and 0.18 m for lapilli tuff. The distinctive monomictic, reversely graded lapilli tuff lithofacies is thin to medium bedded and consists of a sharp basal contact filled with tuff that grades upward into a matrix-supported, reversely coarse-tail graded, fiamme-rich lapilli tuff with tuffaceous mudstone. Pumice lapilli tuff and lapillistone occur as ~5–10 cm thick intervals in the middle of the unit; they are similar to the dominant lithofacies in Unit IV. Unit V is interpreted to have an origin similar to Units I and III, with the addition of monomictic lapilli tuff with a likely origin as eruption fed seafloor-hugging density currents described for Unit II. The base of Unit V is defined as the last interval above the first thick interval of polymictic lapilli tuff of Unit VI.

Unit VI extends from 1320.00 to 1459.80 mbsf (interval 350-U1437E-28R-1, 0 cm, to 42R-3, 60 cm). As with Units II and IV, this unit is characterized by a higher abundance of tuff (32% of described rocks) and lapilli tuff (57%) and lesser tuffaceous mudstone (11%) than in the unit above. The top of Unit VI is marked by the first appearance of multiple intervals of thickly to very thickly bedded (up to 2.8 m) matrix-supported polymictic lapilli tuff and continues downward through intervals that are dominated by tuff and lapilli tuff rather than tuffaceous mudstone. Unit VI is in-

truded by the 1.2 m thick rhyolite-dacite sheet of igneous Unit 1 (see below). Lapilli tuff intervals include monomictic and polymictic varieties and matrix- and clast-supported varieties. Average bed thicknesses are 0.25 m for tuffaceous mudstone, 0.24 m for tuff, and 0.41 m for lapilli tuff and lapillistone. Igneous vitric and lithic clasts >2 cm become more common toward the base of the unit. Unit VI is interpreted similarly to Unit IV. The base of Unit VI is marked by the lapilli tuff above the first normally graded dense glass–rich interval of Unit VII.

Unit VII begins at 1459.80 mbsf and extends to the bottom of Hole U1437E at 1806.50 mbsf (interval 350-U1437E-42R-3, 60 cm, to 79R-03, 83 cm). The bulk (89%) of Unit VII consists of thin to extremely thick intervals of graded or nongraded lapilli tuff, lapillistone, tuff breccia, and breccia (0.63 m average bed thickness) and contains angular lithic andesite clasts ranging from pebble to cobble in size. The remaining 11% is tuff (0.21 m average bed thickness). There is only one thin-bedded (0.11 m) tuffaceous mudstone in the entire 340 m thick unit. Unit VII comprises two main lithofacies. A distinctive black evolved lapilli tuff and lapillistone occurs mostly in the upper part of the unit and has a matrix of slightly to moderately altered glass plus isolated plagioclase and pyroxene crystals. Polymictic evolved lapilli tuff, lapillistone, tuff-breccia, and volcanic consolidated breccia exclusively occur in the lower part of the unit. It is more altered (green-colored, altered glass) and coarser than the upper lithofacies. Clasts with unbroken quench margins suggest proximity to the source. Evidence of in situ emplacement is restricted to a few levels, where jigsaw-fit textures (hyaloclastite) and/or baked and peperitic margins are observed.

Igneous Unit 1 occurs at 1388.86 to 1390.07 mbsf (interval 350-U1437E-35R-1, 76 cm, to 35R-2, 55 cm). It is a 1.21 m thick moderately phyric quartz-hornblende-feldspar rhyolite-dacite interpreted as an intrusive sheet with chilled margins and basal peperite. It occurs within a continuous interval of clast-supported polymictic pumice lapilli tuff that is baked at both contacts with igneous Unit 1. The unit has a porphyritic texture with sieve-textured subhedral plagioclase (up to 4 mm, ~7%), euhedral hornblende (up to 0.5 mm, ~3%), anhedral to subhedral quartz (up to 8 mm, ~1%) with fresh glassy melt inclusions, minor opaque minerals, and rare zircon (20 µm in size). The groundmass varies from cryptocrystalline near the upper and lower contacts to fine-grained in the center of the unit. Flow banding is observed across the entire unit in various orientations.

### *Geochemistry*

**Headspace.** Samples for hydrocarbon gas analysis from headspace ($n$ = 184) were collected and analyzed for every core at Site U1437 in compliance with the shipboard hydrocarbon safety program. At shallow depths, methane abundances gradually increase with depth with the highest abundances at ~750–1459 mbsf. The zone of methanogenesis is unusually deep because of a release of sulfate below the sulfate reduction zone that may be buffering the methanogenesis by anaerobic methanogens. Deeper than ~1459 mbsf, methane concentrations decrease again. Minor amounts of ethane occur at 1105 mbsf. In samples with detectable methane ($C_1$) and ethane ($C_2$), $C_1/C_2$ values are <100, which is consistent with mature organic matter producing thermogenic aliphatic hydrocarbons. $C_1/C_2$ never reached critical thresholds to halt drilling operations according to the shipboard safety program.

**Pore water.** Chemical analyses for interstitial water samples from Site U1437 (0–684 mbsf; $n$ = 67) display systematic downhole trends. Depth variations in pore fluid chemistry suggest at least three major processes controlling the changes in major and trace element distribution in a fluid that started out as sediment-trapped seawater. These processes may be interdependent and operate simultaneously but can be ranked according to increasing impact with depth: (1) biologic activity (0–100 mbsf), which is primarily controlled by sulfate reduction of organic material; (2) lateral fluid transport (deeper than 100 mbsf) interpreted from increasing alkalinity and sulfate back toward near-seawater values away from the zone of microbial sulfate reduction, with spikes in Li indicating that this process is likely fracture or formation controlled; and (3) diagenesis (0–684 mbsf) evident through progressive downhole alteration of volcanic glass and dissolution of siliceous diatoms producing gradual decreases in Mg and increases in Si, respectively. Deeper than ~450–500 mbsf, increases in Ca and Na coupled with a sharp decrease in Mg may indicate progressive clay formation by alteration of volcanic ash.

**Mud and mudstone bulk geochemistry.** A total of 218 sediment samples were collected at Site U1437 and analyzed for concentrations of $CaCO_3$, TC, TOC, and TN. $TOC/TN_{at}$ ratios were calculated to determine the source of the sedimentary organic matter. TC and $CaCO_3$ contents are highly variable and show generally the same trend over the cored sequence, suggesting that most of the TC consists of inorganic carbon. Highly variable sedimentary $CaCO_3$ abundances over short vertical distances likely result from varying inputs of volcanic ash or terrigenous clay, which dilute biogenic carbonate. TOC and TN contents are generally low, but TOC and TN are com-

paratively elevated in the uppermost ~230 m of the cored sequence. Deeper, TN contents decrease continuously, probably as a result of nitrogen loss during diagenesis. $TOC/TN_{at}$ ratios vary from 2.33 to 213 with an average of 18.6, suggesting a mixed input of both marine-derived and terrestrial-derived organic matter.

Bulk mud compositions by ICP-AES ($n$ = 11) and pXRF ($n$ = 38) indicate downhole increases in clay and ash content (represented by $TiO_2$) relative to $CaCO_3$. The increasing prevalence of clay and ash correlates approximately with the transition from lithostratigraphic Units III to IV (~1019 mbsf) and continues to the bottom of Hole U1437E, where mud intervals become rare. Zr/Y in mud decreases with depth from ~4 (6 mbsf) to ~2 (1424 mbsf), paralleling a decrease in Rb from 103 to 11 ppm. These depth trends suggest that shallow mud intervals are more strongly influenced by terrigenous clay or distal ash (e.g., from the Ryukyu arc where Zr/Y and Rb are high relative to the proximal Izu arc-front and rear-arc volcanoes) than deeper intervals.

**Volcanic geochemistry.** In an effort to constrain the geochemistry of various volcanic deposits observed at Site U1437 (tuff, lapilli, and lava), both a pXRF ($n$ = 227) and ICP-AES ($n$ = 50) were utilized. ICP-AES analyses were completed for samples of ash and tuff ($n$ = 26), lapilli tuff and lapillistone ($n$ = 14), igneous clasts ($n$ = 10), and a rhyolite intrusion ($n$ = 1). The discrete ash layers in lithostratigraphic Unit I (0–682 mbsf) plot within the low-K field relative to $SiO_2$ and have low Zr/Y. Their low $K_2O$ and Zr/Y values indicate that the ash is likely derived from the Izu volcanic front. A few deposits, commonly coarser grained with cross bedding and hornblende, have elevated $K_2O$ and Zr/Y. The samples younger than 3 Ma (0–440 mbsf) that contain elevated $K_2O$ and Zr/Y relative to $SiO_2$ are more ambiguous in origin. Pervasive alteration at depths >720 mbsf compromises most major and trace elements. Major element compositions of samples >720 mbsf trend toward compositions equivalent to hydrothermally altered Manji Seamount rocks. Fluid-immobile Zr and Zr/Y are elevated for coarse-grained volcaniclastic rocks between ~684 and 1120 mbsf (top of Unit II to Unit IV), indicating the effects of higher degrees of differentiation, higher abundances of incompatible trace elements in the source, and possibly hornblende fractionation. All three characteristics are consistent with a proximal rear-arc origin. The presence of low Zr/Y samples within the same depth interval, however, indicates continued deposition of tephra and volcaniclastic sediment from sources similar to modern Izu arc-front volcanoes. Variability in Zr/Y and $K_2O$ values in Unit V (1120–1312 mbsf) indicates a mixture of lithologies similar to dredged rear-arc and Quaternary volcanic front lava from a comparable stratigraphic interval. Deeper than 1320 mbsf to the total depth of 1807 mbsf (comprising Units VI and VII), most ICP-AES samples

(typically representing large single clasts) are dominantly intermediate in composition. The samples have Zr abundances as low as 34 ppm and Zr/Y < 3, which are characteristic for modern basalt-dominant island arc volcanoes of the Izu arc front. One exception is a conspicuous quartz-, hornblende-, and zircon-bearing rhyolite (igneous Unit 1) in Sections 350-U1437E-35R-1 and 35R-2 (1388.9–1391.1 mbsf), which has the lowest CaO analyzed for any rock collected at Site U1437 but comparatively high Zr/Y (5.9). Overall, the presence of Manji seamount chain-like rocks identified by high Zr/Y is well established for Units II–IV, whereas such rocks are more infrequently encountered in Units I, V, VI, and VII. Preliminary geochemical modeling using major and trace element compositions for mud and volcaniclastic sediment or rock, weighed by their abundance throughout the section drilled at Site U1437, indicates that the Izu rear arc is significantly depleted in incompatible trace elements (e.g., $K_2O$ and Rb) relative to upper continental crust but less so than the arc-front magmas.

### *Physical properties*

Physical properties measurements were performed to obtain information on the density, porosity, NGR, shear strength, thermal conductivity, MS, *P*-wave velocity, and reflectance of the recovered sequence. After letting the core reach thermal equilibrium with the ambient temperature at ~20°C, gamma ray attenuation density, MS, and *P*-wave velocity were measured using a Whole-Round Multisensor Logger and NGR was measured on the whole-round Natural Gamma Radiation Logger. Thermal conductivity was measured in soft sediments and rocks with the needle and puck probes, respectively. Discrete measurements of *P*-wave velocity, moisture and density, and shear strength were performed on working section halves. Finally, color reflectance and MS were measured on the archive section halves using a spectrophotometer and the point magnetic susceptibility sensor on the Section Half Multisensor Logger.

Thirteen physical properties (PP) units were differentiated based on distinct offsets in otherwise continuous profiles that define boundaries between intervals and interval characteristics such as magnitude, rate of change, and relative scatter of measurements.

PP Unit 1 (0–430 mbsf) is characterized by a downhole increase in bulk density and *P*-wave velocity and a corresponding downhole decrease in porosity.

The top of PP Unit 2 (430–550 mbsf) is marked by an initial increase in porosity followed by a downhole continuation of the decrease observed through PP Unit 1, as well as a decrease in the reflectance L* and a* values.

The upper part of PP Unit 3 (550–682 mbsf) is characterized by a sharp increase in porosity and corresponding decrease in bulk density. This initial offset is followed by more gradual downhole trends, similar to those seen in PP Unit 2. The reflectance ratios of a*/b* data show a decrease in the scatter, indicating that color is less variable through PP Unit 3 than in PP Units 1 and 2.

The upper boundary of PP Unit 4 (682–728 mbsf) corresponds to the lithostratigraphic Unit I/II boundary and is marked by an increase in the scatter of density and porosity, an increase in *P*-wave velocity and MS values, and a decrease in the NGR and reflectance b* values.

The top of PP Unit 5 (728–794 mbsf) corresponds to the upper boundary of lithostratigraphic Unit III and is defined by an increase in NGR values and a decrease in the scatter of *P*-wave velocity. This is followed downhole by the continuation of the increasing *P*-wave trend observed in PP Unit 3.

PP Unit 6 (794–846 mbsf) is defined by an increased scatter in *P*-wave velocity and reflectance a*/b* values.

The upper boundary of PP Unit 7 (846–1018 mbsf) is marked by an initial decrease in bulk density and a corresponding increase in porosity, followed downhole by trends similar to those in PP Unit 6. The top of this unit is also characterized by an abrupt decrease in MS values.

The top of PP Unit 8 (1018–1140 mbsf) corresponds to the top of lithostratigraphic Unit IV and is defined by an increase in the MS values and abrupt decreases in *P*-wave velocity and thermal conductivity.

The upper boundary of PP Unit 9 (1140–1315 mbsf) is 20 m below the upper boundary of lithostratigraphic Unit V and is defined by decreased scatter in density, porosity, *P*-wave velocity, and NGR measurements, as well as a downhole decrease in thermal conductivity.

The upper boundary of PP Unit 10 (1315–1460 mbsf) coincides with the top of lithostratigraphic Unit VI and is marked by an abrupt decrease in the NGR values relative to PP Unit 9, as well as a slight downhole increase in thermal conductivity values.

The top of PP Unit 11 (1460–1580 mbsf) corresponds to the top of lithostratigraphic Unit VII. PP Unit 11 is characterized by an abrupt decrease in MS and decreased scatter

in density, porosity, and *P*-wave velocity values. NGR data from the upper part of PP Unit 11 are higher than in PP Unit 10 and then decrease again in the lower part of PP Unit 11.

The upper boundary of PP Unit 12 (1580–1742 mbsf) is defined by an abrupt increase in MS relative to PP Unit 11. Density and *P*-wave velocity increase downhole, whereas porosity decreases.

The top of PP Unit 13 (1742–1800.3 mbsf) is marked by a decrease in *P*-wave velocity and thermal conductivity, which then increase downhole to the maximum drilling depth.

The upper boundaries of PP Units 2, 3, 6, 7, 9, 12, and 13 do not correspond to lithostratigraphic boundaries. Therefore, we suggest that changes in the physical properties at the mentioned boundaries may reflect postdepositional processes like diagenetic and hydrothermal dissolution and recrystallization, which may affect primary color, porosity, density, and consequently, *P*-wave velocity of the recovered sediments and rocks.

### *Magnetostratigraphy*

Magnetostratigraphy at Site U1437 was determined from 30 mT demagnetization and measurement of natural remanent magnetization of archive section halves using the SRM, supported by polarity identified by measurement of discrete samples after alternating field or thermal demagnetization. A total of 29 magnetostratigraphic datums, marking the tops and bases of normal polarity chrons and subchrons, were identified. Every chron and subchron in the sequence down to Subchron C3An.2n (6.436 Ma; 1056.65 mbsf) was recognized. Where biostratigraphic datums were available, they agreed very well and consistently with the magnetostratigraphic interpretation, but magnetostratigraphy became the main control on the depositional age model deeper than 550 mbsf.

Normal polarity of Subchron C3An.2n persisted to the bottom of Hole U1437D, but cores in Hole U1437E, which started at the same subbottom depth as the base of Hole U1437D, commenced immediately in reversed polarity. We suggest that a normal fault at or near the base of Hole U1437D has caused a loss of section between the two holes. Pattern matching of the polarity record in Hole U1437E indicated that the reversed polarity interval began immediately above normal Subchron C4n.1n, and the magnetostratigraphy could then be followed down as far as the top of Chron C4An

(8.771 Ma) at 1302 mbsf. Magnetostratigraphy in Units VI and VII was impossible to recognize, with the exception of reversed polarity seen in Sample 350-U1437E-35R-1, 125 cm, from igneous Unit 1, which was the first indication that coring had proceeded below the base of normal Chron C5n.2n (9.984–11.056 Ma) spanning the upper part of the lowest nannofossil age range.

Extrapolating the magnetostratigraphy from the last datum at 8.771 Ma (1302 mbsf) near the base of lithostratigraphic Unit V, to Sample 350-U1437E-36R-CC (1402 mbsf) substantially underestimates the age of the nannofossil datum of 10.97–11.85 Ma at this depth. The most likely explanation is a hiatus at the lithostratigraphic Unit V/VI boundary.

Although magnetostratigraphy was surprisingly successful at Site U1437, this is not to say that the polarity record was easily obtained; magnetic sulfides in Holes U1437B and U1437D and a dominantly multidomain magnetite mineralogy in Hole U1437E required a variety of strategies for recognizing polarity, including the use of liquid nitrogen cooling in field-free space to reduce the effect of high-stability overprints in discrete samples.

The paleomagnetic team also provided direct support to the lithostratigraphers. The sample in igneous Unit 1 demagnetized along a simple single-component path after removal of the drilling overprint, and this had an appropriate inclination; this provided part of the evidence that this feature was indeed emplaced in situ. Demagnetization analyses of samples of selected clasts in Unit VII were also conducted in order to determine if they were emplaced hot or cold. These experiments were only partly successful due to multidomain overprinting, but clasts hosting Samples 350-U1437E-66R-5, 106–108 cm, and 66R-6, 16–18 cm, display characteristic reversed polarity that might be consistent with hot emplacement.

### *Rock magnetism*

Rock magnetic studies at Site U1437 spanned the gamut of techniques available onboard, including SIRM acquisition, backfield demagnetization of SIRM by a 300 mT field to yield the $S_{-0.3T}$ ratio, stepwise acquisition of pARM, thermal demagnetization analysis, and AMS. Both pARM coercivity spectra and thermal demagnetization behavior confirmed the presence of magnetic iron sulfide (presumed to be greigite in the absence of shipboard X-ray diffraction data during Expedition 350), at least within the interval cored in Holes U1437B and U1437D. This sulfide is present in addition to magnetite, which is the dominant magnetic mineralogy.

Sooty black sulfides typically including greigite were visibly identified in association with worm burrows, bioturbation, and glaucony/glauconite. They are likely to host concentrated magnetic sulfides and were avoided in sampling discrete paleomagnetic samples. This practice, and the weaker intensity of the drill string overprinting field near the center of the core, made the record of polarity in discrete samples often more reliable than the SRM record.

Through Holes U1437B and U1437D a number of significant features in the downhole distribution of rock magnetic properties correlated with features of the physical properties, interstitial water geochemistry, and organic geochemistry records. Overall, the rock magnetic properties show a downhole trend suggesting that after initial biologically mediated reduction in the sulfate reduction zone to produce greigite, the proportion of greigite gradually decreased, presumably though slow completion of the iron sulfide reduction chain to convert this ferrimagnetic sulfide to paramagnetic pyrite. Superimposed on this trend is a break at ~400 mbsf, where SIRM/k, $S_{-0.3T}$, and magnetic foliation all show step changes. This represents a sudden downhole increase in the proportion of magnetic sulfides, followed by gradual returns to trend over the 300 m below. The return to trend in SIRM and $S_{-0.3T}$ occurs in the lower part of lithostratigraphic Unit I and appears to be complete by the Unit I/II boundary at ~680 mbsf, corresponding also to the top of PP Unit 2. After initial sulfate reduction, sulfate recovers and reaches a plateau concentration from ~275 to ~400 mbsf; over this interval $S_{-0.3T}$ values drop to below 0.97, suggesting renewed and enhanced production of greigite. Deeper than ~400 mbsf, sulfate increases again downhole to near seawater concentrations at ~460 mbsf, corresponding to the highest value of SIRM/k in all samples measured at Site U1437, and remains high to the deepest IW sample taken at 700 mbsf. Transport of sulfate in pore fluid appears to have been responsible for a history of renewed magnetic authigenesis. The step reduction in AMS foliation at ~400 mbsf can also be explained by renewed growth of magnetic sulfides, which would have a compaction history reset at zero at this subbottom depth. The deep methanogenesis zone also matches the rock magnetic record, corresponding to the highest $S_{-0.3T}$ values encountered at this site to date. Such high $S_{-0.3T}$, indicating a very low coercivity magnetic assemblage, suggests not only complete conversion of greigite to pyrite but probably also dissolution of fine-grained magnetite; both may reflect further reduction of the sediments related to deep and ongoing microbial activity stimulated by influx of sulfate-rich pore fluids.

Surprisingly, given the apparent continuity of broadly similar lithologies through lithostratigraphic Units I–V across Holes U1437B, U1437D, and U1437E, rock mag-

netic properties in Hole U1437E do not follow the trends seen through Holes U1437B and U1437D. The background log-linear downhole decrease in SIRM/k that persists throughout Units I–IV is absent from Units V and VI. Instead, SIRM/k values appear to be randomly scattered over a wide range. Coercivity spectra from pARM analysis also show a wide range, from very magnetically soft (peak coercivity < 20 mT) to harder (broad coercivity peak from 20 to 30 mT) without any systematic downhole trends.

### *Biostratigraphy*

The biochronology for Site U1437 was established based on planktonic foraminifers and calcareous nannofossils. Core catcher samples and several extra samples from within the core from Holes U1437B, U1437D, and U1437E were analyzed for planktonic foraminifer and calcareous nannofossil content. Deeper than 1403 mbsf, no age-diagnostic microfossils were found. Both fossil groups show that the upper 1403 m part of the succession spans from the lower Pleistocene to the upper Miocene (maximum age detectable ~12 Ma). The timing of bioevents agrees well with magnetostratigraphic data. Deeper than 1403 mbsf, the bioevents were difficult to establish because of poor preservation and low microfossil abundance. The decrease in preservation/abundance corresponds to a lithologic change from a succession dominated by mud and mudstone to one dominated by volcanic material.

**Foraminifers.** A total of 146 core catcher samples were examined for planktonic and benthic foraminifer content. In the upper ~543 m of the succession (Samples 350-U1437B-1H-CC through 350-U1437D-13R-CC; Holocene to lower Pliocene) planktonic foraminifers are generally abundant, diverse, and show moderate to good preservation. Recognizing foraminifer datums deeper than ~543 mbsf (from Sample 350-U1437D-14R-CC downhole) became increasingly challenging because of a combination of low foraminifer abundance, lack of age-diagnostic species in most of the assemblages, poor preservation, and/or induration of sediments. Induration posed great difficulties in extracting the foraminifers. In interval 350-U1437D-40R-CC through 63R-CC (805–1009 mbsf, lithostratigraphic Unit III), many samples are barren of foraminifers, or where foraminifers are present, they show strong evidence of both plastic deformation and recrystallization, presumably due to compaction. Less deformed foraminifers were recovered from Samples 350-U1437D-64R-CC through 72R-CC (1021–1088 mbsf), but most are present as internal molds.

In terms of datums, the Pliocene/Pleistocene boundary (2.588 Ma) is placed somewhere between 372 and 416 mbsf based on the recognition of the top of *G. decoraperta*

(top of 2.75 Ma ± 0.03 Ma) in Sample 350-U1437B-53X-CC (416 mbsf), and the top of *G. pseudomiocenica* (top of 2.39 Ma) in Sample 48X-CC (372 mbsf). Many typical age-diagnostic fauna (e.g., *Globigerinoides fistulosus* and *Globoturborotalita nepenthes*) are very rare or absent in this succession. The datums in the lower part of the succession (deeper than ~570 mbsf) are tentatively assigned to include the top and bottom of *Globorotalia margaritae* (3.85 ± 0.03 Ma and 6.08 ± 0.03 Ma, respectively), bottom of *Globorotalia crassaformis* sensu lato (4.31 ± 0.04 Ma), and top of *Sphaeroidinellopsis kochi* (4.53 ± 0.17 Ma). An additional bioevent, the extinction of the benthic foraminifer genus *Stilostomella* in the Middle Pleistocene (Sample 11F-CC; 94 mbsf), is not used to establish the biochronology but corroborates it.

**Calcareous nannofossils.** Calcareous nannofossils were abundant and well preserved throughout Holes U1437B and U1437D down to Sample 350-U1437D-26R-CC (669 mbsf). From 27R-CC downhole (677–1806 mbsf), moderate to poor preservation is recorded and several samples are barren in nannofossils. The Middle–Upper Pleistocene sequence is defined by the bottom of *E. huxleyi* in Sample 350-U1437B-3H-CC (19.51 mbsf) and the top of *P. lacunosa* in Sample 6H-5, 75–76 cm (51.48 mbsf). The top common occurrence (Tc) and bottom common occurrence (Bc) of *Reticulofenestra asanoi* (Samples 15F-3, 80–81 cm [110 mbsf], and 16F-CC [113 mbsf], respectively) and bottom of *Gephyrocapsa omega* (113 mbsf) define the bottom of Chron Cn14a. The bottoms of Chrons CN13a, CN12d, and CN12c are defined by the top of *D. brouweri* (248 mbsf), top of *D. pentaradiatus* (337 mbsf), and top of *D. surculus* (367 mbsf), respectively. In Hole U1437D, the succession spans the upper Miocene to Pliocene. The bottom of Chron CN12b is defined by the top of *Discoaster tamalis* (384 mbsf). The top of *Reticulofenestra pseudoumbilicus* in Sample 350-U1437D-19R-3, 32 cm (595 mbsf), defines the bottom of Chron CN12a. The last reliable datum indicator is the top of *Triquetrorhabdulus rugosus* (Sample 48R-CC; 871 mbsf). Since the preservation of nannofossils quickly deteriorates below Sample 27R-CC (677 mbsf), it was not possible to recognize other bioevents in the middle Pliocene to upper Miocene part of the succession. The preservation in Hole U1437E is very poor, and from Sample 350-U1437E-27R-CC (1312 mbsf) downhole the majority of the samples are barren in nannofossils. A broad age range is provided for Sample 36R-CC (1403 mbsf) by the presence of the species *Coccolithus miopelagicus* (top = 10.97 Ma) and the absence of *Coccolithus floridanus* (top = 11.85 Ma), which confirms a sequence falling within the biozone Chron CN5b. Biozones from Chrons CN10a to CN6 are not identifiable because preservation issues affect the presence of markers (e.g., the different species of *Discoaster*, *Catinaster*, and *Minylitha convallis*).

### *Age model*

At Site U1437 it was possible to identify a Pleistocene to upper Miocene succession. Fourteen biostratigraphic and 29 magnetostratigraphic datums obtained in the upper 1303 mbsf of the succession were selected to construct the age-depth model. The age model has not been extended deeper than 1303 mbsf because no biostratigraphic or magnetostratigraphic datums are detectable in the interval 1303–1806 mbsf. Also, no biostratigraphic datums are recognized deeper than 867 mbsf; thus, the age model for the interval 867–1303 mbsf was constructed only using magnetic reversal datums. Deeper than 1303 mbsf, the only age constraint from microfossils is given by a calcareous nannofossil assemblage, which suggests an age range between 10.97 and 11.85 Ma at 1403 mbsf. This age range is consistent with the magnetostratigraphic datums.

Seven intervals were selected to calculate the LSR, assuming constant sedimentation rates within those intervals. The LSRs range from a minimum of 98 m/My to a maximum of 259 m/My. The highest LSR (259 m/My) is found from the top of lithostratigraphic Unit II through the upper part of Unit III, to ~825 mbsf. A minimum LSR of 98 m/My is recorded from 825 to 844 mbsf. Lithostratigraphic Units IV and V record an increase in LSR with values of 157 and 105 m/My.

An offset in LSR between intervals 868–1056 and 1122–1302 mbsf corresponds to the change from Hole U1437D to Hole U1437E and also to a missing interval in the magnetostratigraphy. The probable explanation is a normal fault between the two holes, resulting in a partial loss of section within lithostratigraphic Unit IV. If LSR within lithostratigraphic Unit V is extrapolated to Unit VI, ages are not consistent with the age constraint given by the nannofossil assemblage in Sample 350-U1437E-36R-CC (10.97–11.85 Ma at 1403 mbsf); a hiatus is the most likely explanation for this.

The total MAR, calculated from dry bulk density, ranges between 12 and 35 g/cm$^2$/ky, with the highest values in the intervals 2–2.5 and 4.2–4.7 Ma. High MAR (29 g/cm$^2$/ky) is also recorded in the lower part of Unit III (860 mbsf) to the upper part of Unit IV.

The carbonate accumulation rates are low over the entire succession ranging between 3 and 8.3 g/cm$^2$/ky, with the highest values in the intervals 4.2–4.7 and 5.2–6.4 Ma.

## Preliminary scientific assessment

Operations went perfectly smoothly for most of the expedition. On the way to the main objective Site U1437 in the Izu rear arc, we drilled for 1 day at Site U1436 (IBM-4GT) in the Izu fore arc. The goal of this effort was to drill a 150 m deep geotechnical test hole for potential future deep drilling (5500 mbsf) at proposed Site IBM-4 using the *Chikyu*. This goal was achieved. Furthermore, the core from this site was used to test and refine a new descriptive scheme for volcaniclastic rocks. Core from Site U1436 yielded a rich record of Late Pleistocene explosive volcanism, including distinctive black glassy mafic ash layers that may record large-volume eruptions on the Izu arc front. The expedition then proceeded to the main objective site on the rear arc, Site U1437, where drilling went very well. Site U1437 had excellent core recovery in Holes U1437B and U1437D, and we succeeded in hanging the longest casing in the history of *JOIDES Resolution* scientific drilling (1085.6 m) in Hole U1437E. Recovery declined and drilling slowed in the lower part of Hole U1437E, so it began to look unlikely that we would reach our very optimistic target depth of 2100 mbsf, although if drilling rate did not slow appreciably, we hoped to reach ~2000 mbsf. Unfortunately, after drilling to 1806.5 mbsf and pulling out of the hole for a routine bit change, the fiber optic cable on the reentry camera failed, so we were unable to reoccupy the hole for continued drilling; furthermore, Hole U1437E could not be logged. We have requested that one of the other IBM expeditions return to Hole U1437E while it is still in good condition and do the downhole logging. We decided to make use of the ~4 days left to us by returning to Site U1436 to drill three additional holes (Holes U1436B, U1436C, and U1436D), in an attempt to get better recovery of the black glassy mafic ash layers and enclosing sediments. This was highly successful.

The primary scientific objective for Site U1437 was to characterize "the missing half of the subduction factory." Numerous ODP and Integrated Ocean Drilling Program sites had previously been drilled in the arc to fore-arc region, but this was the first site to be drilled in the rear part of the Izu arc. Rocks collected by dredges from the surface of rear-arc volcanoes were shown to be different from arc-front rocks, and drilling in the "missing half" was proposed in order to fully characterize this asymmetry and determine if it developed early or late in the ~52 My history of the arc system. This is important for determining whether the asymmetry is an inherent feature of arcs, for making mass balance and flux calculations for crustal evolution, and for testing models of intracrustal evolution. Volcaniclastic rocks in the fore arc had previously been shown to provide a faithful record of arc evolution (e.g., Gill et al., 1994; Straub, 2003; Bryant et al., 2003), and recent improvements in microanalytical techniques (e.g.,

single crystal grains or glass fragments) makes this approach more promising than ever. To this end, the expedition was highly successful. However, the temporal record might be shorter than expected, as discussed below.

The deposits drilled at Site U1437 were in general much finer grained than expected, making shipboard geochemical analysis more difficult; clasts were not large enough to be analyzed individually by ICP, except in lithostratigraphic Units VI and VII, so bulk analysis was required for most units. However, shore-based microanalytical techniques will overcome this problem. Alteration resulted in destruction of fresh glass from the top of Unit III downward (except for the black glassy lapilli tuff in Unit VII), so shipboard geochemical interpretations below Unit II relied on immobile elements to infer types of magmas represented (e.g., rhyolite versus andesite versus basalt) and source types (e.g., arc front versus rear arc). Shore-based geochemical analysis will therefore need to rely more on minerals, which are less altered than the glass for most samples taken deeper than ~750 mbsf.

Site U1437 is much more mud rich than expected; ~60% for the section as a whole and 89% in the thickest lithostratigraphic unit (Unit I, 433 m; Table **T4**); this obviously lessens the opportunities for studying the chemistry of volcanic clasts and grains. Furthermore, the volcaniclastic fraction of the section (40%) is relatively fine grained, composed half of ash/tuff and half of lapilli tuff of generally fine grain size (clasts < 3 cm); volcanic blocks were only sparsely scattered through Units VI and VII, which in turn make up only ~20% of the recovered material. The fine grain size of the tephra makes it more likely that many of them provide a record of arc-front (rather than rear arc) volcanism and limits the scope for studying submarine volcanic eruption processes because most of the record is relatively distal. However, shore-based geochemical techniques are expected to allow better distinction of volcanic source areas than was possible shipboard. Additionally, future shore-based geochemical work will be aimed at understanding the provenance of the mud/mudstone, which accumulated at unusually high rates for such fine-grained material.

Due to compaction and alteration, the lowest biostratigraphic datum was ~850 mbsf and the lowest paleomagnetic datum was at ~1300 mbsf (~9 Ma). Both a nannofossil assemblage constraint and a preliminary U-Pb zircon date generated shortly after the expedition indicate an age range of ~11–15 Ma for the depth interval 1389–1403 mbsf. The section is much younger than predicted from seismic interpretation of relations between the basin fill and the bounding volcanoes. Lithostratigraphic Unit II forms a reflector that was interpreted to correlate with the Manji Volcano (dated at

~6.5 Ma), but that unit is only ~4.3 Ma (Fig. F24). The Miocene/Oligocene boundary (~23 Ma) was inferred to lie at ~1250 mbsf, but strata at that depth are much younger (~8.5 Ma). Thus, the section dated so far provides a shorter temporal record than expected. The age of the lowest ~25% of the section (Units VI and VII) will not be conclusively known until shore-based radiometric dating of the volcaniclastic rocks is complete.

# Operations

## Site U1436

The transit from Keelung, Taiwan, started on 4 April 2014 and ended at 1142 h on 8 April, marking the beginning of operations at Site U1436. All times reported here are ship local time, which was UTC + 9. See Table T5 for coring summary.

### Hole U1436A (32°23.883′N, 140°21.928′E; 1775 m water depth)

An APC/XCB BHA was built and deployed to a depth of 1781 meters below rig floor (mbrf). The subsea camera was lowered to the bottom and a seafloor survey was conducted to determine if any subsea communications cables could be found in the drilling area. None were found. After visually confirming that the drill pipe tagged the seafloor, the camera was retrieved. Coring in Hole U1436A commenced at 0705 h on 9 April. Cores 350-U1436A-1H through 9H (0–59.7 m) cored with the APC system yielded 59.4 m of core (99% recovery). Cores 10F through 12F (59.7–65.0 m) drilled with the HLAPC system retrieved a total of 5.22 m of core (98% recovery). The rate of penetration with the HLAPC decreased exponentially, and we switched to the XCB system. Cores 13X through 21X (65.0–150.0 m; total depth) recovered only 7.1 m of core (8% recovery). The drill string was recovered and the bit cleared the rotary table at 1245 h, ending operations in Hole U1436A. Hole U1436A was completed with a total of 21 cores for a total of 150 m cored and 71.6 m recovered (average recovery = 48%). The rig was secured for transit to Site U1437 (proposed Site IBM-3C).

## Return to Site U1436

After operations were prematurely terminated at Site U1437, the science party decided to use the remaining time to attempt to recover undisturbed sections containing conspicuous black ash layers found 7 weeks earlier at ~50 mbsf in Hole U1436A that was severely disturbed by coring. This would better constrain the thickness to as-

sist in determining the explosivity of the eruption that generated them. The short transit to Site U1436 took from 0930–1700 h on 25 May 2014.

### Hole U1436B (32°23.896′N, 140°21.929′E; 1774 m water depth

An APC/XCB BHA was made up and deployed to the seafloor. Hole U1436B was positioned 20 m north of Hole U1436A, and coring was initiated at 0015 h on 25 May. Cores 350-U1436B-1H through 14H (0–61.8 mbsf) obtained 61.79 m (100% recovery). After the target depth of ~62 mbsf was reached, the bit was raised and cleared the seafloor at 1425 h.

### Hole U1436C (32°23.873′N, 140°21.930′E; 1774.5 m water depth)

The ship moved 20 m south of Hole U1436A, where Hole U1436C was initiated at 1545 h on 25 May. Cores 350-U1436C-1H through 18F (0–70.4 mbsf) obtained 70.38 m (100% recovery). The sequence recovered in Hole U1436C had less coring disturbance than sequences obtained in Holes U1436A and U1436B, particularly over the target interval near 50 mbsf, presumably owing to the more extensive use of the HLAPC. Operations in Hole U1436C ended when the bit cleared the seafloor at 1255 h on 27 May.

### Hole U1436D (32°23.885′N, 140°21.942′E; 1774.5 m water depth)

We decided to make a last attempt to recover the black mafic ash layer undisturbed in the shortest amount of time possible. The ship moved 20 m east of Hole U1436A, where Hole U1436D was initiated at 1355 h on 27 May, using a center bit to wash down to 40 mbsf. Cores 350-U1436D-2F through 9F (40–62.0 mbsf) obtained 22.07 m (100% recovery). Although several cores in Hole U1436D were plagued by a large proportion of impenetrable tephra that fell into the hole from further up in the formation, presumably due to washing down to 40 mbsf, we did eventually, after a discussion of the circumstances with the Tool Pusher on shift, recover excellent cores containing the targeted tephra layers. The last core of Expedition 350, Core 9F, arrived on deck at 0210 h on 28 May.

The ship remained on station at Site U1436 until departure for Yokohama, Japan, at 0930 h on 29 May. The transit took 24 h to the pilot station, and the ship was dockside at 1100 h on 30 May, ending Expedition 350.

## Site U1437

### Hole U1437A (31°47.390′N, 139°01.580′E; 2115.8 m water depth)

The 77 nm transit from Site U1436 to Site U1437 was completed in 7.5 h. All times reported here are ship local time, which was UTC + 9. A beacon was dropped at 2304 h on 10 April 2014, marking the beginning of operations at Hole U1437A.

An APC/XCB BHA was made up and deployed to a depth of 2110 mbrf. The subsea camera system was lowered to depth, and a seafloor survey was conducted to confirm that no subsea cables were present at the site. The seafloor was tagged at 2127 mbrf with visual confirmation through the camera. After the camera was recovered, Hole U1437A was initiated at 0915 h on 11 April for a jet-in test to ~25 mbsf. Upon completion of the jet-in test, the ship was repositioned 10 m north of Hole U1436A to begin coring in Hole U1437B.

### Hole U1437B (31°47.391′N, 139°01.579′E; 2116.1 m water depth)

Coring in Hole U1437B commenced at 1035 h on 11 April. Cores 350-U1437B-1H through 10H (0–89.2 mbsf), drilled with the full-length APC system, recovered 89.2 m of core (100% recovery). Pulling the core barrels from the formation became increasingly harder at the bottom of that interval, and we therefore switched to the HLAPC system. Cores 11F through 24F (89.2–145.7 mbsf) recovered 56.5 m of core (100% recovery). When the rate of penetration decreased to a critical point, we changed to the XCB system. Coring in Hole U1437B was completed with Cores 25X through 55X (145.7–439.1 mbsf), recovering 96.9 m of core for the 293.4 m interval drilled (33% recovery). The last core from Hole U1437B arrived on deck at 0000 h on 14 April. We cored 439.1 m and recovered 242.6 m in Hole U1437B (55% recovery). The drill string was recovered and the bit cleared the rig floor at 0645 h on 14 April, ending the hole.

### Hole U1437C (31°47.381′N, 139°01.579′E; 2116.0 m water depth)

A RCB BHA was made up with three stands of drill collars, and a core barrel with a center bit was installed. Our plan was to drill without coring to 425 mbsf, several meters above the total depth cored in Hole U1437B, and then start RCB coring. The ship moved 20 m south of Hole U1437B, and the bit was lowered to the seafloor. Drilling in Hole U1437C began at 1530 h on 14 April. At 232 mbsf, the center bit was pulled for inspection and then deployed again. Circulation and rotation was lost at 309.7 mbsf. The stuck pipe was worked for several hours without success. The ship was offset 140 m to allow the rig crew to pull the center bit and run the rotary shifting tool

to drop the bit. A single joint of drill pipe was laid out at this time as well. With the bit dropped, the ship moved back to the Hole U1437C coordinates and the pipe was worked for another 2 h. The drill pipe was finally worked free at 0910 h on 15 April. The bit was raised to 183.7 mbsf using the top drive. After the top drive was set back, the drill string was retrieved, clearing the seafloor at 1055 h and the rig floor at 1305 h on 15 April, and ending operations in Hole U1437C.

### Hole U1437D (31°47.387′N, 139°01.573′E; 2116.0 m water depth)

A new mechanical bit release (MBR) and RCB bit were made up, and the drill string was run into the hole while the vessel was repositioned 10 m west of Hole U1437A.

Drilling without coring in Hole U1437D began at 2250 h on 15 April and extended from the seafloor to 427.2 mbsf. The center bit was retrieved and a RCB core barrel was deployed. The first core (350-U1437D-2R) arrived on deck at 2045 h on 16 April. RCB coring continued until 21 April with Cores 2R through 59R (427.2–980.4 m) recovering 434.56 m (79% recovery). At this time, the bit had been rotating for 51.5 h and required changing, so we decided to stop coring and collect wireline log data.

A free-fall funnel (FFF) was deployed, and the drill string was pulled out of the hole to drop the bit in preparation for logging. When we attempted to reenter Hole U1437D without the bit, the top connection of the MBR, which has razor sharp edges, was unable to slide into the FFF and the reentry was aborted. The drill string was retrieved, with the end of the pipe clearing the rotary table at 0430 h on 22 April. The MBR top connection was removed, and a logging bit was made up to the BHA. The drill string was then lowered and Hole U1437D was reentered at 1207 h on 22 April. The logging bit was set at 92.4 mbsf.

Three logging strings were deployed in Hole U1437D. The first tool string deployed consisted of the triple combo with the MSS. The triple combo/MSS tool string reached ~960 mbsf, indicating ~20 m of fill had accumulated at the bottom of the hole. The data recorded from this first run show that the hole was in excellent condition, with a diameter barely exceeding the bit size for most of the hole. The second tool string deployed (FMS-sonic) was able to record high-quality velocity data and electrical images to a maximum depth of 950 mbsf. The final logging run was a VSP that obtained data at 14 depths spaced every 50 m from the maximum depth of 875 mbsf. All logging operations were completed within 24 h and the equipment was rigged down by 1330 h on 23 April.

The subsea camera system was lowered to observe the drill string exiting the FFF; however, a fishing line was observed tangled on the drill pipe ~300 m below the ship, so the camera system was brought back up. The drill string was then pulled out of the hole, the drill string recovered, and the logging bit cleared the rig floor at the 2235 h on 23 April.

A new RCB bit was made up to the BHA and Hole U1437D was reentered at 0630 h on 24 April. The drill string was lowered without circulation or rotation to 950 mbsf. The hole was then washed to the bottom of the hole (980.4 mbsf) and coring resumed. Hole U1437D was deepened to 1104.6 mbsf by the morning of 26 April. Cores 350-U1437D-60R through 73R (980.4–1104.6 mbsf) recovered 69.29 m (56%). At that time, hole-cleaning time was exceeding coring time because of crushed rock in the borehole that was difficult to remove, requiring a large number of mud sweeps. Also, packing of mud around the bottom of the core barrel indicated a malfunction. The drill string was recovered and the bit cleared the rig floor at 2040 h on 26 April, ending Hole U1437D. The total cored interval in Hole U1437D was 677.4 m, with 503.8 m recovered (74%).

At this point, we decided to drill and case a new hole to the total depth of Hole U1437D and then core and log it as deep as time permitted. This decision was prompted by (1) the increasing risk with penetration depth of not being able to clean a hole, particularly a deep noncased hole, and (2) the fact that the ship was carrying ~1100 m of 11.75 inch casing, just enough to cover the interval cored to date, which made this the optimal time to install the casing.

### Hole U1437E (31°47.390′N, 139°01.591′E; 2115.8 m water depth)

The ship moved ~20 m northeast to begin installation of casing in Hole U1437E. The reentry cone, equipped with 20.7 m of 20 inch casing, was run to the seafloor. The subsea camera system was deployed to observe the jetting in of the casing and landing of the reentry cone on the seafloor. Deployment was complete at 1905 h on 27 April when the bit cleared the reentry cone. The drill string was retrieved back on the rig floor at 0030 h on 28 April.

A drilling assembly consisting of an 18.5 inch tricone bit and an underreamer was made up to drill the hole for the 264 m long, 16 inch casing. The underreamer was set to enlarge the hole to 22 inches and tested to confirm that the arms opened at a mud pump rate of 25 strokes/min. The drill string was deployed to the seafloor, followed by deployment of the subsea camera to guide the reentry into Hole U1437E at

1105 h. After successful reentry, the camera system was retrieved and Hole U1437E was drilled to the target depth of 271.7 mbsf by 0400 h on 29 April. The hole was swept with 60 bbl of high-viscosity mud to remove drill cuttings. The drill string was then raised to 12.7 mbsf and lowered back down to total depth (271.7 mbsf) while circulating seawater to ensure the borehole was clear. No obstruction or fill at the bottom of the hole was detected. Another 60 bbl high-viscosity mud sweep was circulated. The drill string was pulled out of the hole with the bit clearing the seafloor at 0910 h and arriving at the rig floor at 1300 h on 29 April.

The 264 m long 16 inch casing was assembled in an 8 h effort. The casing running tool was installed, and the casing string was lowered to the seafloor by 0145 h on 30 April. The camera system was deployed to guide the reentry into Hole U1437E, which was completed at 0350 h. The casing was lowered into the hole, and the top of the casing was latched into the casing hanger in the reentry cone at 0600 h. The latch was verified with 10,000 lb of pull from the rig.

To ensure the casing would act as the circulation conduit during future coring in Hole U1437E, the bottom of the casing had to be cemented firmly to the formation. With the casing running tool forming a seal at the top of the 16 inch casing, 20 bbl of 14.5 lb/gal cement was mixed and pumped from the rig floor through the drill string and through the 60 m stinger extending from the casing running tool down into the hole. The cement emplacement was followed with 295.8 bbl of seawater, a volume calculated to displace the cement to the bottom of the casing such that half the cement volume would extend upward between the formation and the base of the casing and the other half would remain inside the bottom of the casing to be drilled out later. The cement was in place at 0720 h on 30 April. The casing running tool was released, and the drill string and standpipe manifold were flushed clean with seawater. The camera was retrieved, the top drive was disengaged, and the drill string was tripped to the surface, with the running tool clearing the rig floor at 1220 h on 30 April.

The next operation was to drill out the cement and then a 14.75 inch hole to 1104 mbsf (the total depth of Hole U1437D) for the 10.75 inch casing. After breaking down the running tool and the underreamer assembly, a BHA with a 14.75 inch tricone drill bit was installed and the drill string was tripped back to the seafloor. The camera was deployed to guide the reentry into Hole U1437E, which was completed at 2245 h on 30 April, and was then retrieved back to the rig floor. At 0030 h on 1 May, the top drive was picked up and the bit was lowered to the bottom of Hole U1437E. At 0330 h, the bit tagged the top of the cement plug at 264.7 mbsf, 1 m below the 16 inch casing

shoe. Cement should have been contacted ~10 m above the shoe. This indicated that the cement had been displaced several meters too far down the 16 inch casing and that the casing likely had not been cemented to the formation as planned, thereby requiring a second cementing round trip.

The drill string was pulled back to 230.7 mbsf, the top drive was disengaged, and the drill string was tripped to the surface, clearing the seafloor at 0440 h and arriving at the rig floor at 1030 h on 1 May. The casing running tool and logging bit were made up once more, the drill string was lowered to the seafloor, and the subsea camera was deployed to guide reentry into Hole U1437E, which was completed at 1740 h on 1 May. After tripping into the hole to 55.7 mbsf using the top drive, weight was applied through the drill string to ensure the casing running tool sealed the top of the casing in preparation for cement delivery. When circulation was attempted by pumping seawater into the hole and around the bottom of the 16 inch casing, a pressure increase was observed, indicating that the bottom of the casing was actually sealed off, either by the first cementing job or by the formation sealing off around the casing since. The second cementing job was therefore aborted at 1830 h. The drill string was raised to 18.1 mbsf, the top drive disengaged, the camera system retrieved, and the drill string tripped to the surface, clearing the drill floor at 2350 h on 1 May.

The 14.75 inch tricone bit was installed again, lowered to the seafloor, and Hole U1437E was reentered for the seventh time at 0605 h on 2 May. The bit was lowered to 230.7 mbsf, the camera used to guide reentry was retrieved, and the top drive was engaged to wash the hole down to 266.7 mbsf, where the cement plug was encountered. The cement plug, which extended to 271.7 mbsf, was drilled out and the hole was flushed with high-viscosity mud. Hole U1437E was drilled (without coring) to the target depth of 1104 mbsf (the total depth of RCB coring in Hole U1437D) at 1745 h on 5 May. The hole was cleaned with a 41 bbl mud sweep before the bit was raised to 988 mbsf and the top drive was disengaged. The bit was then further raised to 18.0 mbsf and lowered again to 260.1 mbsf, just above the bottom of the 16 inch casing string. The drill string remained in that position while the rig crew was slipping and cutting the drilling line.

A wiper trip was conducted to ensure the hole was clear. The bit was lowered into the hole without the top drive from 259.7 to 1016.7 mbsf. The top drive was then picked up to wash and ream to 1104 mbsf; fill was encountered at 1022.7 mbsf. High torque occurred at 1063.7 mbsf, and after raising the bit to 1035.7 mbsf, the hole was finally washed and reamed to total depth (1104 mbsf) at 0545 h on 6 May. The hole was

swept with 40 bbl of high-viscosity mud, and the bit was raised to 1035.7 mbsf, where another 60 bbl high-viscosity mud sweep was circulated to ensure the hole was clean. The bit was then raised to 1016.7 mbsf, where the top drive was disengaged. The drill string was tripped out of the hole, clearing the seafloor at 1115 h and the rig floor at 1500 h on 5 May.

The 1085.6 m long 10.75 inch casing string was assembled with a total of 85 joints, with the couplings of the bottom 7 joints welded in 4 places and the rest of the couplings tack-welded in 2 places. The casing hanger was installed, the running tool was engaged, and the complete assembly was hung from the moonpool doors while the casing stinger was assembled. A mud motor and underreamer were made up and tested. When the underreamer arms failed to open, a backup unit was installed, which performed as expected with the arms opening at a circulation rate of 35 strokes/min. The stinger BHA and the running tool were made up and run and latched into the casing by 1945 h on 7 May. The casing was tripped to the seafloor, the camera was deployed, and Hole U1437E was reentered with the 10.75 inch casing at 2115 h. When the bit had passed below the 16 inch casing shoe (264.1 mbsf; 2200 h), the camera system was raised above the running tool at the top of the casing string, to be lowered together with the casing string. Tripping of the casing continued to 1000.7 mbsf, where the top drive was engaged. After further lowering the casing string to 1034.7 mbsf (0145 h on 8 May), fill was encountered in the hole. The pumps were engaged and the casing was washed down to 1086.7 mbsf. At that point, the 10.75 inch casing hanger latched into the 16 inch casing hanger at the reentry cone. The latch was verified with 20,000 lb of pull from the rig floor. The casing was released and the stinger assembly was raised to 1057.7 mbsf. The top drive was disengaged and the trip to the surface continued, with a stop at 796.7 mbsf to retrieve the camera, and the bit cleared the seafloor at 0610 h and arrived at the rig floor at 1100 h on 8 May.

The underreamer and mud motor were removed, and a cementing BHA was made up consisting of a bullnose, two stands of drill collars, the casing running tool, and one stand of drill collars above. The cementing assembly was lowered to the seafloor, and after the camera was deployed, reentered Hole U1437E at 1700 h on 8 May. The running tool was landed in the reentry cone with the bit at 55.8 mbsf. Attempts to establish circulation failed, indicating that the bottom of the casing was sealed, and the cement job was aborted. The cementing string was raised and cleared the seafloor at 1830 h, and after recovering the camera, was tripped to the surface clearing the rig floor at 2235 h on 8 May. This ended the deepest casing deployment in the history of the *JOIDES Resolution*.

After several hours of routine rig maintenance, we were ready to resume RCB coring. An RCB coring bit was assembled and lowered to the seafloor, which was followed by the deployment of the camera to guide reentry of the bit into Hole U1437E at 0930 h on 9 May. The bit was lowered to 1048 mbsf, where the top drive was engaged, and the bit reached the bottom of the hole (1104 mbsf) at 1345 h. The hole was swept with 20 bbl of mud, and coring in Hole U1437E began at 1500 h on 9 May. The first core arrived on deck at 1815 h.

The rotation rate (and thus the coring rate) was kept low while the 95 m long BHA was still within the 10.75 inch casing that extended to 1086 mbsf. Drill collars in the BHA have a larger diameter than the regular drill pipe above and may compromise the casing and/or deviate the hole from vertical if not advanced into the formation below the (uncemented) casing shoe with care.

Cores 350-U1437E-4R though 24R (1104.0–1290.8 mbsf) obtained 140.43 m (75% recovery). Although recovery was generally good to excellent (two cores with >100% recovery), we also had two barrels with (near) zero recovery, presumably as a result of losing a perfectly cut core because it could not be broken off the formation (evidence found in one core), or, upon retrieval, could not be kept in the barrel by the core catchers.

On 13 May, the expected bit life cycle (~50 h of rotation with weight on bit) expired and a new bit needed to be installed. The bit was pulled from the bottom of the hole to 1077 mbsf with the top drive engaged. High torque, temporary loss of circulation, and the up to 40,000 lb overpull required to raise the drill string indicated that the hole was packing off at 1281–1242 mbsf. After circulation was reestablished and torque and pull returned to normal levels, the top drive was removed with the bit at 1077 mbsf, and the drill string was retrieved with the bit clearing the seafloor at 1025 h and the rig floor at 1400 h on 13 May.

After a few hours of rig maintenance, including installation of the upper guide horn, a new RCB bit was installed and lowered to the seafloor. The camera was lowered to the seafloor to guide reentry into Hole U1437E with the new RCB bit at 0010 h on 14 May. When the bit could not easily pass 1176 mbsf, it was raised to 1164 mbsf and the top drive was engaged. The hole was washed to 1206 mbsf, where another obstruction and high torque were encountered. After raising the bit back to 1174 mbsf, where normal torque was reestablished, the bit was washed down to 1290 mbsf and

no fill was detected in the bottom of the hole. The hole was swept with 40 bbl of high-viscosity mud, and RCB coring resumed at 0915 h on 14 May.

Cores 350-U1437E-25R through 31R penetrated from 1290.8 to 1359.0 mbsf and obtained 44.66 m of core (65% recovery). After Core 31R was recovered, a wiper trip was conducted from 1291 to 1359 mbsf (0930–1630 h on 15 May) to clear the hole of drill cuttings. The procedure included two sweeps with 30 and 40 bbl of high-viscosity mud, respectively.

RCB coring in Hole U1437E continued until the expected safe bit life (50 h of rotation with weight on bit) had expired again after Core 350-U1437E-54R (1573.0–1582.7 mbsf) arrived on deck at 0005 h on 19 May. Cores 32R through 54R (1359.0–1582.7 mbsf) recovered 94.81 m (42% recovery). The hole was swept with high-viscosity mud before the bit was raised with the top drive from 1583 to 1485 mbsf. The top drive was disengaged for the remainder of the trip, and the bit cleared the seafloor at 0515 h on 19 May. The drilling line was slipped and cut on the rig floor as part of general rig maintenance before the drill string was retrieved; the bit arrived back at the rig floor at 1100 h on 19 May.

A new bit was installed and lowered to the seafloor. The camera was deployed, and Hole U1437E was reentered at 1710 h on 19 May. The camera was retrieved, and the bit was lowered to 1489 mbsf, where resistance was encountered. The bit was pulled back to 1475 mbsf to engage the top drive and washed to the bottom (1582.7 mbsf) by 0215 h on 20 May. RCB coring resumed and continued until 0800 h on 24 May, except for 6 h on 22 May when rough seas forced us to suspend coring.

Cores 350-U1437E-55R through 79R penetrated from 1582.7 to 1806.5 mbsf and recovered 107.55 m of core (48% recovery). At 0800 h on 24 May, the expected safe bit life (50 h) had expired again. The hole was swept with 30 bbl of high-viscosity mud before the bit was raised to 1708.7 mbsf with the top drive. The top drive was disengaged for the remainder of the trip, with the bit clearing the seafloor at 1320 h and the rig floor at 1645 h on 24 May.

After installing the new bit, the drill string was lowered to the seafloor (1800–2200 h). At that time the camera transmission test, carried out routinely before the camera is lowered to the seafloor to guide reentry into the hole, failed to transmit a signal, indicating that the last of three fiber optic cables had broken. Measurements confirmed that the fiber was damaged at ~4000 m from the camera end of the cable—an interval that was never unspooled during Expedition 350. The other two fiber optic strands

had been broken before our expedition, and a replacement cable was scheduled for installation during the next port call in Yokohama, Japan. We lowered the camera to the seafloor to see if decompression from the spool might bring back the connectivity, without success. This prematurely ended our expedition's operations in Hole U1437E. Hole U1437E is currently in excellent condition for logging and/or further coring operations, preferably attempted soon, before the hole deteriorates.

Cores 350-U1437E-4R through 79R (1104.0–1806.5 mbsf) recovered 387.45 m (55% recovery). The drill string was recovered with the bit clearing the drill floor at 0730 h. The rig was secured for transit, ending Hole U1437E and Site U1437 at 0800 h on 24 May. Total time in Hole U1437E was 683.25 h or 28.5 days.

At 0930 h, the ship was under way for contingency operations at Site U1436.

# References


Allen, S.R., Hayward, B.W., and Mathews, E., 2006. A facies model for a submarine volcaniclastic apron: the Miocene Manukau Subgroup, New Zealand. *Geological Society of America Bulletin,* 119(5–6):725–742. **http://dx.doi.org/10.1130/B26066.1**

Arculus, R., Ishizuka, O., and Bogus, K.A., 2013. Izu-Bonin-Mariana arc origins: continental crust formation at intraoceanic arc: foundations, inceptions, and early evolution. *International Ocean Discovery Program Scientific Prospectus,* 351. **http://dx.doi.org/10.2204/iodp.sp.351.2013**

Baker, P.A., Gieskes, J.M., and Elderfield, H., 1982. Diagenesis of carbonates in deep-sea sediments: evidence from Sr/Ca ratios and interstitial dissolved $Sr^{2+}$ data. *Journal of Sedimentary Research,* 52(1):71–82. **http://dx.doi.org/10.1306/212F7EE1-2B24-11D7-8648000102C1865D**

Bandy, W.L., and Hilde, T.W.C., 1983. Structural features of the Bonin arc: implications for its tectonic history. *Tectonophysics,* 99(2–4):331–353. **http://dx.doi.org/10.1016/0040-1951(83)90111-7**

Bloomer, S.H., Taylor, B., MacLeod, C.J., Stern, R.J., Fryer, P., Hawkins, J.W., and Johnson, L., 1995. Early arc volcanism and the ophiolite problem: a perspective from drilling in the western Pacific. *In* Taylor, B., and Natland, J. (Eds.), *Active Margins and Marginal Basins of the Western Pacific*. Geophysical Monograph, 88:1–30. **http://dx.doi.org/10.1029/GM088p0001**

Brumsack, H.-J., and Zuleger, E., 1992. Boron and boron isotopes in pore waters from ODP Leg 127, Sea of Japan. *Earth and Planetary Science Letters,* 113(3):427–433. **http://dx.doi.org/10.1016/0012-821X(92)90143-J**

Bryant, C.J., Arculus, R.J., and Eggins, S.M., 2003. The geochemical evolution of the Izu-Bonin arc system: a perspective from tephras recovered by deep-sea drilling. *Geochemistry, Geophysics, Geosystems*, 4(11):1094. **http://dx.doi.org/10.1029/2002GC000427**

Busby-Spera, C.J., 1985. A sand-rich submarine fan in the lower Mesozoic Mineral King caldera complex, Sierra Nevada, California. *Journal of Sedimentary Research,* 55(3):376–391. **http://dx.doi.org/10.1306/212F86D9-2B24-11D7-8648000102C1865D**

Busby-Spera, C.J., 1988. Evolution of a middle Jurassic back-arc basin, Cedros Island, Baja California: evidence from a marine volcaniclastic apron. *Geological Society of America Bulletin,* 100(2):218–233. **http://dx.doi.org/10.1130/0016-7606(1988)100<0218:EOAMJB>2.3.CO;2**

Busby-Spera, C.J., and White, J.D.L., 1987. Variation in peperite textures associated with differing host-sediment properties. *Bulletin of Volcanology,* 49(6):765–776. **http://dx.doi.org/10.1007/BF01079827**

Cambray, H., and Cadet, J.P., 1994. Testing global synchronism in peri-Pacific arc volcanism. *Journal of Volcanology and Geothermal Research,* 63(3–4):145–164. **http://dx.doi.org/10.1016/0377-0273(94)90071-X**

Carey, S., 1997. Influence of convective sedimentation on the formation of widespread tephra fall layers in the deep sea. *Geology,* 25(9):839–842. **http://dx.doi.org/10.1130/0091-7613(1997)025<0839:IOCSOT>2.3.CO;2**

Carey, S., 2000. Volcaniclastic sedimentation around island arcs. *In* Sigurdsson, H., Houghton, B.F., McNutt, S.R., Rymer, H., and Stix, J. (Eds.), *Encyclopedia of Volcanoes:* San Diego (Academic Press), 627–642

Carey, S.N., and Schneider, J.-L., 2011. Volcaniclastic processes and deposits in the deep sea. *In* Hüneke, H., and Mulder, T. (Eds.), *Developments in Sedimentology* (Vol. 63)*: Deep-Sea Sed-*

*iments:* Oxford, UK (Elsevier), 457–515. **http://dx.doi.org/10.1016/B978-0-444-53000-4.00007-X**

Carey, S., and Sigurdsson, H., 1984. A model of volcanogenic sedimentation in marginal basins. *In* Kokelaar, B.P., and Howells, M.F. (Eds.), *Marginal Basin Geology: Volcanic and Associated Sedimentary and Tectonic Processes in Modern and Ancient Marginal Basins*. Geological Society Special Publication, 16(1):37–58. **http://dx.doi.org/10.1144/GSL.SP.1984.016.01.04**

Cas, R.A.F., and Wright, J.V., 1987. *Volcanic Successions, Modern and Ancient: a Geological Approach to Processes, Products and Successions:* London (Allen and Unwin).

Casalbore, D., Romagnoli, C., Chiocci, F., and Frezza, V., 2010. Morpho-sedimentary characteristics of the volcaniclastic apron around Stromboli volcano (Italy). *Marine Geology,* 269(3–4):132–148. **http://dx.doi.org/10.1016/j.margeo.2010.01.004**

Chen, J., An, Z., Liu, L., Ji, J., Yang, J., and Chen, Y., 2001. Variations in chemical compositions of the eolian dust in Chinese Loess Plateau over the past 2.5 Ma and chemical weathering in the Asian inland. *Science in China Series D: Earth Sciences,* 44(5):403–413. **http://dx.doi.org/10.1007/BF02909779**

Cosca, M.A., Arculus, R.J., Pearce, J.A., and Mitchell, J.G., 1998. $^{40}Ar/^{39}Ar$ and K-Ar geochronological age constraints for the inception and early evolution of the Izu-Bonin-Mariana arc system. *Island Arc,* 7(3):579–595. **http://dx.doi.org/10.1111/j.1440-1738.1998.00211.x**

Dickinson, W.R., and Hatherton, T., 1967. Andesitic volcanism and seismicity around the Pacific. *Science,* 157(3790):801–803. **http://dx.doi.org/10.1126/science.157.3790.801**

Expedition 334 Scientists, 2012. Expedition 334 summary. *In* Vannucchi, P., Ujiie, K., Stroncik, N., Malinverno, A., and the Expedition 334 Scientists, *Proceedings of the Integrated Ocean Drilling Program,* 334: Tokyo (Integrated Ocean Drilling Program Management International, Inc.). **http://dx.doi.org/10.2204/iodp.proc.334.101.2012**

Farquharson, G.W., Hamer, R.D., and Ineson, J.R., 1984. Proximal volcaniclastic sedimentation in a Cretaceous back-arc apron, northern Antarctic Peninsula. *In* Kokelaar, B.P., and Howells, M.F. (Eds.), *Marginal Basin Geology: Volcanic and Associated Sedimentary and Tectonic Processes in Modern and Ancient Marginal Basins*. Geological Society Special Publication, 16:219–229. **http://dx.doi.org/10.1144/GSL.SP.1984.016.01.17**

Fisher, R.V., 1961. Proposed classification of volcaniclastic sediments and rocks. *Geological Society of America Bulletin,* 72(9):1409–1414. **http://dx.doi.org/10.1130/0016-7606(1961)72[1409:PCOVSA]2.0.CO;2**

Fisher, R.V., 1984. Submarine volcaniclastic rocks. *In* Kokelaar, B.P., and Howells, M.F. (Eds.), *Marginal Basin Geology: Volcanic and Associated Sedimentary Processes in Modern and Ancient Basins*. Geological Society Special Publication, 16:5–27. **http://dx.doi.org/10.1144/GSL.SP.1984.016.01.02**

Fisher, R.V., and Schmincke, H.-U., 1984. *Pyroclastic Rocks:* Berlin (Springer-Verlag). **http://dx.doi.org/10.1007/978-3-642-74864-6**

Fisher, R.V., and Schmincke, H.-U., 1994. Volcaniclastic sediment transport and deposition. *In* Pye, K. (Ed.), *Sediment Transport and Depositional Processes:* Oxford, UK (Blackwell Science Publishing), 351–388.

Fisher, R.V., and Smith, G.A., 1991. Volcanism, tectonics and sedimentation. *In* Fisher, R.V., and Smith, G.A. (Eds.), *Sedimentation in Volcanic Settings*. Special Publication—SEPM (Society for Sedimentary Geology), 45:1–5. **http://dx.doi.org/10.2110/pec.91.45.0001**

Funck, T., Dickmann, T., Rihm, R., Krastel, S., Lykke-Andersen, H., and Schmincke, H.-U., 1996. Reflection seismic investigations in the volcaniclastic apron of Gran Canaria and implications for its volcanic evolution. *Geophysical Journal International,* 125(2):519–536. **http://dx.doi.org/10.1111/j.1365-246X.1996.tb00015.x**

Gamberi, F., 2001. Volcanic facies associations in a modern volcaniclastic apron (Lipari and Vulcano offshore, Aeolian Island arc). *Bulletin of Volcanology,* 63(4):264–273. **http://dx.doi.org/10.1007/s004450100143**

Gill, J.B., 1981. *Minerals and Rocks* (Vol. 16): *Orogenic Andesites and Plate Tectonics:* Berlin (Springer-Verlag). **http://dx.doi.org/10.1007/978-3-642-68012-0**

Gill, J.B., Hiscott, R.N., and Vidal, P., 1994. Turbidite geochemistry and evolution of the Izu-Bonin arc and continents. *Lithos,* 33(1–3):135–168. **http://dx.doi.org/10.1016/0024-4937(94)90058-2**

Harris, R.N., Sakaguchi, A., Petronotis, K., Baxter, A.T., Berg, R., Burkett, A., Charpentier, D., Choi, J., Diz Ferreiro, P., Hamahashi, M., Hashimoto, Y., Heydolph, K., Jovane, L., Kastner, M., Kurz, W., Kutterolf, S.O., Li, Y., Malinverno, A., Martin, K.M., Millan, C., Nascimento, D.B., Saito, S., Sandoval Gutierrez, M.I., Screaton, E.J., Smith-Duque, C.E., Solomon, E.A., Straub, S.M., Tanikawa, W., Torres, M.E., Uchimura, H., Vannucchi, P., Yamamoto, Y., Yan, Q., and Zhao, X., 2013. Expedition 344 summary. *In* Harris, R.N., Sakaguchi, A., Petronotis, K., and the Expedition 344 Scientists, *Proceedings of the Integrated Ocean Drilling Program,* 344: College Station, TX (Integrated Ocean Drilling Program). **http://dx.doi.org/10.2204/iodp.proc.344.101.2013**

Hein, J.R., O'Neil, J.R., and Jones, M.G., 1979. Origin of authigenic carbonates in sediment from the deep Bering Sea. *Sedimentology,* 26(5):681–705. **http://dx.doi.org/10.1111/j.1365-3091.1979.tb00937.x**

Hochstaedter, A., Gill, J., Peters, R., Broughton, P., Holden, P., and Taylor, B., 2001. Across-arc geochemical trends in the Izu-Bonin arc: contributions from the subducting slab. *Geochemistry, Geophysics, Geosystems,* 2(7):1019. **http://dx.doi.org/10.1029/2000GC000105**

Hochstaedter, A.G., Gill, J.B., Kusakabe, M., Newman, S., Pringle, M., Taylor, B., and Fryer, P., 1990a. Volcanism in the Sumisu Rift, I. Major element, volatile, and stable isotope geochemistry. *Earth and Planetary Science Letters,* 100(1–3):179–194. **http://dx.doi.org/10.1016/0012-821X(90)90184-Y**

Hochstaedter, A.G., Gill, J.B., and Morris, J.D., 1990b. Volcanism in the Sumisu Rift, II. Subduction and non-subduction related components. *Earth and Planetary Science Letters,* 100(1–3):195–209. **http://dx.doi.org/10.1016/0012-821X(90)90185-Z**

Hochstaedter, A.G., Gill, J.B., Taylor, B., Ishizuka, O., Yuasa, M., and Morita, S., 2000. Across-arc geochemical trends in the Izu-Bonin arc: constraints on source composition and mantle melting. *Journal of Geophysical Research: Solid Earth,* 105(B1):495–512. **http://dx.doi.org/10.1029/1999JB900125**

Houghton, B.F., and Landis, C.A., 1989. Sedimentation and volcanism in a Permian arc-related basin, southern New Zealand. *Bulletin of Volcanology,* 51(6):433–450. **http://dx.doi.org/10.1007/BF01078810**

Ingram, R.L., 1954. Terminology for the thickness of stratification and parting units in sedimentary rocks. *Geological Society of America Bulletin,* 65(9):937–938. **http://dx.doi.org/10.1130/0016-7606(1954)65[937:TFTTOS]2.0.CO;2**

Ishizuka, O., Kimura, J.-I., Li, Y.B., Stern, R.J., Reagan, M.K., Taylor, R.N., Ohara, Y., Bloomer, S.H., Ishii, T., Hargrove, U.S., III, and Haraguchi, S., 2006a. Early stages in the evolution of Izu-Bonin arc volcanism: new age, chemical, and isotopic constraints. *Earth and Planetary Science Letters,* 250(1–2):385–401. **http://dx.doi.org/10.1016/j.epsl.2006.08.007**

Ishizuka, O., Taylor, R.N., Milton, J.A., and Nesbitt, R.W., 2003a. Fluid-mantle interaction in an intraoceanic arc: constraints from high-precision Pb isotopes. *Earth and Planetary Science Letters,* 211(3–4):221–236. **http://dx.doi.org/10.1016/S0012-821X(03)00201-2**

Ishizuka, O., Taylor, R.N., Milton, J.A., Nesbitt, R.W., Yuasa, M., and Sakamoto, I., 2006b. Variation in the mantle sources of the northern Izu arc with time and space—constraints from high-precision Pb isotopes. *Journal of Volcanology and Geothermal Research,* 156(3–4):266–290. **http://dx.doi.org/10.1016/j.jvolgeores.2006.03.005**

Ishizuka, O., Taylor, R.N., Yuasa, M., and Ohara, Y., 2011. Making and breaking an island arc: a new perspective from the Oligocene Kyushu-Palau arc, Philippine Sea. *Geochemistry, Geophysics, Geosystems,* 12(5):Q05005. **http://dx.doi.org/10.1029/2010GC003440**

Ishizuka, O., Uto, K., and Yuasa, M., 2003b. Volcanic history of the back-arc region of the Izu-Bonin (Ogasawara) arc. *In* Larter, R.D., and Leat, P.T. (Eds.), *Tectonic and Magmatic Processes*. Geological Society Special Publication, 219(1):187–205. **http://dx.doi.org/10.1144/GSL.SP.2003.219.01.09**

Ishizuka, O., Uto, K., Yuasa, M., and Hochstaedter, A.G., 1998. K-Ar ages from seamount chains in the back-arc region of the Izu-Ogasawara arc. *Island Arc,* 7(3):408–421. **http://dx.doi.org/10.1111/j.1440-1738.1998.00199.x**

Ishizuka, O., Yuasa, M., and Uto, K., 2002. Evidence of porphyry copper-type hydrothermal activity from a submerged remnant back-arc volcano of the Izu-Bonin arc: implications for the volcanotectonic history of back-arc seamounts. *Earth and Planetary Science Letters,* 198(3–4):381–399. **http://dx.doi.org/10.1016/S0012-821X(02)00515-0**

Jordan, E.K., Lieu, W., Stern, R.J., Carr, M.J., Feigenson, M.D., and Gill, J.B., 2012. Data from: CentAm & IBM Geochem Database version 1.02. *Integrated Earth Data Applications*. **http://dx.doi.org/10.1594/IEDA/100053**

Karátson, D., and Németh, K., 2001. Lithofacies associations of an emerging volcaniclastic apron in a Miocene volcanic complex: an example from the Börzsöny Mountains, Hungary. *International Journal of Earth Sciences,* 90(4):776–794. **http://dx.doi.org/10.1007/s005310100193**

Karig, D.E., and Moore, G.F., 1975a. Tectonic complexities in the Bonin arc system. *Tectonophysics,* 27(2):97–118. **http://dx.doi.org/10.1016/0040-1951(75)90101-8**

Karig, D.E., and Moore, G.F., 1975b. Tectonically controlled sedimentation in marginal basins. *Earth and Planetary Science Letters,* 26(2):233–238. **http://dx.doi.org/10.1016/0012-821X(75)90090-4**

Kennett, J.P., and Thunell, R.C., 1975. Global increase in Quaternary explosive volcanism. *Science,* 187(4176):497–502. **http://dx.doi.org/10.1126/science.187.4176.497**

Kodaira, S., Sato, T., Takahashi, N., Ito, A., Tamura, Y., Tatsumi, Y., and Kaneda, Y., 2007a. Seismological evidence for variable growth of crust along the Izu intraoceanic arc. *Journal of Geophysical Research: Solid Earth,* 112(B5):B05104. **http://dx.doi.org/10.1029/2006JB004593**

Kodaira, S., Sato, T., Takahashi, N., Miura, S., Tamura, Y., Tatsumi, Y., and Kaneda, Y., 2007b. New seismological constraints on growth of continental crust in the Izu-Bonin intra-oceanic arc. *Geology,* 35(11):1031–1034. **http://dx.doi.org/10.1130/G23901A.1**

Kodaira, S., Sato, T., Takahashi, N., Yamashita, M., No, T., and Kaneda, Y., 2008. Seismic imaging of a possible paleoarc in the Izu-Bonin intraoceanic arc and its implications for arc evolution processes. *Geochemistry, Geophysics, Geosystems,* 9(10):Q10X01. **http://dx.doi.org/10.1029/2008GC002073**

Kuno, H., 1959. Origin of Cenozoic petrographic provinces of Japan and surrounding areas. *Bulletin of Volcanology,* 20(1):37–76. **http://dx.doi.org/10.1007/BF02596571**

Littke, R., Fourtanier, E., Thurow, J., and Taylor, E., 1991. Silica diagenesis and its effects on lithification of Broken Ridge deposits, central Indian Ocean. *In* Weissel, J., Peirce, J., Taylor, E., Alt, J., et al., *Proceedings of the Ocean Drilling Program, Scientific Results,* 121: College Station, TX (Ocean Drilling Program), 261–272. **http://dx.doi.org/10.2973/odp.proc.sr.121.179.1991**

Machida, S., and Ishii, T., 2003. Backarc volcanism along the en echelon seamounts: the Enpo Seamount chain in the northern Izu-Ogasawara arc. *Geochemistry, Geophysics, Geosystems,* 4(8):9006. **http://dx.doi.org/10.1029/2003GC000554**

Machida, S., Ishii, T., Kimura, J.-I., Awaji, S., and Kato, Y., 2008. Petrology and geochemistry of cross-chains in the Izu-Bonin back arc: three mantle components with contributions of hydrous liquids from a deeply subducted slab. *Geochemistry, Geophysics, Geosystems*, 9(5):Q05002. **http://dx.doi.org/10.1029/2007GC001641**

Mahood, G.A., and Halliday, A.N., 1988. Generation of high-silica rhyolite: a Nd, Sr, and O isotopic study of Sierra La Primavera, Mexican Neovolcanic Belt. *Contributions to Mineralogy and Petrology,* 100(2):183–191. **http://dx.doi.org/10.1007/BF00373584**

Manville, V., and Wilson, C.J.N., 2004. Vertical density currents: a review of their potential role in the deposition and interpretation of deep-sea ash layers. *Journal of the Geological Society,* 161(6):947–958. **http://dx.doi.org/10.1144/0016-764903-067**

McPhie, J., Doyle, M., and Allen, R., 1993. *Volcanic Textures: A Guide to the Interpretation of Textures in Volcanic Rocks:* Hobart (Tasmanian Government Printing Office).

Meyers, P.A., 1994. Preservation of elemental and isotopic source identification of sedimentary organic matter. *Chemical Geology,* 114(3–4):289–302. **http://dx.doi.org/10.1016/0009-2541(94)90059-0**

Mitchell, S.F., 2000. Facies analysis of a Cretaceous–Paleocene volcaniclastic braid-delta. [presented at the Geological Society of Trinidad and Tobago 2000 SPE Conference and Exhibition, Port of Spain, Trinidad, 10–13 July 2000]. (Paper SS03) **http://archives.datapages.com/data/gstt/SS03F.PDF**

Morse, J.W., and Mackenzie, F.T., 1990. *Geochemistry of Sedimentary Carbonates:* Amsterdam (Elsevier). **http://dx.doi.org/10.1016/S0070-4571(08)70329-7**

Müller, P.J., 1977. C/N ratios in Pacific deep-sea sediments: effect of inorganic ammonium and organic nitrogen compounds sorbed by clays. *Geochimica et Cosmochimica Acta,* 41(6):765–776. **http://dx.doi.org/10.1016/0016-7037(77)90047-3**

Orton, G.J., 1996. Volcanic environments. *In* Reading, H.G. (Ed.), *Sedimentary Environments: Processes, Facies and Stratigraphy:* Oxford, UK (Blackwell Science Publishing), 485–573.

Palmer, B.A., and Walton, A.W., 1990. Accumulation of volcaniclastic aprons in the Mount Dutton Formation (Oligocene–Miocene), Marysvale volcanic field, Utah. *Geological Society of America Bulletin,* 102(6):734–748. **http://dx.doi.org/10.1130/0016-7606(1990)102<0734:AOVAIT>2.3.CO;2**

Pearce, J.A., Reagan, M.K., Stern, R.J., and Petronotis, K., 2013. Izu-Bonin-Mariana fore arc: testing subduction initiation and ophiolite models by drilling the outer Izu-Bonin-Mariana fore arc. *International Ocean Discovery Program Scientific Prospectus,* 352. **http://dx.doi.org/10.14379/iodp.sp.352.2013**

Plank, T., 2014. The chemical composition of subducting sediments. *In* Rudnick, R.L. (Ed.), *Treatise on Geochemistry* (2nd ed.) (Vol. 4): *The Crust*. Holland, H.D., and Turekian, K.K.

(Series Eds.): Oxford, UK (Elsevier), 607–629. **http://dx.doi.org/10.1016/B978-0-08-095975-7.00319-3**

Plank, T., and Langmuir, C.H., 1998. The chemical composition of subducting sediment and its consequences for the crust and mantle. *Chemical Geology,* 145(3–4):325–394. **http://dx.doi.org/10.1016/S0009-2541(97)00150-2**

Reading, H.G., and Richards, M., 1994. Turbidite systems in deep-water basin margins classified by grain size and feeder system. *AAPG Bulletin,* 78(5):792–822. **http://aapgbull.geoscienceworld.org/cgi/content/abstract/78/5/792**

Reagan, M.K., Ishizuka, O., Stern, R.J., Kelley, K.A., Ohara, Y., Blichert-Toft, J., Bloomer, S.H., Cash, J., Fryer, P., Hanan, B.B., Hickey-Vargas, R., Ishii, T., Kimura, J.-I., Peate, D.W., Rowe, M.C., and Woods, M., 2010. Fore-arc basalts and subduction initiation in the Izu-Bonin-Mariana system. *Geochemistry, Geophysics, Geosystems,* 11(3):Q03X12. **http://dx.doi.org/10.1029/2009GC002871**

Richards, M.T., 2009. Deep-marine clastic systems. *In* Emery, D., and Myers, K. (Eds.), *Sequence Stratigraphy:* London (Blackwell Science Publishing), 178–210. **http://dx.doi.org/10.1002/9781444313710.ch9**

Riedel, M., Collett, T.S., and Malone, M., 2010. Expedition 311 synthesis: scientific findings. *In* Riedel, M., Collett, T.S., Malone, M.J., and the Expedition 311 Scientists, *Proceedings of the Integrated Ocean Drilling Program, Expedition,* 311: Washington, DC (Integrated Ocean Drilling Program Management International, Inc.). **http://dx.doi.org/10.2204/iodp.proc.311.213.2010**

Rudnick, R.L., and Gao, S., 2004. Composition of the continental crust. *Treatise on Geochemistry,* 3:1–64. **http://dx.doi.org/10.1016/B0-08-043751-6/03016-4**

Sample, J.C., and Karig, D.E., 1982. A volcanic production rate for the Mariana island arc. *Journal of Volcanology and Geothermal Research,* 13(1–2):73–82. **http://dx.doi.org/10.1016/0377-0273(82)90020-8**

Shipboard Scientific Party, 1995. Background, objectives, and principal results of Madeira Abyssal Plain drilling. *In* Schmincke, H.-U., Weaver, P.P.E., Firth, J.V., et al., *Proceedings of the Ocean Drilling Program, Initial Reports,* 157: College Station, TX (Ocean Drilling Program), 5–10. **http://dx.doi.org/10.2973/odp.proc.ir.157.101.1995**

Scudder, R.P., Murray, R.W., and Plank, T., 2009. Dispersed ash in deeply buried sediment from the northwest Pacific Ocean: an example from the Izu-Bonin arc (ODP Site 1149). *Earth and Planetary Science Letters,* 284(3–4):639–648. **http://dx.doi.org/10.1016/j.epsl.2009.05.037**

Smith, G.A., 1987. Sedimentology of volcanism-induced aggradation in fluvial basins: examples from the Pacific Northwest, U.S.A. *In* Ethridge, F.G., Flores, R.M., and Harvey, M.D. (Eds.), *Recent Developments in Fluvial Sedimentology.* Special Publication—SEPM (Society for Sedimentary Geology), 39:217–228. **http://dx.doi.org/10.2110/pec.87.39.0217**

Smith, G.A., and Landis, C., 1995. Intra-arc basins. *In* Busby, C.J., and Ingersoll, R.V. (Eds.), *Tectonics of Sedimentary Basins:* Oxford, UK (Blackwell Science Publishing), 263–298.

Stern, R.J., Fouch, M.J., and Klemperer, S., 2003. An overview of the Izu-Bonin-Mariana subduction factory. *In* Eiler, J. (Ed.), *Inside the Subduction Factory.* Geophysical Monograph, 138:175–222. **http://dx.doi.org/10.1029/138GM10**

Stow, D.A.V., Reading, H.G., and Collinson, J.D., 1996. Deep seas. *In* Reading, H.G. (Ed.), *Sedimentary Environments: Processes, Facies and Stratigraphy:* Oxford, UK (Blackwell Science Publishing), 395–453.

Straub, S.M., 2003. The evolution of the Izu Bonin-Mariana volcanic arcs (NW Pacific) in terms of major elements. *Geochemistry, Geophysics, Geosystems,* 4(2):1018. **http://dx.doi.org/10.1029/2002GC000357**

Straub, S.M., Goldstein, S.L., Class, C., Schmidt, A., and Gomez-Tuena, A., 2010. Slab and mantle controls on the Sr–Nd–Pb–Hf isotope evolution of the post 42 Ma Izu–Bonin volcanic arc. *Journal of Petrology,* 51(5):993–1026. **http://dx.doi.org/10.1093/petrology/egq009**

Stroncik, N.A., and Schmincke, H.-U., 2002. Palagonite; a review. *International Journal of Earth Sciences,* 91(4):680–697. **http://dx.doi.org/10.1007/s00531-001-0238-7**

Suyehiro, K., Takahashi, N., Ariie, Y., Yokoi, Y., Hino, R., Shinohara, M., Kanazawa, T., Hirata, N., Tokuyama, H., and Taira, A., 1996. Continental crust, crustal underplating, and low-Q upper mantle beneath an oceanic island arc. *Science,* 272(5260):390–392. **http://dx.doi.org/10.1126/science.272.5260.390**

Tamura, Y., 1994. Genesis of island arc magmas by mantle-derived bimodal magmatism: evidence from the Shirahama Group, Japan. *Journal of Petrology,* 35(3):619–645. **http://dx.doi.org/10.1093/petrology/35.3.619**

Tamura, Y., 1995. Liquid lines of descent of island arc magmas and genesis of rhyolites: evidence from the Shirahama Group, Japan. *Journal of Petrology,* 36(2):417–434. **http://dx.doi.org/10.1093/petrology/36.2.417**

Tamura, Y., Busby, C., and Blum, P., 2013. Izu-Bonin-Mariana Rear Arc: the missing half of the subduction factory. *International Ocean Discovery Program Scientific Prospectus,* 350. **http://dx.doi.org/10.2204/iodp.sp.350.2013**

Tamura, Y., Gill, J.B., Tollstrup, D., Kawabata, H., Shukuno, H., Chang, Q., Miyazaki, T., Takahashi, T., Hirahara, Y., Kodaira, S., Ishizuka, O., Suzuki, T., Kido, Y., Fiske, R.S., and Tatsumi, Y., 2009. Silicic magmas in the Izu-Bonin oceanic arc and implications for crustal evolution. *Journal of Petrology,* 50(4):685–723. **http://dx.doi.org/10.1093/petrology/egp017**

Tamura, Y., Ishizuka, O., Aoike, K., Kawate, S., Kawabata, H., Chang, Q., Saito, S., Tatsumi, Y., Arima, M., Takahashi, M., Kanamaru, T., Kodaira, S., and Fiske, R.S., 2010. Missing Oligocene crust of the Izu-Bonin arc: consumed or rejuvenated during collision? *Journal of Petrology,* 51(4):823–846. **http://dx.doi.org/10.1093/petrology/egq002**

Tamura, Y., and Nakamura, E., 1996. The arc lavas of the Shirahama Group, Japan: Sr and Nd isotopic data indicate mantle-derived bimodal magmatism. *Journal of Petrology,* 37(6):1307–1319. **http://dx.doi.org/10.1093/petrology/37.6.1307**

Tamura, Y., Tani, K., Chang, Q., Shukuno, H., Kawabata, H., Ishizuka, O., and Fiske, R.S., 2007. Wet and dry basalt magma evolution at Torishima Volcano, Izu-Bonin arc, Japan: the possible role of phengite in the downgoing slab. *Journal of Petrology,* 48(10):1999–2031. **http://dx.doi.org/10.1093/petrology/egm048**

Tamura, Y., Tani, K., Ishizuka, O., Chang, Q., Shukuno, H., and Fiske, R.S., 2005. Are arc basalts dry, wet, or both? Evidence from the Sumisu Caldera Volcano, Izu-Bonin arc, Japan. *Journal of Petrology,* 46(9):1769–1803. **http://dx.doi.org/10.1093/petrology/egi033**

Tamura, Y., and Tatsumi, Y., 2002. Remelting of an andesitic crust as a possible origin for rhyolitic magma in oceanic arcs: an example from the Izu-Bonin arc. *Journal of Petrology,* 43(6):1029–1047. **http://dx.doi.org/10.1093/petrology/43.6.1029**

Tamura, Y., Tatsumi, Y., Zhao, D., Kido, Y., and Shukuno, H., 2002. Hot fingers in the mantle wedge: new insights into magma genesis in subduction zones. *Earth and Planetary Science Letters,* 197(1–2):105–116. **http://dx.doi.org/10.1016/S0012-821X(02)00465-X**

Tani, K., Fiske, R.S., Dunkley, D.J., Ishizuka, O., Oikawa, T., Isobe, I., and Tatsumi, Y., 2011. The Izu Peninsula, Japan: zircon geochronology reveals a record of intra-oceanic rear-arc magmatism in an accreted block of Izu-Bonin upper crust. *Earth and Planetary Science Letters,* 303(3–4):225–239. **http://dx.doi.org/10.1016/j.epsl.2010.12.052**

Tatsumi, Y., and Stern, R.J., 2006. Manufacturing continental crust in the subduction factory. *Oceanography,* 19(4):104–112. **http://dx.doi.org/10.5670/oceanog.2006.09**

Taylor, B., 1992. Rifting and the volcanic-tectonic evolution of the Izu-Bonin-Mariana arc. *In* Taylor, B., Fujioka, K., et al., *Proceedings of the Ocean Drilling Program, Scientific Results,* 126: College Station, TX (Ocean Drilling Program), 627–651. **http://dx.doi.org/10.2973/odp.proc.sr.126.163.1992**

Taylor, B., Fujioka, K., et al., 1990. *Proceedings of the Ocean Drilling Program, Initial Reports,* 126: College Station, TX (Ocean Drilling Program). **http://dx.doi.org/10.2973/odp.proc.ir.126.1990**

Taylor, R.N., and Nesbitt, R.W., 1998. Isotopic characteristics of subduction fluids in an intra-oceanic setting, Izu-Bonin arc, Japan. *Earth and Planetary Science Letters,* 164(1–2):79–98. **http://dx.doi.org/10.1016/S0012-821X(98)00182-4**

Tollstrup, D., Gill, J., Kent, A., Prinkey, D., Williams, R., Tamura, Y., and Ishizuka, O., 2010. Across-arc geochemical trends in the Izu-Bonin arc: contributions from the subducting slab, revisited. *Geochemistry, Geophysics, Geosystems,* 11(1):Q01X10. **http://dx.doi.org/10.1029/2009GC002847**

Wentworth, C.K., 1922. A scale of grade and class terms for clastic sediments. *Journal of Geology,* 30(5):377–392. **http://dx.doi.org/10.1086/622910**

White, J.D.L., and Busby-Spera, C.J., 1987. Deep marine arc apron deposits and syndepositional magmatism in the Alisitos group at Punta Cono, Baja California, Mexico. *Sedimentology,* 34(5):911–927. **http://dx.doi.org/10.1111/j.1365-3091.1987.tb00812.x**

White, J.D.L., and Houghton, B.F., 2006. Primary volcaniclastic rocks. *Geology* 34(8):677–680. **http://dx.doi.org/10.1130/G22346.1**

Wright, I.C., 1996. Volcaniclastic processes on modern submarine arc stratovolcanoes: side-scan and photographic evidence from Rumble IV and V volcanoes, southern Kermadec arc (SW Pacific). *Marine Geology,* 136(1–2):21–39. **http://dx.doi.org/10.1016/S0025-3227(96)00054-0**

Yamazaki, T., and Stern, R.J., 1997. Topography and magnetic vector anomalies in the Mariana Trough. *JAMSTEC Deep Sea Res.,* 13:31–45.

Yamazaki, T., and Yuasa, M., 1998. Possible Miocene rifting of the Izu–Ogasawara (Bonin) arc deduced from magnetic anomalies. *Island Arc,* 7(3):374–382. **http://dx.doi.org/10.1111/j.1440-1738.1998.00196.x**

Yuasa, M., and Kano, K., 2003. Submarine silicic calderas on the northern Shichito-Iwojima Ridge, Izu-Ogasawara (Bonin) arc, western Pacific. *In* White, J.D.L., Smellie, J.L., and Clague, D.A. (Eds.), *Explosive Subaqueous Volcanism*. Geophysical Monograph, 140:231–243. **http://dx.doi.org/10.1029/140GM15**

**Table T1.** Definition of lithostratigraphic and lithologic units, descriptive intervals, and domains, Expedition 350.

| *JOIDES Resolution* | Typical thickness range (m) | *JOIDES Resolution* data logging spreadsheet context | Traditional sediment drilling | Traditional igneous rock drilling | Comparable nondrilling terminology |
|---|---|---|---|---|---|
| Lithostratigraphic unit | $10^{1}$~$10^{3}$ | One row per unit in "lithostrat" summary tab; numbered I, II, IIa, IIb, III, etc. | Used as specified; however, often referred to as lithologic unit in the past. | Typically not used when only igneous rocks are drilled. | Not specified during field campaign. Formal names need to be approved by stratigraphic commission. |
| Lithologic unit | $10^{-1}$~$10^{1}$ | One row per unit in "lith_unit" summary tab; numbered 1, 2, 3, 4, etc. | Typically not used because descriptive intervals correspond to beds, which are directly summarized in lithostratigraphic units. Similar concept: facies type; however, those are not contiguous. | Often defined previously as lava flows, etc., and used in the sense of a descriptive interval. Enumerated contiguously as Unit 1, 2, 3, etc. As defined here, units may correspond to one or more description intervals. | Sedimentology: group of beds. |
| Descriptive interval | $10^{-1}$~$10^{1}$ | Primary descriptive entity that can be readily differentiated during time available. One row per interval in principal logging tab (lithology specific) | Typically corresponds to beds. If beds are too thin, a thicker interval of "intercalated…" is created, and 2–3 domains describe the characteristics of the different types of thin beds. | Typically corresponds to the lithologic unit. As defined here, a lithologic unit may correspond to one or more description intervals. | Sedimentology: thinnest bed to be measured individually within a preset interval (e.g., 0.2 m, 1 m, 5 m, etc.), which is determined based on time available. |
| Domain | Same as parent descriptive interval | Additional rows per interval in principal logging tab, below the primary description interval row; numbered 1, 2, etc. (with description interval numbered 0) | Describes types of beds in an intercalated sequence can be specified in detail as a group. | Describes multiple lithologies in a thin section or textural domains in a macroscopic description. | Feature description within descriptive interval, as needed. |

**Table T2.** Explanation of nomenclature for extrusive and hypabyssal volcanic rocks.

| Prefix | | Main name | Suffix |
|---|---|---|---|
| 1st: % of phenocrysts | 2nd: relative abundance of phenocrysts | If phyric: | |
| Aphyric (<1%) | Sorted by increasing abundance from left to right, separated by hyphens | Basalt: black to dark gray, typically olivine-bearing volcanic rock | Massive lava: massive core, brecciated or vesiculated flow top and bottom, >1 m thick |
| Sparsely phyric (1%–5%) | | Andesite: dark to light gray, contains pyroxenes and/or feldspar and/or amphibole and is typically devoid of olivine and quartz | Pillow lava: subrounded bodies separated by glassy margins and/or hyaloclastite with radiating fractures 0.2 to 1 m wide |
| Moderately phyric (5%–20%) | | Rhyolite-dacite: light gray to pale white, and/or quartz and/or biotite-bearing volcanic rock | Intrusive sheet: dyke or sill, massive core with unvesiculated chilled margin, from millimeters to several meters thick |
| Highly phyric (>20%) | | | Lithic clast, pumice clast, scoria clast: volcanic or plutonic lapilli or blocks >2 cm, to be defined as sample domain |
| | | If aphyric: | Hyaloclastite: breccia made of glassy fragments |
| | | Basalt: dark colored | Breccia |
| | | Rhyolite: light colored | |

**Table T3.** Relative abundances of volcanogenic material, Expedition 350.

| Volcanic component (%) | Volcaniclastic lithology type | Example A | Example B |
|---|---|---|---|
| 0–25 | Sedimentary | **Sand**, sandstone | **Unconsolidated breccia**, consolidated breccia |
| 25–75 | Tuffaceous | **Tuffaceous sand**, tuffaceous sandstone | **Tuffaceous unconsolidated breccia**, tuffaceous consolidated breccia |
| 75–100 | Volcanic | **Ash**, tuff | **Unconsolidated volcanic breccia**, consolidated volcanic breccia |

Volcanic component percentage are sensu stricto Fisher and Schmincke (1984). Components may include volcanic glass, pumice, scoria, igneous rock fragments, and magmatic crystals. Volcaniclastic lithology types modified from Fisher and Schmincke (1984). Bold particle sizes are nonlithified (i.e., sediment).

**Table T4.** Summary of lithostratigraphic units, Site U1437.

| Unit | Interval | Depth (mbsf) Top | Depth (mbsf) Bottom | Thickness (m) Cored | Thickness (m) Described | Mud/Mudstone Thickness (m) | Mud/Mudstone (%) | Ash/Tuff Thickness (m) | Ash/Tuff (%) | Lapilli tuff, lapillistone, and tuff breccia Thickness (m) | Lapilli tuff, lapillistone, and tuff breccia (%) |
|---|---|---|---|---|---|---|---|---|---|---|---|
| | 350- | | | | | | | | | | |
| I | U1437B-1H-1, 0 cm, to U1437D-28R-2, 112 cm | 0.00 | 682.12 | 682.12 | 433 | 382 | 89 | 48 | 11 | 1 | 0 |
| II | U1437D-28R-2, 112 cm, to 32R-CC, 7 cm | 682.12 | 726.50 | 44.38 | 29 | 7 | 23 | 12 | 40 | 11 | 37 |
| III | U1437D-32R-CC, 7 cm, to 64R-1A, 8 cm | 726.50 | 1017.88 | 291.38 | 222 | 141 | 65 | 76 | 34 | 3 | 1 |
| IV | U1437D-64R-1A, 8 cm, to U1437E-6R-3, 122 cm | 1017.88 | 1120.11 | 78.81 | 59 | 13 | 22 | 31 | 53 | 15 | 25 |
| V | U1437E-6R-3, 122 cm, to 28R-1, 0 cm | 1120.11 | 1320.00 | 192.25 | 142 | 98 | 69 | 21 | 15 | 22 | 16 |
| VI | U1437E-28R-1, 0 cm, to 42R-3, 60 cm | 1320.00 | 1459.80 | 139.80 | 100 | 11 | 11 | 32 | 32 | 57 | 57 |
| VII | U1437E-42R-3, 60 cm, to 79R-3, 83 cm | 1459.80 | 1800.30 | 340.50 | 133 | 0 | 0 | 15 | 11 | 119 | 89 |
| 1 | U1437E-35R-1, 76 cm, to 35R-2, 55 cm | 1388.86 | 1390.07 | | 1.2 | | | | | | |
| | | | | Total: | 1120 | 652 | 59 | 236 | 21 | 228 | 20 |

**Table T5.** Coring summary, Expedition 350.

| Hole | Latitude | Longitude | Water depth (m) | Penetration DSF (m) | Cored interval (m) | Recovered length (m) | Recovery (%) | Drilled interval (m) | Total cores (*N*) | Time on hole (days) | Comments |
|---|---|---|---|---|---|---|---|---|---|---|---|
| U1436A | 32°23.8834′N | 140°21.9284′E | 1775.0 | 150.0 | 150.0 | 71.64 | 48 | | 21 | 2.01 | |
| U1436B | 32°23.8960′N | 140°21.9293′E | 1773.9 | 61.8 | 61.8 | 61.79 | 100 | | 14 | 0.92 | New bit |
| U1436C | 32°23.8734′N | 140°21.9298′E | 1774.5 | 70.4 | 70.4 | 70.38 | 100 | | 18 | 0.94 | |
| U1436D | 32°23.8849′N | 140°21.9419′E | 1774.5 | 62.0 | 22.0 | 22.07 | 100 | 40.0 | 8 | 0.84 | |
| | | Site U1436 totals: | | 344.2 | 304.2 | 225.88 | 87 | 40.0 | 61 | 4.71 | |
| U1437A | 31°47.39′N | 139°01.58′E | 2115.8 | 25.0 | | | 0 | 25.0 | 0 | 0.56 | Jet-in test to 25 mbsf |
| U1437B | 31°47.3911′N | 139°01.5788′E | 2116.1 | 439.1 | 439.1 | 242.63 | 55 | | 55 | 2.84 | Total depth: 439.1 mbsf |
| U1437C | 31°47.3814′N | 139°01.5794′E | 2116.0 | 309.7 | | | 0 | 309.7 | 0 | 1.26 | Left in hole |
| U1437D | 31°47.3872′N | 139°01.5730′E | 2116.0 | 1104.6 | 677.4 | 503.85 | 74 | 427.2 | 72 | 11.32 | |
| U1437E | 31°47.3879′N | 139°01.5914′E | 2115.8 | 1806.5 | 702.5 | 387.45 | 55 | 1104.0 | 76 | 28.47 | |
| | | Site U1437 totals: | | 3684.9 | 1819.0 | 1133.93 | 61 | 1865.9 | 203 | 44.45 | |
| | | Expedition 350 totals: | | | 2123.2 | 1359.81 | | 1905.9 | 264 | 49.16 | |

**Figure F1. A.** Tectonic setting of IBM arc (from Taylor, 1992; Tamura and Tatsumi, 2002). The IBM arc-trench system forms the convergent margin between the Pacific and Philippine Sea plates. Double lines indicate spreading centers, active in the Mariana Trough and relict in the Shikoku and Parece Vela Basins. Izu-Bonin, West Mariana, and Mariana arcs are outlined by the 3 km bathymetric contour, and other basins and ridges are outlined by the 4 km contour. Box shows area of B. **B.** Map of the 16 Quaternary volcanoes on the arc front (from Tamura et al., 2009), showing Expedition 350 site positions (Site U1436 in fore arc and Site U1437 in rear arc) and previous ODP site locations. Dotted line along arc front indicates locations of 103 ocean-bottom seismometers, deployed at ~5 km intervals (Kodaira et al., 2007a, 2007b); for profile see Figure F5.

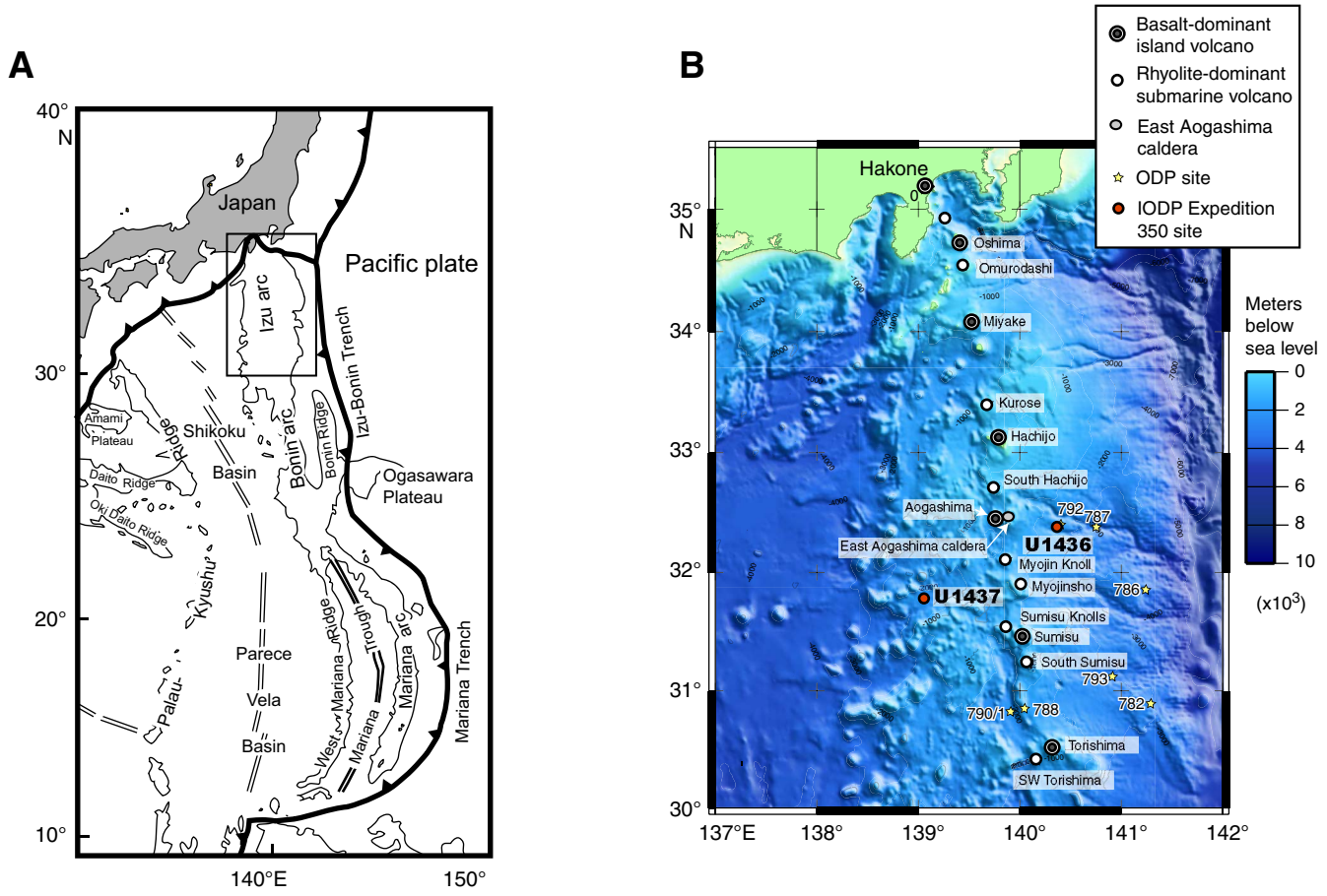

**Figure F2.** Evolution of IBM arc and adjacent Philippine Sea (from Ishizuka et al., 2011). **A.** ~40–35 Ma arc rocks are shown as the Eocene arc and the Kyushu-Palau arc. Also shown: Cretaceous crust in the north and seafloor spreading (West Philippine Basin) and mantle plume magmatism (Oki-Daito) in the south. **B.** 35–25 Ma: arc magmatism continues along the front and rear of the Kyushu-Palau arc, whereas seafloor spreading in the West Philippine Basin wanes but Oki-Daito plume influence extends to the southern part of the Kyushu-Palau arc. **C.** Kyushu-Palau arc is rifted penecontemporaneously along its length, and seafloor spreading begins in the Shikoku and Parece Vela Basins by ~25 Ma, separating the rear arc from the arc front and producing the Kyushu-Palau Ridge remnant arc. **D.** ~22–17 Ma: spreading of Shikoku and Parece Vela Basins. **E.** 17–6 Ma: Neogene IBM arc front roughly coincides with the Paleogene arc front with the active rear arc behind it.

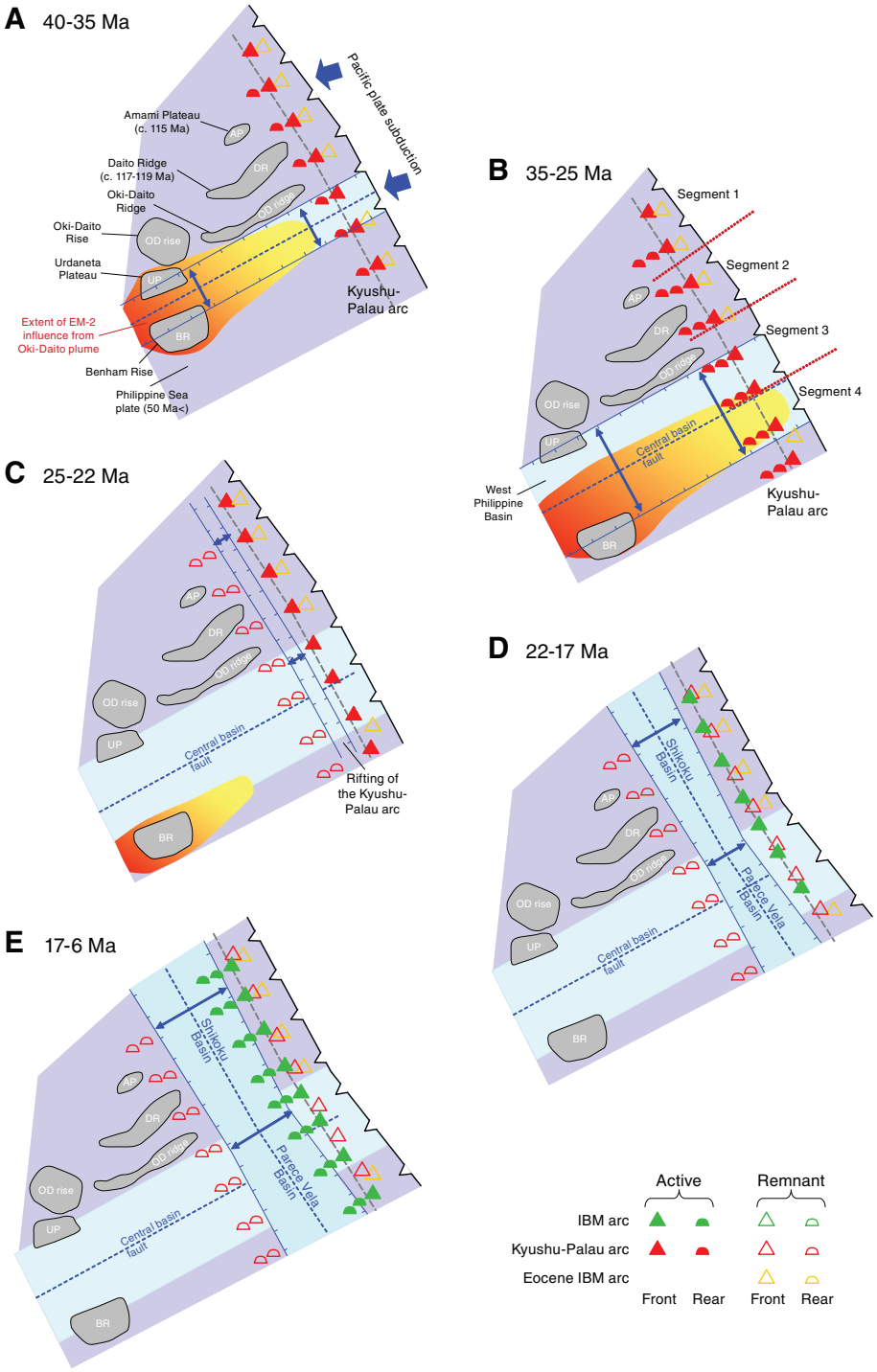

**Figure F3.** Bathymetric features of the eastern Philippine Sea, IBM arc system, and Expedition 350 (Site U1436 in fore arc and Site U1437 in rear arc) and 351 and 352 sites positions. Dashed lines = wide-angle seismic profiles; the north–south seismic profiles (along the present-day volcanic front and rear arc ~150 km west of the volcanic front) are shown in Figure F5. The lines of circles = conspicuous north–south rows of long-wavelength magnetic anomalies, attributed to loci of Oligocene magmatic centers by Yamazaki and Yuasa (1998). Site U1436 is on the fore-arc anomaly (fore arc high/Shin-Kurose Ridge); Site U1437 is on the rear-arc anomaly (Nishi-shichito Ridge).

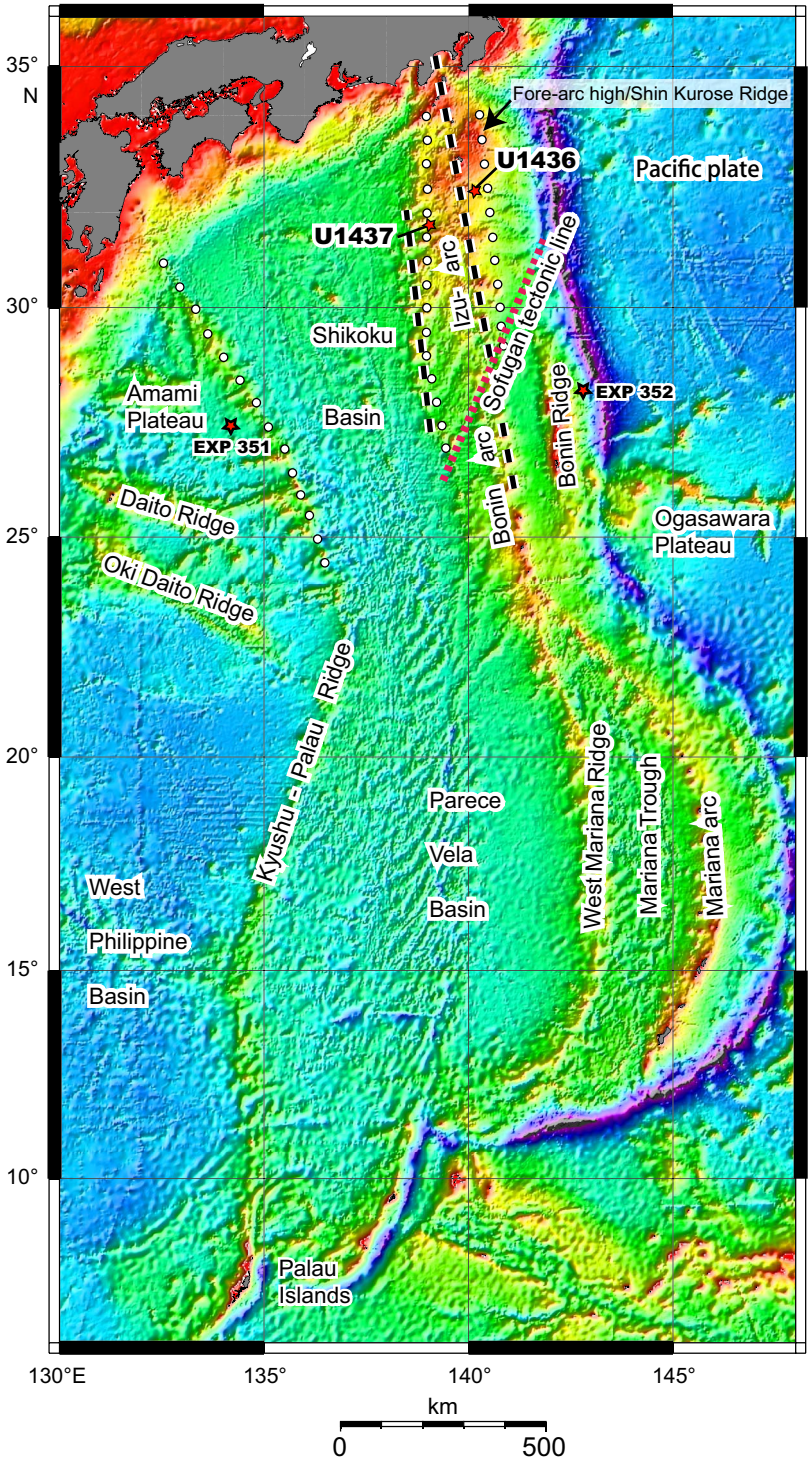

**Figure F4.** Location of wide-angle seismic profile along the rear arc (red line) 150 km west of the present-day volcanic front (profile shown in Fig. F5). Black line shows location of a wide-angle seismic profile along the Izu arc front (Kodaira et al., 2007b; also shown in Fig. F5). A–E = rear-arc segments with thick middle crust matched to arc-front segments. Kodaira et al. (2008) interpret the Nishi-shichito Ridge in the rear arc as a paleo-arc that was obliquely rifted off of the arc front, with an extension direction parallel to the Sofugan Tectonic Line (SFG-TL), which forms the tectonic boundary between the Izu and Bonin arcs (Fig. F3). Images from Kodaira et al. (2008). Hcj = Hachijo-jima, Ags = Aoga-shima, Sms = South Sumisu, Tsm = Torishima, Tnp = Tempo Seamount, Omc = Omachi Seamount.

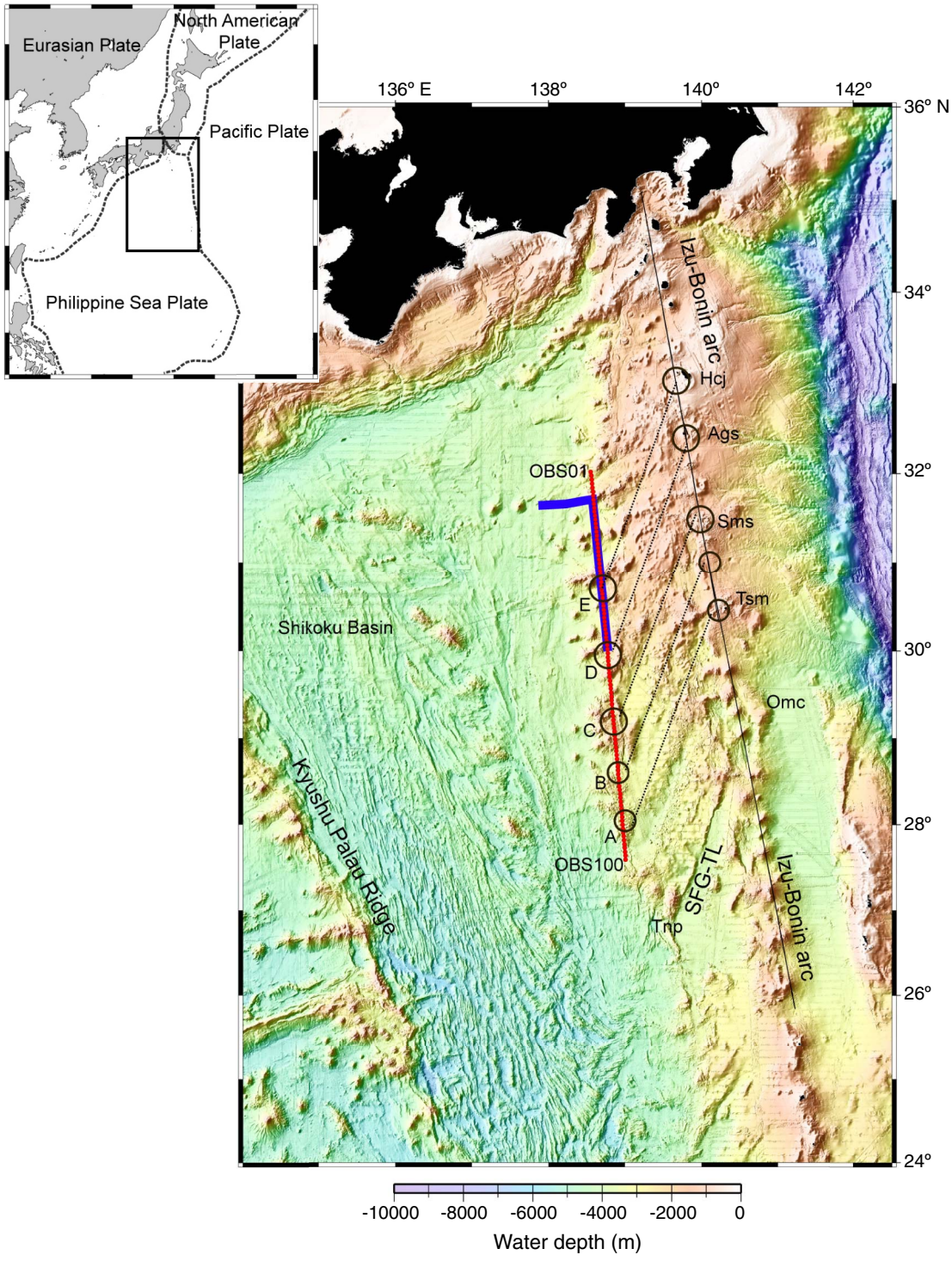

**Figure F5.** Wide-angle seismic profiles (Kodaira et al., 2008) showing middle-crust thickness variation beneath volcanic front/arc front and along rear-arc Nishi-shichito Ridge used to infer that rear-arc crust was obliquely rifted off the arc front (Fig. F4), probably during the opening of the Shikoku and Parece Vela Basins (~25 Ma; Fig. F2C). The 6.0–6.8, 7.1–7.3, and 7.8 km/s layers correspond to middle crust, lower crust, and upper mantle, respectively. Basalt-dominant Quaternary volcanoes on volcanic front: Mi = Miyake, Ha = Hachijo, Ao = Aogashima, Su = Sumisu, To = Torishima; andesite Oligocene volcano east of front: Om = Omachi Seamount. ODP Sites 787, 792, and 793 also shown.

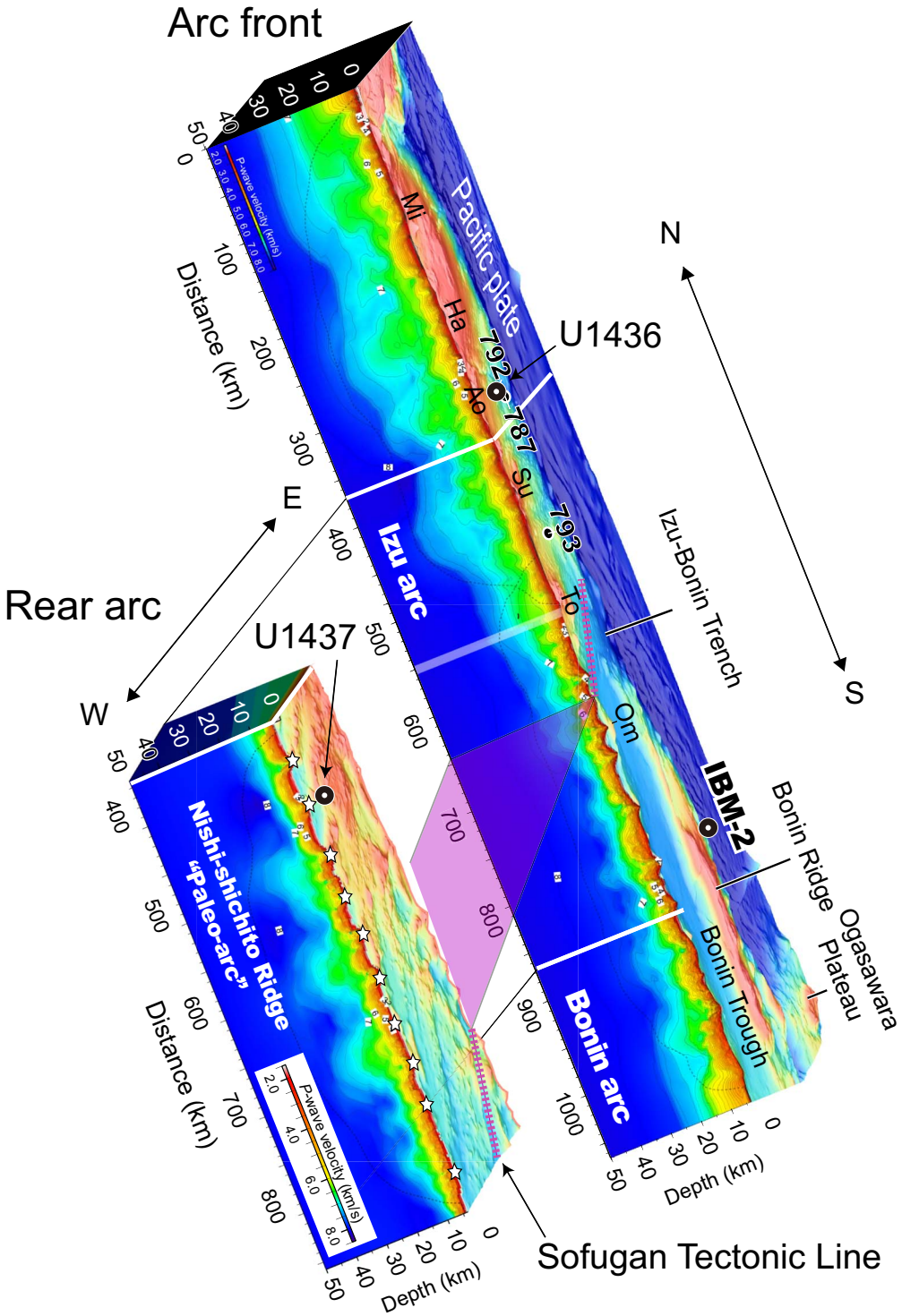

**Figure F6.** Volcano-tectonic domains within Izu arc. The well-defined arc (volcanic) front is formed of the largest volcanoes, including island volcanoes, the largest are named here. Arc crust underlays the region behind the arc front (i.e., west of the arc, farther from the trench), the rear arc, which is bounded to the west by the Shikoku Basin, which is floored by oceanic crust. The rear arc is divided into tectonic zones, from west to east (also oldest to youngest): (1) rear-arc seamount chains (~100 km long; ~17–3 Ma) span basalt to rhyolite compositional range (Fig. F12A); (2) extensional zone (~100 km wide; <3 Ma) overlaps the eastern half of the rear-arc seamount chains and is characterized by ~north–south normal faults with small bimodal volcanoes (back-arc knolls); and (3) active rift, a narrower extensional zone that consists of a series of north–south rift basins immediately behind the arc front, also with bimodal volcanoes. Magmatism in the active rifts and extensional zone is referred to as rift-type magmas and in the rear-arc seamount chains as rear-arc seamount chain–type magmas. White stars = Site U1436 (fore arc) and Site U1437 (rear arc). Box = area of Figure F22.

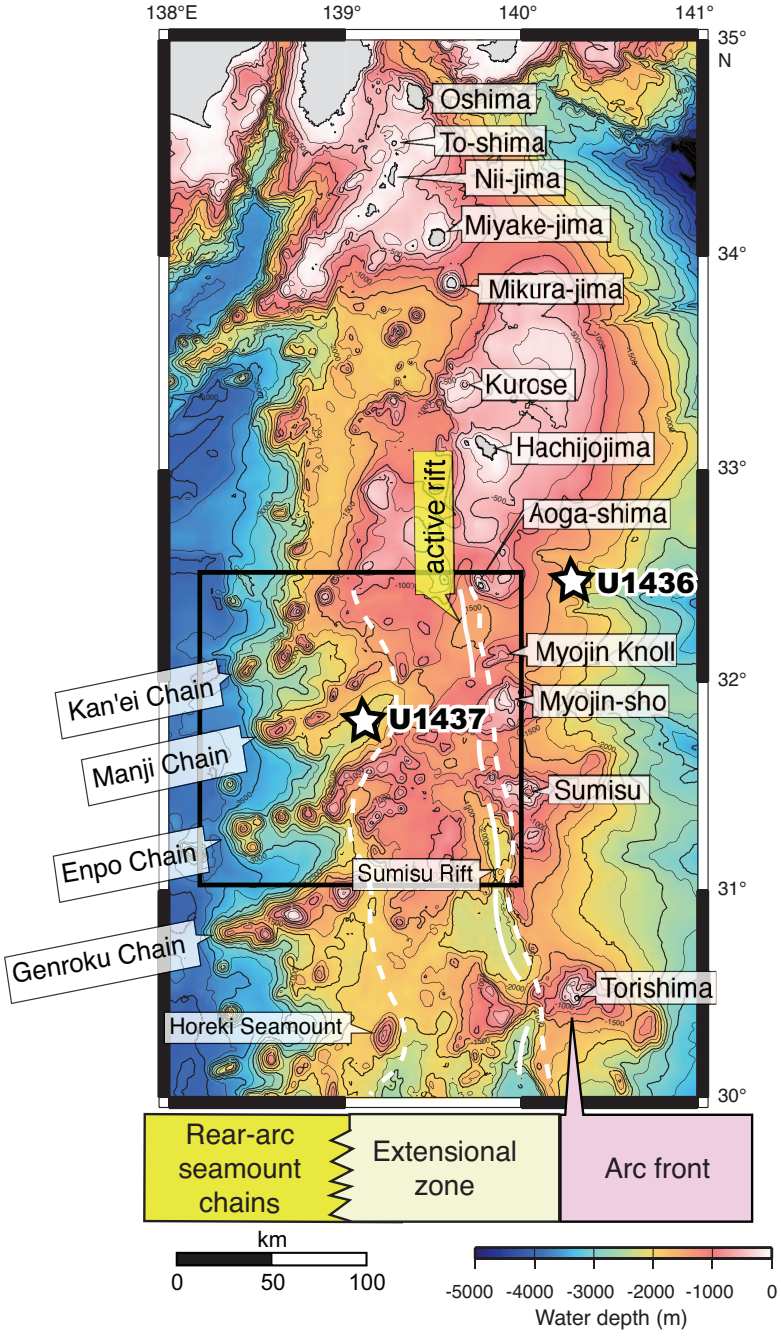

**Figure F7. A.** Time-migrated MCS Section IBM4-EW5 E-W profile through proposed Site IBM-4 (M. Yamashita, pers. comm., 2014). In order to better image the intracrustal structure and to precisely define the upper/middle crust boundary beneath Site IBM-4, seismic experiments were conducted in 2008 using the JAMSTEC's R/V *Kairei* (KR08-09) to deploy a wide-angle OBS array with 1 km intervals. iso-$V_P$ contours of 5 and 6 km/s are inferred to represent upper crust and middle crust, respectively. **B.** Lithostratigraphic Units I–VI described from ODP Site 792 (Taylor et al., 1992) and inferred intracrustal structure below 886 mbsf.

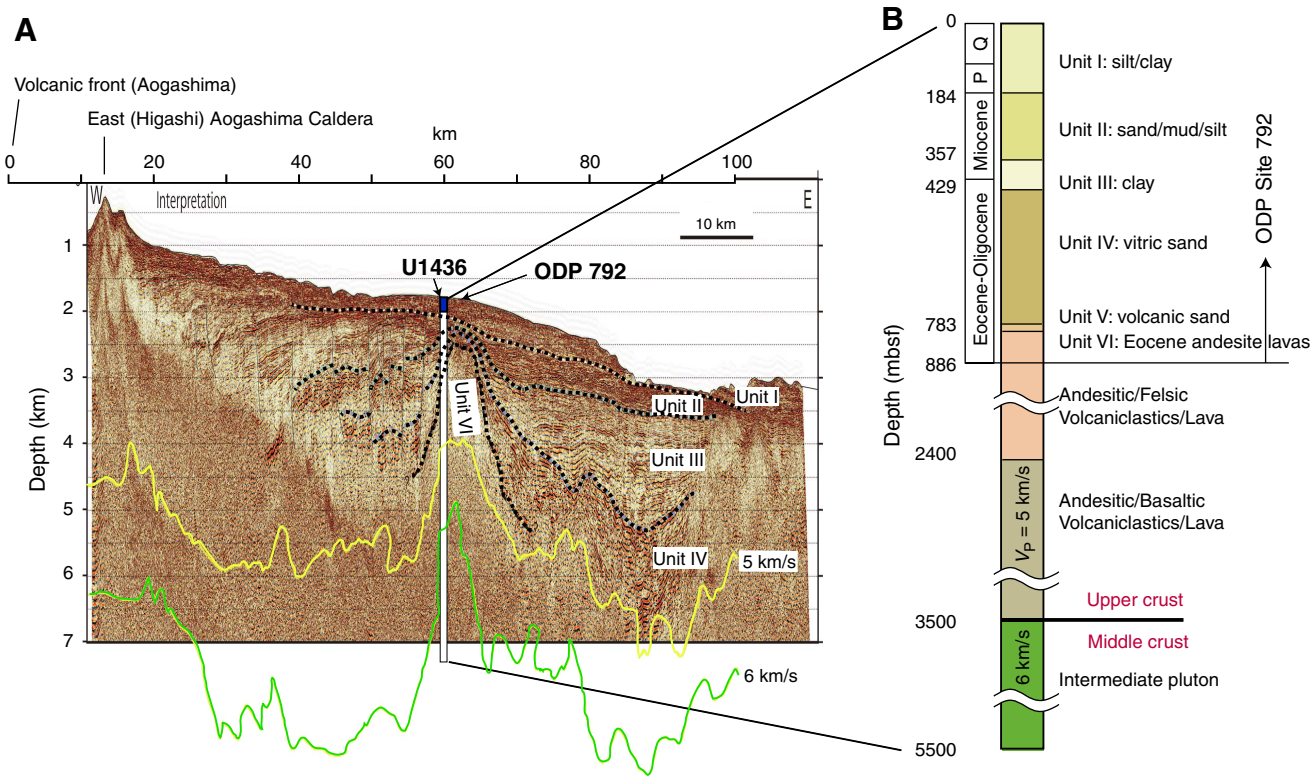

**Figure F8.** Periodic variation in average crustal thickness (wavelength ~ 80–100 km) (modified from Tamura et al., 2009). **A.** Dotted line = along-arc crustal structure (thickness of middle crust with $V_P$ = 6.0–6.8 km/s at 5–20 km depths) and solid squares = average $SiO_2$ content of volcanic rocks sampled and dredged from the 16 Izu arc Quaternary volcanoes (Fig. F1B). The basalt-dominant island volcanoes produce small volumes of rhyolites referred to as R1 by Tamura et al. (2009). Rhyolite-dominant submarine volcanoes erupt mostly rhyolite that is compositionally distinct from R1, referred to as R2 by Tamura et al. (2009). **B.** Schematic crustal structure of the Izu volcanic front showing basalt-dominant island and rhyolite-dominant submarine volcanoes of South Hachijo, Myojin Knoll, and Myojinsho, which have thick and thin middle crust and erupt R1 and R2 rhyolite, respectively.

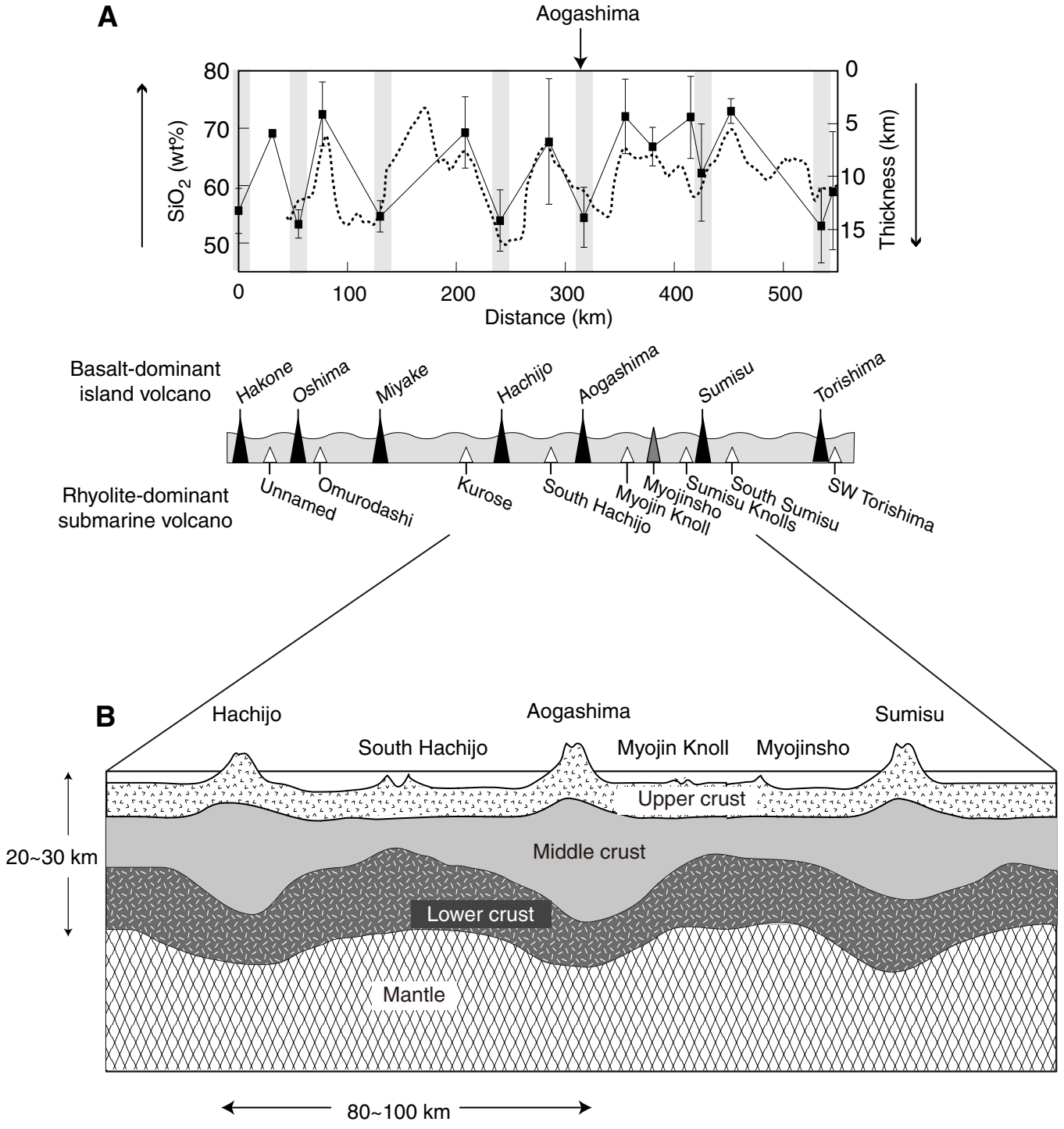

**Figure F9.** Sr, Nd, and Pb isotopes from basalt- and rhyolite-dominated volcanoes along the Izu arc front (modified from Tamura et al., 2007, 2009, and data sources cited therein: Taylor and Nesbitt, 1998, Ishizuka et al., 2003a, 2003b, Tamura et al., 2005, 2007). Volcano location from Figure **F1B.** Lava from active rifts (behind volcanic front) and from rear-arc volcanoes is also shown.

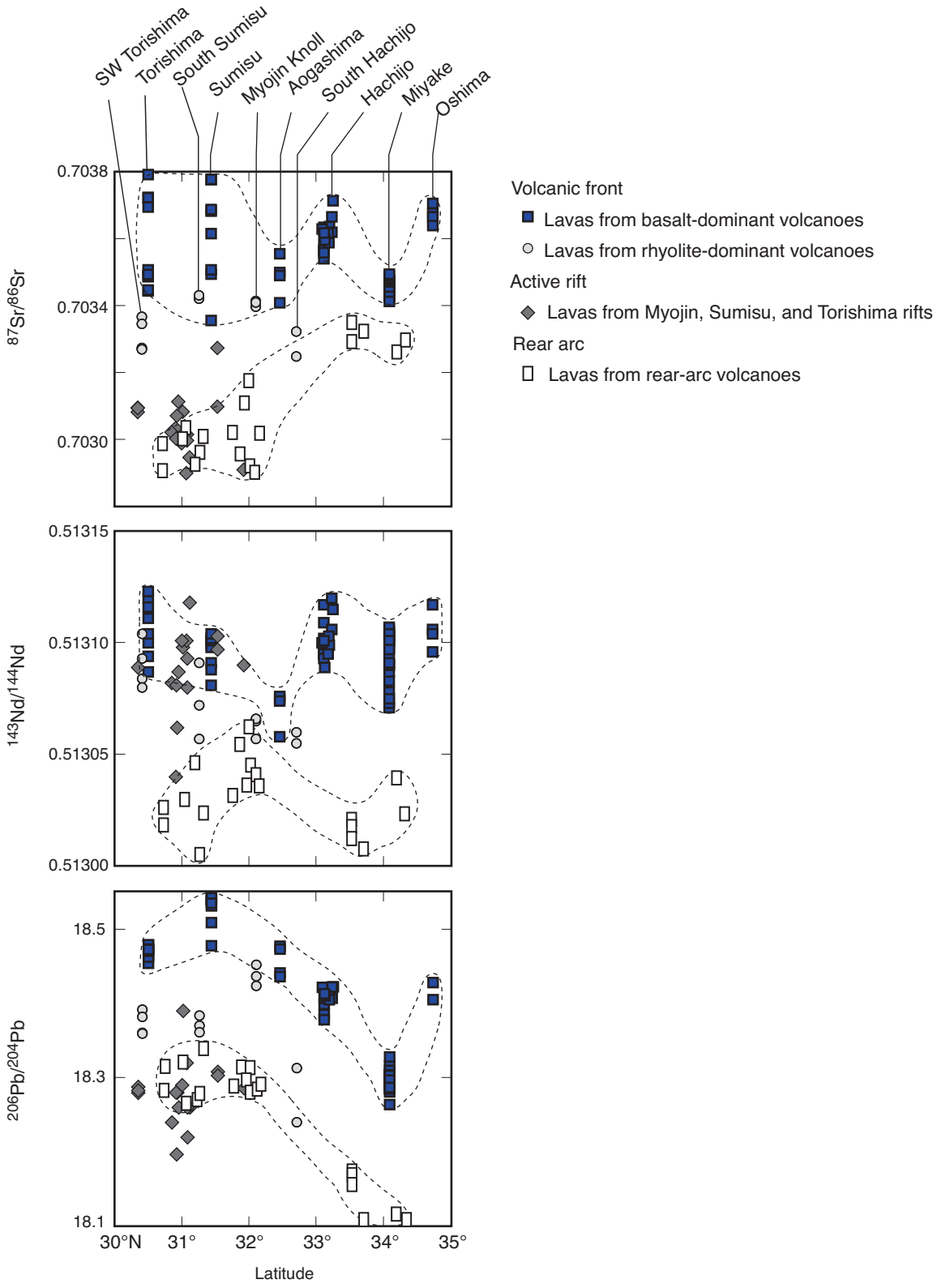

**Figure F10.** Wide-angle seismic profile across Izu arc with *P*-wave velocities for upper, middle, and lower crust (greens) and for mantle (blues) (Suyehiro et al., 1996). ODP and IODP sites are projected onto this line of section. Site U1437 is the first site drilled in the broad region of long-lived rear-arc seamount chains (shown on Fig. F4). ODP Site 791 is also in the rear arc, but it is a narrow, young, active Sumisu rift (see Fig. F4). Site U1436 and ODP Sites 792, 793, and 786 are in the modern fore arc. MORB = mid-ocean-ridge basalt.

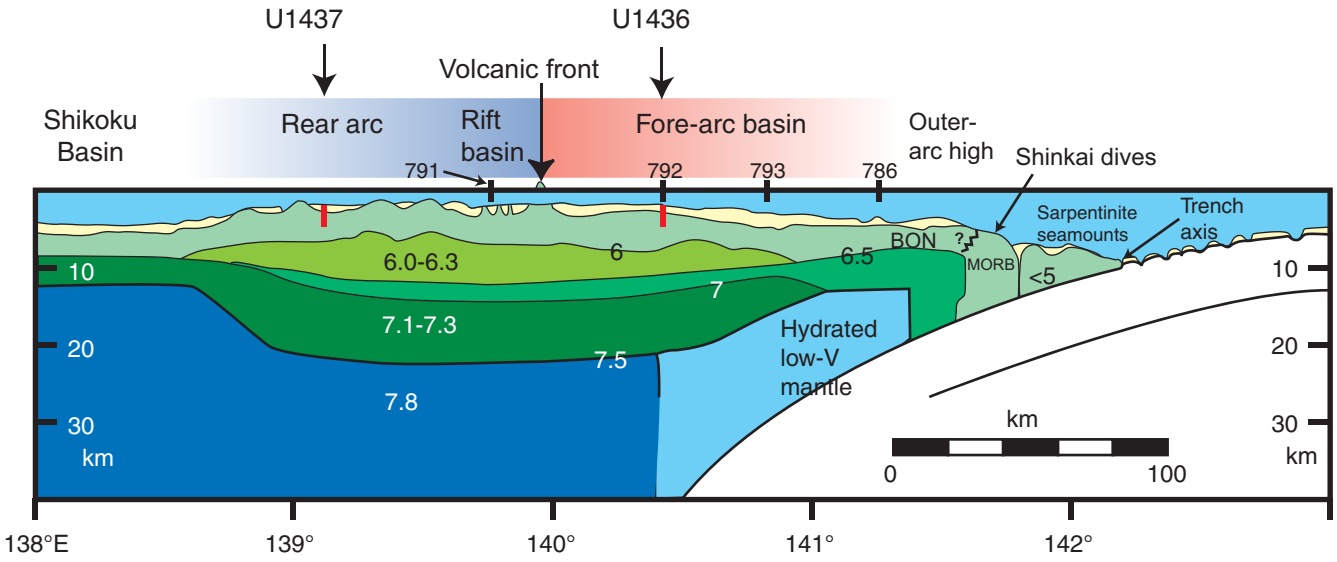

**Figure F11.** Hot fingers hypothesis of Tamura et al. (2002) proposed for NE Japan but suggested for Izu rear-arc seamount chains. Hypothetically, mantle convection above the subducting slab produces fingerlike hot regions in the mantle wedge below the rear-arc plate, and these extend toward the arc front with time.

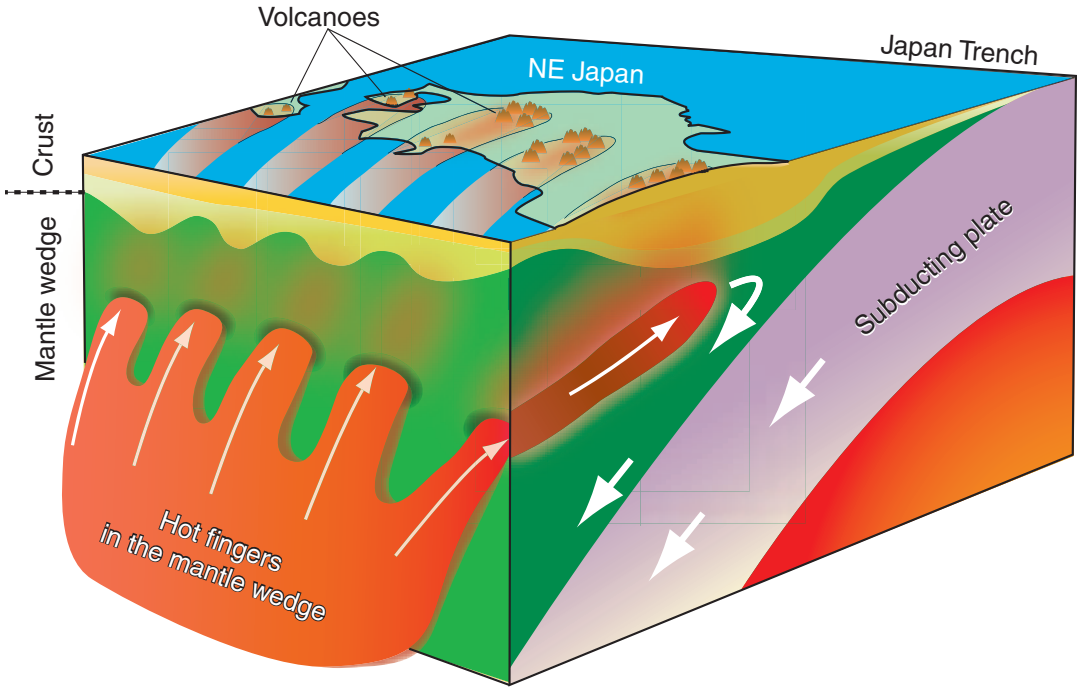

**Figure F12. A.** $K_2O$ vs. $SiO_2$ of Izu arc front lava compared with those of the rear-arc seamount chains. Average continental crust from Rudnick and Gao (2004). **B.** Chondrite-normalized rare earth element abundances of Izu arc front lava compared with those of the rear-arc seamount chain. In both A and B, rear-arc seamount chain patterns are similar to average continental crust. Figure modified from Tamura et al. (2007 and references therein)

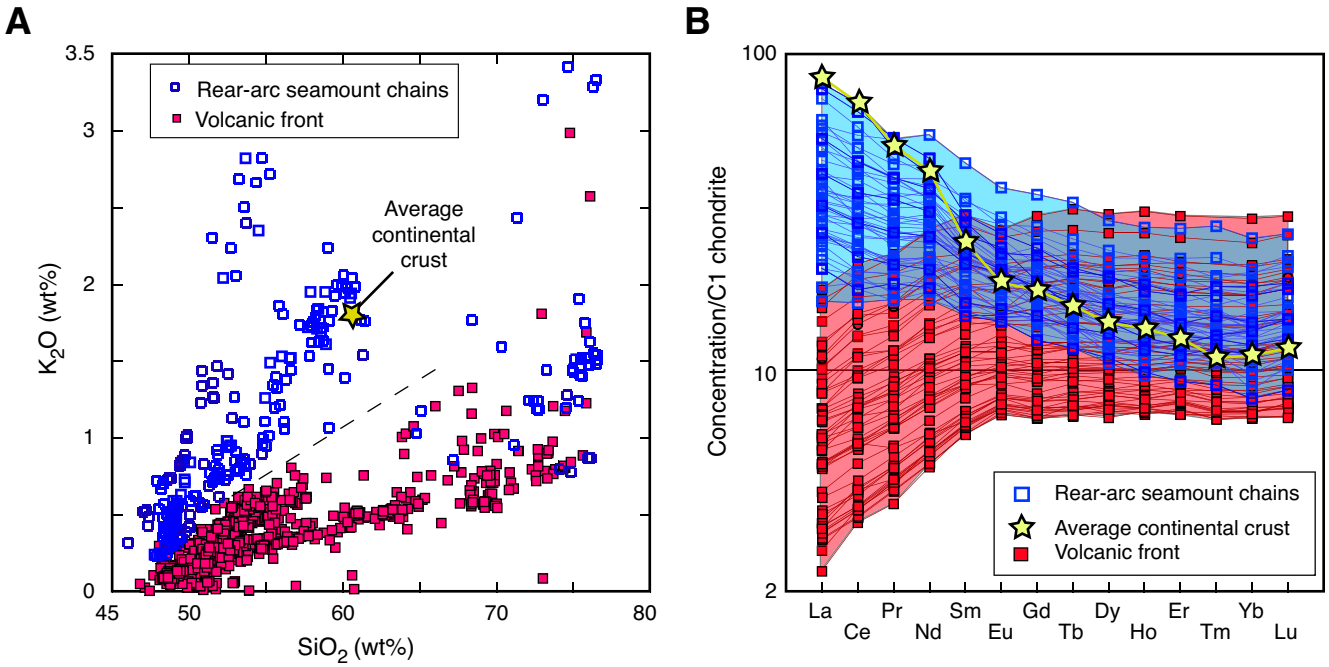

**Figure F13.** Two hypotheses for the evolution of Izu arc crust: from the beginning and from the middle. Red = crust rich in fluid-mobile recycled slab components and strongly depleted in mantle-derived fluid-immobile elements typical of the modern arc front; blue = crust created where diminished slab signature and lower degrees of mantle melting producing crust enriched in mantle-derived fluid immobile elements typical of the rear-arc seamount chains, which are more similar to average continental crust than are arc front magmas (Fig. F12). Thus, the Neogene Izu arc is asymmetric in geochemical characteristics. In the "from the beginning" hypothesis, the geochemical asymmetry has always existed; in the "from the middle" hypothesis, the asymmetry developed over time. Each model has implications for the mechanisms involved in generation of arc magmas and of continental crust.

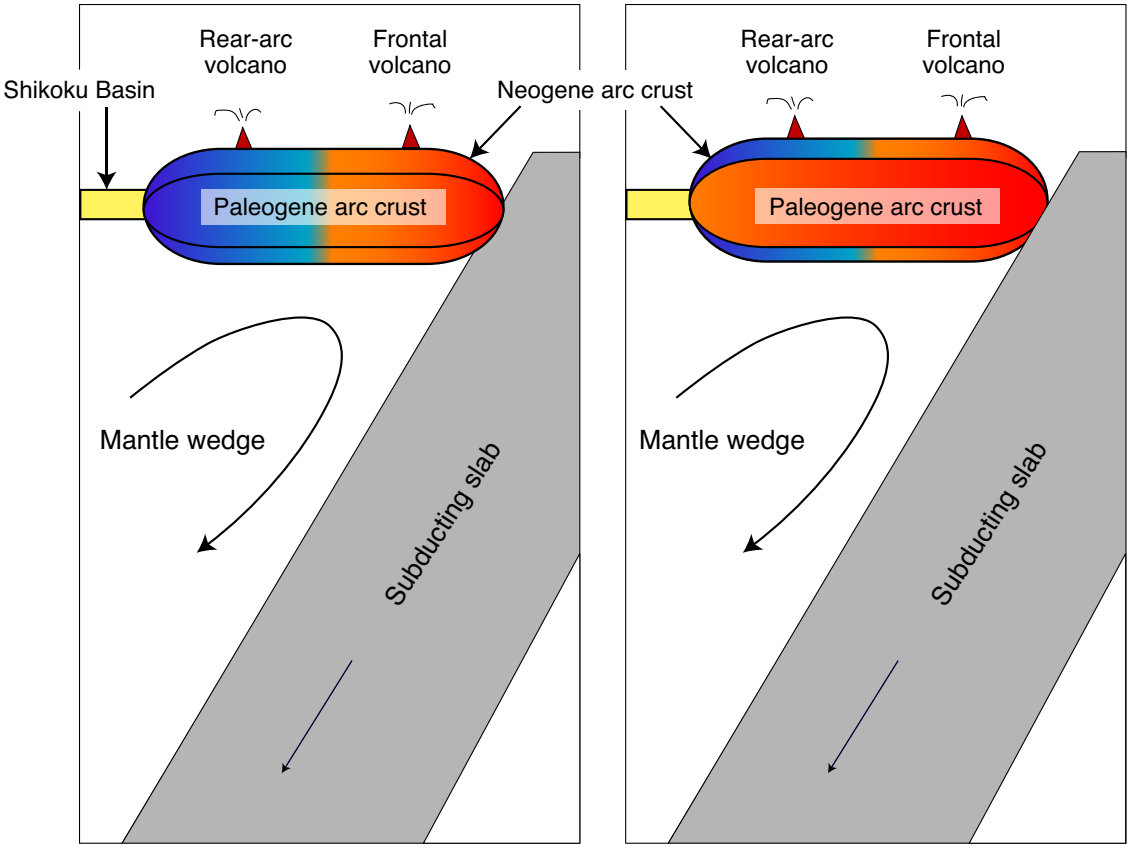

**Figure F14.** Two main basin types recognized within arcs, as defined by Smith and Landis (1995). **A.** Volcano-bounded basin: small, irregular basins between individual volcanoes; larger linear troughs between volcanic chains; and thick basin fill preserved only in oceanic arcs, below sea level. Low areas between the series of rear-arc seamount chains shown on Figure F11 are volcano-bounded basins formed during growth of the chains at ~17–3 Ma. Site U1437 is located in one of these, which we refer to as the Enpo-Manji Basin (Fig. F15A). **B.** Fault-bounded basin: rapidly subsiding basins, deep (up to 10 km) with very high sediment accumulation rates (~1 km/My), and in continental and oceanic arcs. A fault-bounded basin is currently forming in the <1.5 Ma active rift (Fig. F6), and the broader zone of extension (<3 Ma) produced faults within the eastern half of the volcano-bounded basins between the rear-arc seamount chains (some visible on Fig. F15B); however, the bounding volcanic chains (not the <3 Ma extensional zone faults) exerted the primary control on accommodation in the basin drilled at Site U1437 (Fig. F15A).

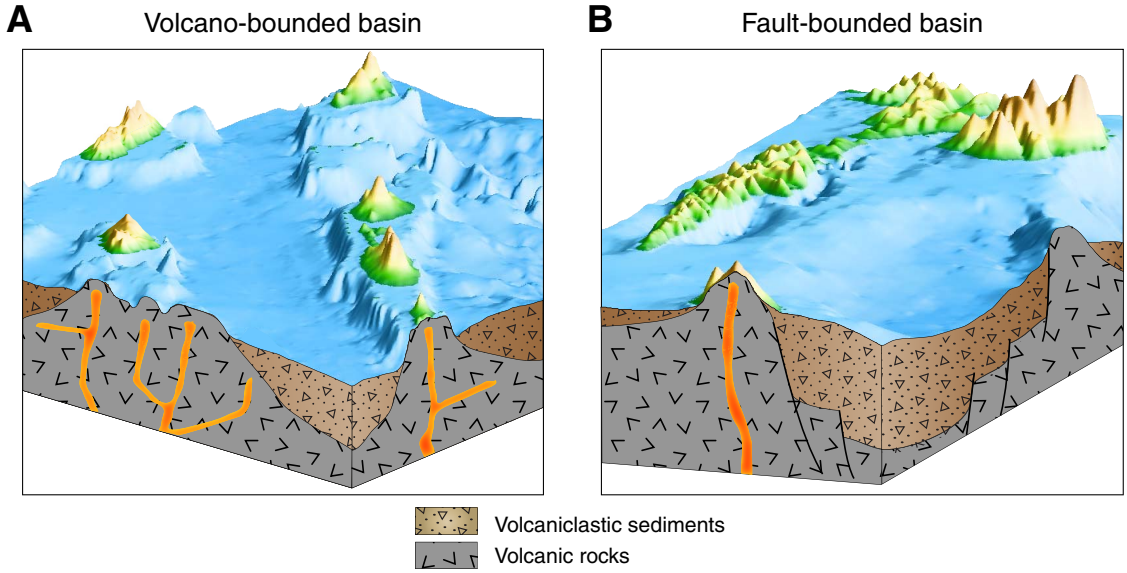

**Figure F15. A.** Seismic Line IBM3-NW5 (see Fig. F22B) (M. Yamashita, per. comm., 2014) runs from the Manji rear-arc seamount chain (northwest) to the Enpo rear-arc seamount chain (southeast). The two volcanic chains are separated by a volcano-bounded basin, herein named the Enpo-Manji Basin. Manji has $^{40}Ar/^{39}Ar$ ages of 6.86 and 6.53 Ma, and the unnamed southeast volcano has a $^{40}Ar/^{39}Ar$ age of 1.96 Ma (see Fig. F22A). **B.** Interpreted seismic layers in the Enpo-Manji Basin.

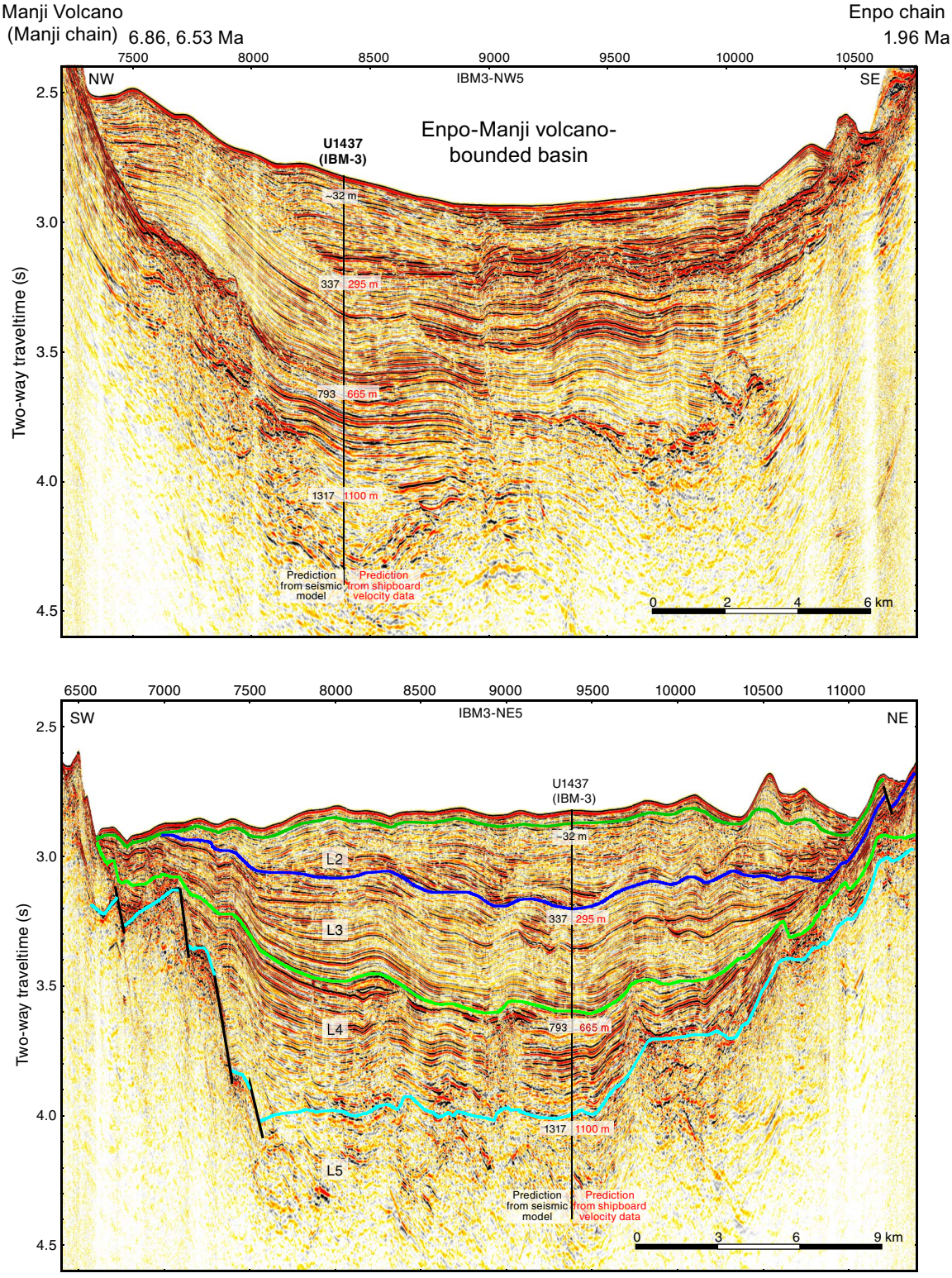

**Figure F16. A.** New sedimentary and volcaniclastic lithology naming conventions based on relative abundances of grain and clast types. Principal lithology names are compulsory for all intervals. Prefixes are optional except for "tuffaceous" lithologies. Suffixes are optional and can be combined with any combination of prefix/principal name. First-order division is based on abundance of volcanic-derived grains and clasts: >25% volcanic grains is either "volcanic" (>75% volcanic grains; named from grain size classification of Fisher and Schmincke, 1984 [orange]) or "tuffaceous" (25%–75% volcanic grains). Tuffaceous lithologies: if dominant nonvolcanic grain component is siliciclastic, the grain size classification of Wentworth (1922; green) was used; if not siliciclastic, it is named by the dominant type of carbonate, chemical, or biogenic grain (blue). 0%–25% volcanic grains are classified as nonvolcanic and treated similarly to tuffaceous lithologies: when nonvolcanic siliciclastic sediment dominates, the grain size classification of Wentworth (1922; green) is used; when the combined carbonate, other chemical, and biogeneic sediment dominate, the principal lithology is taken from the dominant component type (blue). Closely intercalated intervals can be grouped as domains to avoid repetitive entry at the small-scale level. (Continued on next page.)

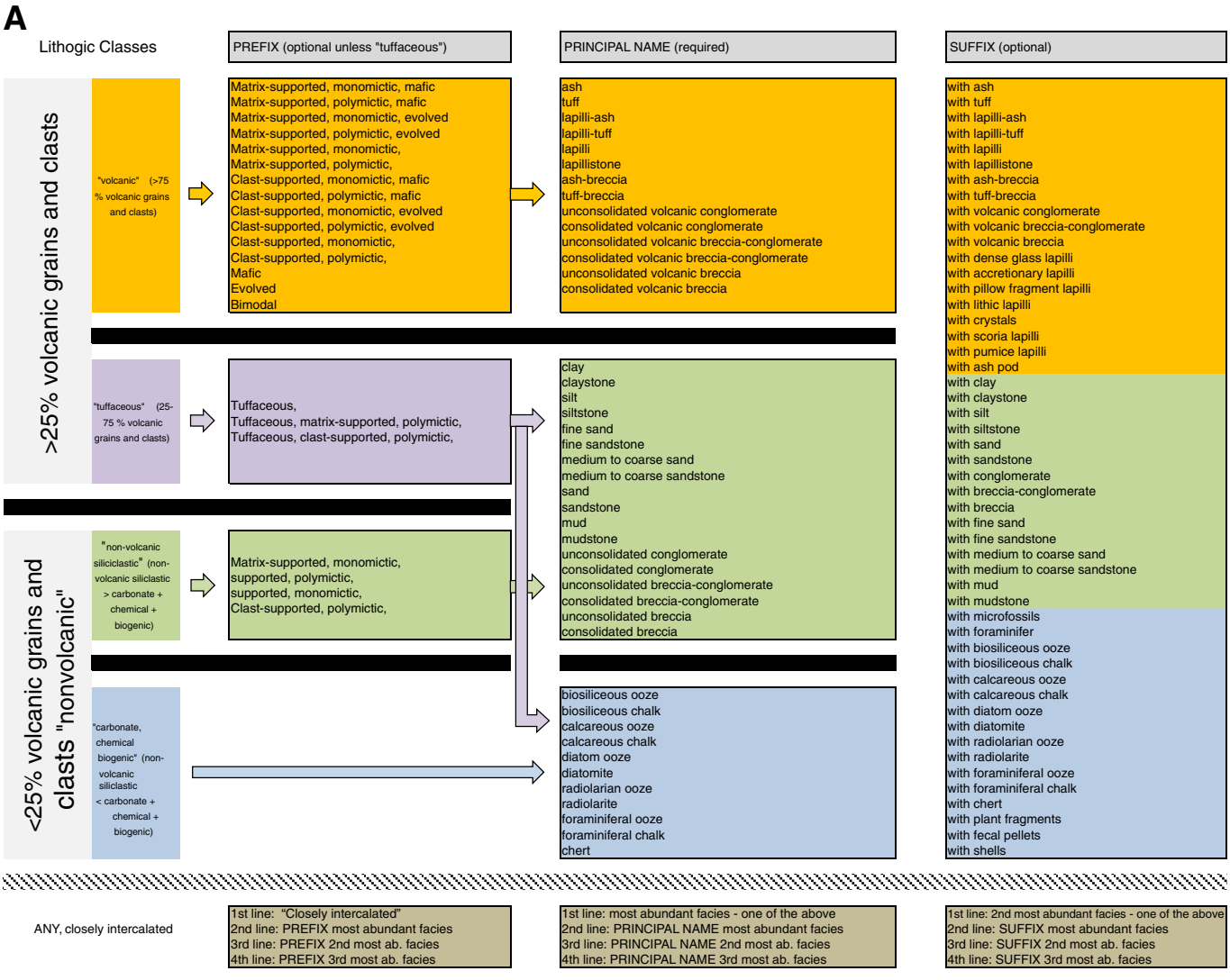

**Figure F16 (continued). B.** Ternary diagram of volcaniclastic grain size terms and their associated sediment and rock types (modified from Fisher and Schmincke, 1984).

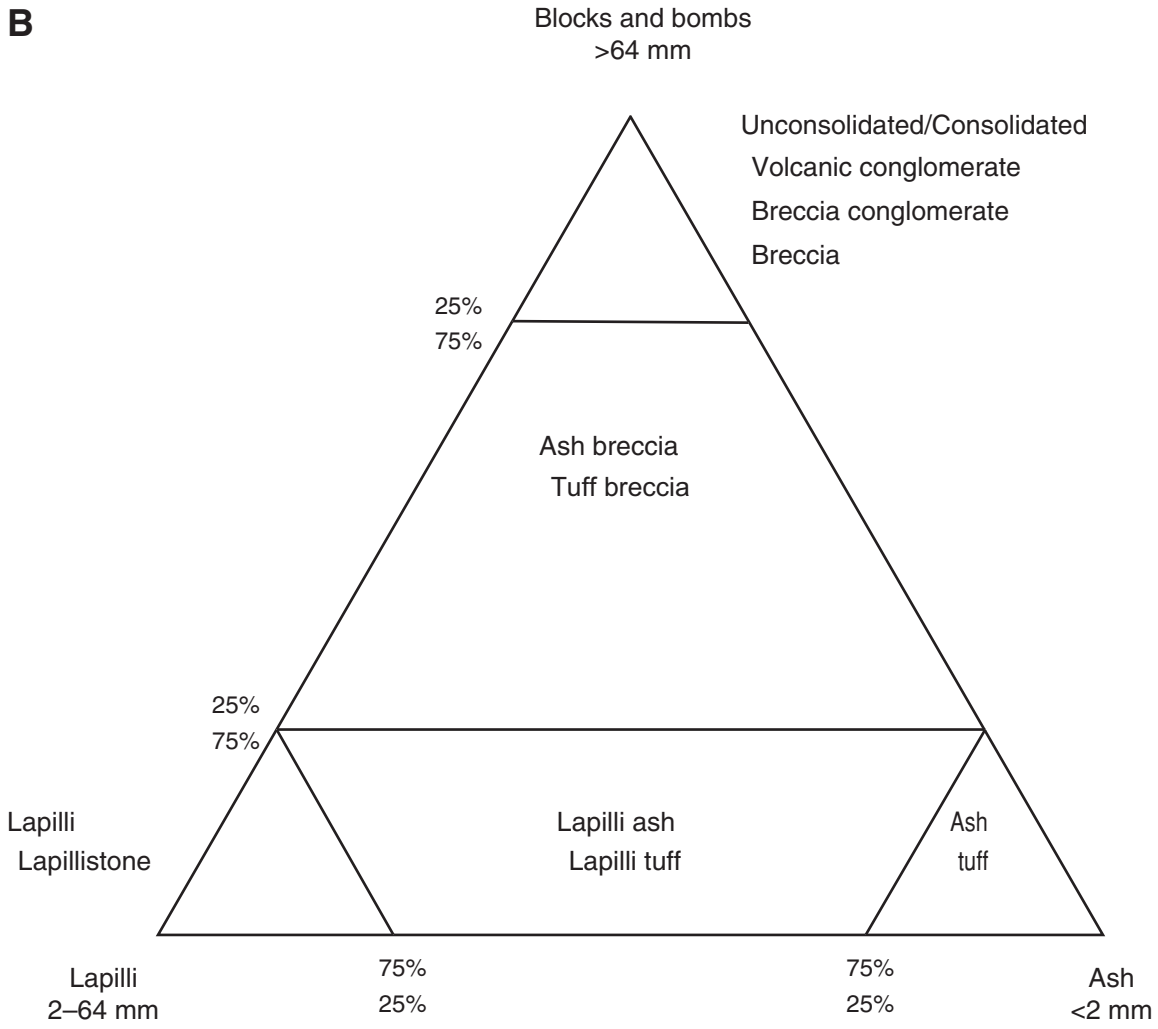

**Figure F17.** Location of Site U1436 (proposed Site IBM-4GT) and ODP Sites 792, 786, and 787. Site U1436 lies 60 km east of Aogashima, an arc-front mafic volcano that forms a small inhabited island. East of that is the East Aogashima submarine caldera.

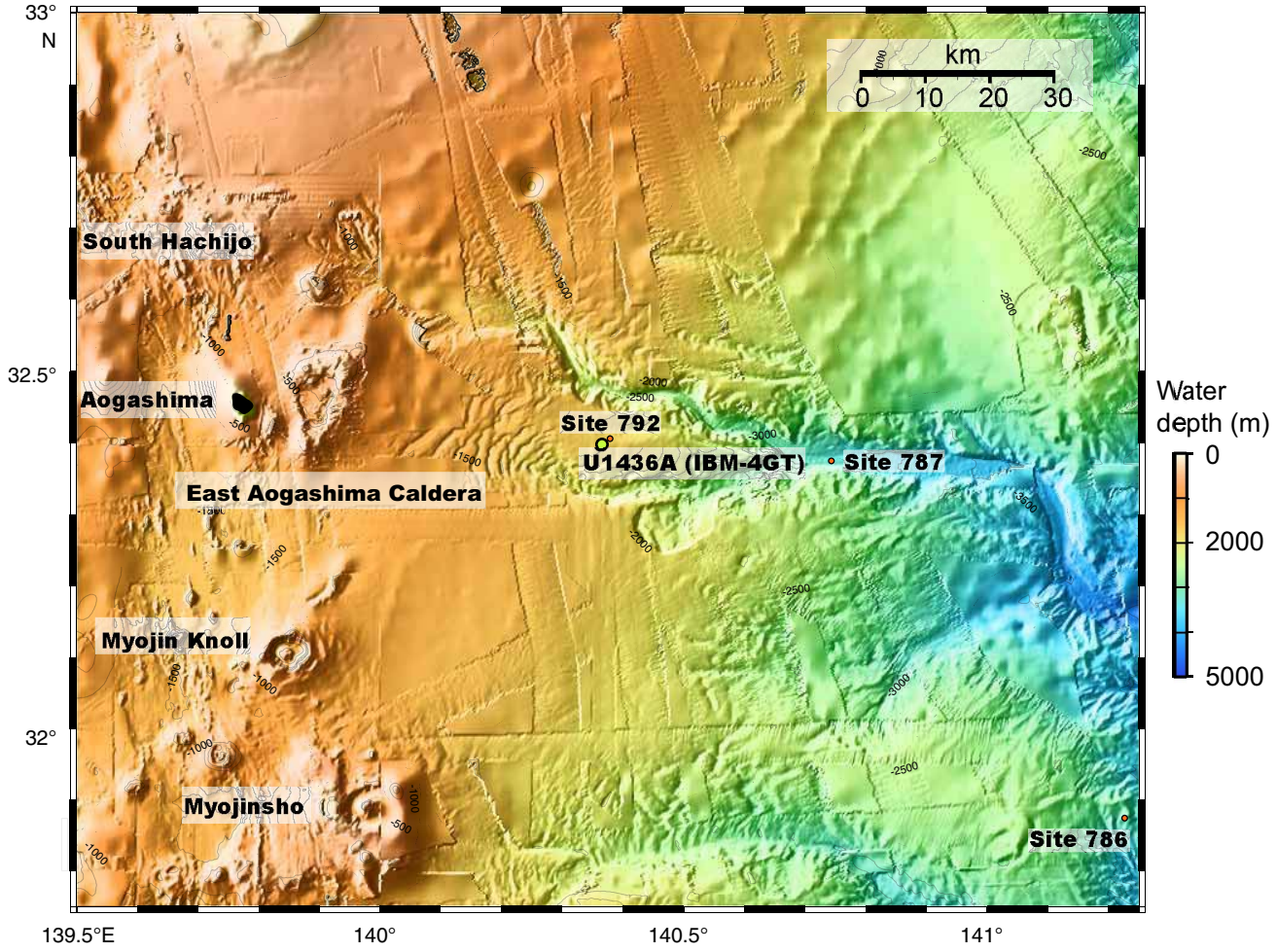

**Figure F18.** Shipboard age model and calculated sedimentation/accumulation rates, Site U1436. LSR = linear sedimentation rate, MAR = mass accumulation rate. T = top, B = bottom, X = crossover.

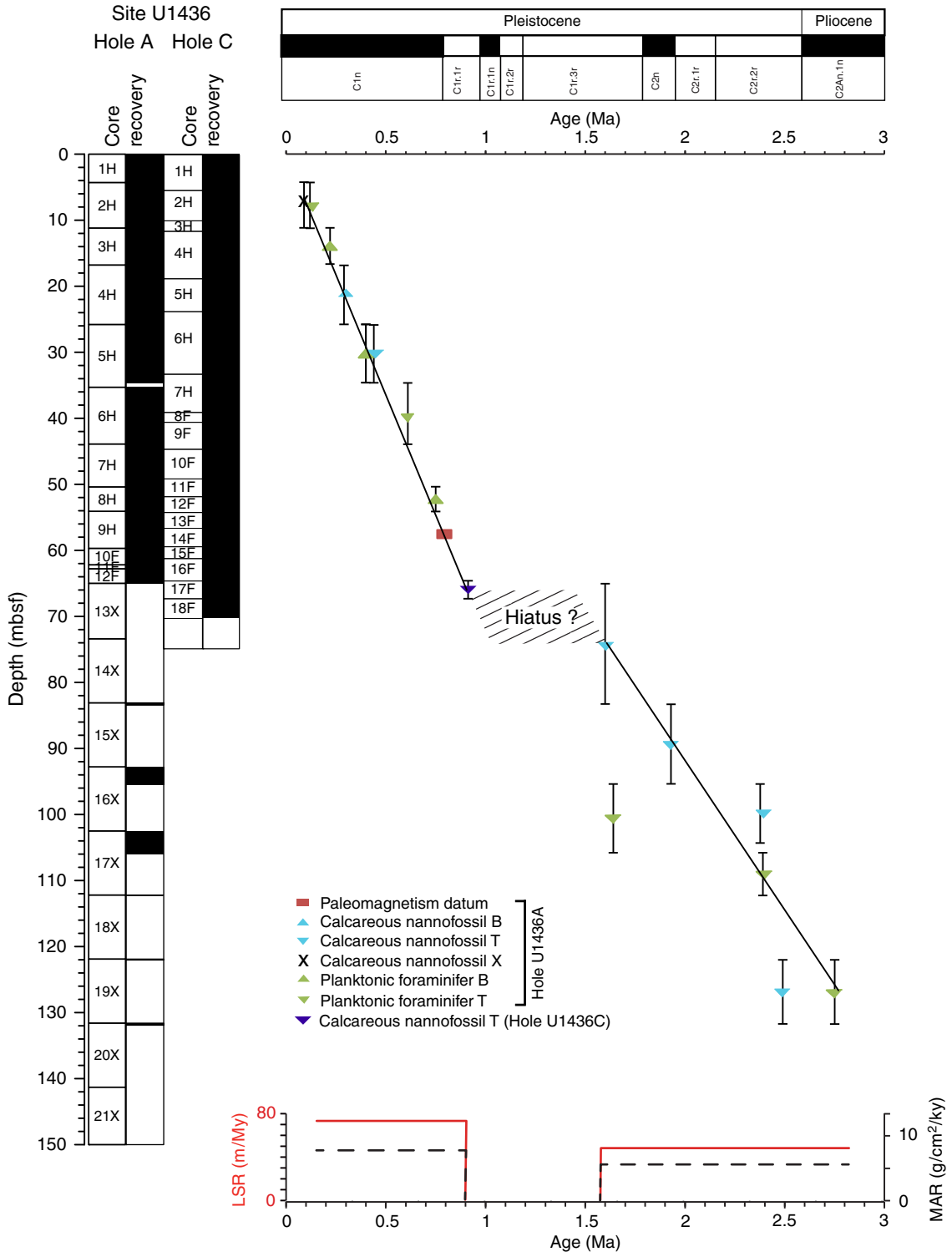

**Figure F19. A.** Summary lithostratigraphic log, Hole U1346A. (Continued on next page.)

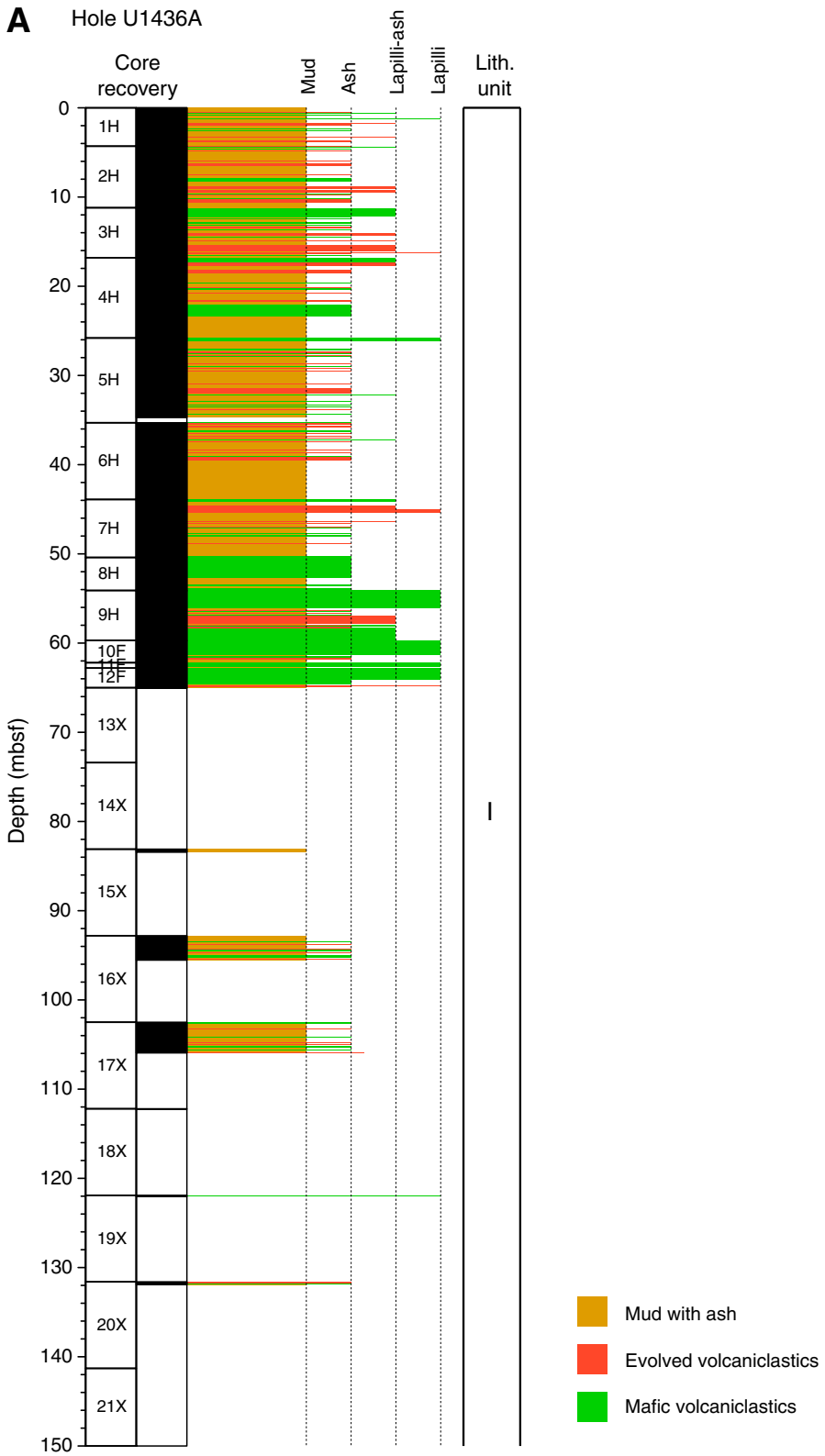

**Figure F19 (continued). B.** Downhole evolution in relative proportions of main lithofacies in Hole U1436A: mud with ash, evolved tephra, and mafic tephra. Relative abundances are the normalized total thickness of each lithofacies per core. No values are plotted when recovery is too low or when core disturbance is too severe.

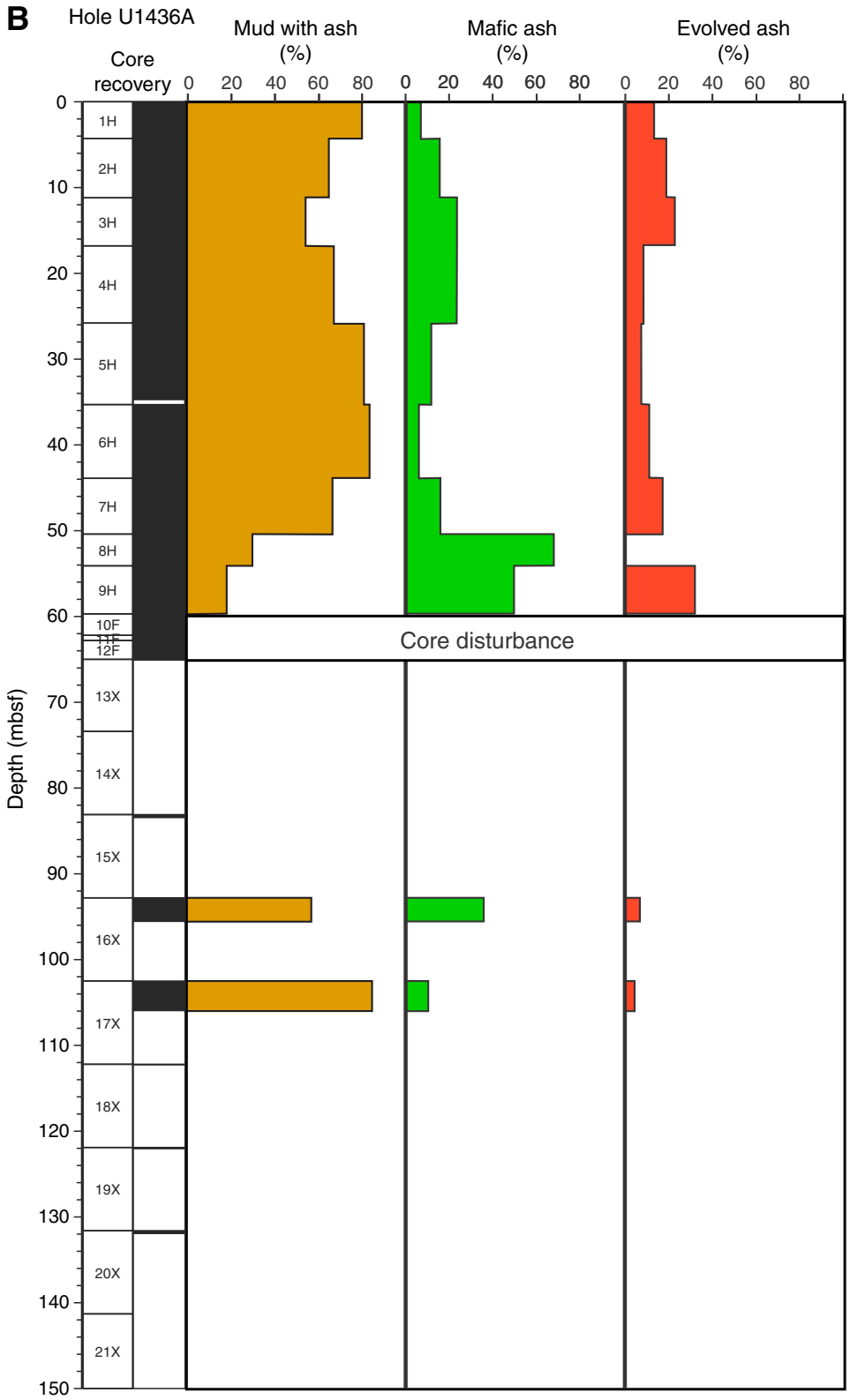

**Figure F20.** Hole U1436A lithologies. **A.** Tuffaceous mud lithofacies with mafic ash and evolved ash lithofacies (3H-2, 2–86 cm). **B.** Evolved ash lithofacies with basal fine-grained lapilli and normally graded ash intercalated with tuffaceous mud lithofacies (4H-2A, 10–29 cm). **C.** Black, glassy mafic ash lithofacies underlain and overlain by mud with ash lithofacies (8H-3A, 48–66 cm). This interval was not observed in Holes U1436B, U1436C, and U1436D and thus resulted from core disturbance of the black, glassy mafic ash interval, was recovered in Hole U1436D (Continued on next page.)

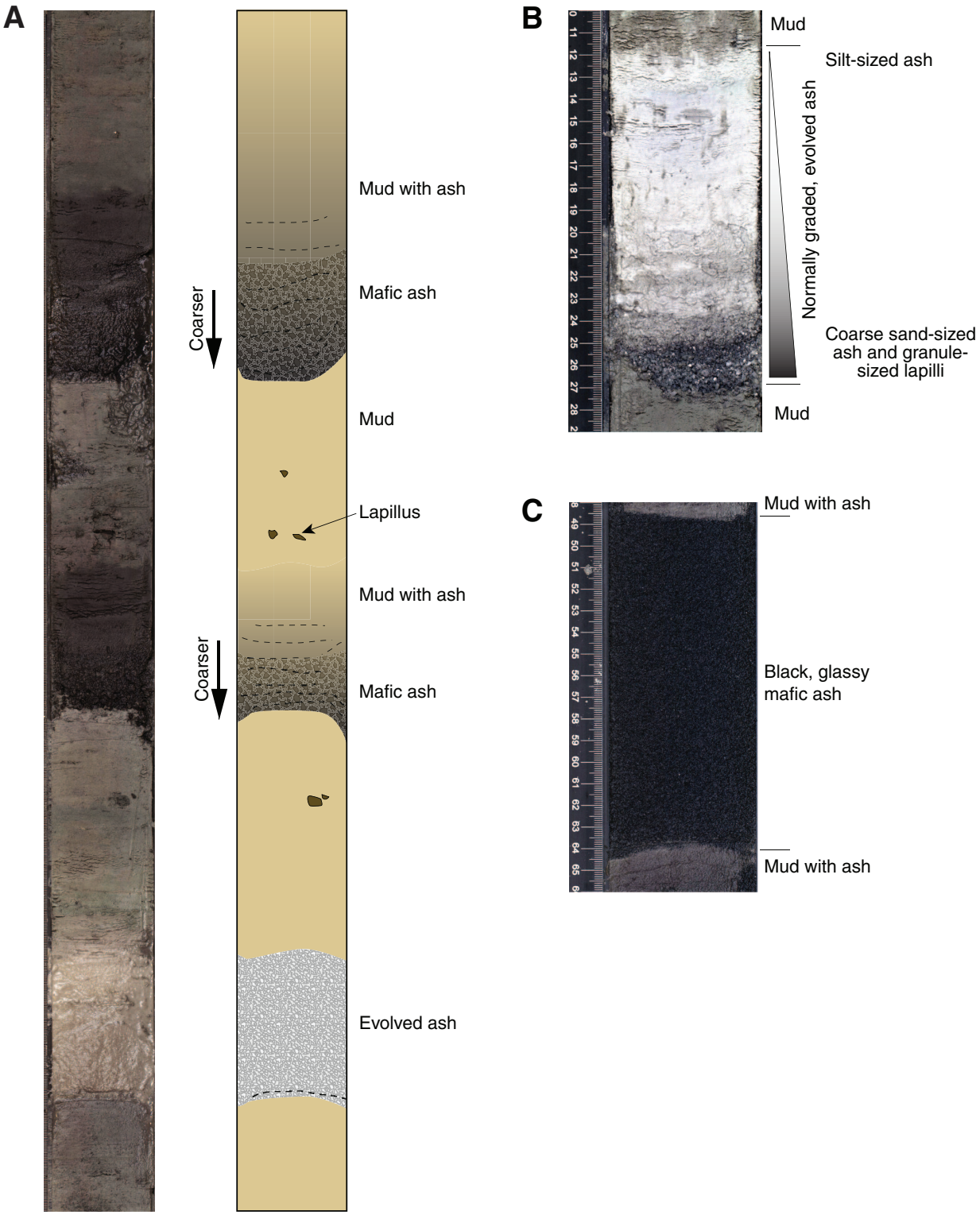

**Figure F20 (continued). D.** Shards in the black, glassy mafic ash (8H-2-W, 97–99 cm; TS03).

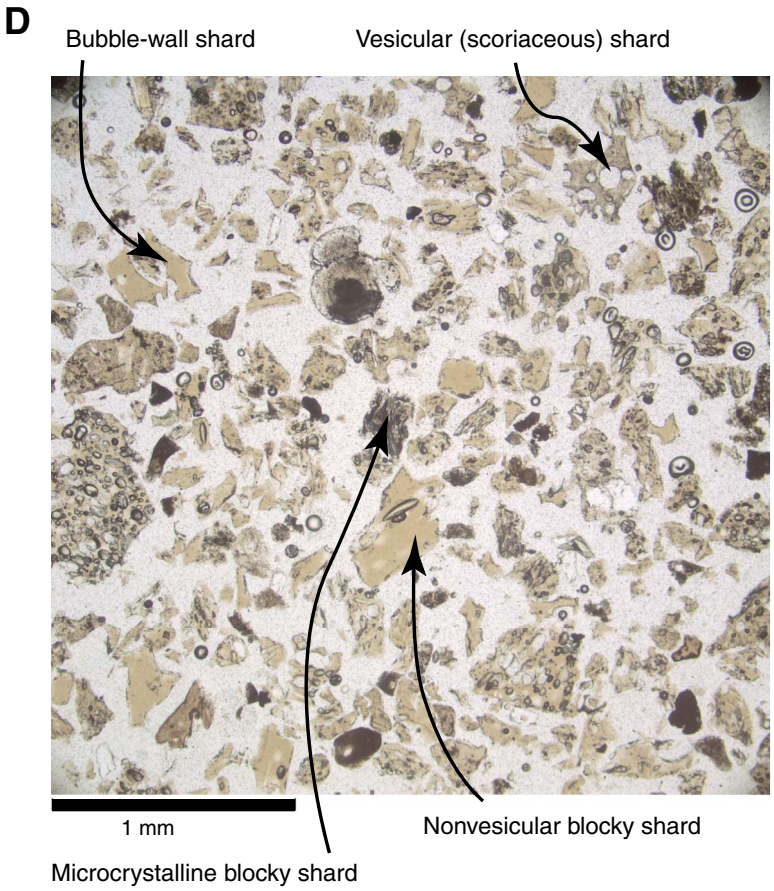

**Figure F21.** Portable X-ray fluorescence analyses results, Site U1436.

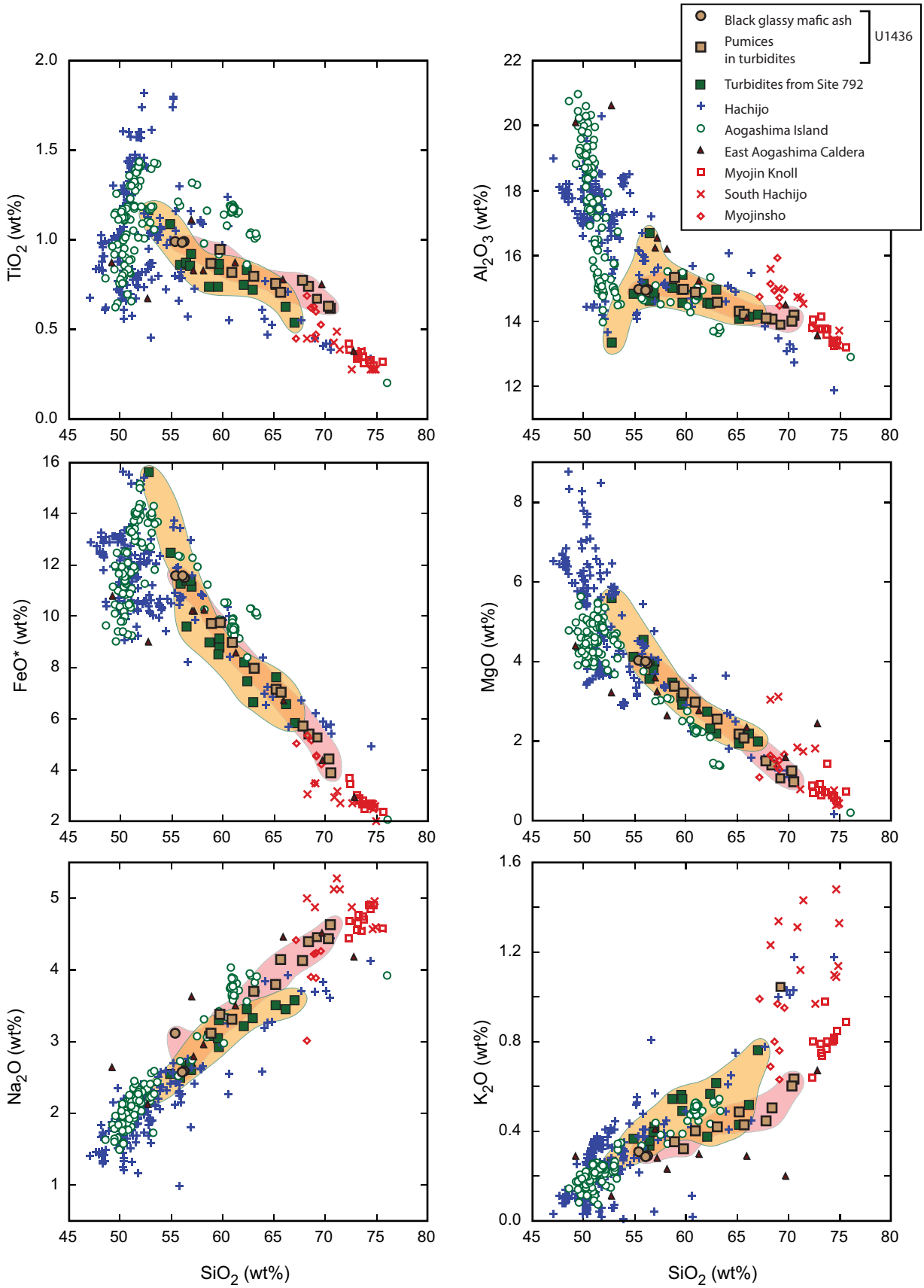

**Figure F22. A.** Bathymetric map of rear-arc region behind Aogashima, Myojin Knoll, Myojinsho, and Sumisu arc-front volcanoes (shown in Fig. F11). $^{40}Ar/^{39}Ar$ and K-Ar ages from Ishizuka et al. (2003b). Older ages (~12.5–3 Ma) from basalts to rhyolites of the rear-arc seamount chain volcanoes; younger ages (<3 Ma) from bimodal volcanic rocks in the broad zone of extension that overlaps with the eastern half of the rear-arc seamount chains; youngest ages (<1 Ma) from bimodal volcanic rocks of the narrow active rift (see Fig. F6). Site U1437 lies in a volcano-bounded basin (Fig. F15A) between the Manji and Enpo rear-arc seamount chains, at the foot of the flat-topped Manji Volcano, which was presumably beveled by wave action. (Continued on next page.)

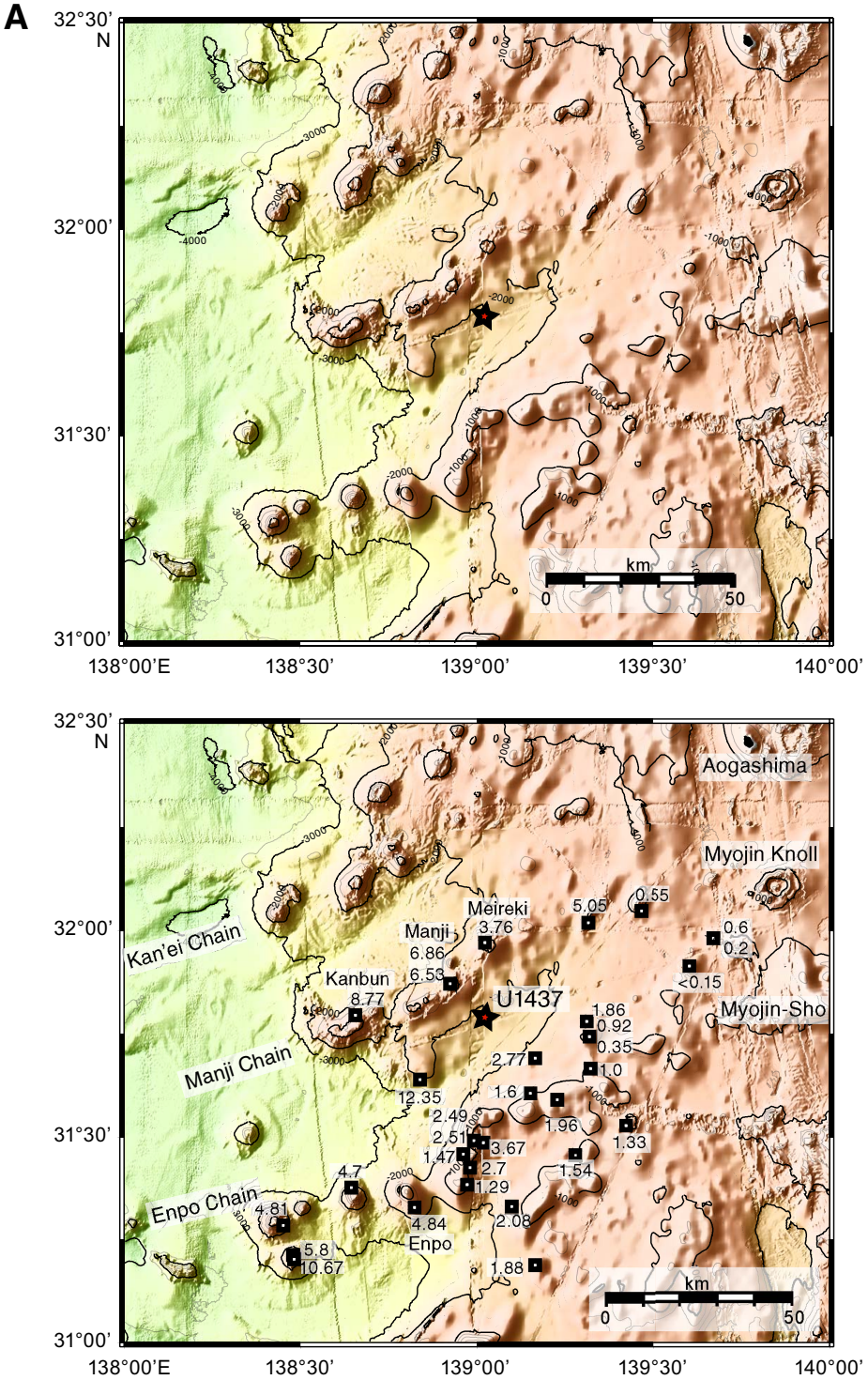

**Figure F22 (continued). B.** Locations of three MCS profiles by Japan Agency for Marine-Earth Science and Technology (M. Yamashita, per. comm., 2014) shown in Figures **F15** and **F23.**

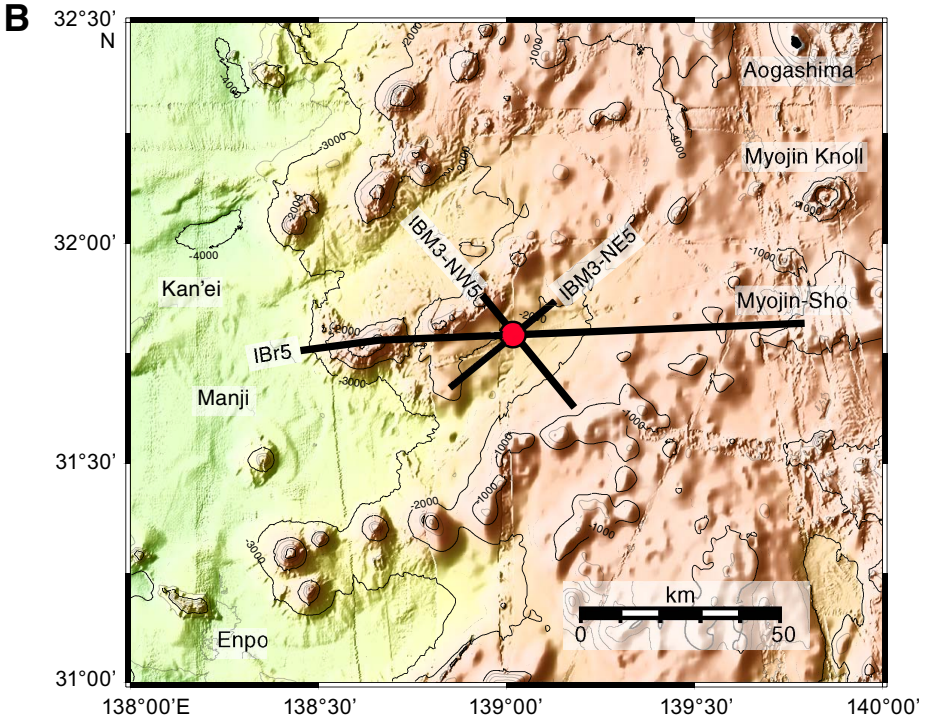

**Figure F23.** Seismic Line IBr5, which runs east from the Manji rear-arc seamount chain in the west to the arc front in the east, plotted on Figure F22B (M. Yamashita, per. comm., 2014). **A.** Seismic velocity image obtained from wide-angle ocean-bottom seismometer (OBS) data, with OBSs deployed every 5 km along Line IBr5. **B.** Depth-converted multichannel seismic (MCS) reflection profile along Line IBr5. Dashed yellow lines = iso-velocity contours of 5 and 6 km/s obtained from seismic velocity image in Figure F13A, which are interpreted as the depth to igneous basement (upper crust) and middle crust, respectively (M. Yamashita, per. comm., 2014).

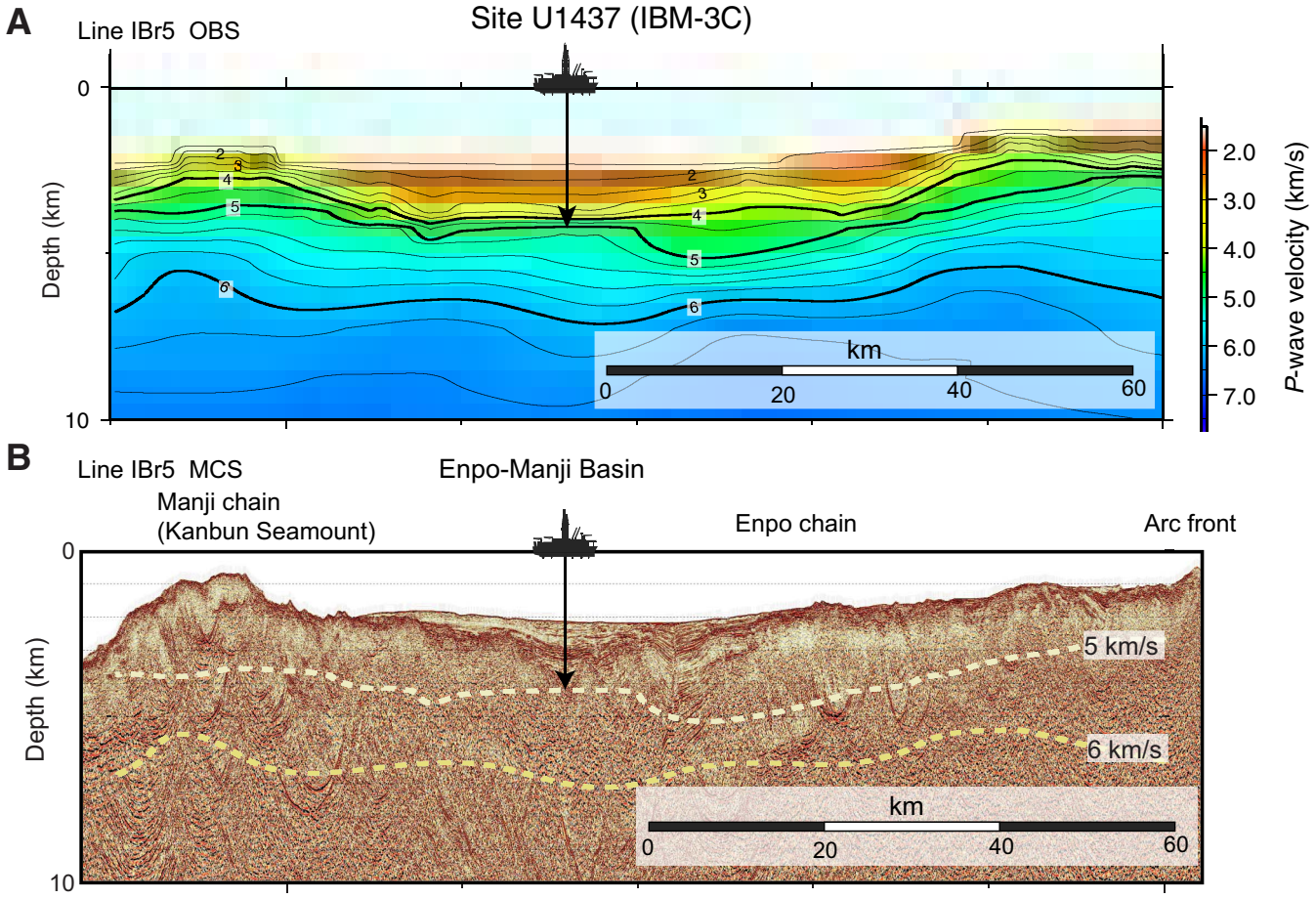

**Figure F24.** Shipboard biostratigraphic and magnetostratigraphic datums, age-depth model, and sedimentation (LSR)/accumulation (MAR) rates. LSR, total MAR, carbonate MAR (CAR), and noncarbonate MAR (nCAR) are calculated from the age model. T = top, B = bottom, X = crossover.

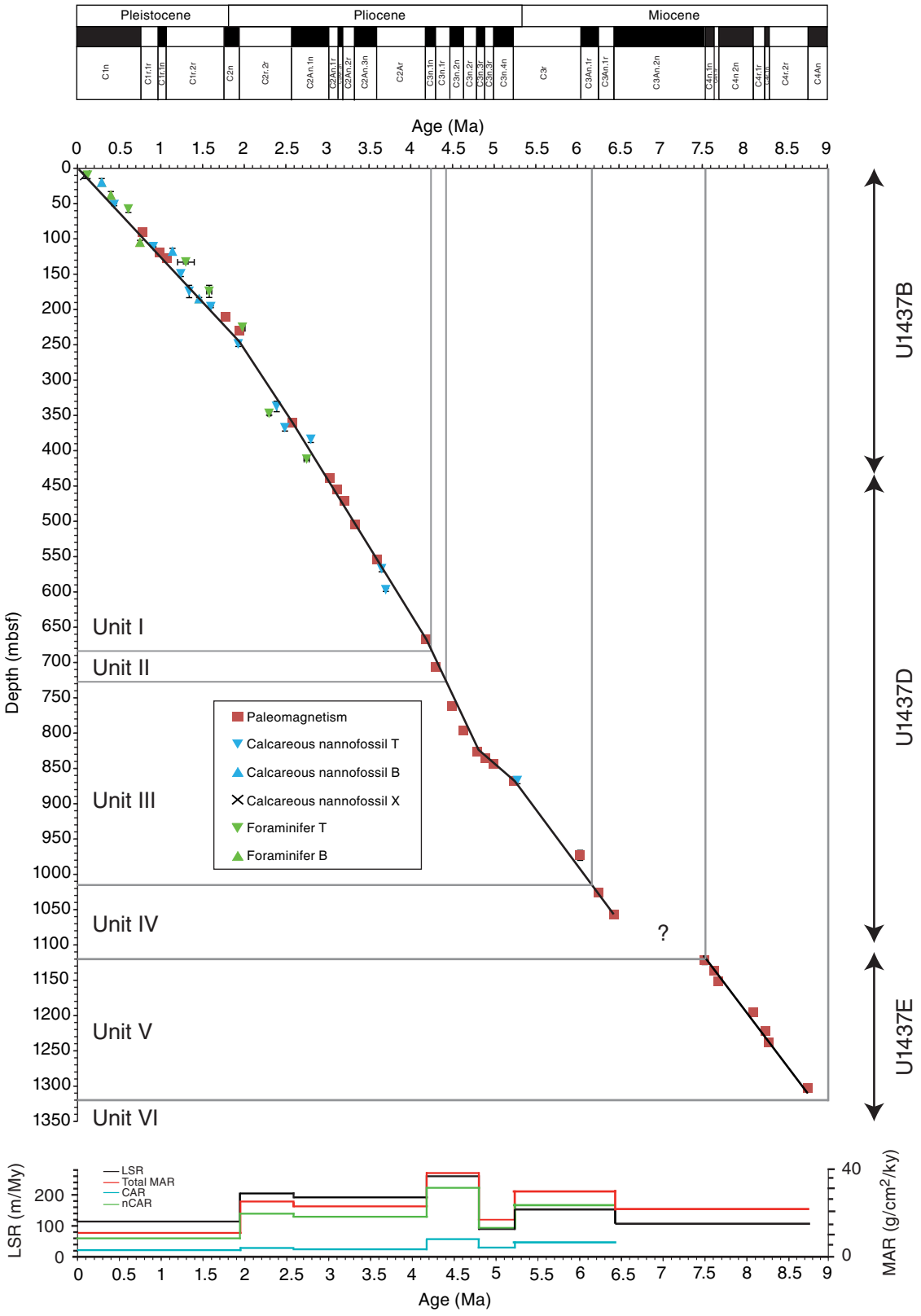

**Figure F25. A.** Summary lithostratigraphic log, Site U1437. The boundary between coarse- and fine-grained volcaniclastics is 2 mm (corresponding to the boundary between ash and lapilli-sized particles). (Continued on next two pages.)

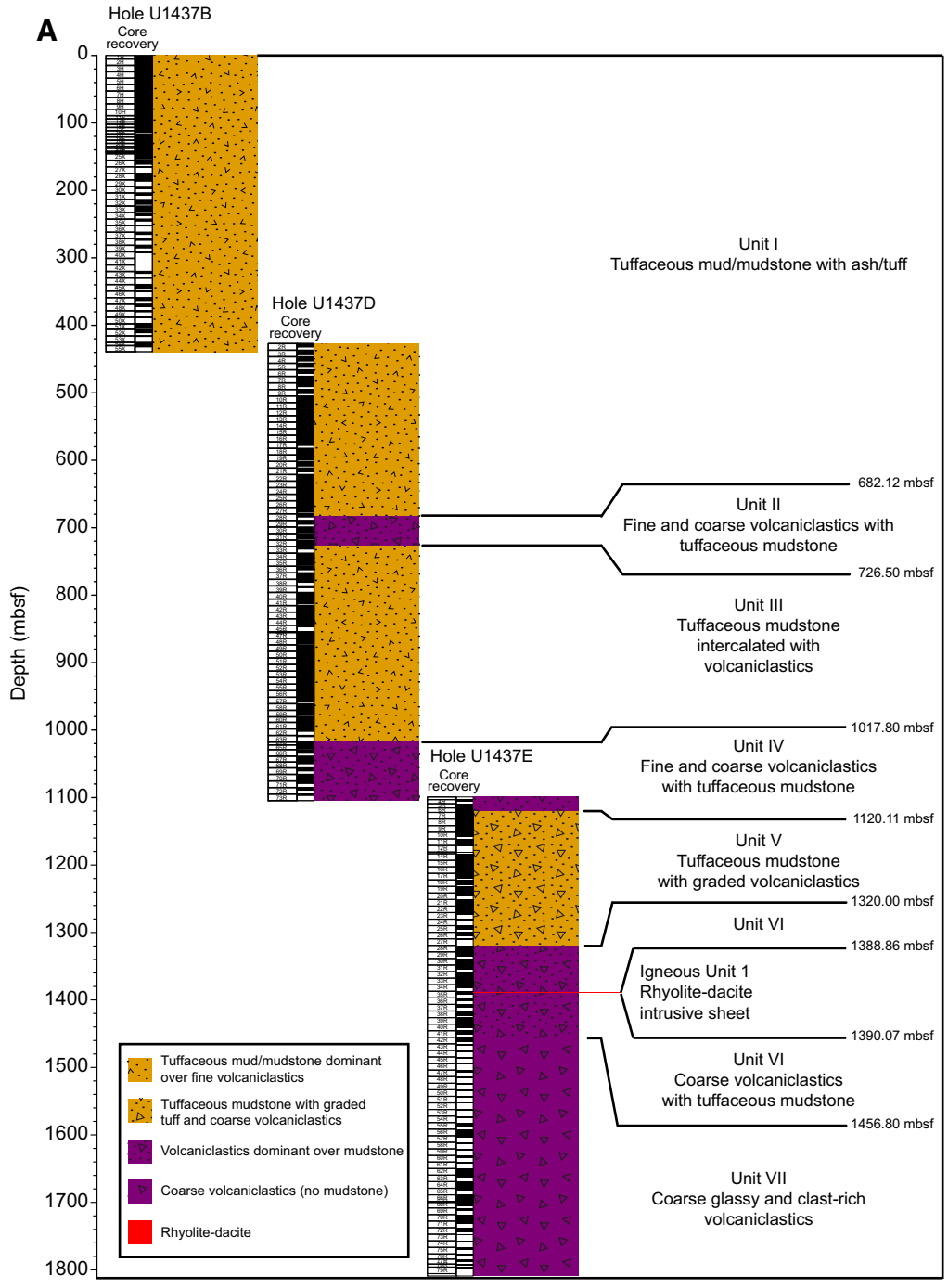

**Figure F25 (continued). B.** Physical properties summary, 0–1100 mbsf, Holes U1437B and U1437D. APC = advanced piston corer, XCB = extended core barrel, RCB = rotary core barrel. PP = physical properties, NGR = natural gamma radiation. GRA = gamma ray attenuation, MAD = moisture and density (discrete), PWL = *P*-wave logger, PWC = *P*-wave sensor (caliper), PWB = *P*-wave sensor (bayonet), MSL = magnetic susceptibility logger, WRMSL = Whole-Round Multisensor Logger, MSP = point magnetic susceptibility, SHMSL = Section Half Multisensor Logger. (Continued on next page.)

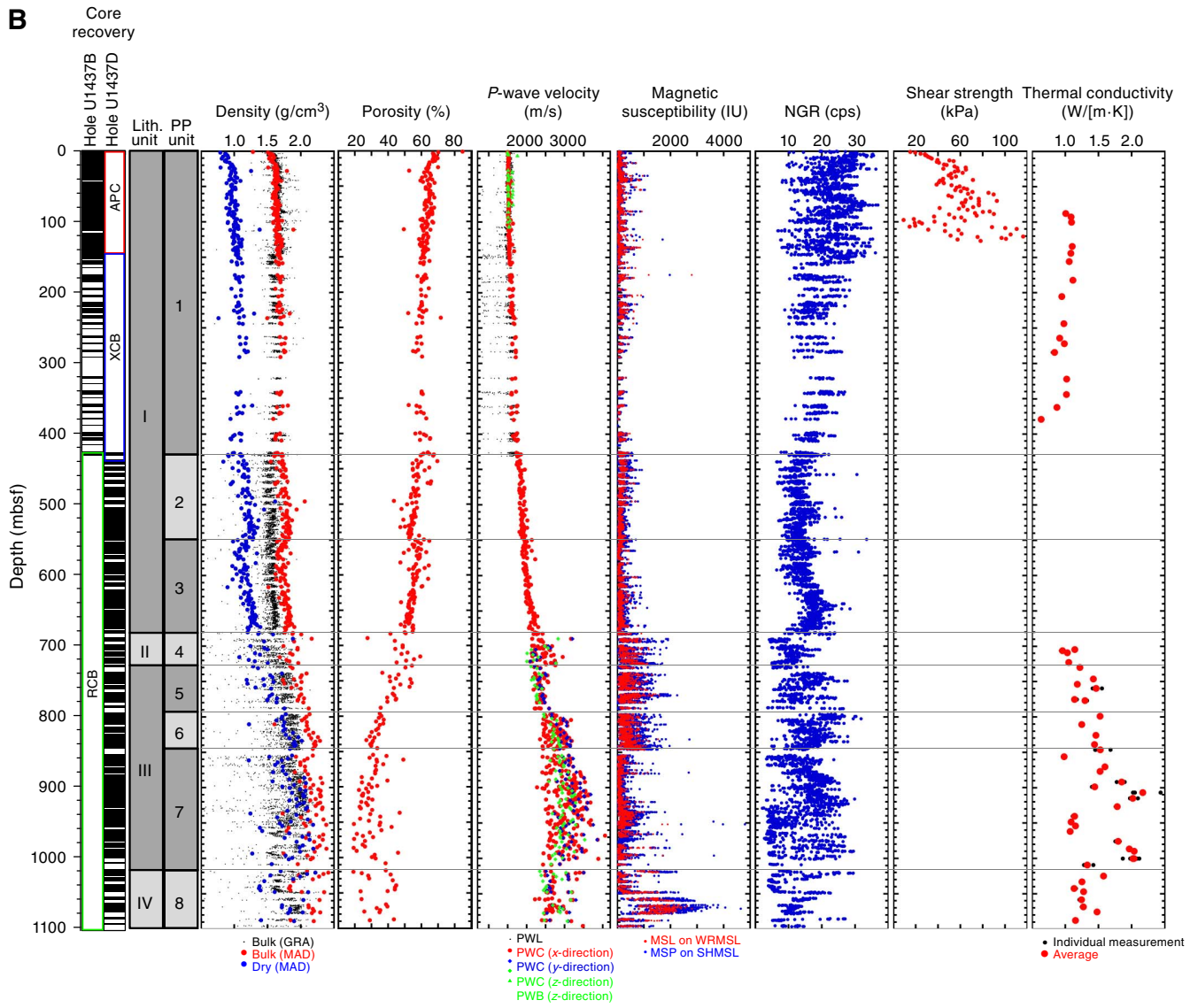

**Figure F25 (continued).** C. Physical properties summary, 1100 mbsf to bottom of Hole U1437E.

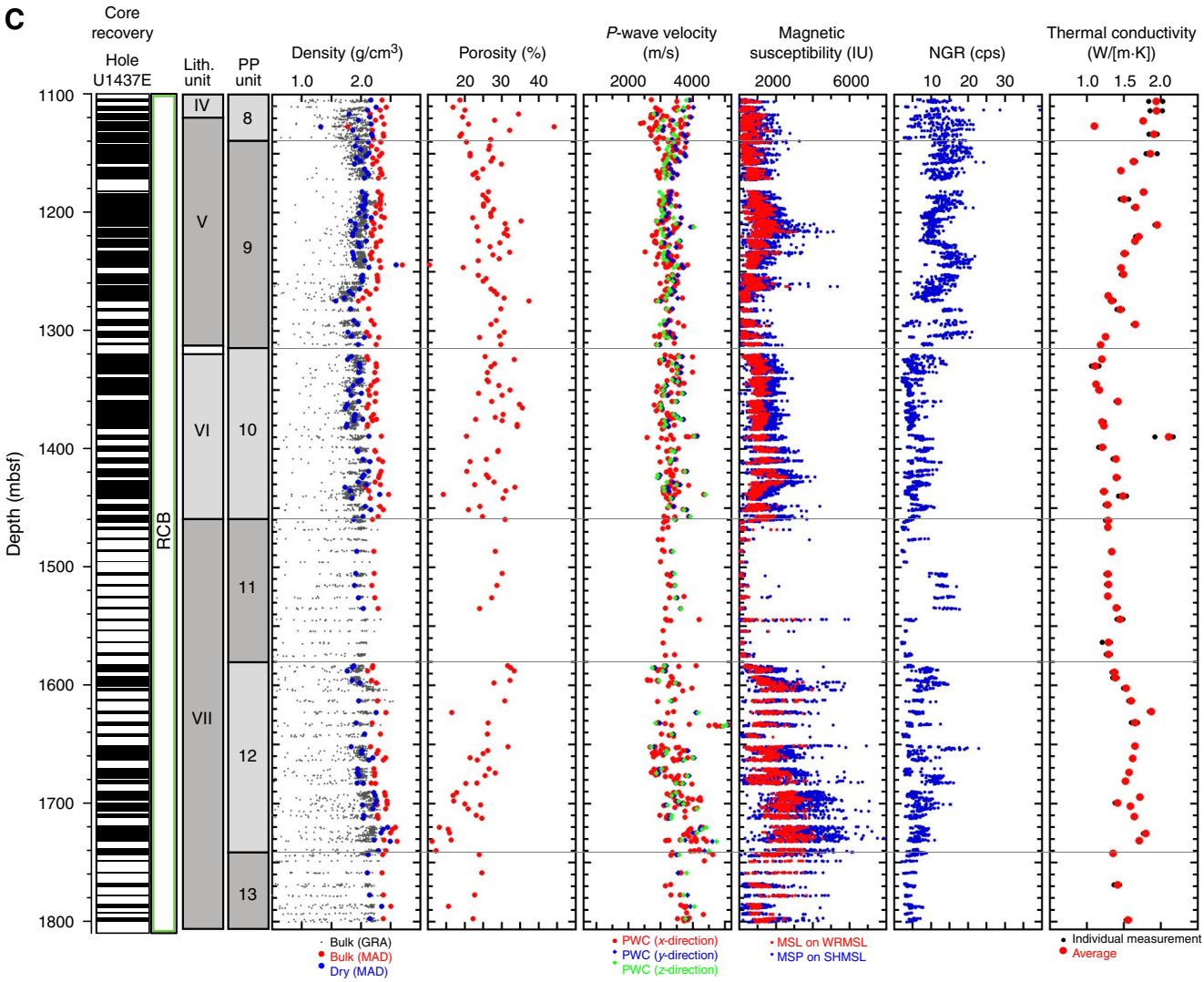

**Figure F26.** Summary lithostratigraphic logs. **A.** Hole U1437B. (Continued on next two pages.)

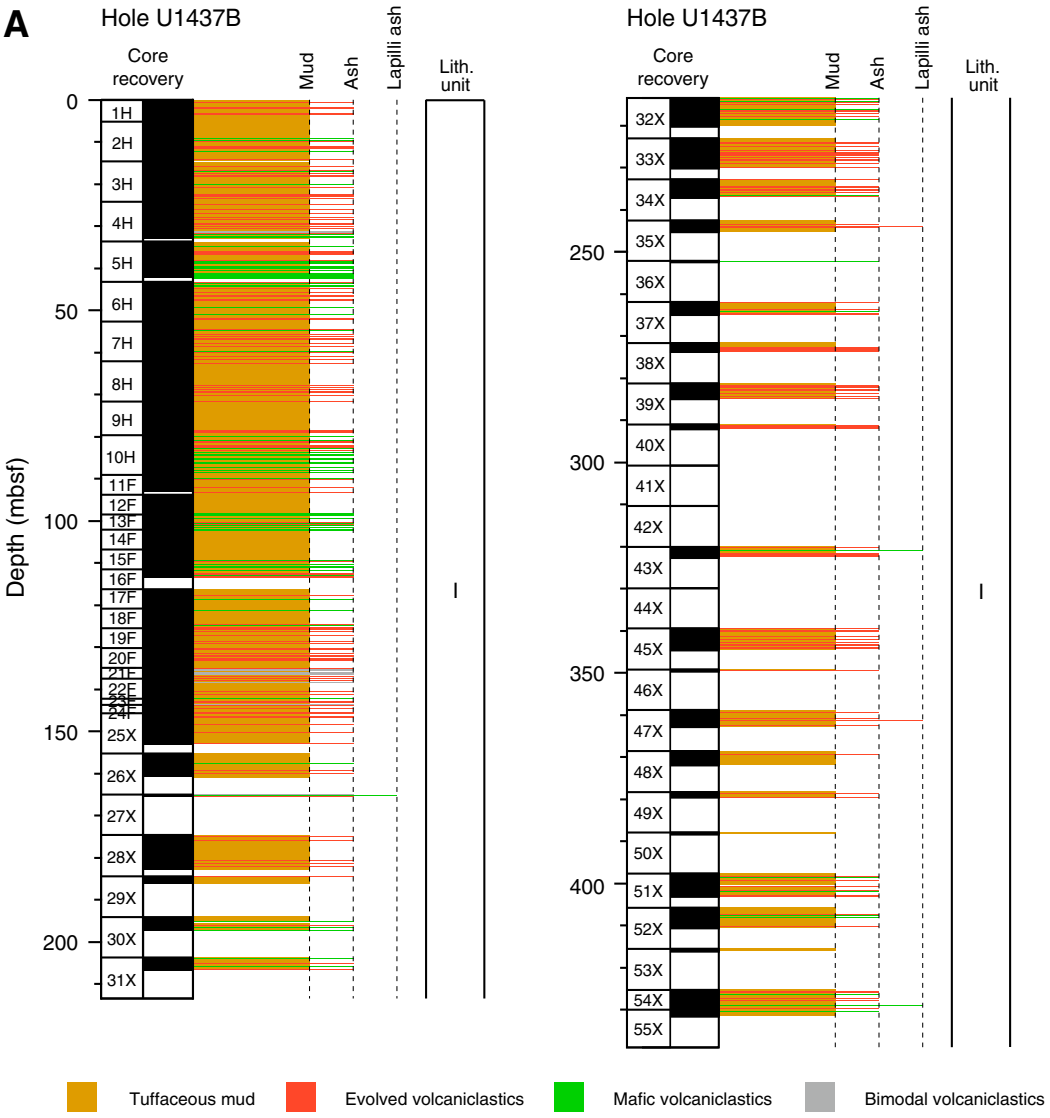

**Figure F26 (continued). B.** Hole U1437D. (Continued on next page.)

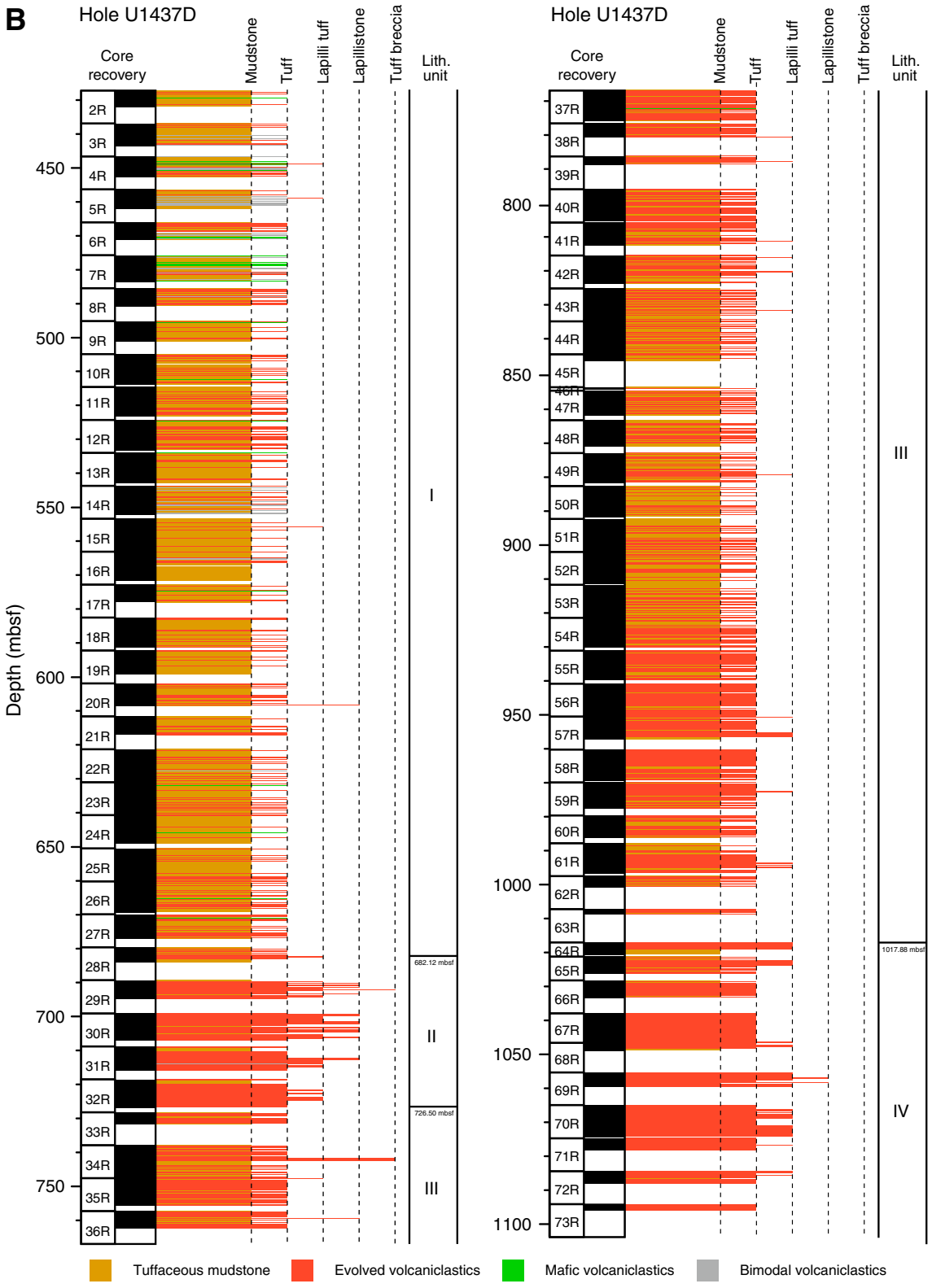

**Figure F26 (continued).** C. Hole U1437E.

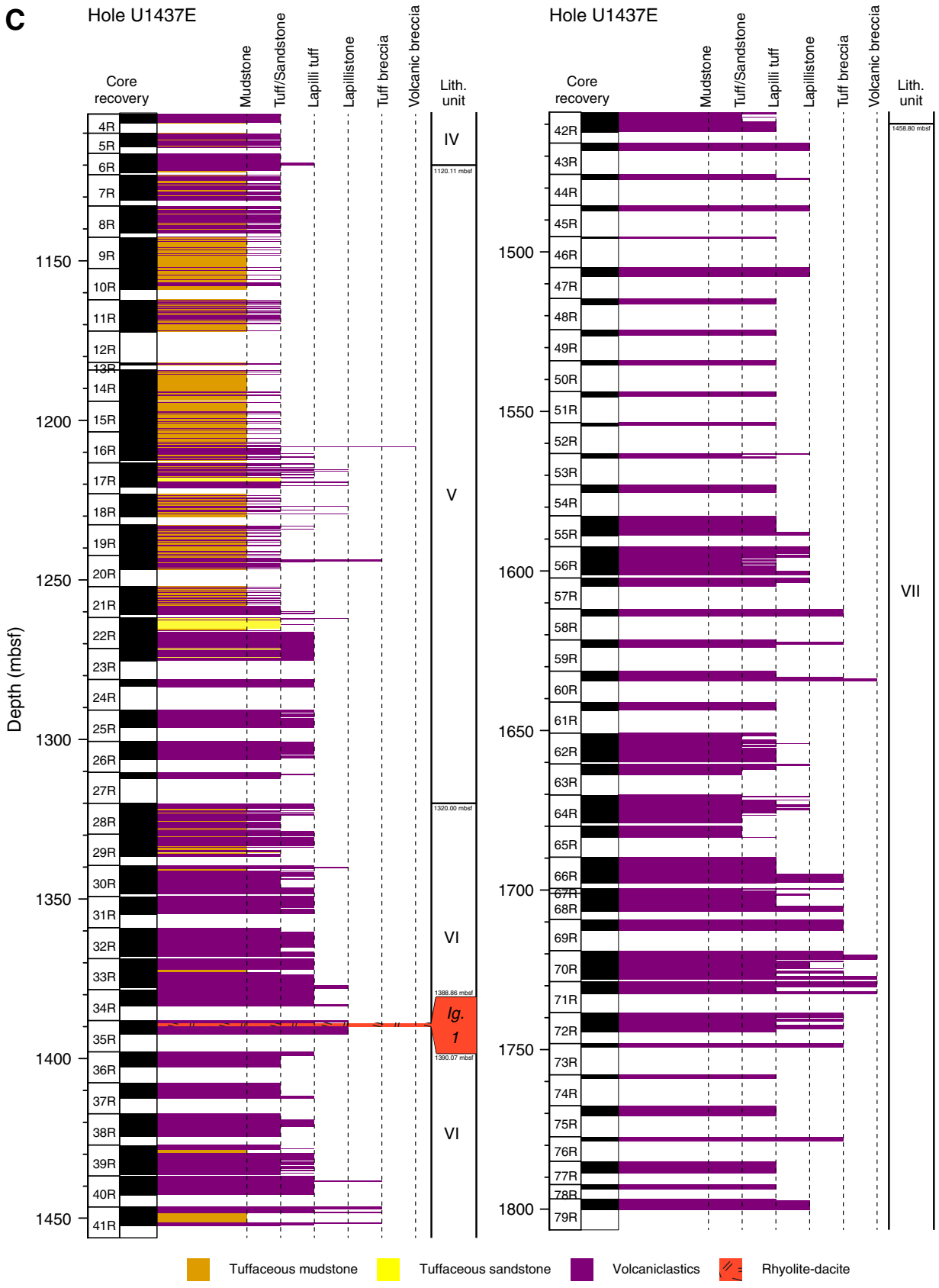

**Figure F27.** Downhole evolution in relative proportions of mud and volcaniclastics, dividing the volcaniclastics further into relative proportions of mafic and evolved materials. Thickness of bars represents core recovery. **A.** Hole U1437B. (Continued on next two pages.)

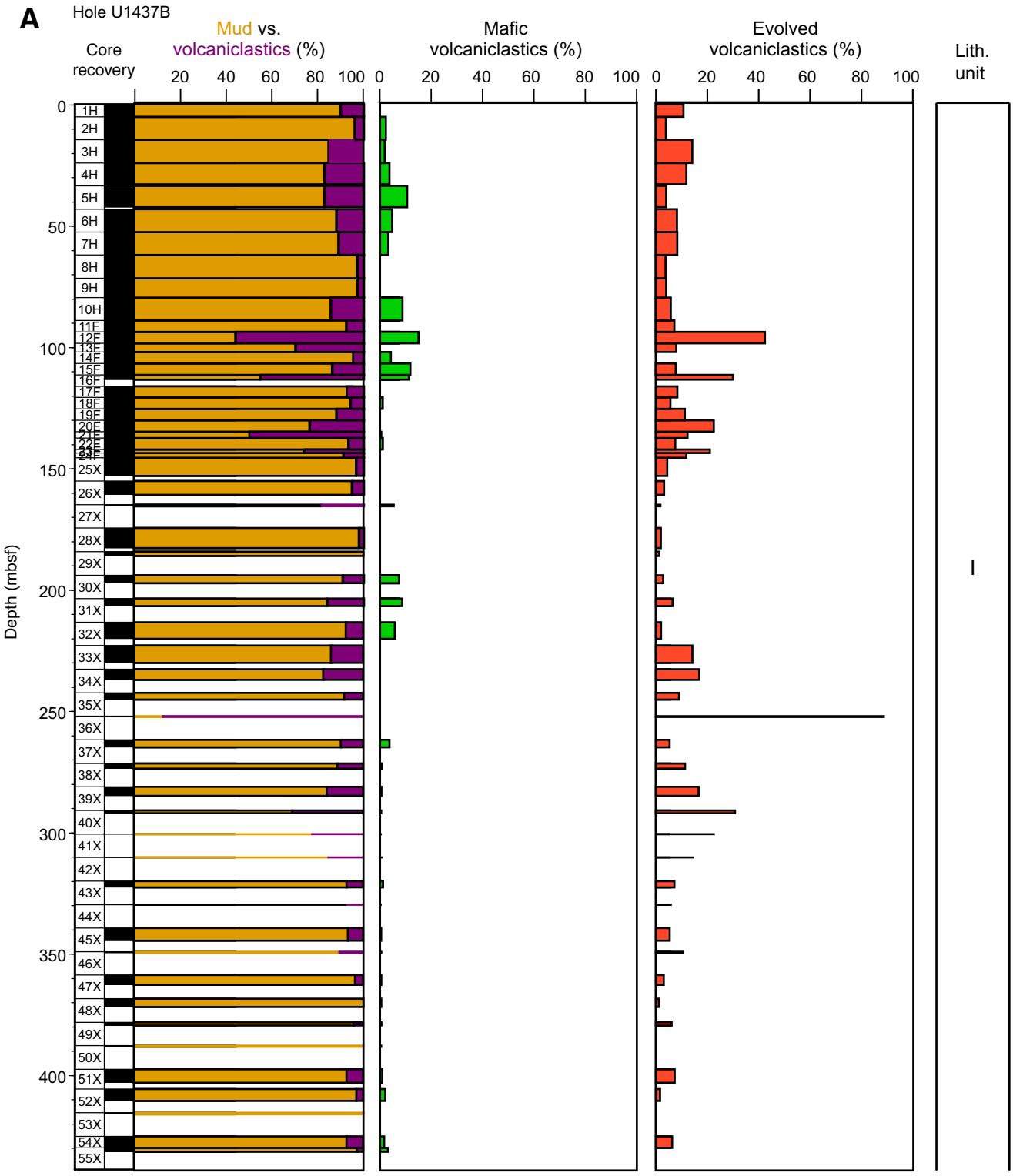

**Figure F27 (continued). B.** Hole U1437D. (Continued on next page.)

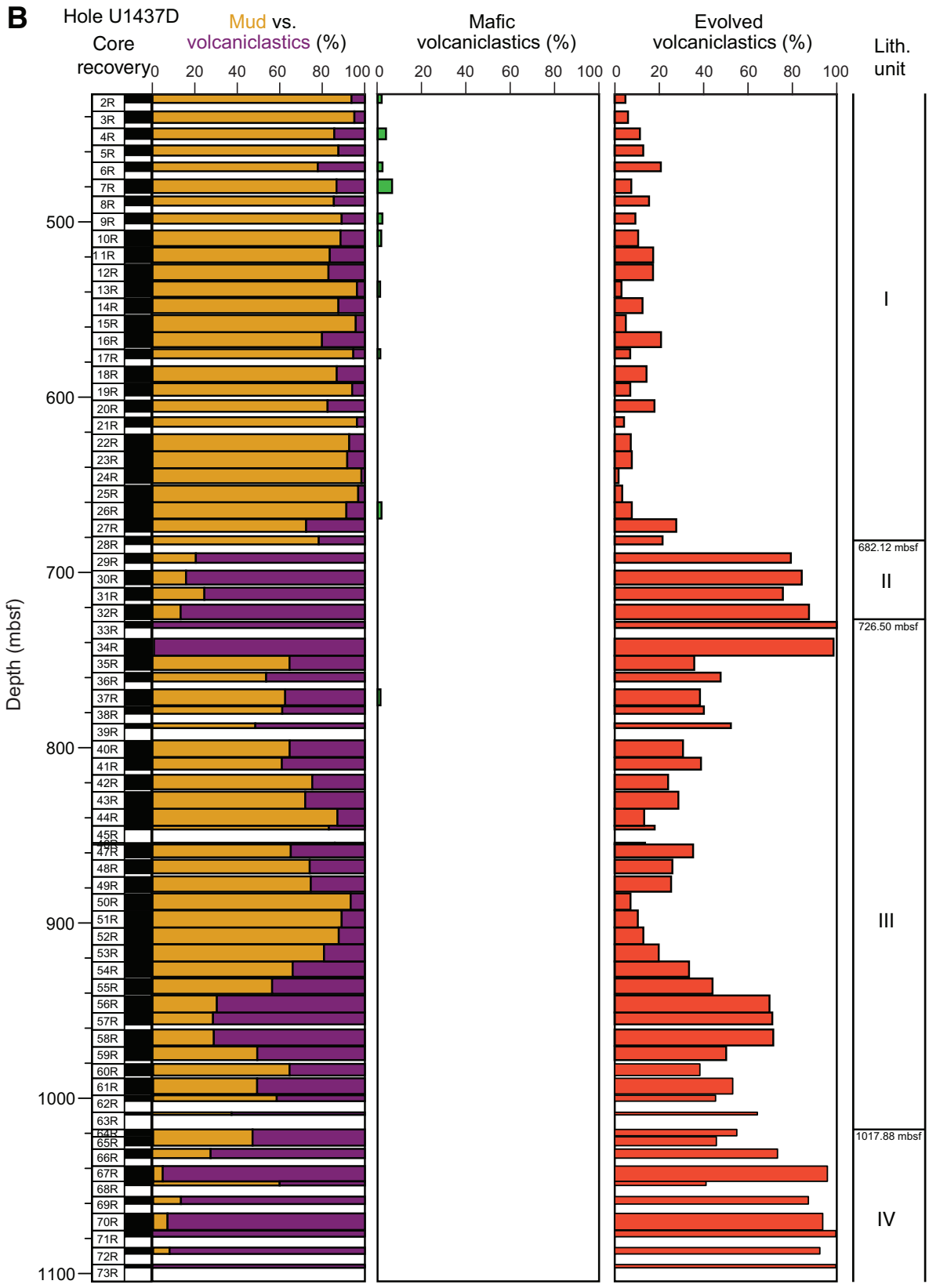

**Figure F27 (continued).** C. Downhole evolution of the relative proportion of tuffaceous mudstone and volcaniclastics and number and composition of volcanic clasts per core, normalized for recovery, Hole U1437E.

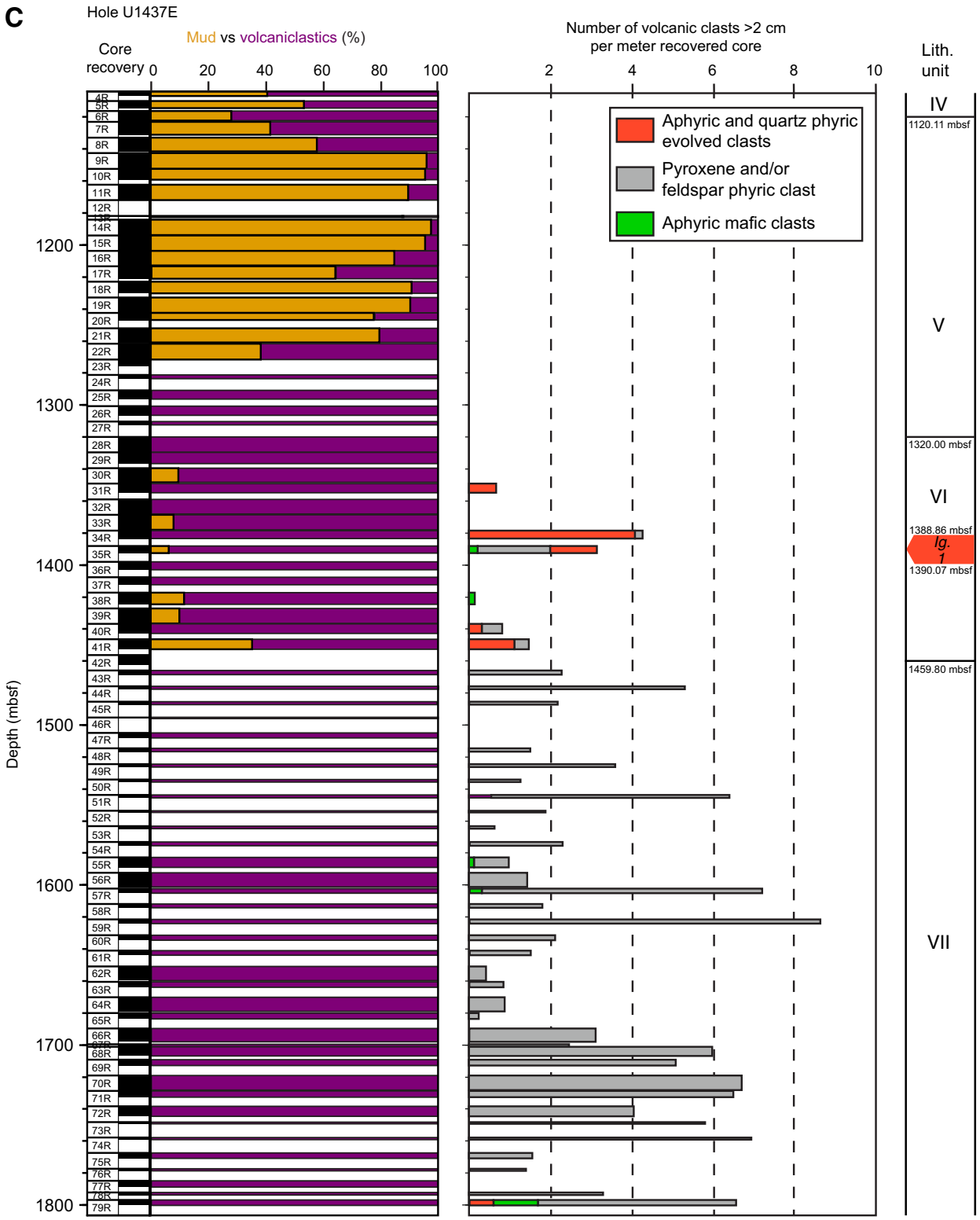

**Figure F28.** Representative lithology/interpretation, Unit I. **A.** 5–10 cm mafic ash intervals with sharp bases and tops grading upward into mud with ash, with mafic ash pods (350-U1437B-10H). **B.** Evolved tuff intervals grading upward into mud with ash and bioturbation (350-U1437D-10R).

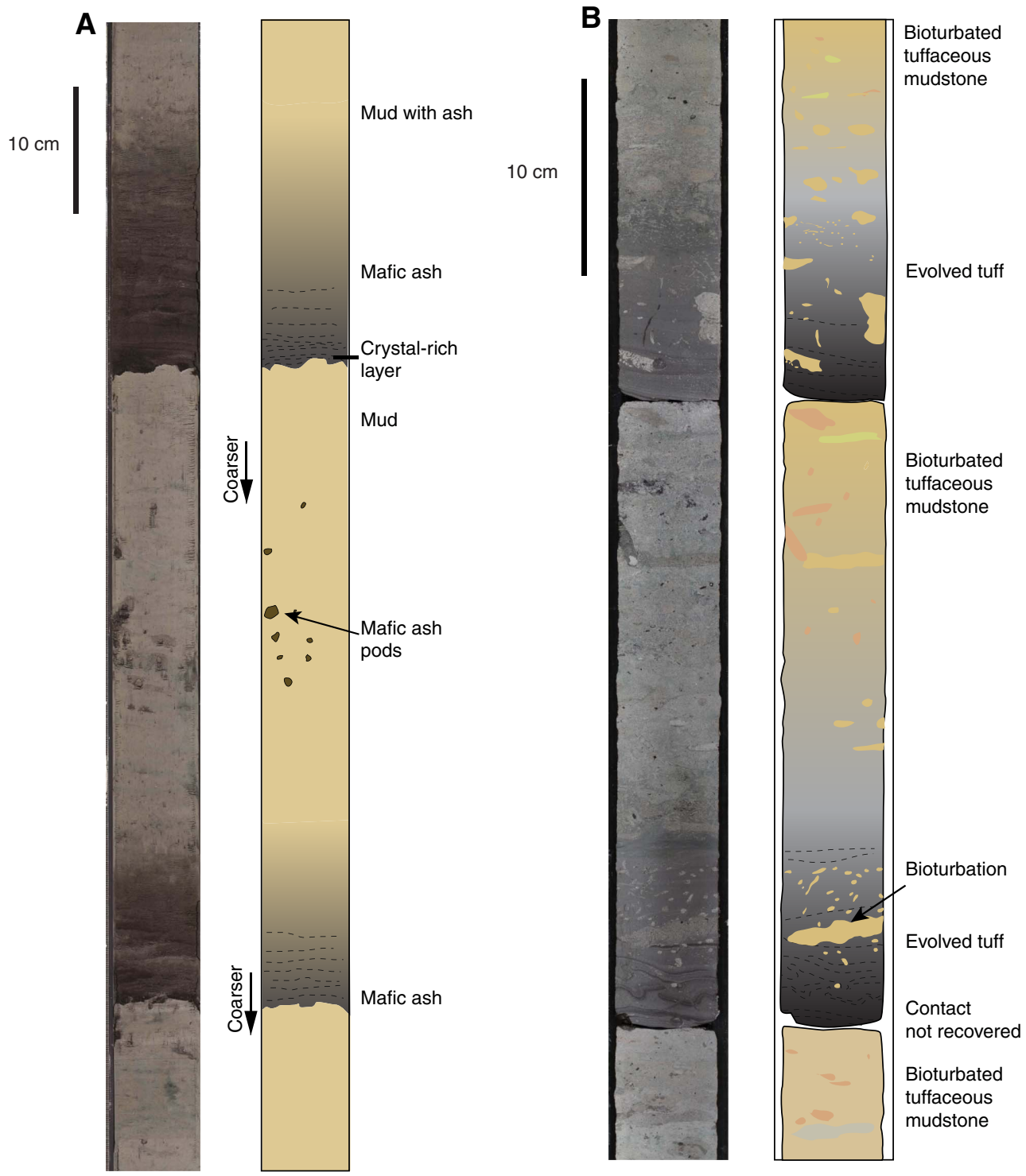

**Figure F29.** Representative lithology/interpretation, Hole U1437D, Unit II. **A.** Closely intercalated monomictic tuff, lapilli tuff, and lapillistone, showing stratification, cross stratification, and normal grading (Core 29R). **B.** Bioturbated tuffaceous mudstone with evolved tuff and lapilli tuff intervals, with normal and reverse grading, soft-sediment deformation, and pumice clasts (Core 31R).

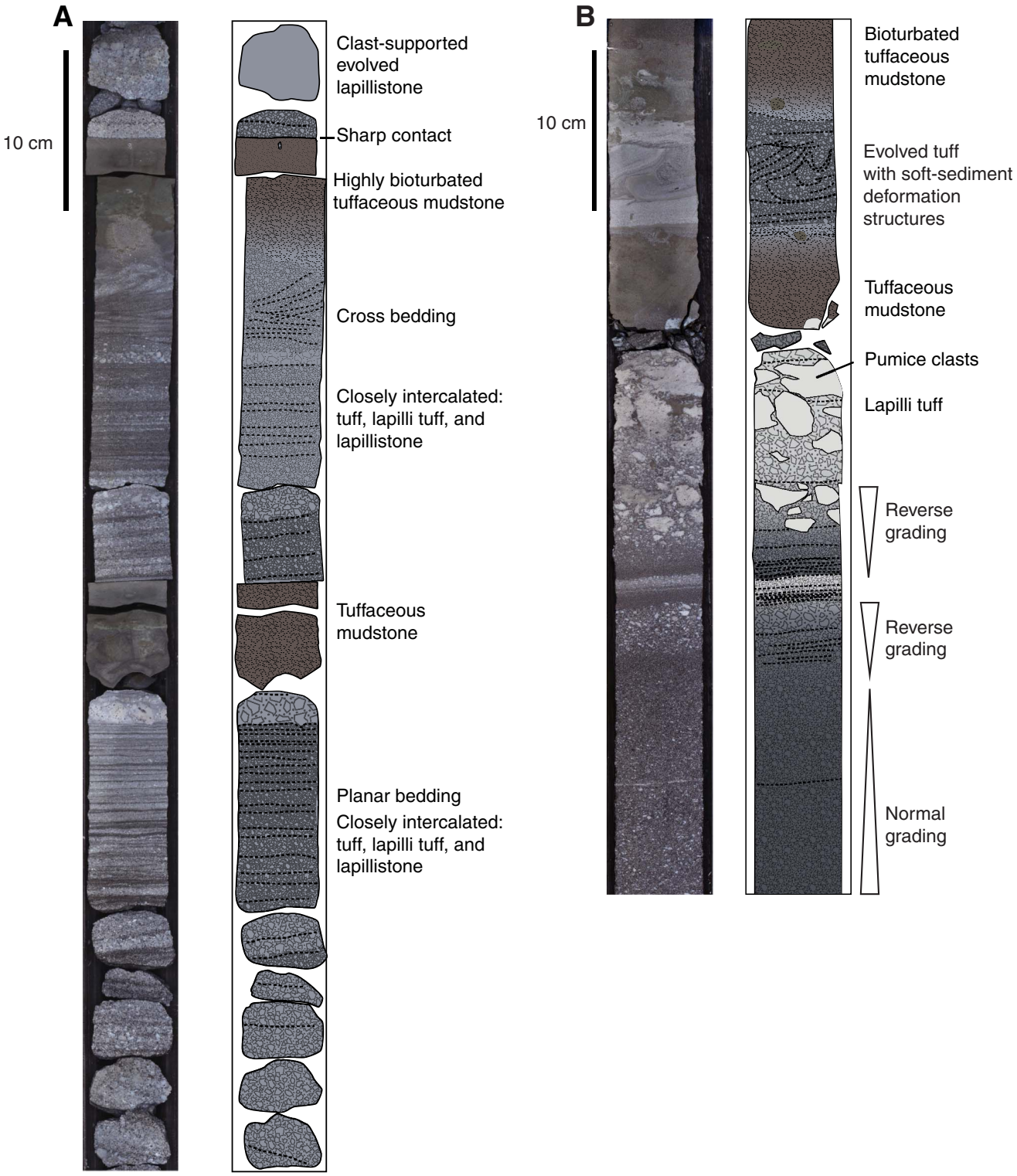

**Figure F30.** Representative lithology and interpretation, Hole U1437D, Unit III. **A.** Dark gray evolved tuff (Core 54R). **B.** Dark and light gray evolved tuff with green alteration showing planar and cross bedded stratification (Core 54R). (Continued on next two pages.)

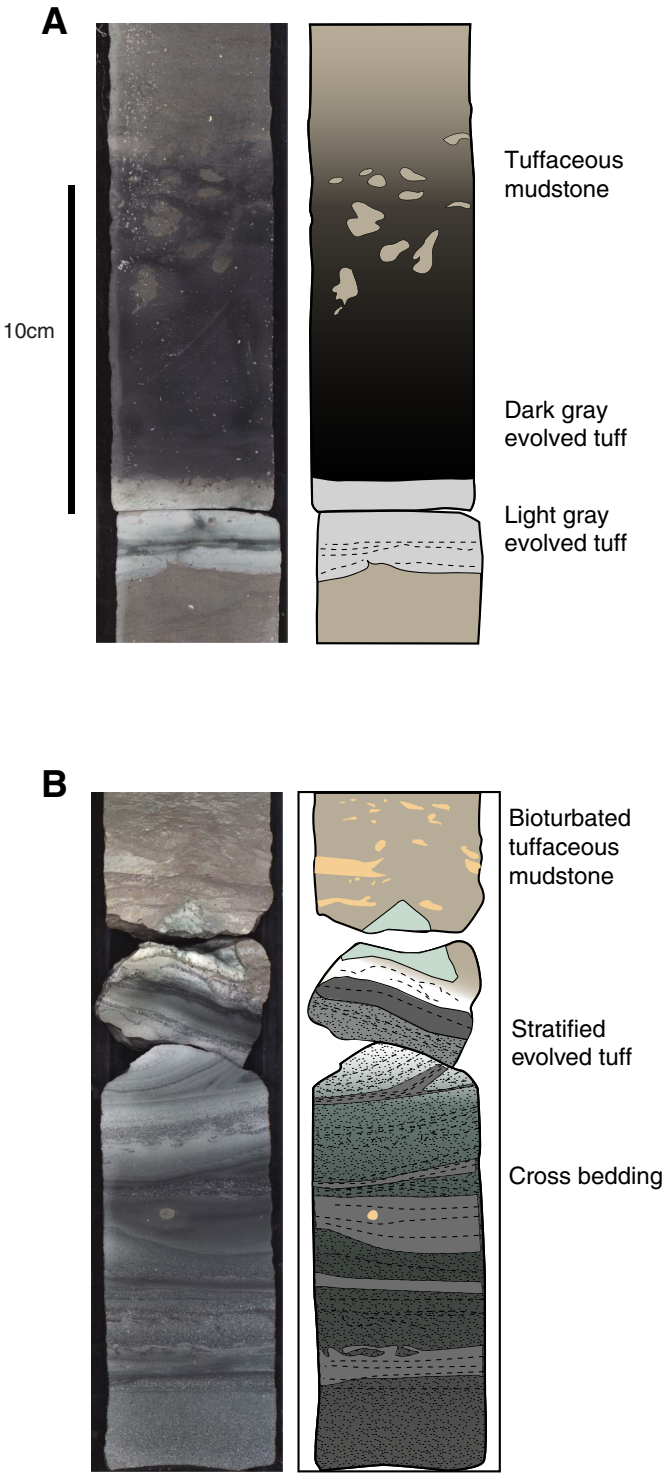

**Figure F30 (continued).** **C.** Planar-bedded evolved tuff with crystals showing a sharp lower contact and a diffuse bioturbated upper contact grading upward into tuffaceous mudstone (Core 41R). **D.** Alternating tuffaceous mudstone, evolved tuff, and evolved lapilli tuff, as well as closely intercalated tuffaceous mudstone and evolved tuff (Core 41R). (Continued on next page.)

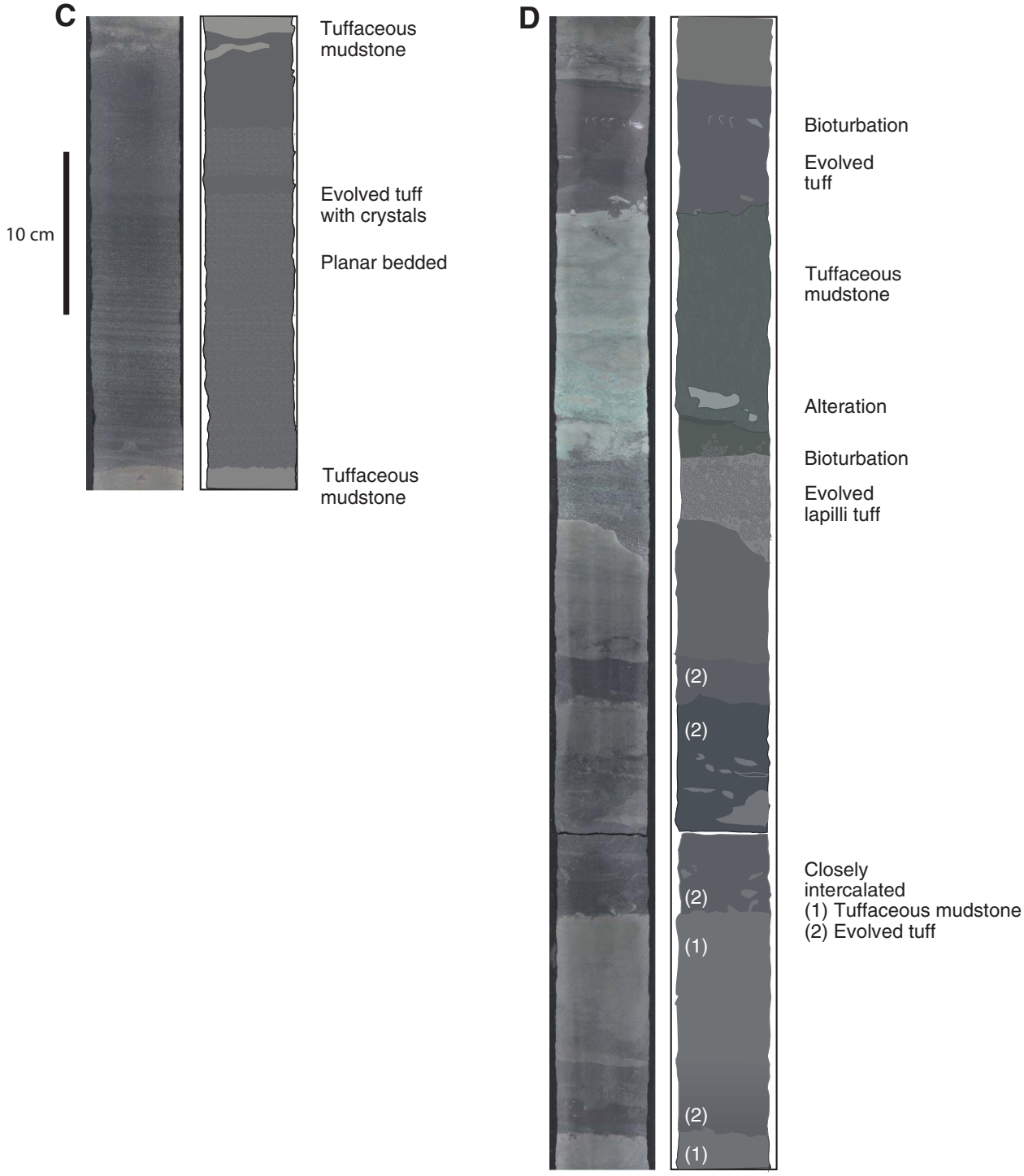

**Figure F30 (continued). E.** Closely intercalated green and white evolved very fine grained tuff with soft-sediment deformation (58R-3, 70–94 cm; 964.16–964.40 mbsf).

**Figure F31.** Representative lithology/interpretation, Hole U1437E, Unit V **A.** Monomictic, reverse-graded lapilli tuff with pumice. Note erosive tuff base and reverse coarse-tail grading of pumice lapilli and fiamme (flattened pumice) upward; the tuff grades upward through tuffaceous mudstone into mudstone (Core 22R; 1266.0–1267.67 mbsf; red box shows location of Fig. F31D. Close-up and interpretation (22R-4, 74–130 cm; 1266.74–1267.30 mbsf). (Continued on next three pages.)

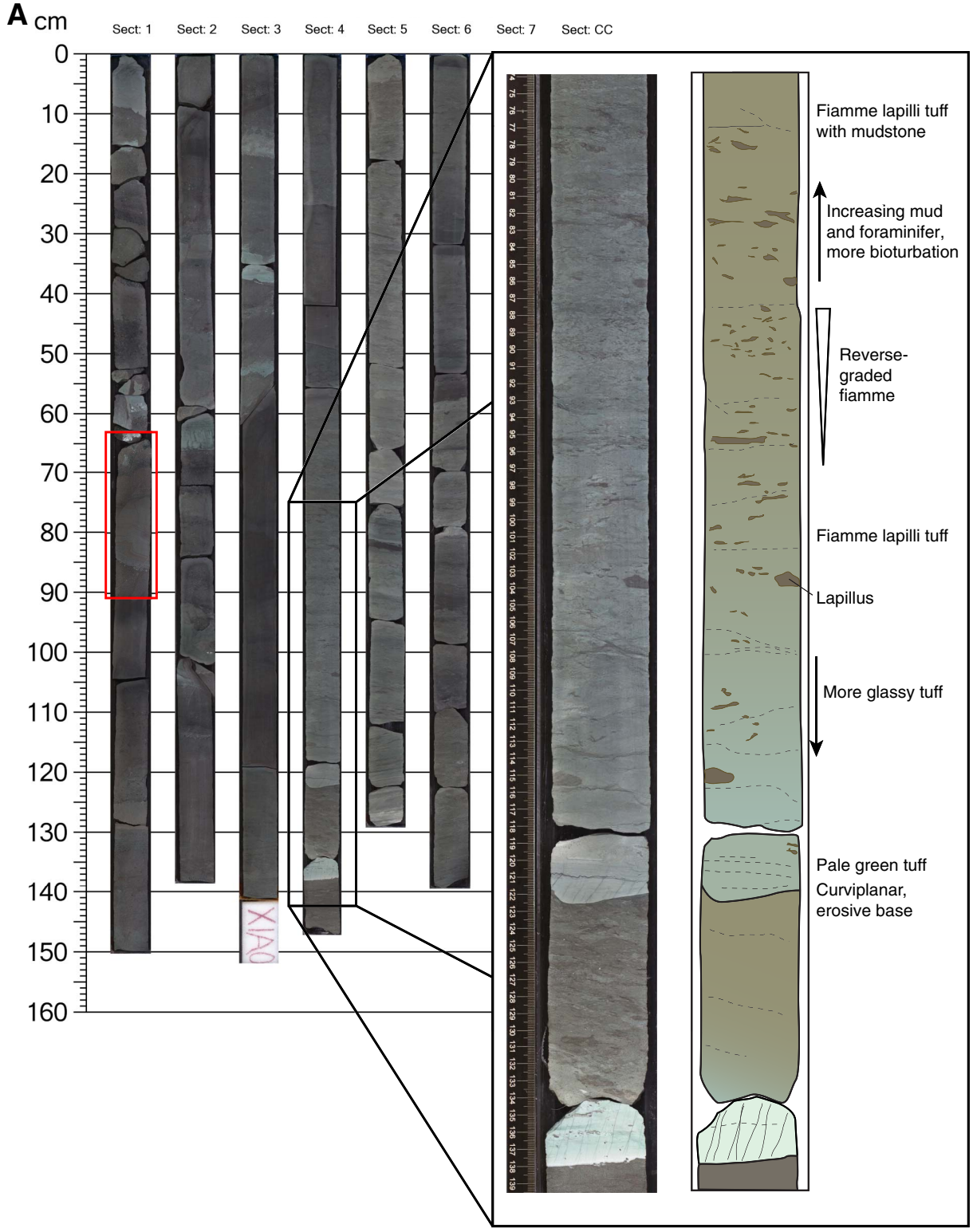

**Figure F31 (continued). B.** Thin section photomicrographs of evolved tuff: (a) light green tuff composed of a formerly glassy matrix with pyroxene and feldspar crystals (8R-4, 45–48 cm; TS83; 1136.45–1136.48 mbsf); (b) intercalated white and gray tuff with a crystal-rich and vitric-rich layers. The crystal-rich layer is composed of plagioclase, clinopyroxene, and amphibole (8R-1, 59–62 cm; TS82; 1133.59–1133.62 mbsf); (c) dark gray tuff composed of altered glassy shards, plagioclase, and opaques (7R-7, 71–73 cm; TS81; 1130.71–1130.73 mbsf); (d) stratified brown tuff composed of altered glass shards, plagioclase, and opaques (19R-1, 81–84 cm; TS95; 1233.81–1233.84 mbsf). (Continued on next page.)

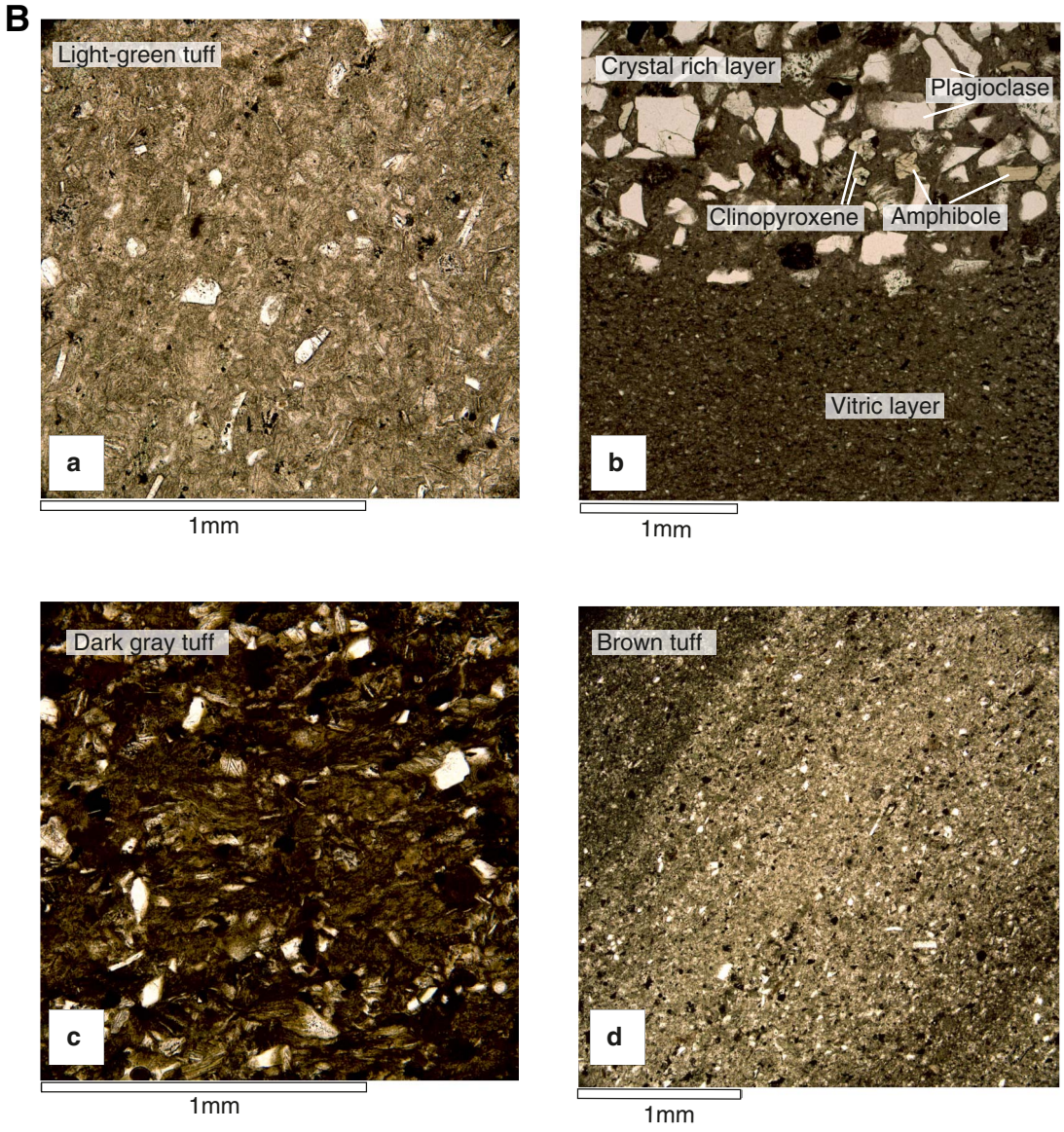

**Figure F31 (continued). C.** Lapilli tuff and lapillistone: (a) white to light-gray lapilli tuff with large pumice lapilli (20R-2, 22–25 cm; TS97; 1244.22–1244.25 mbsf) with matrix composed of glass shards, smaller pumice lapilli, and crystals of plagioclase; (b) clast-supported dark gray-green lapilli tuff with pumice lapilli and volcanic lithic clasts and plagioclase and opaque crystals (16R-6, 114–117 cm; TS91; 1211.14–1211.17 mbsf); (c) clast-supported dark gray-green pumice lapilli tuff with crystals of pyroxene, plagioclase, and opaque minerals (17R-2, 114–117 cm; TS92, 1216.14–1216.17 mbsf). The plagioclase crystals in TS91 and TS92 contain melt inclusions.

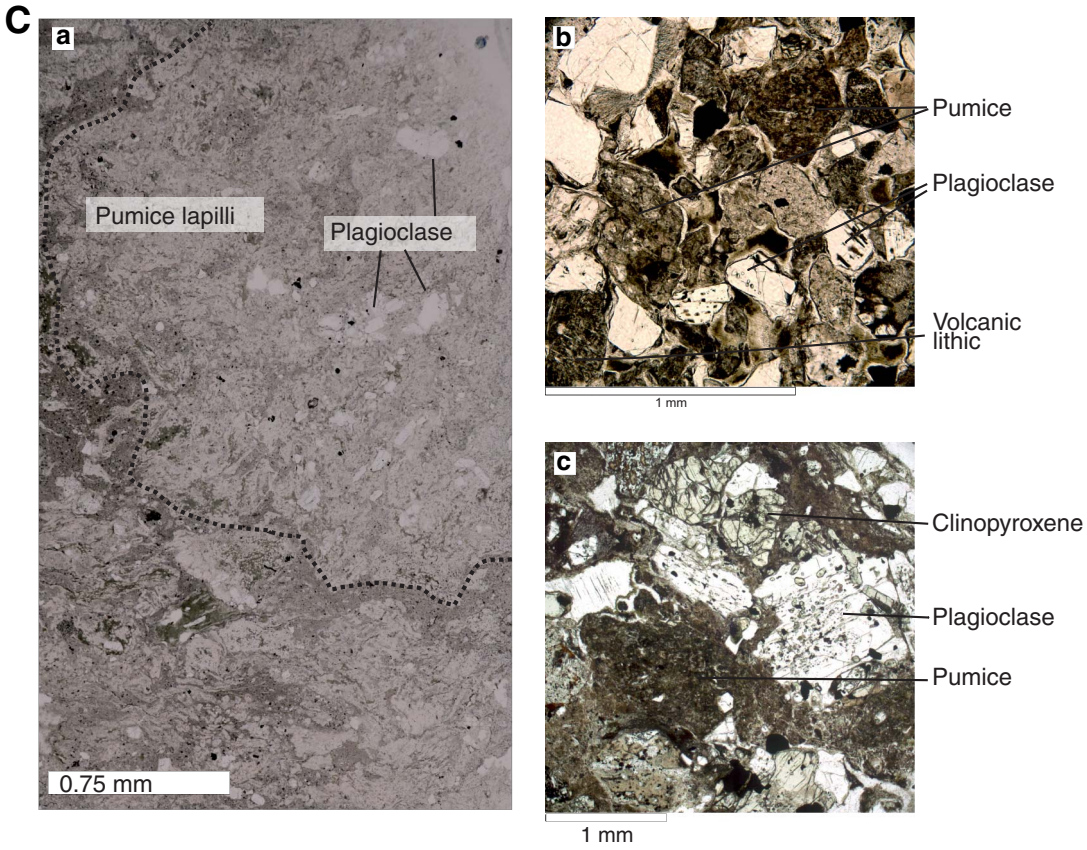

**Figure F31 (continued). D.** Soft-sediment faulting in a sequence of interlayered tuff, tuffaceous mudstone, and tuffaceous sandstone (22R-1, 64–90 cm; 1262.44–1262.70 mbsf).

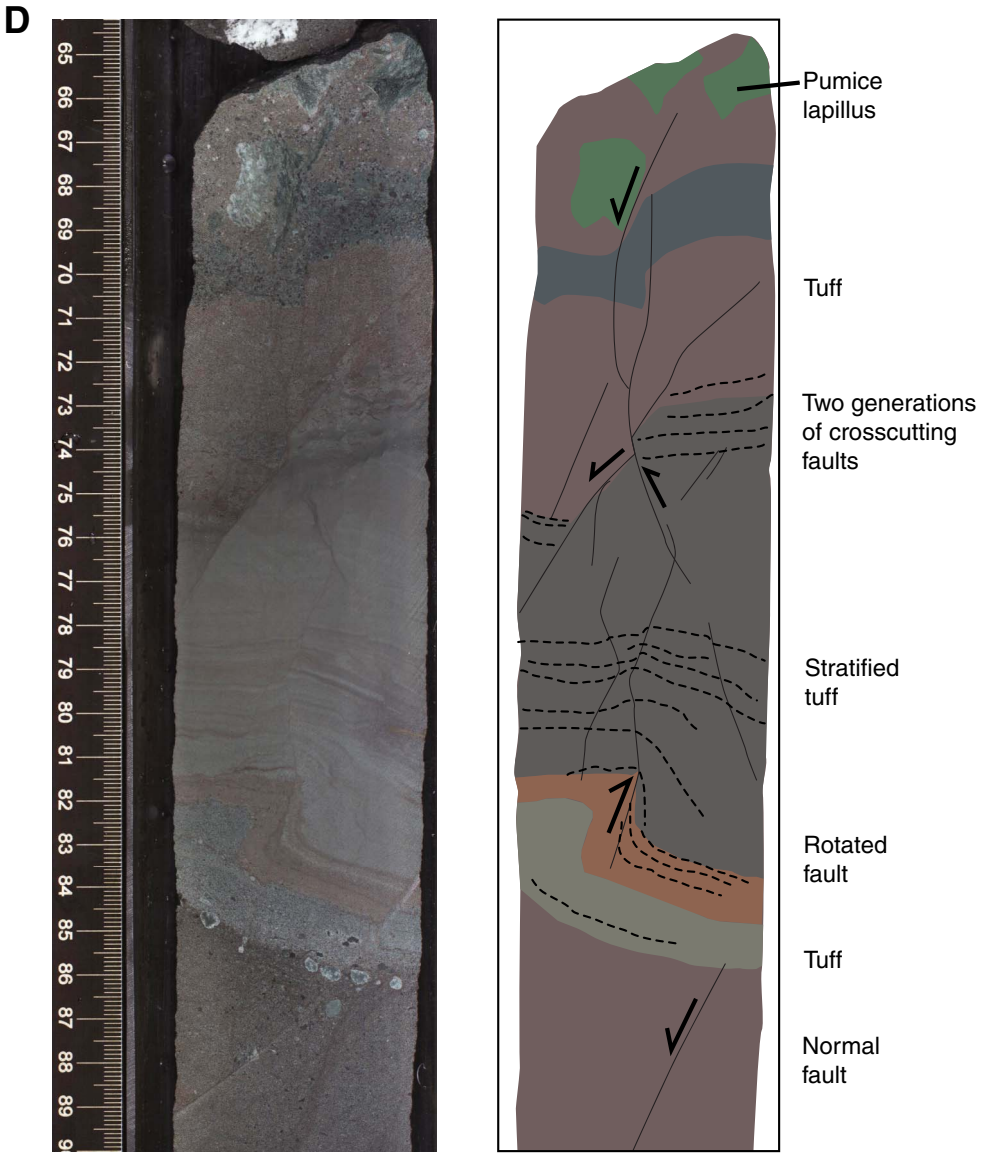

**Figure F32.** Representative lithologies and interpretation, Hole U1437E, Unit VI (Core 39R; 1427.1–1436.35 mbsf). **A.** Matrix-supported monomictic lapilli tuff with fiamme, with stratification and inclined basal contact (39R-6, 0–17 cm; 1433.43–1433.60 mbsf) and matrix-supported monomictic lapilli tuff and tuff intervals (39R-8; 1435.7–1436.35 mbsf). Reddish horizons are mudstone rich. (Continued on next three pages.)

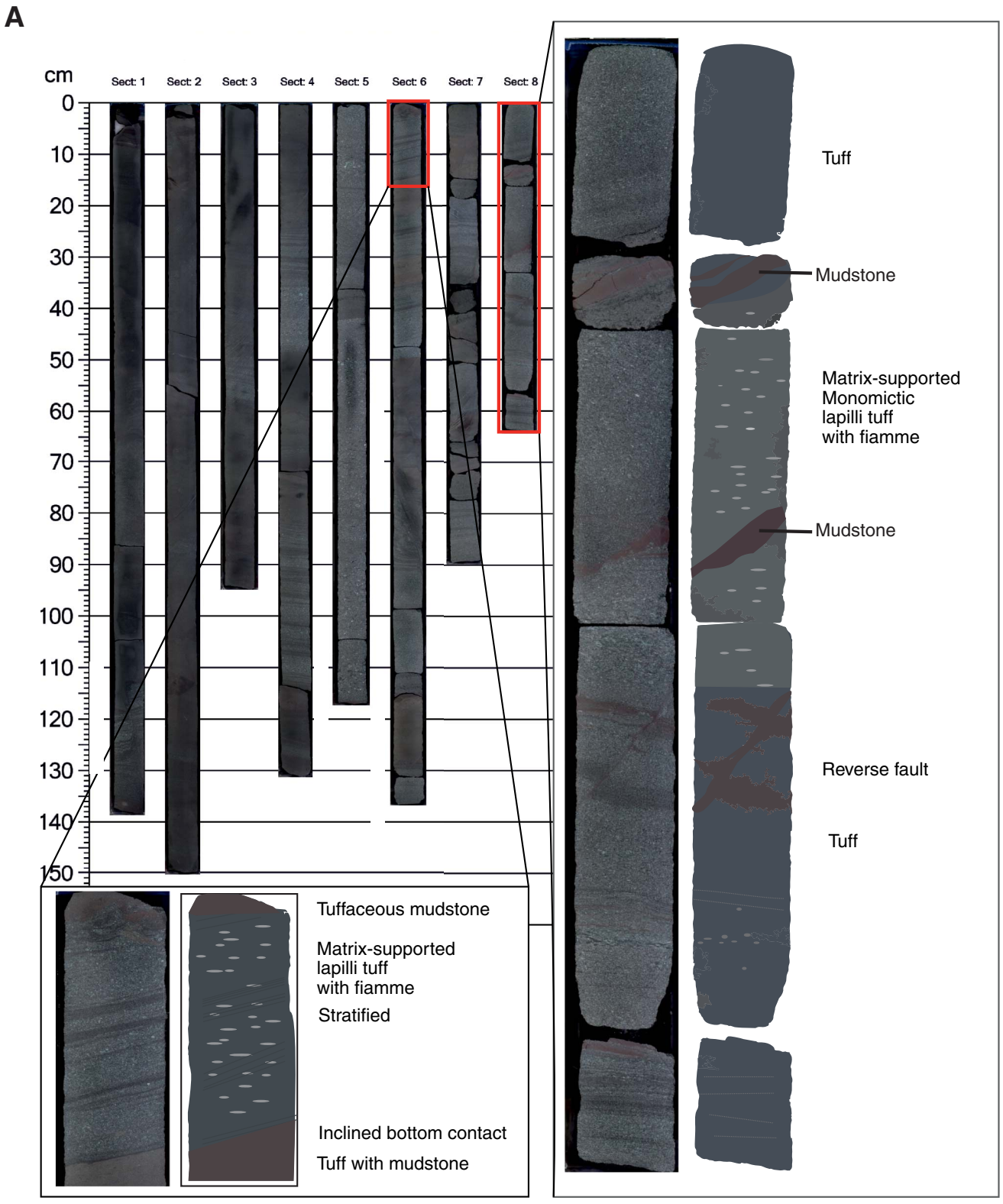

**Figure F32 (continued). B.** Left: clast-supported polymictic lapillistone with vitric clasts (subrounded pumice) and lithic clasts (subrounded mudstone and evolved volcanics) (33R-6, 130–146 cm; 1383.08–1383.21 mbsf). Right: clast-supported polymictic lapilli tuff with vitric clasts (subrounded pumice) and lithic clasts (rounded mafic and evolved volcanics) (34R-5, 8–21 cm; 1376.81–1376.97 mbsf). (Continued on next page.)

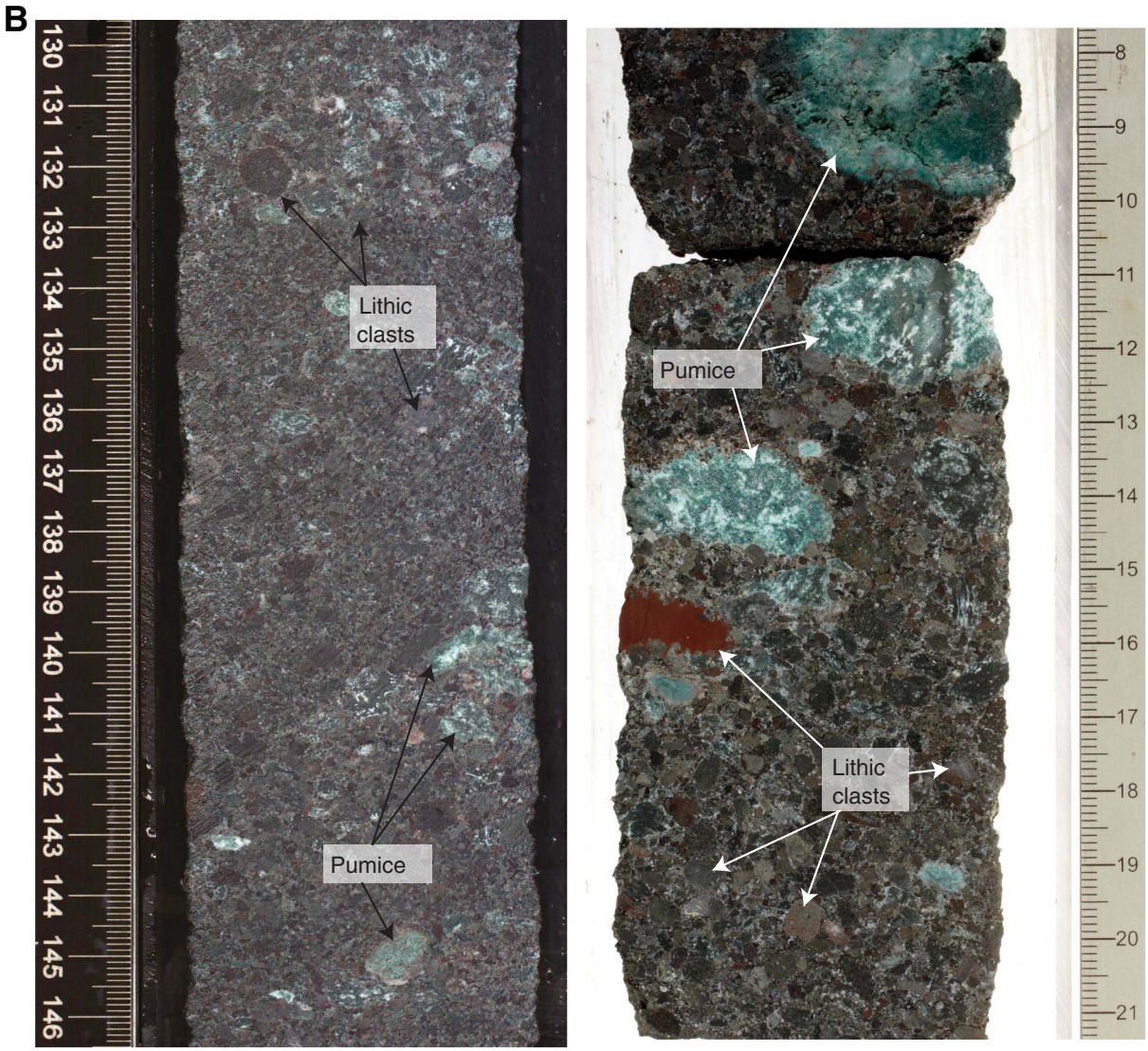

**Figure F32 (continued).** C. Variety of clast types and differences: (top) clast-supported polymictic lapilli tuff (33R-22, 36–39 cm; TS118; 1370.3–1370.33 mbsf); (bottom) matrix-supported polymictic lapilli tuff (29R-3, 38–41 cm; TS112; 1333.08–1333.11 mbsf). (Continued on next page.)

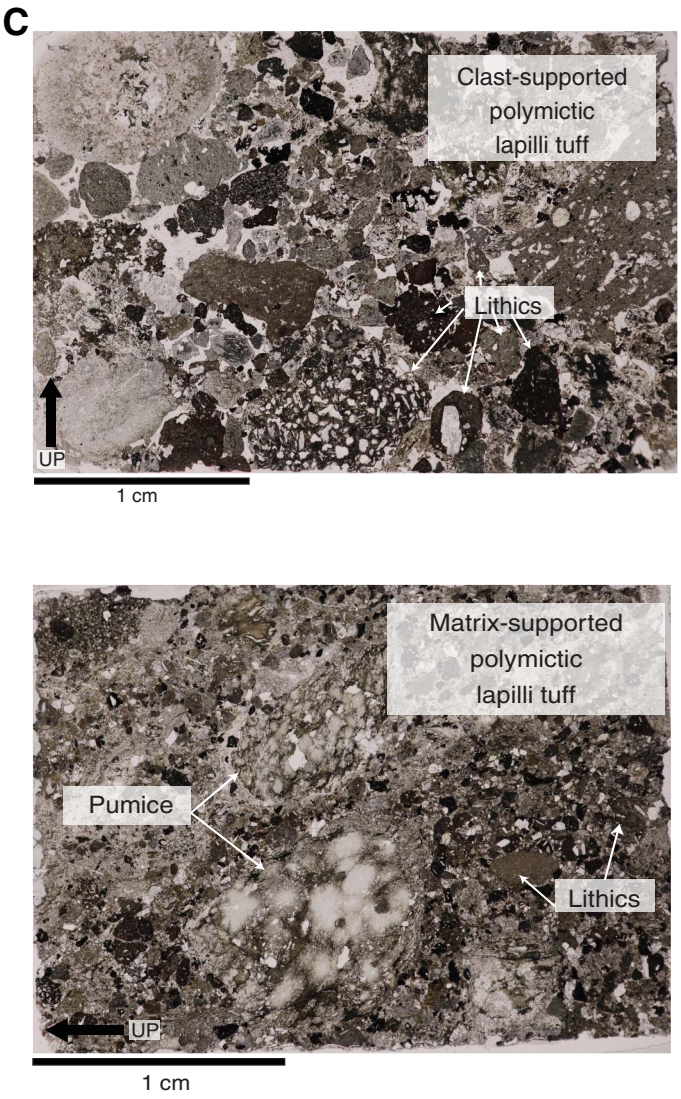

**Figure F32 (continued). D.** Stratified tuff with fiamme on (left) macroscopic and (right) microscopic scale (39R-8, 45–65 cm; 1436.15–1436.35 mbsf).

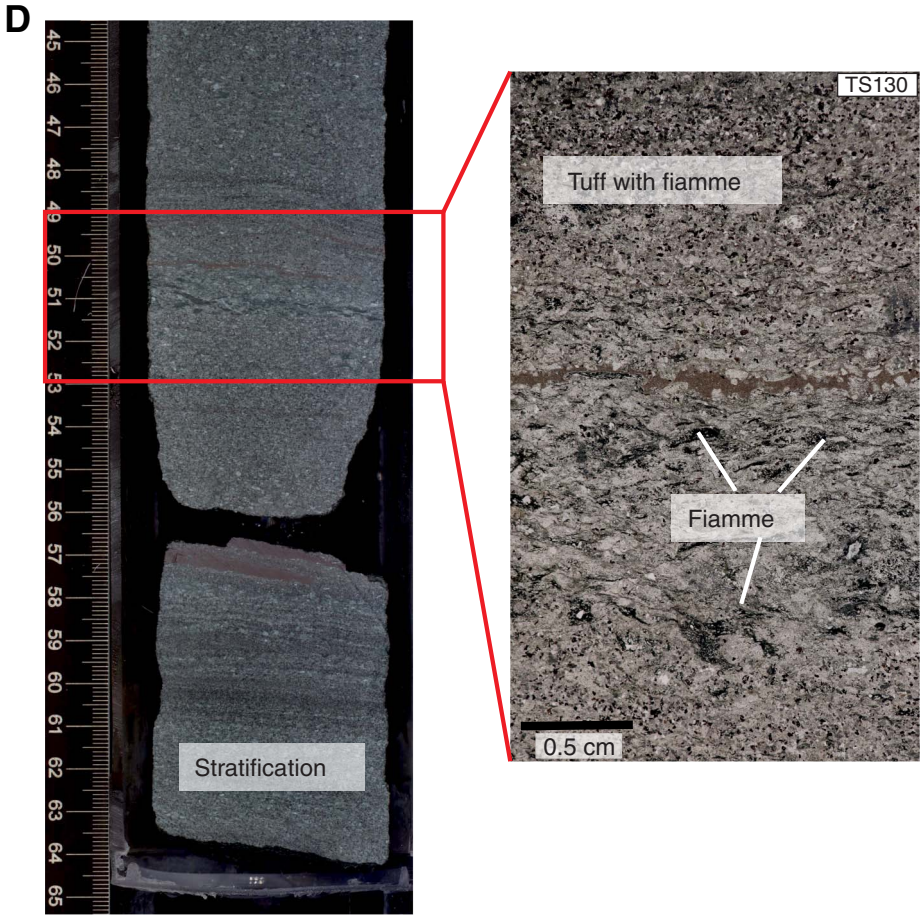

**Figure F33.** Representative lithologies/interpretation, Hole U1437E, igneous Unit 1. **A.** Unit 1 relationship with Unit VI (35R; 1388.1–1397.9 mbsf). Only 1.2 m was recovered but its true thickness may be up to 6.5 m (see text). A second interval of similar material lower in the core (labeled "?") is only 5 cm thick (35R-3, 59–64 cm) and has no recovered contacts; it was therefore described as a clast (note that similar clasts are described from the host Unit VI, see text). (Continued on next two pages.)

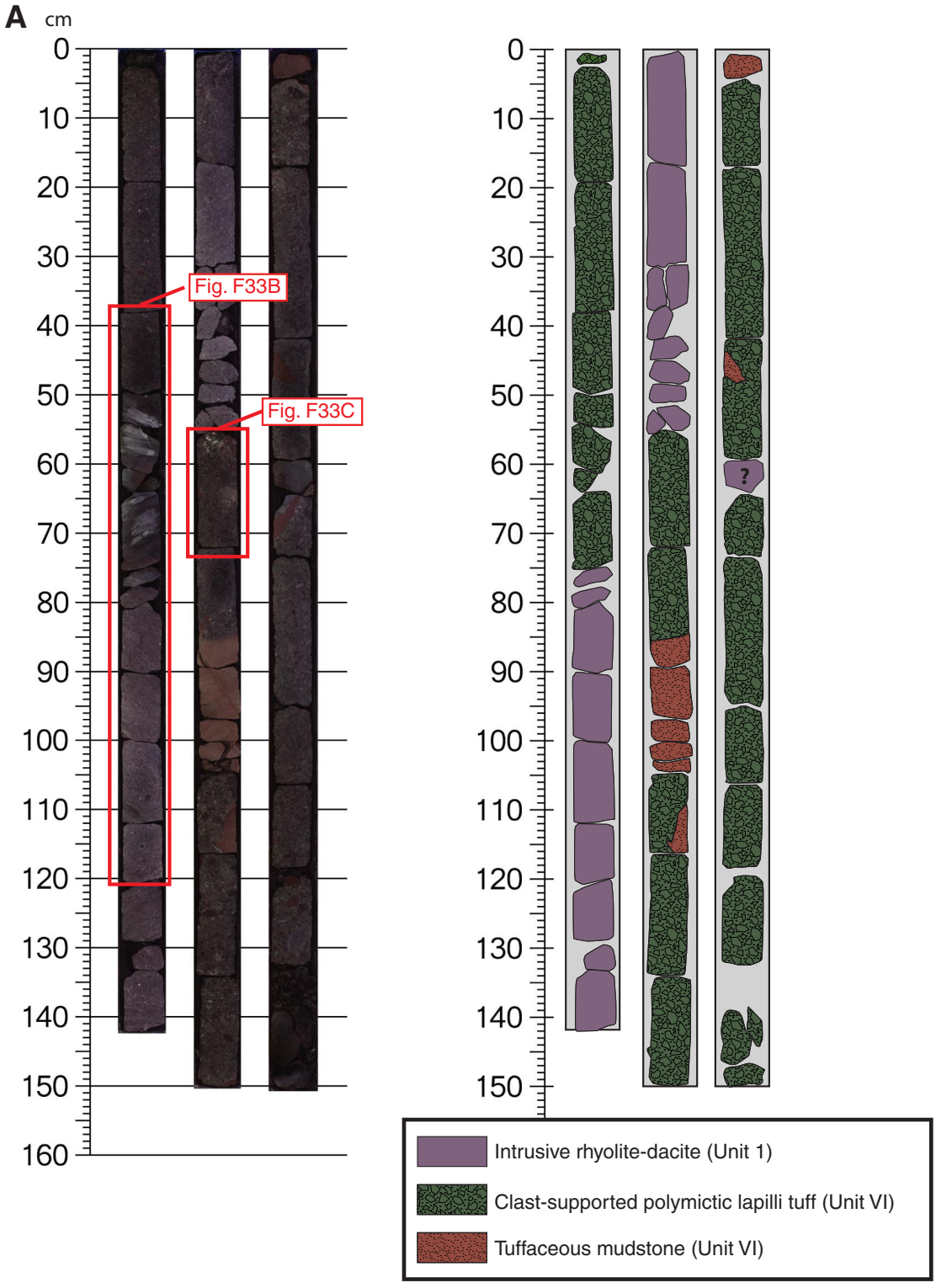

**Figure F33 (continued). B.** Upper contact on igneous Unit 1 intrusive rhyolite and relationship with its host in Unit VI (35R-1; 1388.1–1397.9). For discussion, see text. Photomicrographs of the (a, b) margin (35R-1, 76–78; TS121; 1388.86–1388.88 mbsf) and (c, d) interior (35R-1, 115–118; TS122; 1389.25–1389.27 mbsf) show the chilled upper margin of igneous Unit 1. (Continued on next page.)

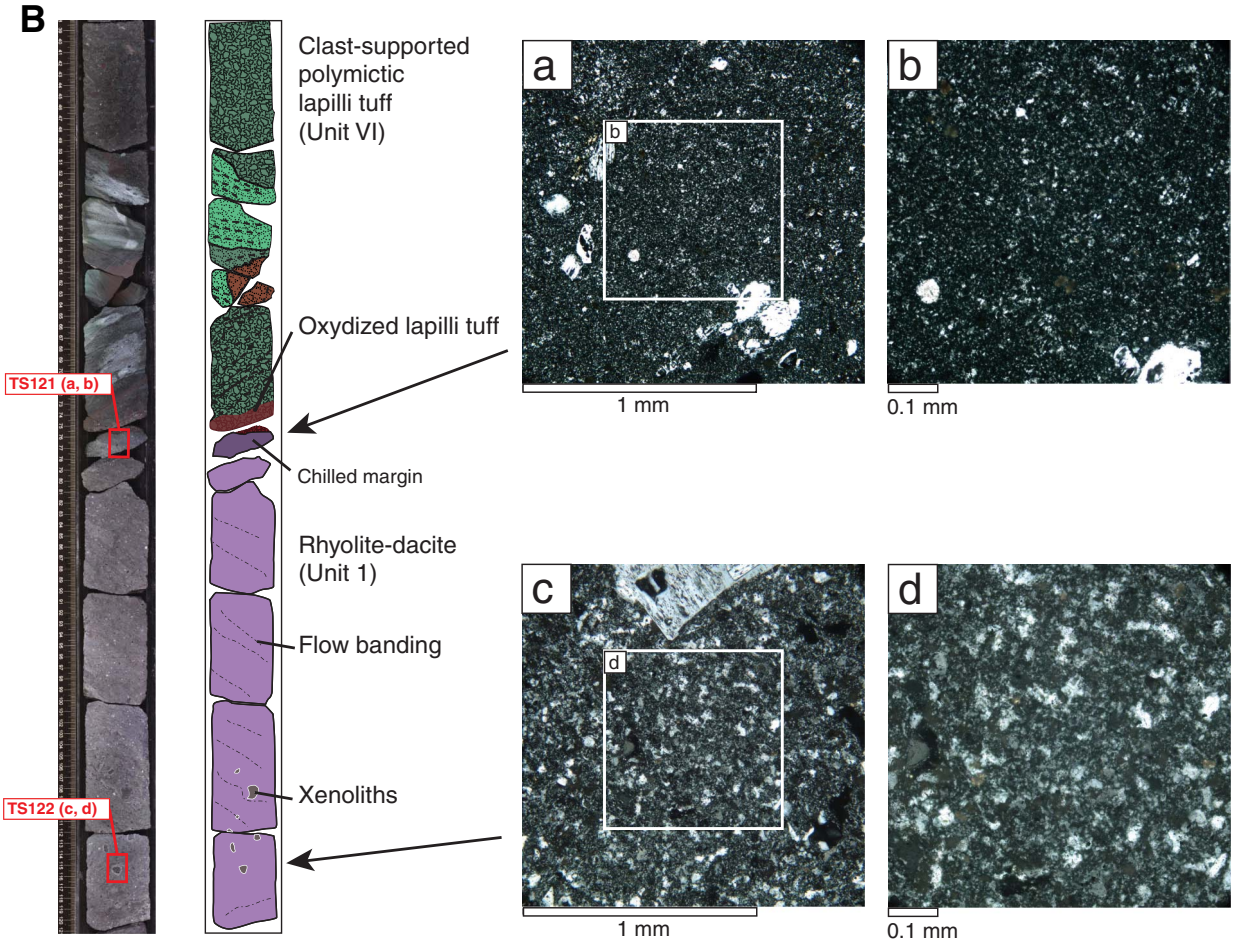

**Figure F33 (continued).** C. Peperitic lower contact on igneous Unit 1 intrusive rhyolite (35R-2, 55–73 cm).

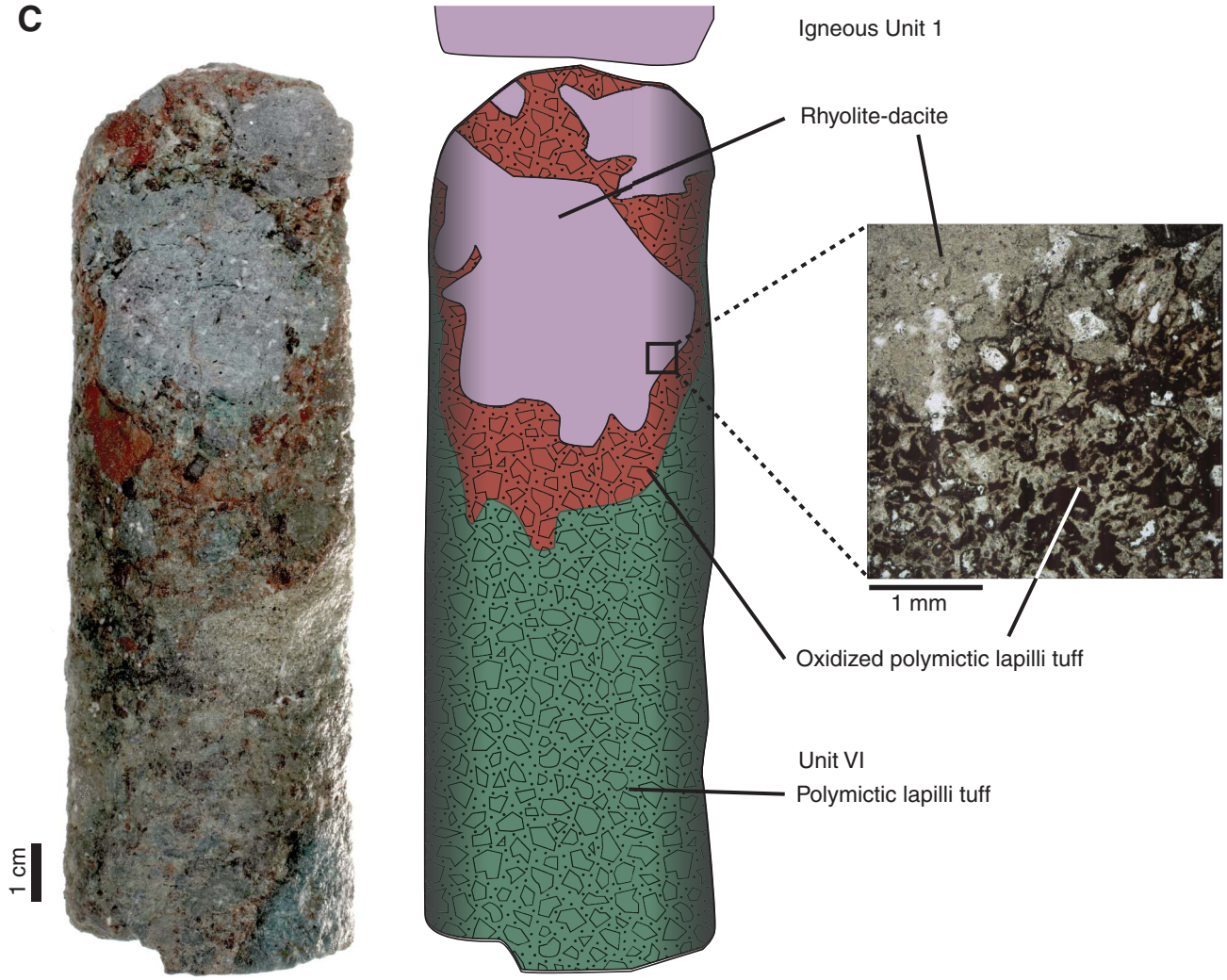

**Figure F34.** Glassy deposit, Hole U1437E, Unit VII. **A.** Homogeneous black glassy lapilli tuff and lapillistone in the upper 183.93 m of Unit VII showing glass, plagioclase (plag), and clinopyroxene (cpx) in (left) plane-polarized light (PPL) and (right) cross-polarized light (XPL) (45R-1, 74–77 cm; TS134; 1486.14–1486.17 mbsf). (Continued on next two pages.)

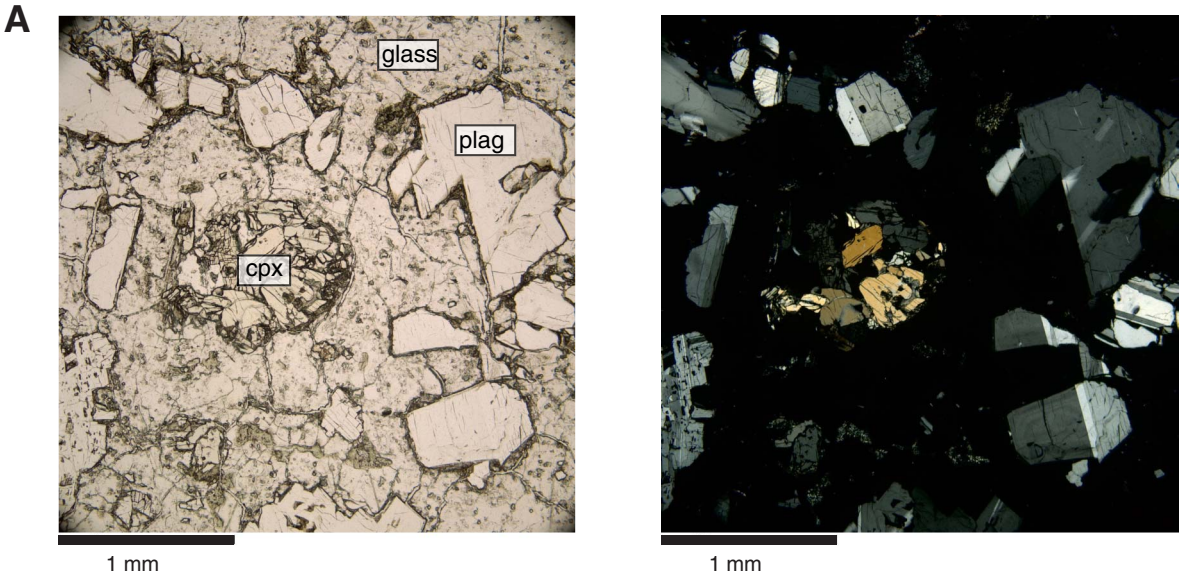

**Figure F34 (continued). B.** Black glassy lapilli tuff and lapillistone with one of the rare lithic clasts, in (left) PPL and (right) XPL. Glass fragments (0.5–3 mm on average) have boundaries that are very poorly defined (43R-1, 36–40 cm; TS142; 1466.26–1466.30 mbsf). (Continued on next page.)

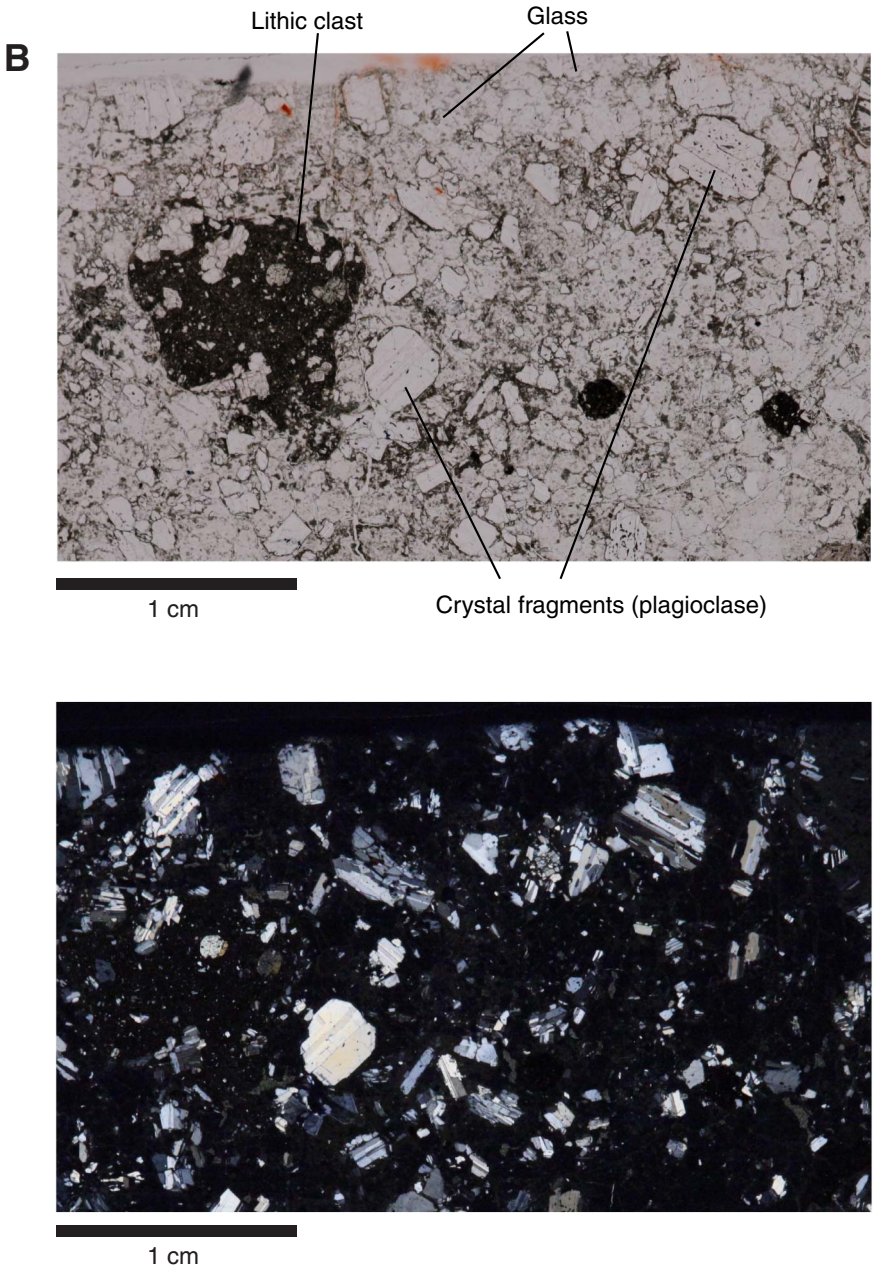

**Figure F34 (continued). C.** Green lithic lapilli tuff with blocks that dominates the lower part of Unit VII (57R-1, 88–105.5 cm). Note the complexly embayed and quenched margins on the blocks, which may represent clasts or the margins of intrusions or lava (see text).

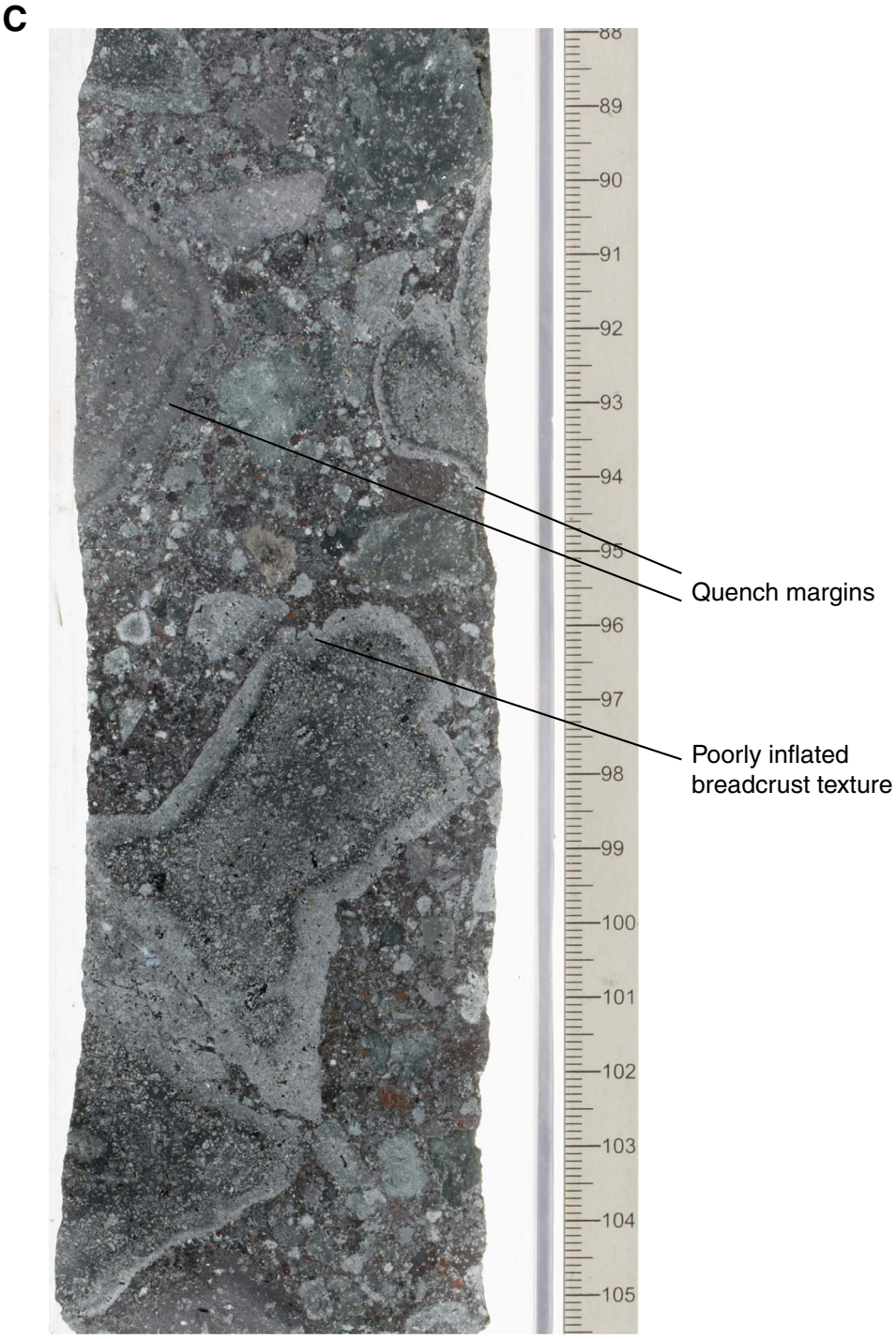

**Figure F35.** Headspace methane and ethane concentrations, Holes U1437B, U1437D, and U1437E. Methane and ethane are plotted at 0 when below detection.

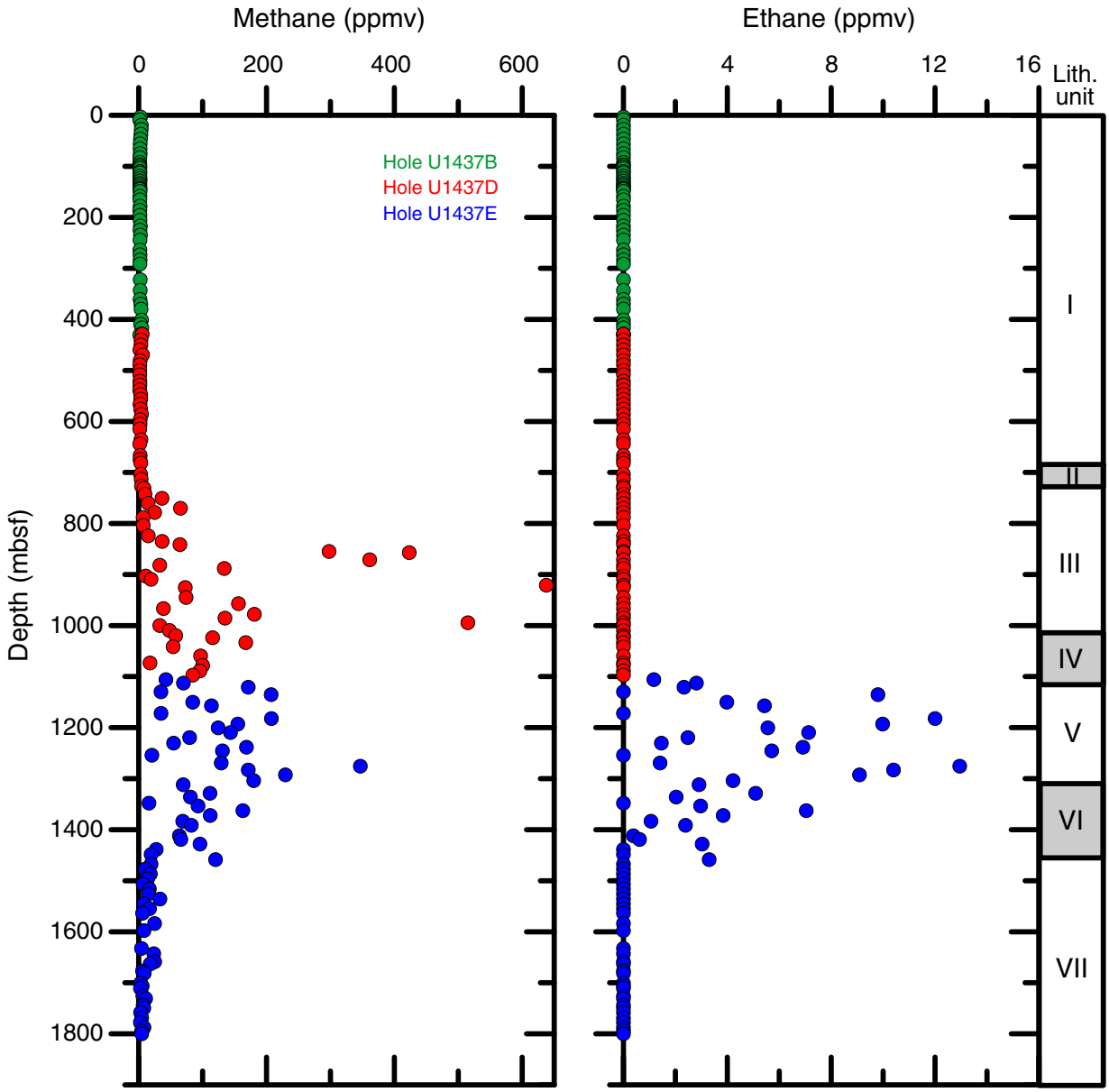

**Figure F36.** Pore water geochemical depth profiles, Holes U1437B and U1437D. Horizontal dashed line =s boundary of Holes U1437B and U1437D. Vertical dashed lines = IAPSO seawater compositions.

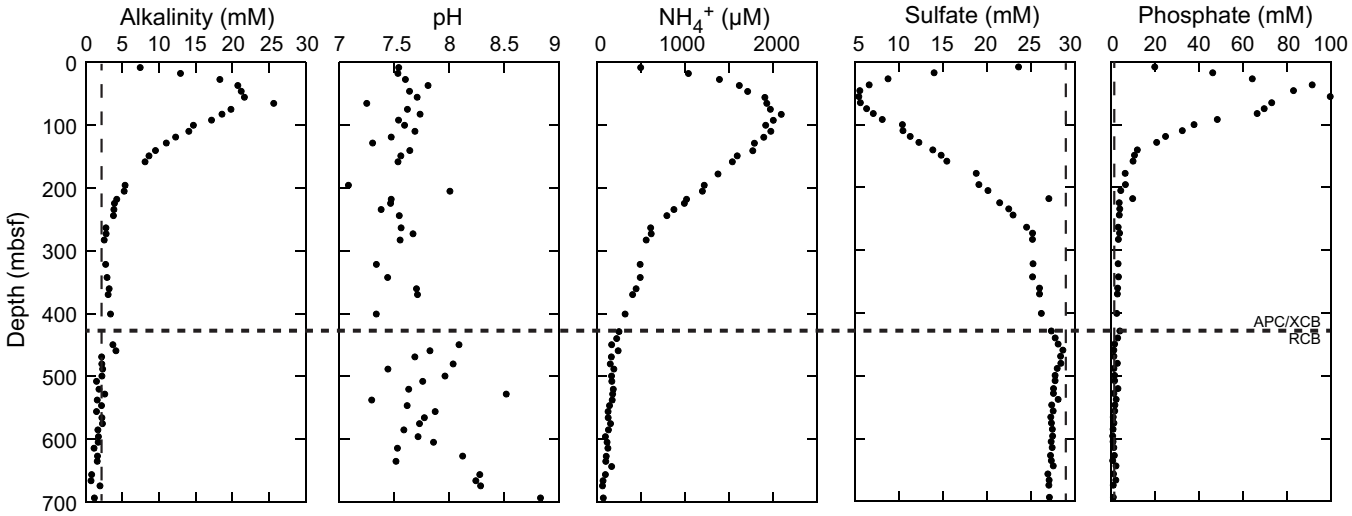

**Figure F37.** Pore water geochemical depth profiles for Na, K, Ca, and Mg (ion chromatography) and Li and Si (ICP-AES), Holes U1437B and U1437D. Horizontal dashed line = boundary of Holes U1437B and U1437D. Vertical dashed lines = IAPSO seawater compositions (seawater Si [99 µM] is below scale).

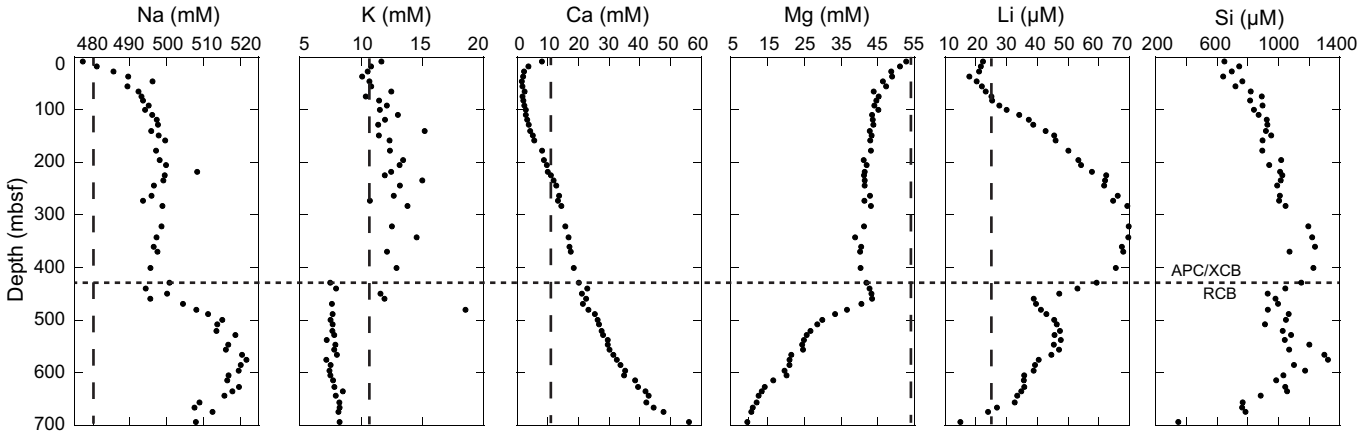

**Figure F38.** Calcium carbonate depth profiles, Holes U1437B–U1437E. $CaCO_3$ values are a 5-point average. For comparison, the atomic ratios of total organic carbon to total nitrogen ($TOC/TN_{at}$) contents are shown. Zero values are assigned when below detection.

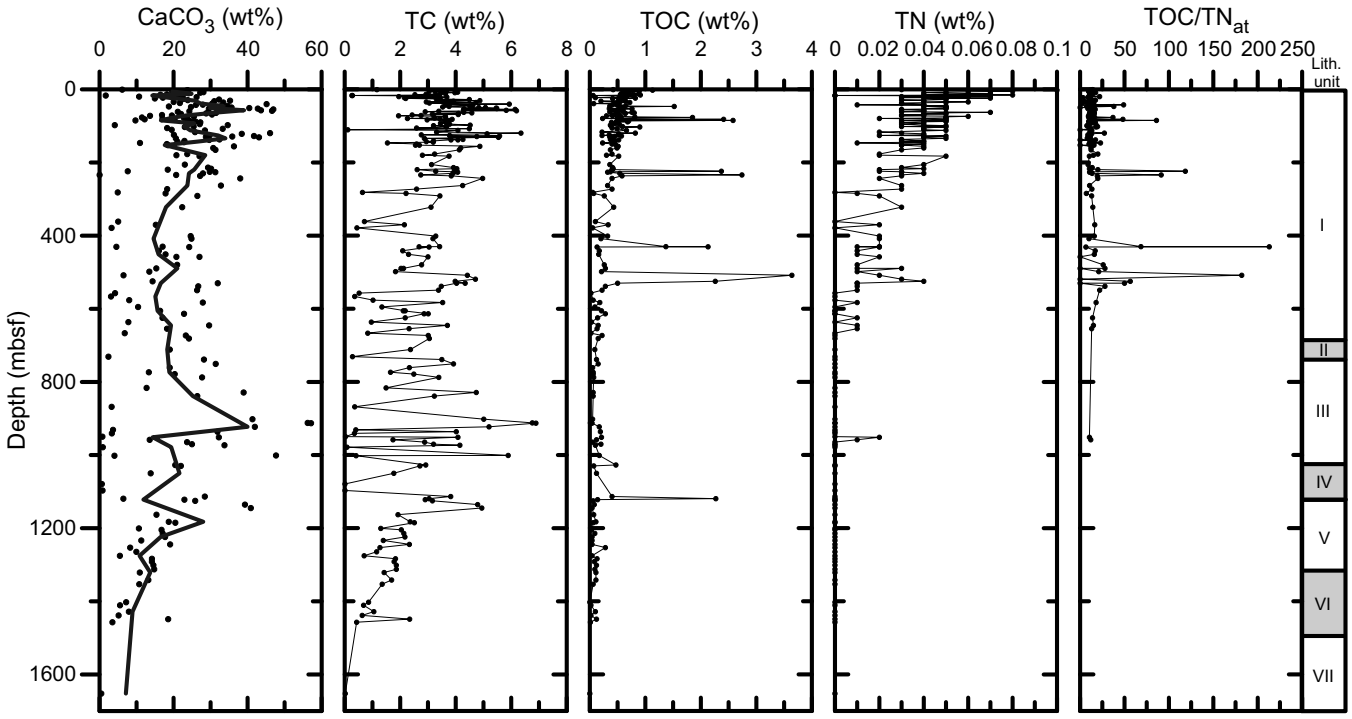

**Figure F39.** Mud and mudstone compositions, Site U1437, determined by inductively coupled plasma–atomic emission spectroscopy (ICP-AES) and portable X-ray fluorescence scanner (pXRF). End-member compositions (averages for Izu arc-front basalt–dominant island volcanoes, Izu arc-front rhyolite–dominant submarine calderas, Izu rear-arc lava, Ryukyu dacite, Chinese loess, and marine carbonate) are plotted together with a schematic mixing triangle. Data plotting outside the triangle can be mostly explained by simplifications in the end-member compositions. Mud data for fore-arc Site U1436 are plotted for comparison. Data sources: Scudder et al. (2009), Morse and Mackenzie (1990).

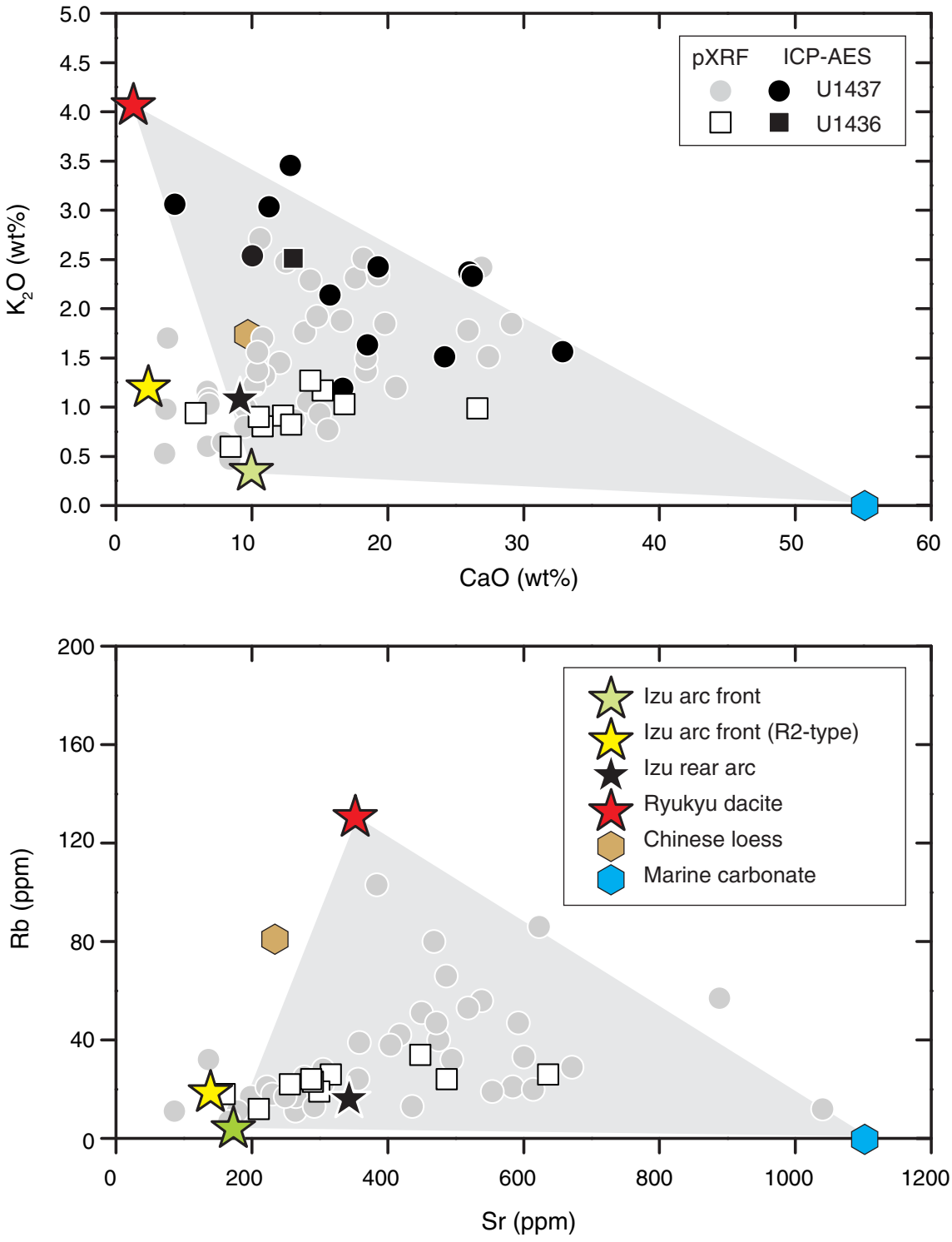

**Figure F40.** Depth variations for mud and mudstone analyzed by coulometry ($CaCO_3$), ICP-AES (Zr, Y, and $TiO_2$), and pXRF (Rb, Zr, Y, and $TiO_2$), Site U1437. Vertical lines = overall average for the site.

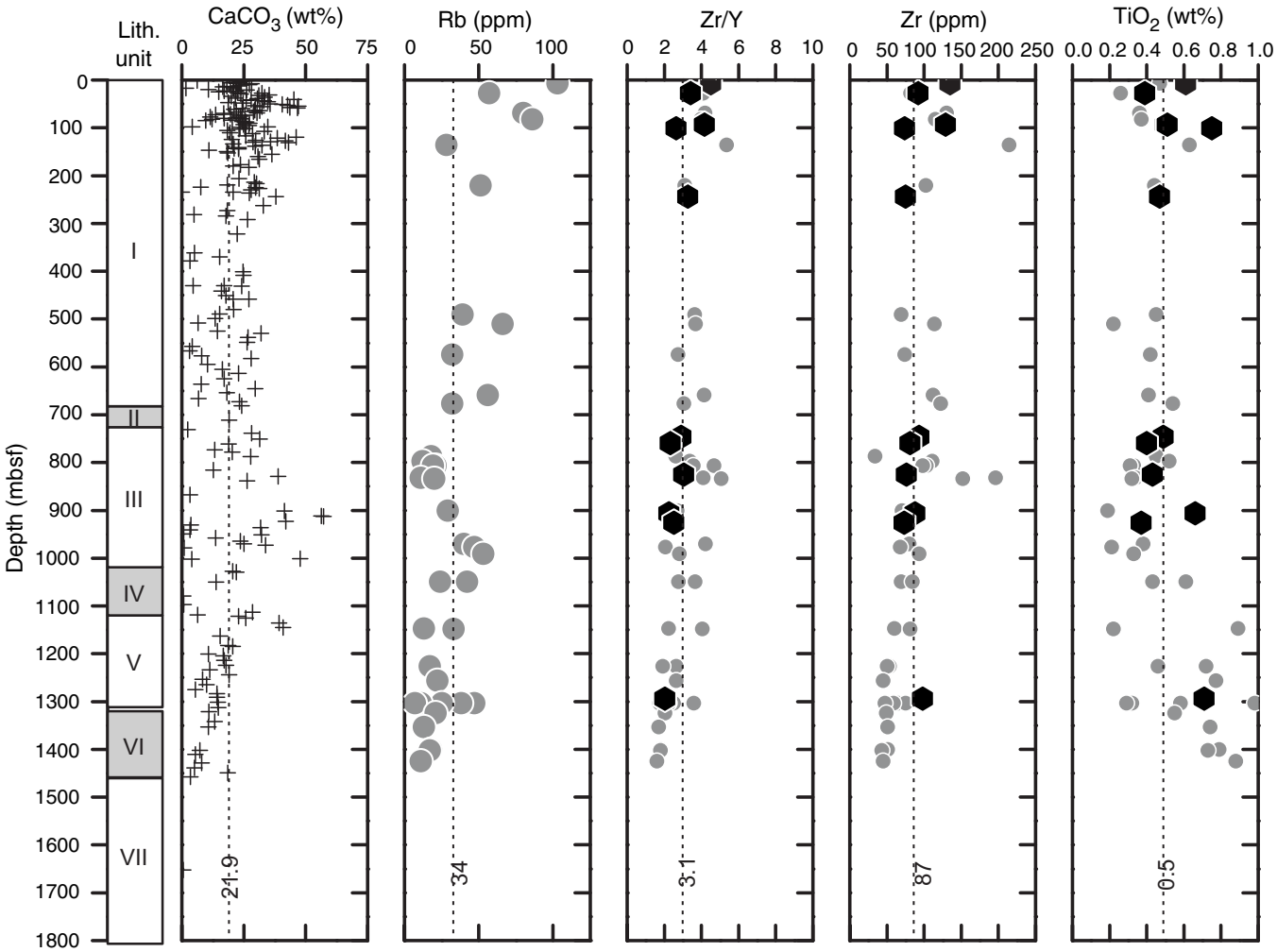

**Figure F41.** Rock-magnetic indexes SIRM/k and $S_{-0.3T}$ plotted against subbottom depth and compared with the pore water sulfate profile for Holes U1437B and U1437D.

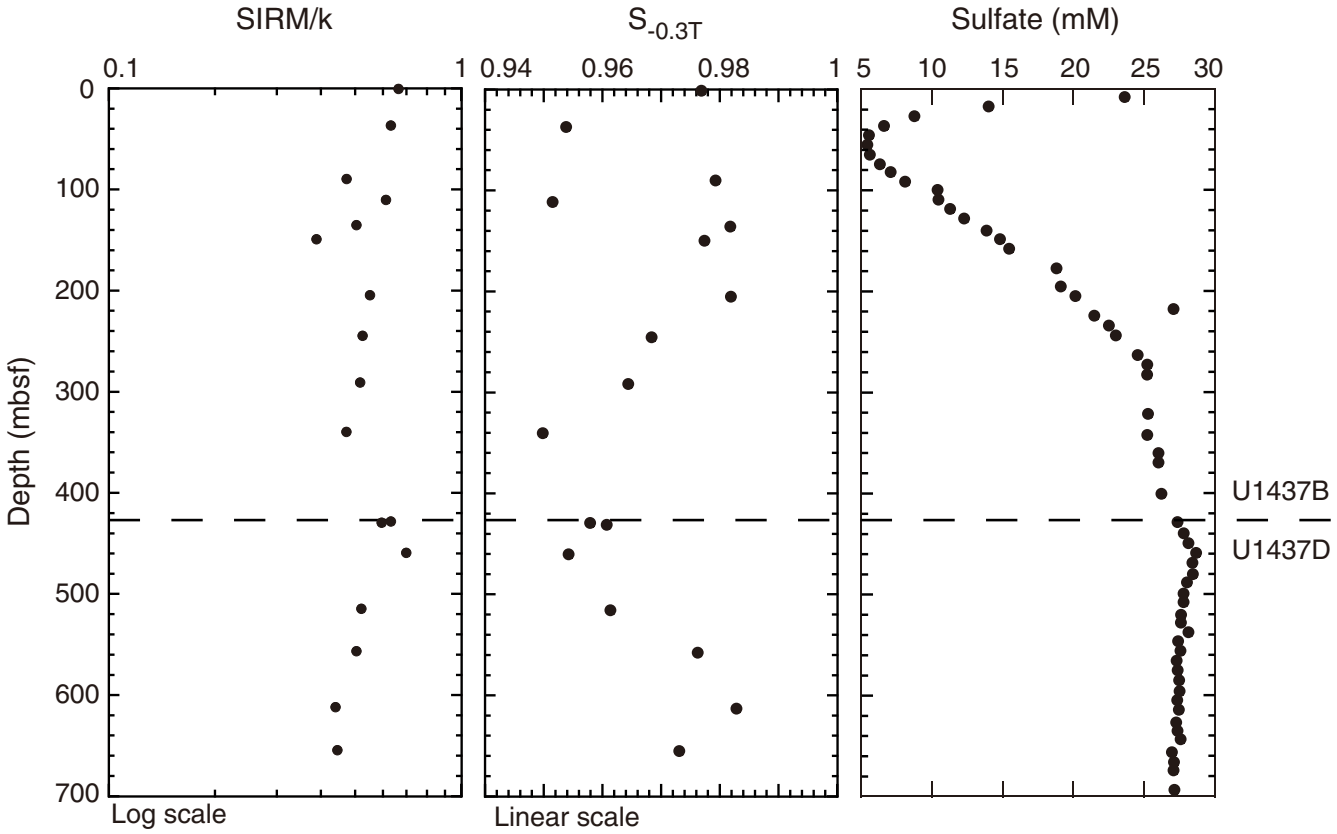

**Figure F42.** Major and trace element compositions vs. $SiO_2$ for volcaniclastic and igneous samples from sedimentary Units I–VII and igneous Unit 1 measured by ICP-AES, Site U1437. Fields circled by red and blue curves represent arc-front and rear-arc fields. **A.** $TiO_2$. **B.** $Al_2O_3$. **C.** FeO*. **D.** MnO. **E.** MgO. **F.** CaO. (Continued on next page.)

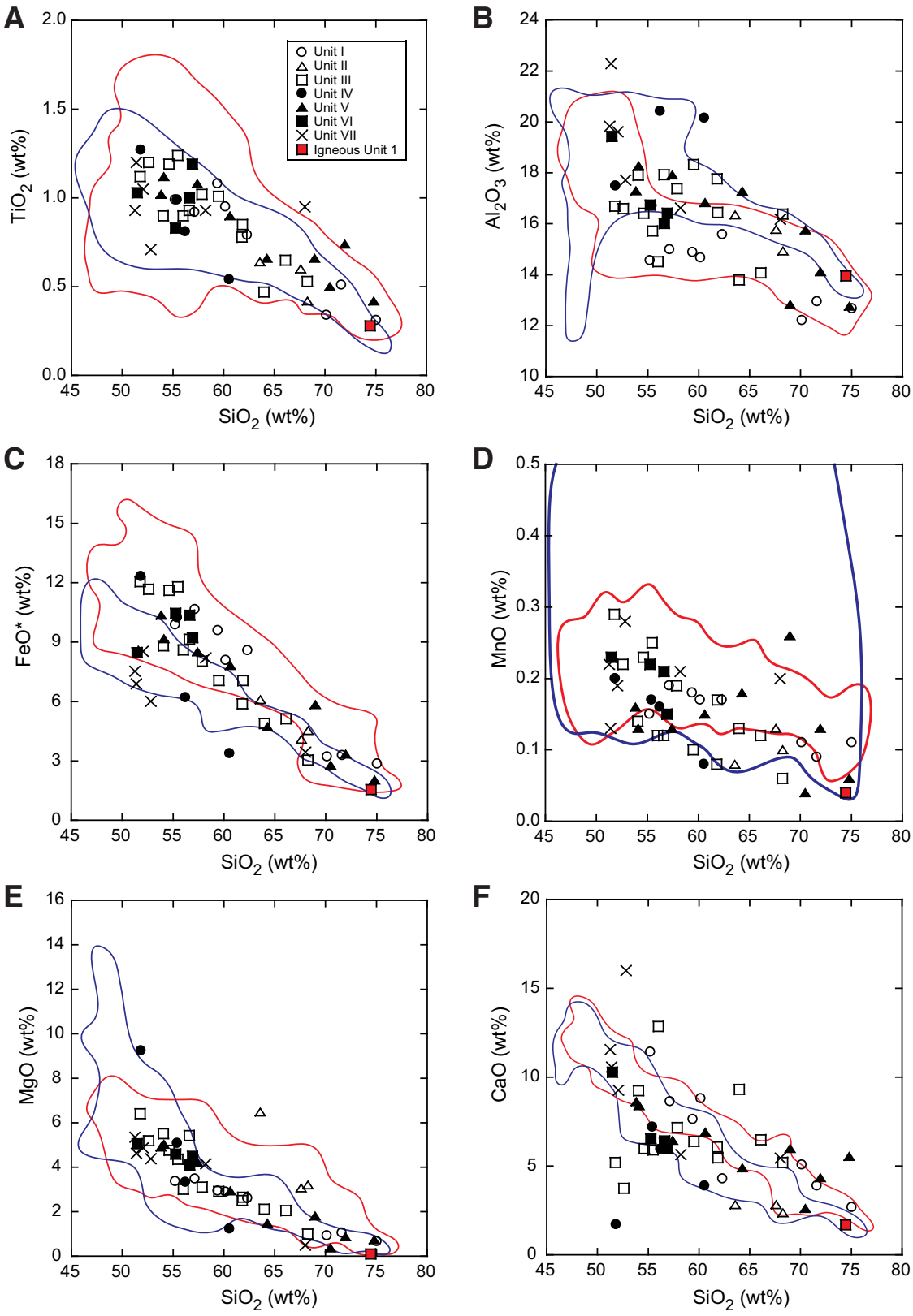

**Figure F42 (continued).** **G.** $Na_2O$. **H.** $K_2O$. **I.** $P_2O_5$. **J.** Sr. **K.** Ba. **L.** Zr.

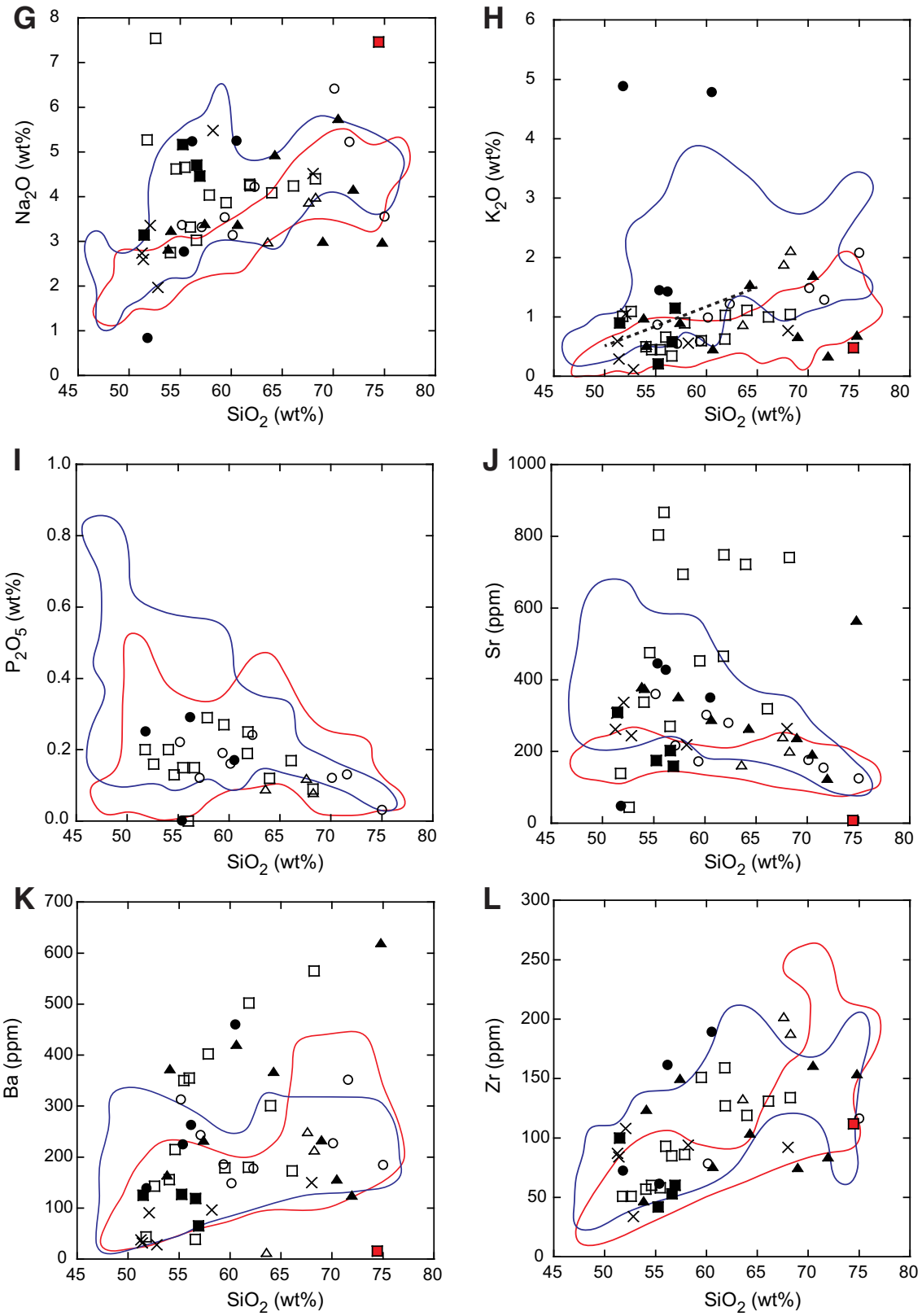

**Figure F43.** Zr/Y vs. $SiO_2$ for volcaniclastic and igneous samples from (**A**) literature and (**B**) sedimentary Units I–VII and igneous Unit 1. Note that R2 rhyolites from the arc front (rhyolite-dominant submarine calderas) are shown as a separate field as a subset of the arc-front data. Data sources: Tamura et al. (2009), Gill et al. (1994), Bryant et al. (2003), Straub et al. (2003, 2010), Hochstaedter et al. (2001), Ishizuka et al. (2002, 2003a, 2003b, 2006), Machida et al. (2003, 2008), Tollstrup et al. (2010). One outlier from the arc front field contains anomalously high Zr/Y and is not included in the "blob."

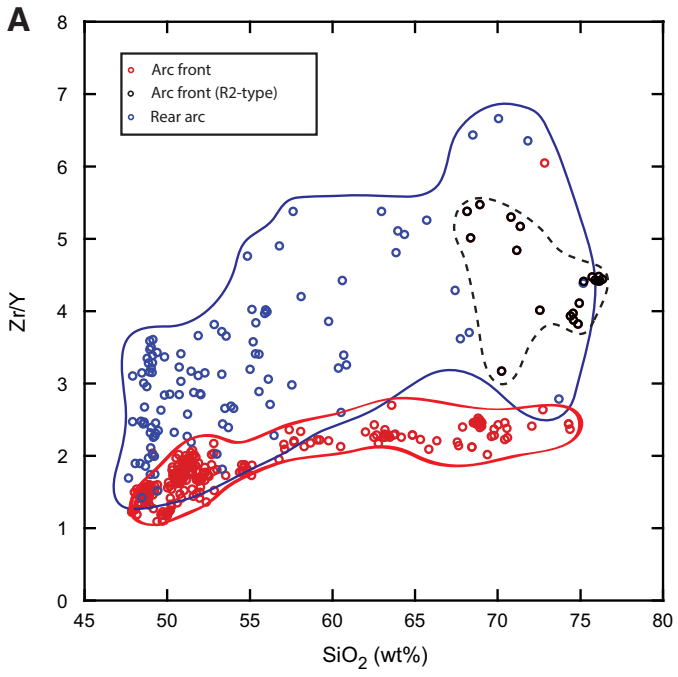


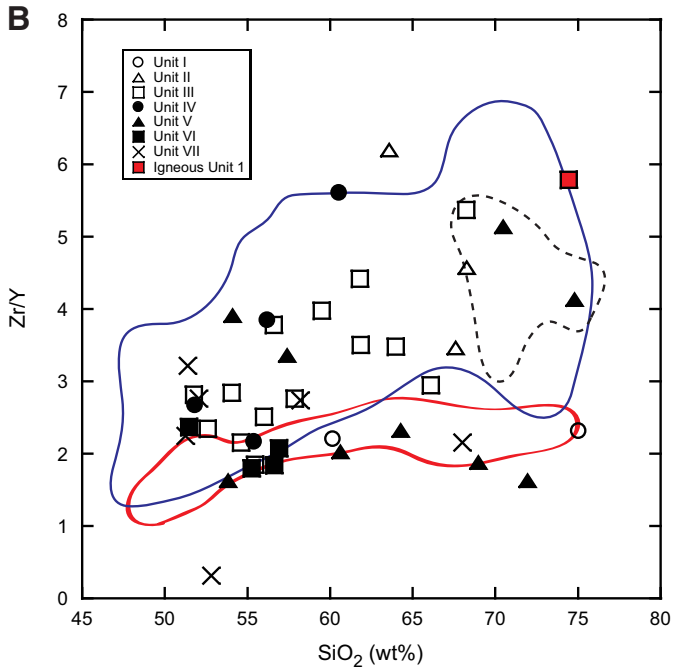

**Figure F44.** Zr and Zr/Y analyzed by pXRF and ICP-AES for volcaniclastic and igneous samples, Site U1437. Probability curves below depth panels show the relative distribution of Zr and Zr/Y in basalt-dominant island volcanoes from the arc front (including R1 rhyolites), rhyolite-dominant submarine calderas in the arc front (R2 rhyolites), and rear-arc volcanic rocks. Vertical lines = composition of the peaks in the literature data distributions. Ig1 = igneous Unit 1. Data sources: Tamura et al. (2009), Gill et al. (1994), Bryant et al. (2003), Straub et al. (2003, 2010), Hochstaedter et al. (2001), Ishizuka et al. (2002, 2003a, 2003b, 2006), Machida et al. (2003, 2008), Tollstrup et al. (2010).

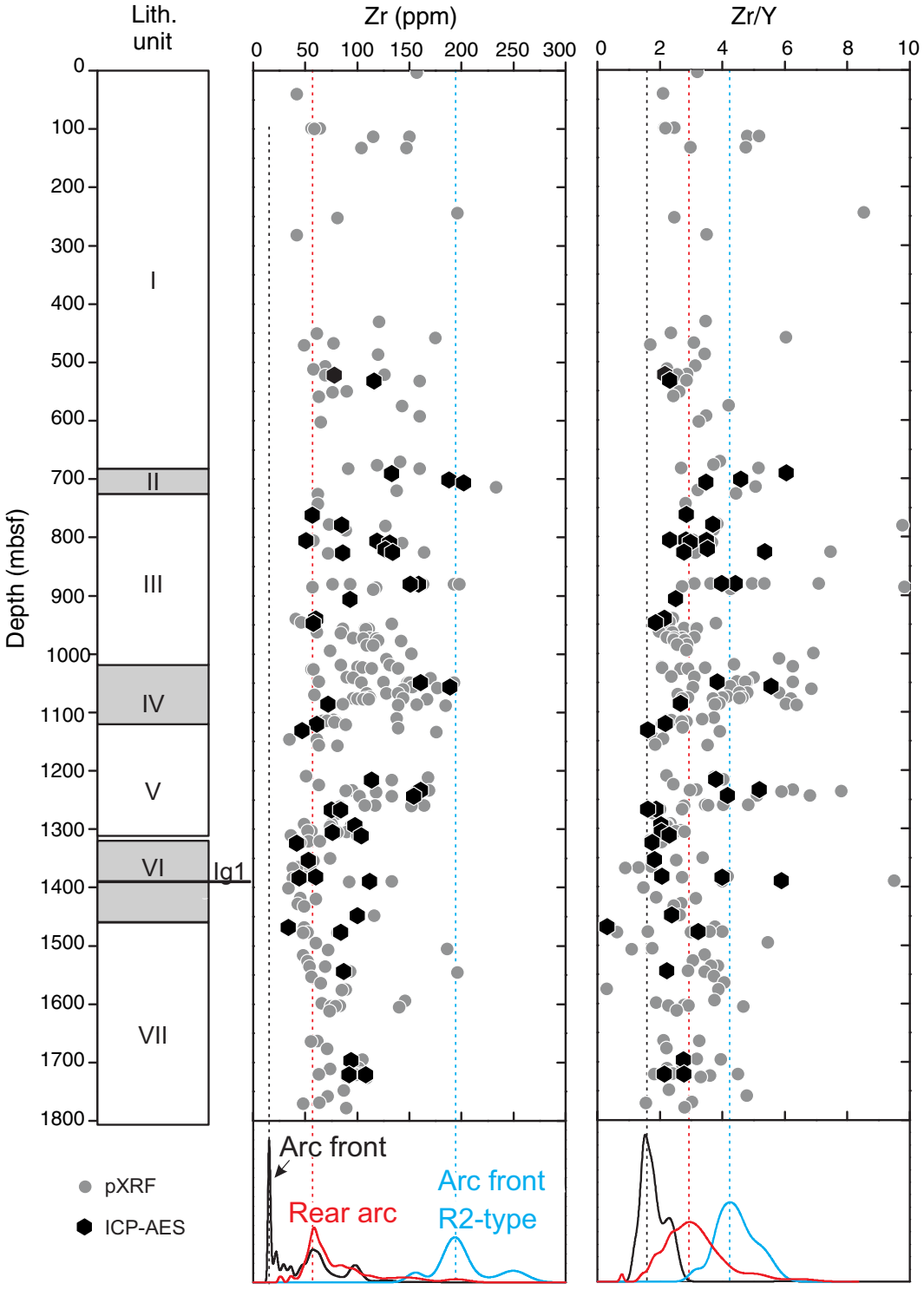

**Figure F45.** Event periodicity from tephra deposited in the past 6.9 My, Site U1437. Thin red line = actual computed frequencies/cored interval, thick red line = frequencies adjusted for core recovery.